UNIVERSITETET
I OSLO

Master's Thesis

Synthesis, Characterization and MOF incorporation of Benzodiazepines

Rafael Cortez Sgroi Pupo

Thesis submitted for a Master's degree in Organic Chemistry
60 credits, Spring 2022

Department of Chemistry
Faculty of mathematics and natural sciences

Preface

The work presented in this project was performed on the time period of February 2021 - June 2022 in the Catalysis research group at the Chemistry Department at the University of Oslo. My supervisors have been Ph.D. candidate Isabelle Gerz, Ph.D. candidate Erlend Aunan and associate professor Mohamed Amedjkouh.

I would like to thank my supervisors Mohamed Amedjkouh for giving me the opportunity of working on this project and many fruitful discussions over the years, Isabelle Gerz for guiding me through the whole project and for always finding time to help me, and last but not least Erlend Aunan for being my MOFervisor, always helping me decipher the complexities of this new field I have found to like.

I would like to thank Knut T. Hylland for always finding the time to help me fully understand my results and many discussions improving then my chemistry knowledge.

To my dear friends, Hannah Merlan Anor, Sahra Abukar Ahmed and Sara Elise Isachsen Moholdt, thank you for always being there for me, for your support throughout my whole master's degree, and everything you do for me, know that without you, this experience wouldn't have been the same. A special thanks to Sahra for proof-reading my thesis.

To my other friends in Norway, thank you for unlimited time and support.

I would like to thank my family and friends outside of Norway for always understanding that sometimes i am a bit too busy with lab/school, but that does not change my love for you.

A special thank you goes to my parents for encouraging and motivating not only on the taking of this degree, but every single day, I love you both from the bottom of my heart.

Thank you

Abstract

While 1,4-benzodiazepines are used intensively in the medicinal industry as antidepressants, 1,3-benzodiazepines have been less investigated. Recent findings in the Catalysis group at the University of Oslo show the formation of 1,3-dibenzodiazepines can be achieved by the reaction of diaminobiphenyls with an aldehyde. In this project, three novel 1,3-dibenzodiazipenes were isolated and were found to absorb and emit light. Their photophysical properties were investigated and compared with computational TD-DFT results. The postsynthetic incorporation of the diazepines in a series of mixed-linker BPDC-$(NH_2)_2$ UiO-67 MOFs was successful, after a thorough investigation on how the different percentages of BPDC-$(NH_2)_2$ linker can affect the MOF internal defects and stability.

Table of Contents

1 Introduction 2

2 Theory and Methods 9

2.1 Synthesis of mixed linker UiO-67 MOFs 9

2.2 Liquid Phase Digestion ^{1}H NMR 9

2.3 Thermogravimetric analysis (TGA) 11

2.4 Powder X-Ray Diffraction (PXRD) 13

2.5 Scanning Electron Microscopy with Energy Dispersive X-Ray Analysis (SEM-EDX) 15

2.6 Quantifying the missing linker defects 15

2.7 Nitrogen adsorption 17

3 Experimental 18

3.1 General considerations 18

3.2 Synthesis of linkers 19

3.2.1 Dimethyl 2,2'-dinitrobiphenyl-4,4'-dicarboxylate (Me_2BPDC-$(NO_2)_2$) 19

3.2.2 Dimethyl 2,2'-diaminobiphenyl-4,4'-dicarboxylate (Me_2BPDC-$(NH_2)_2$) 20

3.2.3 2,2'-diaminobiphenyl-4,4'dicarboxylic acid (H_2BPDC-$(NH_2)_2$) 21

3.2.4 H_2BPDC-**3** 22

3.3 MOF synthesis 23

3.3.1 UiO-67 23

3.3.2 UiO-67-0.1$(NH_2)_2$ 23

3.3.3 UiO-67-0.2$(NH_2)_2$ 24

3.3.4 UiO-67-0.3$(NH_2)_2$ 24

3.3.5 UiO-67-0.5$(NH_2)_2$ 25

3.3.6 UiO-67-0.7$(NH_2)_2$ 25

3.3.7 UiO-67-0.9$(NH_2)_2$ 26

3.4 MOF post-synthetic functionalization 27

3.4.1 UiO-67-0.1(**3**) 27

3.4.2 UiO-67-0.3(**3**) 27

3.4.3 UiO-67-0.5(**3**) ... 28
3.4.4 UiO-67-0.7(**3**) ... 28
4 Results and Discussion ... 29
4.1 Aldehyde screening ... 29
4.2 Exploring the photophysical properties ... 34
4.3 Synthesis of mixed linker UiO-67 MOFs ... 39
4.4 Diazepine incorporation into UiO-67 MOFs ... 53
5 Conclusion and outlook ... 62
6 References ... 63
7 Appendices I-VI ... 68
I. Additional Data ... 68
II. Paper I ... 68
7.1 NMR data ... 70
7.2 PXRD data ... 77

List of abbreviations

BA	Benzoic acid
BPDC	Biphenyl-4,4'-dicarboxylate
BPDC-$(NH_2)_2$	2,2'-diaminobiphenyl-4,4'dicarboxylate
Conc.	Concentrated
CPS	Counts per second
DMA	Dimethylamine
DMF	*N,N*-dimethylformamide
Equiv.	Equivalents
FWHM	Full width at half maximum
H_2BPDC	Biphenyl-4,4'-dicarboxylic acid
H_2BPDC-$(NH_2)_2$	2,2'-diaminobiphenyl-4,4'dicarboxylic acid
H_2TPDC	4,4''-terphenyldicarboxylic acid
Me_2BPDC-$(NH_2)_2$	Dimethyl 2,2'-diaminobiphenyl-4,4'-dicarboxylate
MOF	Metal-organic Framework
NMR	Nuclear magnetic resonance
PXRD	Powder X-ray diffraction
SEM-EDX	Scanning Electron Microscopy with Energy Dispersive X-Ray Analysis
SBU	Secondary building unit
TD-DFT	Time-dependent density-functional theory
TGA	Thermogravimetric analysis

1 Introduction

IUPAC defines metal-organic frameworks, abbreviated as MOFs, as a coordination network, with organic linkers containing potential voids.[1] By this definition, MOFs are a subclass of porous coordination polymers. MOFs are composed of metal ions, or cationic metal clusters, often called secondary building units (SBUs), which are linked together by organic compounds (called linkers), typically polycarboxylic acids creating a repeating crystalline structure in two or three dimensions. By using carboxylic acids, the SBUs are coordinated through two oxygen atoms of the carboxylic acid increasing the stability of the inorganic clusters.[2] The general procedure for the construction of a MOF is shown in Scheme 1.

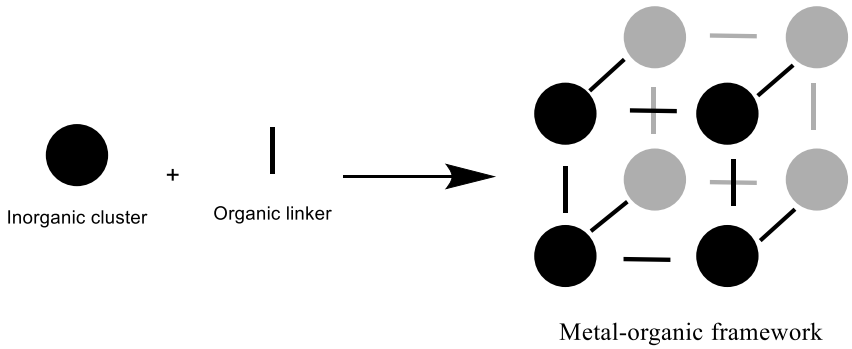

Scheme 1. Simplified general synthesis procedure of a Metal-organic framework.

Although coordination polymers containing both organic and inorganic characters have been reported before, the term metal-organic framework was only first used by Yaghi, *et al.* in 1995.[3] However, this copper 4,4'-bipyridine based MOF lacked stability, being stable only up to 180 °C under inert atmosphere, and for hours in aqueous solution. In 1999, Yaghi, *et al.* found the first stable MOF, the zinc and terephthalic acid (H_2BDC) based MOF-5,[4] shown in Figure 1.

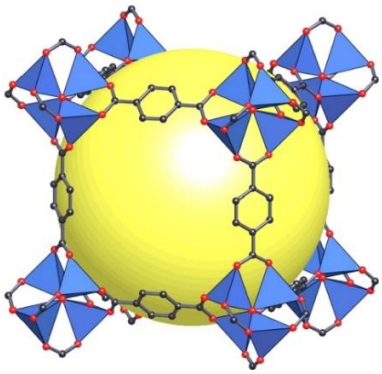

Figure 1. Structure of MOF-5 showing ZnO_4 tetrahedra in blue, oxygen in red and carbon in black. The yellow sphere represents the cavity of the MOF. Hydrogens were omitted for clarity.

The increased stability and high porosity of the MOF-5 (Langmuir surface area of 2900 m^2/g) proved the potential of MOFs in material science.[4] After this MOF was reported, the number of publications containing MOFs has increased exponentially, as shown in Figure 2. In fact, the MOF subset of structures in the Cambridge Structural Database (CSD) is composed of over 110 000 structures, accounting for ca. 10% of the structures in the whole database.[5,6]

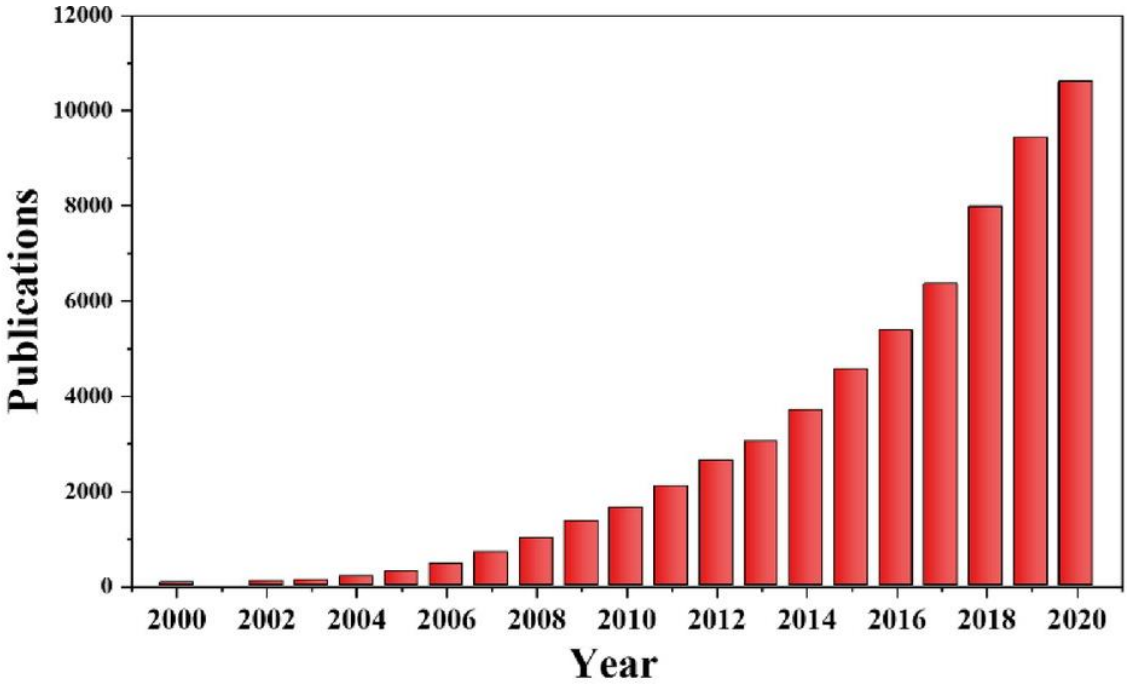

Figure 2. Number of MOF publications from 2000-2020, results from Web of Science. Figure retrieved from review published by Dai, S. *et al.*[7]

The discovery of MOF-5 let the development of MOFs through a concept called 'reticular synthesis'.[8,9] This allowed the synthesis of new MOFs featuring the same SBU, but using different organic linkers, thereby adding extra functionalization to the MOFs. The isoreticular MOF series (IRMOFs) is a series of 16 different Zn based MOFs containing different linkers but maintaining the same network topology. Three of the 16 IRMOFs are shown in Figure 3.

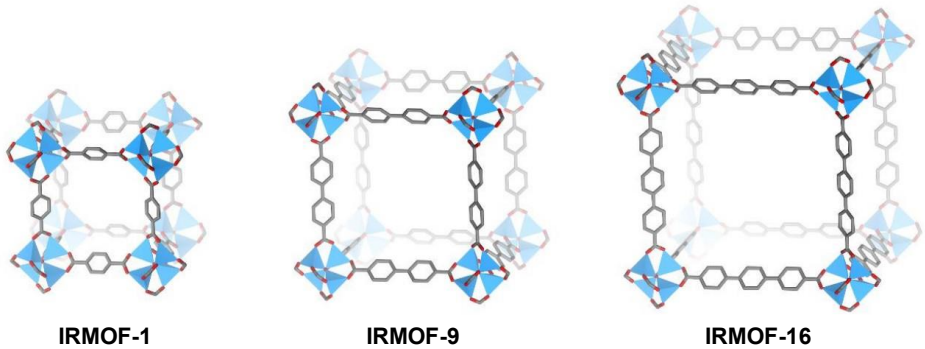

Figure 3. Structure of IRMOF-1 (MOF-5), IRMOF-9 and IRMOF-16, some of the IRMOFs reported by Yaghi in 2002.[9] ZnO4 tetrahedra are shown in blue, oxygen in red and carbon in black. Hydrogens were omitted for clarity.

In 2008, Lillerud *et al.* discovered the UiO MOF series,[10] composed of Zr based MOFs, and along with other MOFs derived from same SBU, it has been considered as the most promising MOF for industrial uses.[11–17] The SBU for the UiO MOF series is composed of the hexametallic $[Zr_6O_4(OH)_4]^{12+}$ cation. As the IR-MOF series, the UiO MOFs are isoreticular and the structures for the UiO-66, UiO-67 and UiO-68 are shown in Figure 4. The difference between these MOF is the number of aromatic rings in the organic linker. It increases from one in the H_2BDC linker of UiO-66, to three rings in the H_2TPDC linker of UiO-68. By increasing the length of the linkers, the MOF gains a higher surface area for the MOF, and it is noted that the increased length of the linkers does not reduce the thermal stability of the MOF (stable at temperatures over 500 °C).[10]

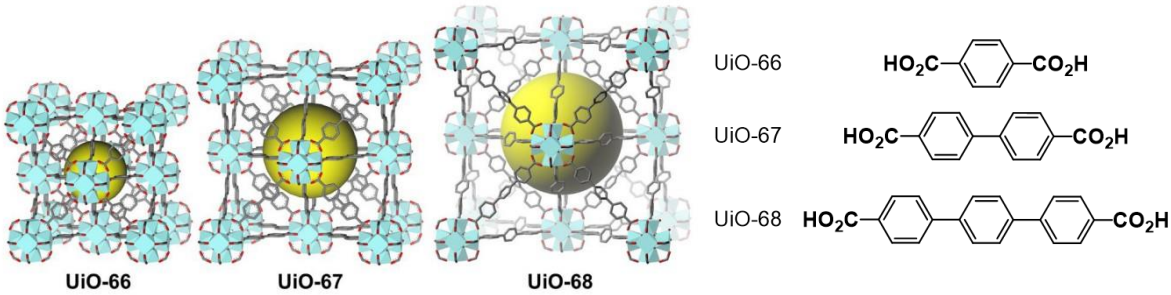

Figure 4. Structure of UiO-66, UiO-67 and UiO-68 showing ZrO_8 as a polyhedron in cyan, oxygen in red and carbon in grey. The yellow sphere represents the octahedral cavity of the MOFs. Hydrogens were omitted for clarity. On the right, the linkers used to make the UiO-66, UiO-67, and UiO-68.

Due to the use of organic linkers, the functionalization of MOFs is very accessible, and increases the applications for MOFs, since it is possible to add functional groups to the organic linkers while keeping the material stable.[18,19] Applications for MOFs include, but are not limited to, catalysis,[20] gas storage, adsorption and separation,[21–24] magnetic materials[25] conductors,[26] drug delivery,[27] luminescence and sensing applications.[28,29]

There are no perfect crystals in nature, and defects, either being structural or physical are present in all solids.[30] Metal organic frameworks are therefore no exception, with two main internal defects found: missing linker defects, and missing cluster defects.[31] Missing linker defects are found in all UiO type MOFs,[32–36] and missing cluster defects are well known to be found in UiO-66,[31,37–39] this type of defect has not been reported for UiO-67 or UiO-68.

When missing linker defects are present, it is known that other ions will occupy the now linker vacant sites, in order to conserve the compound's charge neutrality. Those now vacant sites can be occupied by anions from the metal source; modulators (Scheme 2), H_2O/OH^- pairs,

additives, and anions from solvent hydrolysis.[36,40] The latter is shown in Scheme 3 where formic acid is a product of DMF hydrolysis.

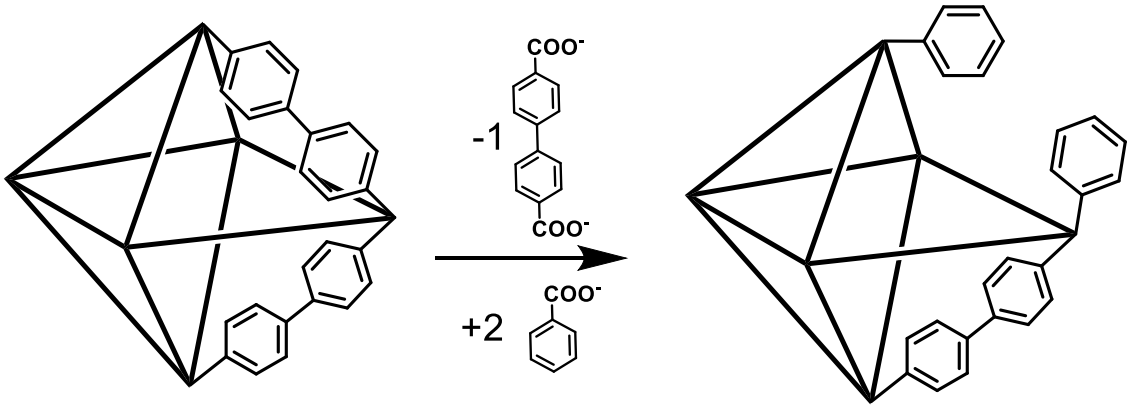

Scheme 2. Theoretical in-situ replacement of one BPDC linker for two benzoate molecules, used as modulator.

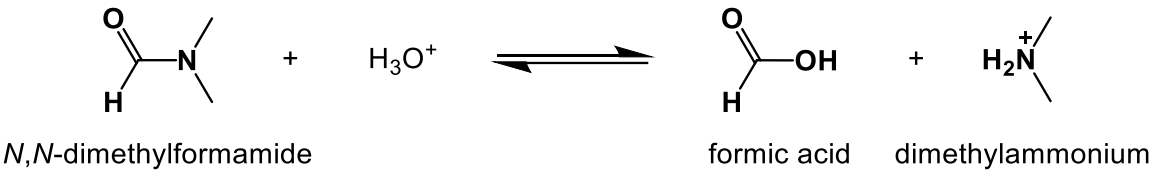

Scheme 3. Hydrolysis reaction of DMF in acidic medium.

Although the UiO-67 MOF has been reported using a Zr(IV) source and BPDC as the linker, reports of modified UiO-67 have been published. These include the substitution of Zr(IV) for Hf(IV),[41] and the use of modified linkers.[42,43]

Another type of modification on MOFs are the so called "mixed-linker" MOFs. This applies when a MOF is composed of more than a single linker in the same crystal structure.[43–46] Those will then present different chemical properties, which might even be further modified post synthetically while maintaining the stability of the original MOF.

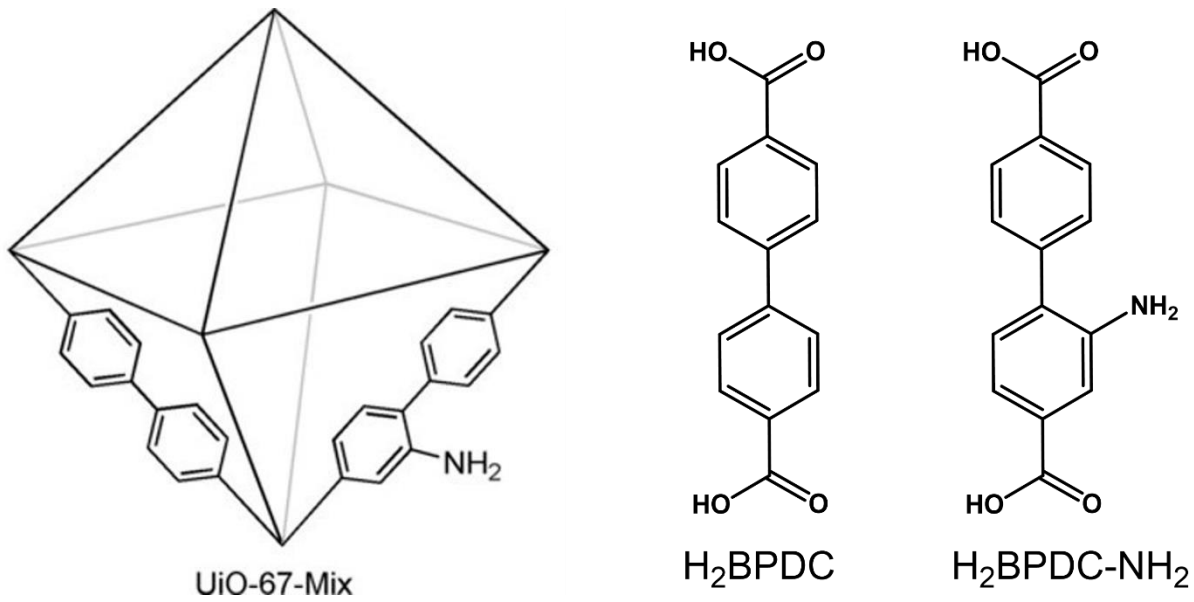

Figure 5. Example of a mixed linker UiO-67 with H_2BPDC and $H_2BPDC\text{-}NH_2$ (2-aminobiphenyl-4,4'-dicarboxylic acid) linkers, published by Sun, R. *et al*.[46]

There are two routes for introducing the new linker into the MOF, the in-situ introduction of the new linker (premade linker synthesis, or PMLS),[46–49] and post-synthetically (post synthetic functionalization (PSF),[50,51] and post synthetic linker exchange (PSLE)).[52–54] These routes are visually represented in Figure 6.

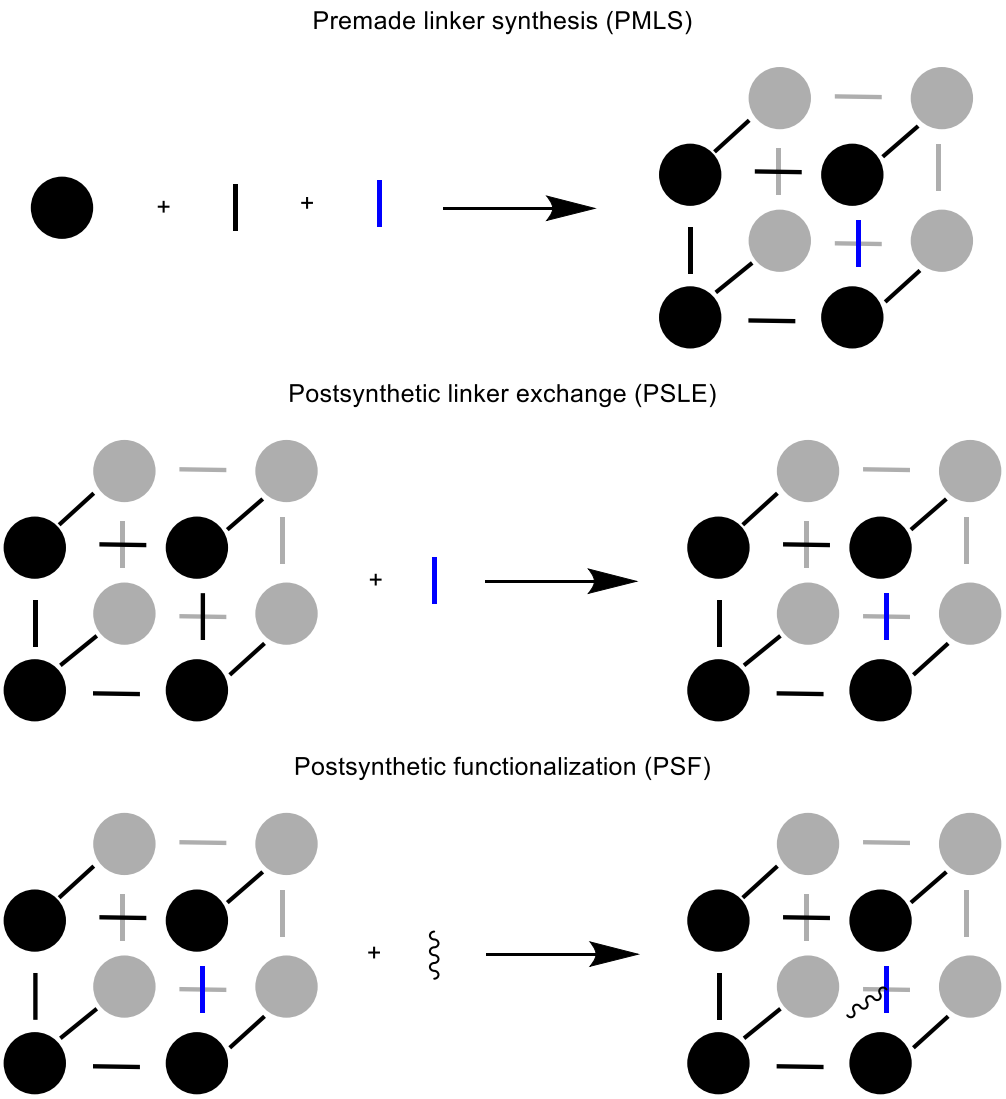

Figure 6. Simplified schemes showing the routes of obtaining and functionalizing mixed-linker MOFs.

The functionalization of the MOF by the addition of new linkers to it, changes the properties of the material, and this w

Another emerging field is the functionalization of polymers and MOFs with 1,3-dibenzodiazepines.[55–58]

Diazepines are seven-membered heterocyclic organic compounds with two nitrogen atoms. The numbering stems from the relative position of the nitrogen atoms inside of the diazepine ring (see Figure 7). Even though 1,4-diazepines are thoroughly used in the pharmaceutical industry,[59,60] 1,3-diazepines are less researched. Recently, there has been a growth in the literature concerning 1,3-benzodiapines.[61–66]

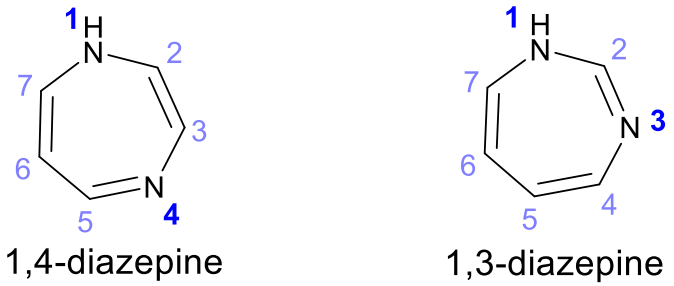

Figure 7. Nomenclature of diazepines.

One route found for the formation of 1,3-dibenzodiapines, is through the reaction of an appropriate 1,4-diamine compound with a carbonyl.[61,63,67,68] Although the use of an aldehyde and a 1,4-diamino compound is common for the synthesis of Schiff-bases,[50,69] it was also found that 1,3-dibenzo-[*d,f*]-diazepines could be another outcome of the reaction.[67,68]

In **paper I**, it was observed that the 1,3-dibenzo[*d,f*]-diazepines contained fluorescent properties. This is interesting since it could increase the applicability of diazepine containing MOFs for the use as a fluorescent chemical sensor.

2 Theory and Methods

The main characterization methods used in this thesis, and its theory is described in this chapter. DFT is discussed in detail on the SI of **Paper I**.

2.1 Synthesis of mixed linker UiO-67 MOFs

The synthesis of UiO-67 has not changed a lot from the original synthesis method for the UiO-66 MOF published by Lillerud in 2008.[10] The procedure uses $ZrCl_4$ as the zirconium(IV) source, using *N,N*-dimethylformamide as the solvent, in high temperatures (130 °C) overnight. The addition of monocarboxylic acids, such as benzoic acid (BA), as modulators has been proven to slow down the nucleation rate by competing with the linkers to form bonds with the SBU, creating then bigger crystalline MOFs.[70–72] The use of aqueous additives such as water or HCl, has also been proven to play a major role in the synthesis of UiO MOFs.[32,34,45] In her thesis, Kaur has investigated the role of the different reaction conditions in the synthesis of UiO-67 MOFs, and has found that the best molar ratio of $ZrCl_4$:DMF:H_2O:BA:Linker used in order to obtain large, crystalline MOFs is of 1:300:3:9:1, with a temperature of 130 °C.[45]

2.2 Liquid Phase Digestion ^{1}H NMR

Nuclear Magnetic Resonance (NMR) is a popular method of characterization of organic molecules. Not only does it give important information about the molecular structure, but its stereochemistry is also obtainable from NMR. This is especially important when trying to understand side-products and purity of a compound, as well as understanding the final product. NMR is based on the interaction of nuclear spins when placed in a magnetic field, this means that only non-zero spins are NMR active (^{12}C and ^{16}O have spin **I** = 0, so they are NMR silent).

The ^{1}H NMR spectrum of digested UiO-67 MOF is shown in Figure 8. In case the MOF is not completely dried of solvents, DMF or acetone peaks will arise upfield, but the peaks used to analyse the MOF composition all arise downfield. In addition to the acidic DMF hydrolysis during MOF synthesis (Scheme 3), the basic conditions of the digestion can generate additional formate from basic DMF hydrolysis (Scheme 4). This is significant information to know when calculating the linker incorporation into the MOF, so that the formate from DMF can be separated from the formate causing linker vacancies in the MOF.

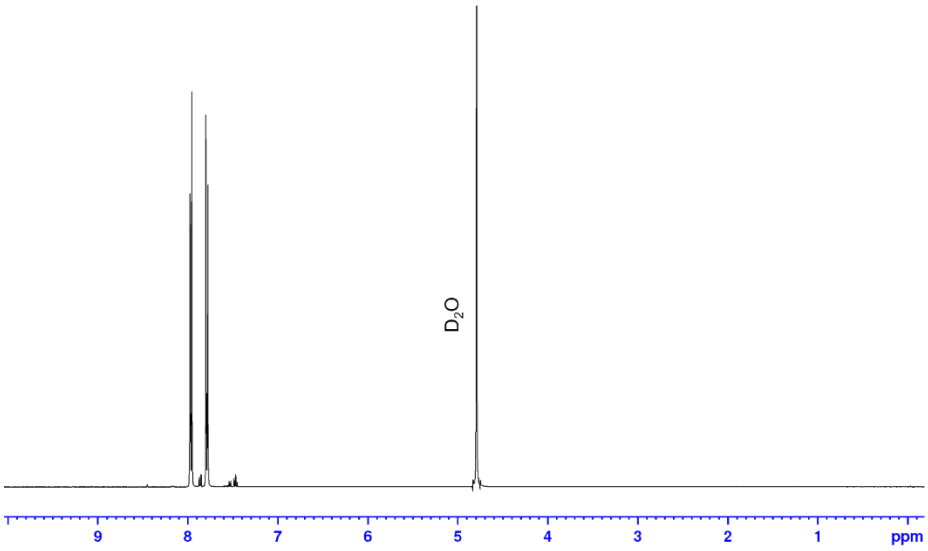

Figure 8. ^{1}H NMR of the digested UiO-67 MOF (400 MHz, 0.1M NaOD/D_2O)

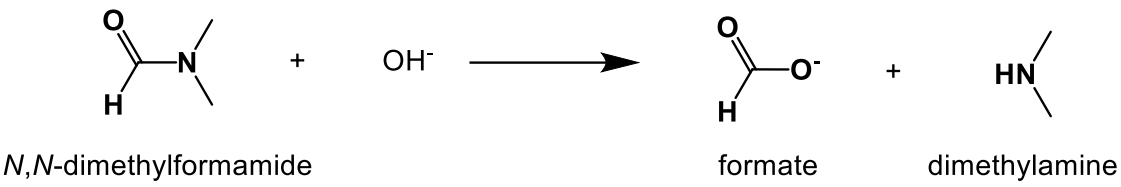

Scheme 4. Hydrolysis of DMF in basic medium.

The regular linker for the UiO-67 is the H_2BPDC (see Figure 4), which gives rise to two signals: two doublets of triplets coming at 7.79 and 7.96 ppm, respectively. Moreover, when missing linker defects are present, it is highly likely that the modulator, in this case benzoate, or formate generated from the solvent are replacing the linker. Benzoate gives rise to three signals, all of which lie in the aromatic region, and their fine structures are complex due to multiple $^{3}J_{H,H}$ and $^{4}J_{H,H}$ couplings. The protons closest to the carboxylate group will give rise to a signal with the highest chemical shift (ca. 7.85, 2 protons), right in between the signals for the H_2BPDC linker. The other protons will give rise to signals at ca. 7.55 and 7.45 ppm, integrating to 1 and 2 protons, respectively. The last peak generally encountered in ^{1}H NMR spectrum of the digested MOF, stems from formate at around 8.45 ppm. The aromatic region of the digestion ^{1}H NMR spectrum for the synthesized UiO-67, is shown in Figure 9.

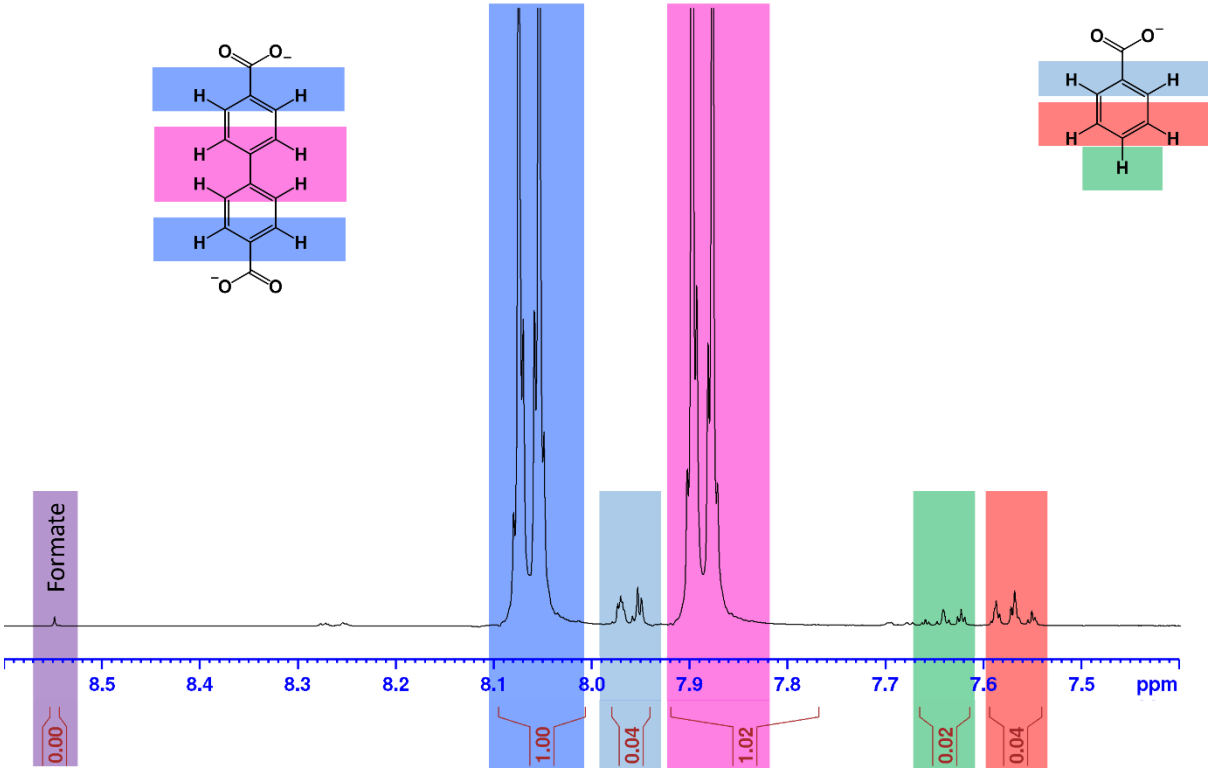

Figure 9. ^{1}H-NMR of the digested UiO-67 MOF (400 MHz, 0.1M NaOD/D_2O), showing an amplified vision of the aromatic region.

2.3 Thermogravimetric analysis (TGA)

Along with digestion NMR, thermogravimetric analysis is the best methods for identifying and quantifying defects in the UiO-67 MOF. By heating the MOF from room temperature to 900°C, three central processes occur. The first process that takes place is the desorption of solvents trapped in the pores of the MOF. Followingly, the dehydration of the UiO-67 MOF from the hydroxylated [$Zr_6O_4(OH)_4$(Linker)$_6$] to the dehydroxylated form [Zr_6O_6(Linker)$_6$] occurs. In this step usually the modulator occupying the linker vacancies decomposes. It is important to note that when using benzoic acid as the modulator, its decomposition will occur on the second process. Lastly, is the combustion of the organic linkers on the MOF, breaking down the MOF from its dehydroxylated form to zirconium dioxide. The latter is crucial to calculate the quantity of linkers per cluster that the non-ideal MOF contains.[73]

The equation of the processes seen during the thermogravimetric analysis for an ideal UiO-67 is shown below:

$$Zr_6O_4(OH)_4(BPDC)_6(s) \leftrightharpoons Zr_6O_6(BPDC)_6(s) + 2H_2O\ (g) \qquad Process\ 1$$

$$Zr_6O_6(BPDC)_6(s) + 87\ O_2(g) \rightarrow 6\ ZrO_2(s) + 84\ CO_2(g) + 24\ H_2O\ (g) \qquad Process\ 2$$

The molar mass for the ideal dehydroxylated UiO-67 is 2084.64 g/mol, corresponding to 2.82 times the weight of the remaining solid after the second step (6 ZrO_2, M_w = 739.34 g/mol). Thus, by normalising the weight in the end of the TGA at 900°C to 100%, the theoretical TGA plateau (W_t) for the ideal solvent-free, dehydroxylated UiO-67 MOF can be calculated using equation 1. This equation can be applied to any Zr_6 MOF, since the only solid left after 900°C is the zirconium dioxide.

$$W_t = \frac{M_{W_{MOF}}}{M_{W_{6\,ZrO_2}}} \cdot 100\% \qquad 1$$

Where $M_{W_{MOF}}$ and $M_{W_{6\,ZrO_2}}$ are the molar mass of the MOF and the molar mass of the remaining 6 ZrO_2, respectively. By applying this equation on the ideal dehydroxylated UiO-67, a theoretical plateau of 282.0% is obtained, as calculated below.

$$W_t = \frac{2084.64\ \mathrm{g/mol}}{739.34\ \mathrm{g/mol}} \cdot 100\%$$

$$W_t = 2.8196 \cdot 100\% \approx 282.0\%$$

However, the presence of linker vacancies causes the plateau observed on the TGA curve to be lower than that for the ideal MOF, meaning that the MOF synthesized is lighter than the ideal one. For the smaller UiO-66 MOF, it is well known that missing cluster defects can be present,[37] and even though it is theoretically possible that this kind of defect is present in the UiO-67 MOF, it has not been reported in the literature. It is therefore, with a slight certainty that the smaller plateau is due to missing linker defects on the UiO-67. An example of how the experimental TGA plateau (W_e) differs from the theoretical TGA plateau (W_t) is shown for the UiO-67 in Figure 10.

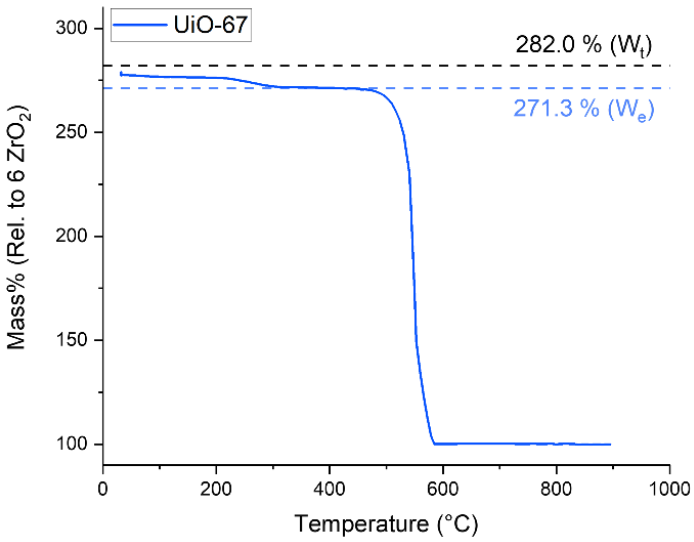

Figure 10. The TGA plot for the UiO-67 synthesized, in blue. The dotted lines represent the theoretical TGA plateau, in black, and the experimental TGA plateau, in light blue.

It is also possible to calculate the theoretical TGA plateau for the hydroxylated MOF ($W_{t,hydro}$), by applying the equation, but this time with the new molar mass, containing the two H_2O molecules that are lost during the dehydration. The $W_{t,hydro}$ for the ideal UiO-67 is as shown below, approximately 286.8%, a value that is 4.8% higher than for the dehydroxylated MOF. That increase is constant and independent of the MOF's molar mass.

$$W_{t,hydro} = \frac{2120.67\ \mathrm{g/mol}}{739.34\ \mathrm{g/mol}} \cdot 100\%$$

$$W_{t,hydro} = 2.8683 \cdot 100\% \approx 286.8\%$$

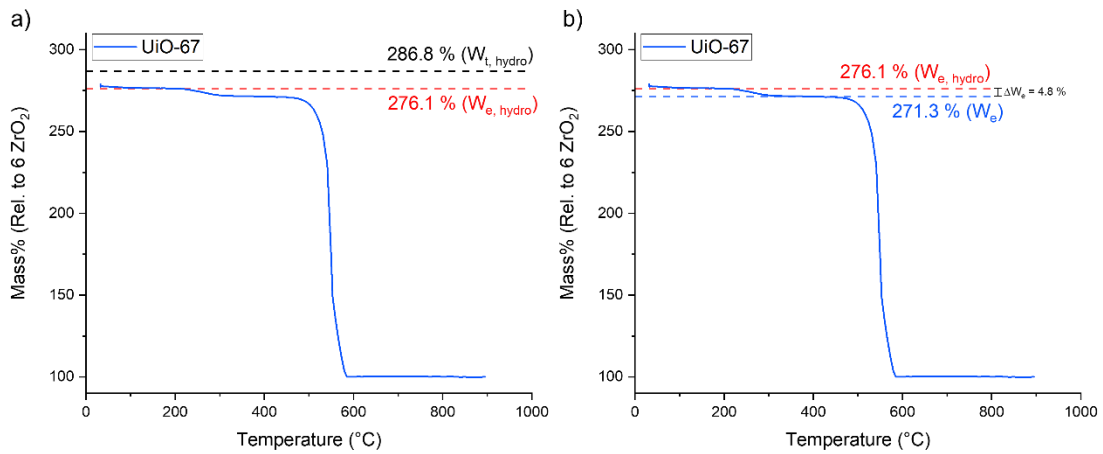

Figure 11. The TGA plot for the UiO-67 synthesized, in Blue.a) highlights the theoretical TGA plateau, in black, and the experimental TGA plateau, in red, both for the hydroxylated MOF. b) highlights the difference (ΔW_e) between the experimental TGA plateaus for the hydroxylated MOF ($W_{e,\ hydro}$), in red, and for the dehydroxylated MOF (W_e).

Due to the presence of little to no formate and solvent residue in the UiO-67 synthesized, such as DMF, trapped in the pores, the hydroxylated plateau has little to no change in weight before the dehydration occurs. It is then, possible to see that even though the UiO-67 synthesized contains missing linker defects, the difference between the hydroxylated and the dehydroxylated MOF remains 4.8%.

2.4 Powder X-Ray Diffraction (PXRD)

One of the best methods for investigating the crystallinity of the MOF synthesized, is powder X-ray diffraction (PXRD). There, a small amount of sample is mounted on a plate, and monochromatic x-rays (of wavelength λ) are beamed into the sample, while the incident angle (θ) of the x-rays change. Due to the positioning of the detector, only when constructive interference is present can the x-rays that are now diffracted at an angle θ, be detected. This occurs when Bragg's law ($n\lambda = 2d\sin\theta$) is sufficed, where n is an integer, and d is the spacing between parallel crystal planes.[74] It is then possible to record a plot of diffraction intensity vs. incident and diffracted angle.

The diffractogram shows peaks with different intensities, since non-crystalline samples don't diffract, the signal to noise ratio can be used for observed whether a crystalline product was obtained. In addition, the S/N can be quite useful for comparing how the crystallinity of a sample changes after any treatment, for example postsynthetic functionalization. The peak shape can also help to understand the mean size of the crystals formed. Scherrer's equation says that the peak's FWHM is inversely proportional to the diameter of the crystals.[75] That means that large crystals gives narrower peaks, while peak broadening can be seen in smaller crystals.

Different lattice types will give rise to peaks at different 2θ angles, and the pattern observed on PXRD gives information about the space group symmetry for a given phase. Not only the space group, but also its lattice parameters *a, b, c* and their respective angles *α, β, γ* can be determined by performing a Pawley refinement on the diffractogram.

The PXRD will also show whether crystalline impurities are present in the sample, since the space group for the UiO-67 MOF is already known to be the face-centered cubic *Fm-3m*, the allowed diffractions are also defined. Any forbidden diffractions peaks are caused by impurities and need to be assessed. For all MOFs synthesized in this thesis, UiO-67 was the desired phase, and no forbidden diffraction peaks were found.

In routine PXRD, only a small quantity of sample is used in order to quickly observe which phase was formed, the sample is kept in place on the glass plate using plastic wrap. This will give rise to a broad peak in range of 20-22°. Another way of mounting the sample is by using a full plate. This method uses a higher quantity of sample and requires more attention. Consequently, because of the higher sample amount, the intensity of all peaks increases, obtaining a diffractogram with a higher signal to noise ratio.

A comparison of the two methods can be observed in Figure 12. There, the intensity of all peaks has doubled when using a full plate comparing to the glass plate. In addition, there is the loss of the peak arising from the plastic wrap. The glass plate method was used for a quick phase identification, while the full plate method was used to obtain diffractograms with high counts, in order to obtain a good fit when performing a Pawley refinement.

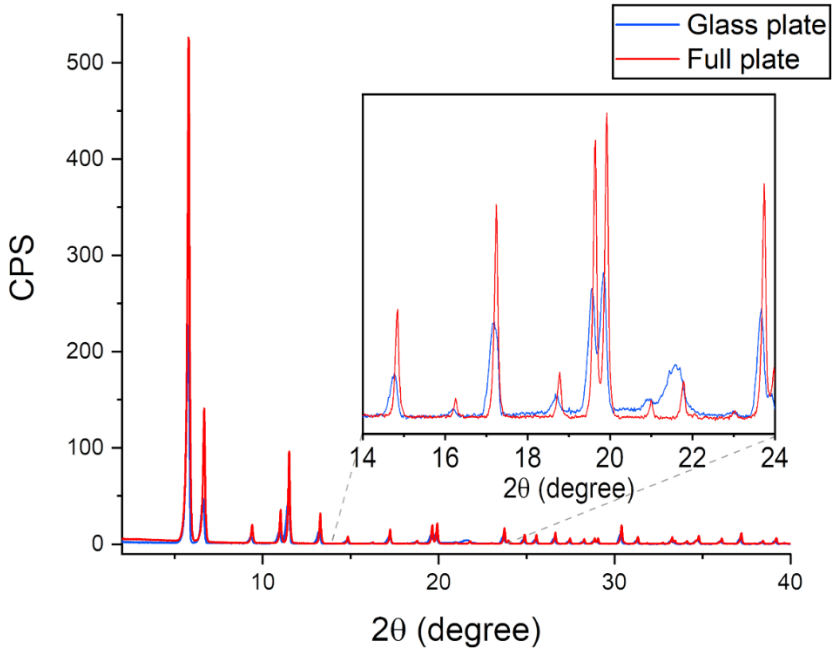

Figure 12. PXRD diffractograms for a sample measured using a glass plate with plastic foil, in blue, and a full plate, in red. Note the broad plastic wrap peak on the blue curve between 21-22°.

2.5 Scanning Electron Microscopy with Energy Dispersive X-Ray Analysis (SEM-EDX)

MOFs are also routinely characterized by SEM-EDX. There, two important kinds of information can be obtained, each from their respective characterization method. SEM allows the visualization of the topology of the MOFs, while EDX allows for the quantification of the relative concentration of the elements present in the sample.

From the elements present in the synthesized MOFs only Zr can reliably be quantified by EDX, but the presence of chloride ions is known to compensate for missing linkers in unmodulated synthesis.[73]

2.6 Quantifying the missing linker defects

To quantify the missing linker defects a mix of the different characterization techniques described in this chapter is used. This quantification is based on a report in literature for UiO-66 and has a few assumptions.[76] It is first assumed that no missing cluster defects are found on the UiO-67 MOF, that is, no low angle forbidden reflections are seen on PXRD. Secondly, it is assumed that benzoic acid and formate decompose at the same time as the BPDC and derivative linkers. The next assumption is that the residue found at 900°C is exclusively ZrO_2.

The molecular formula for a BPDC-$(NH_2)_2$ MOF containing missing linker defects is $Zr_6O_6(BPDC)_x(BPDC\text{-}(NH_2)_2)_y(BA)_z(FA)_w$ where BA and FA are benzoate and formate,

respectively. Therefore, the last assumption is that since the number of coordinating molecules per cluster is 12, 2x + 2y + z + w = 12, and therefore, if the number falls short, it is assumed that H_2O/OH^- pairs are the capping agents missing, unless the presence of chlorine atoms is found by EDX.

For an ideal or defective MOF, the number of linkers per cluster can be found with the help of TGA. It is known that knowing the plateau height and the molar mass of the remaining solids, it is possible to find the molar mass of the MOF (see Section 2.3). By subtracting the molar mass of the cluster, with the molar mass of the MOF, we obtain the molar mass of the organic remains. Therefore, by dividing the molar mass found by TGA with the molar mass of the linker, it is possible to find the number of linkers per Zr-cluster. This information can be summed with the help of the formula below.

$$\frac{n_{linker}}{Zr\text{-}cluster} = \frac{\frac{W_e}{100\ \%} \cdot M_{m,6ZrO_2} - M_{m,cluster}}{M_{m,linker}} \qquad 2$$

For an ideal UiO-67 MOF the number of linkers per Zr-cluster is 6. Since the molar mass of the MOF found by TGA is subtracted by the molar mass of the cluster, in theory either cluster state could be used. However, the dehydroxylated state is preferred since small solvent or water residues could increase the plateau of the hydroxylated MOF. However, for defective MOFs containing organic molecules as capping agents such as formate or benzoate, the use of the molar mass of the linker only, is illogical.

It is important to find the relative molar ratios of the linkers, BA and FA with the use of liquid phase digestion ^{1}H-NMR. That way, it is possible to find the average molar mass for all organic molecules present. This is shown for a UiO-67 MOF in the formula below, where $n_{rel,x}$ is the relative molar ratio of x and is obtained by dividing the integrated relative molar amount ($I_{rel,x}$) with the sum of all molar amounts.

$$M_{m,organic} = M_{m,BPDC} \cdot n_{rel,BPDC} + M_{m,BA} \cdot n_{rel,BA} + M_{m,FA} \cdot n_{rel,FA}$$

$$n_{rel,BPDC} = \frac{I_{rel,BPDC}}{I_{rel,BPDC} + I_{rel,BA} + I_{rel,FA}}$$

This formula can be also used for mixed linker MOFs, where the extra linker will be added as a variable for both the molar mass and the relative molar ratio calculations.

After finding the average molar mass for all organic molecules in the MOF, it is possible to find the number of linkers per Zr-cluster using equation 2. The individual components of the MOF (x, y, z and w) will then be equal to the relative molar ratio of the component times the number of linkers per Zr-cluster.

Reminding that the number of coordinating molecules per Zr-cluster is 12, and in the case that the number found is less than 12, the remaining value is the number of H_2O/OH^- pairs found in the MOF. The number in percent of the missing linker defects will then be dependent on the formate, benzoate and H_2O/OH^- content, as shown below.

$$ML_D = \frac{n_{FA} + n_{BA} + n_{H_2O/OH^-}}{12} \cdot 100\%$$

This method was also used to quantify the percentages of linker incorporated into the MOF.

2.7 Nitrogen adsorption

A well-known technique to determine the surface area of a porous material is through nitrogen adsorption. The adsorption isotherm is measured through reversible nitrogen adsorption and desorption. There are three main methods of measuring the adsorption isotherms: the volumetric, gravimetric, and dynamic method.[77] In this thesis only the volumetric method was used.

There are many theories to obtain the materials surface area from the nitrogen isotherm, but the main methods for this analysis are the Langmuir theory,[78] and the Brunauer–Emmett–Teller (BET) theory.[79]

Even though the Langmuir theory is an older method, it is still used nowadays, however, the Langmuir theory assumes only monolayer adsorption, and will therefore give larger specific surface areas in materials presenting multilayer adsorption. It is possible to use the Langmuir theory in the lower pressure ranges before multilayer adsorption starts to build. However, the Langmuir theory also assumes that there are no interactions between the adsorbed molecules. The BET theory builds from the Langmuir theory, including then multilayer adsorption and interactions between the molecules.

3 Experimental

3.1 General considerations

All chemicals were obtained through commercial sources and used as received. Dimethyl 2,2'-diaminobiphenyl-4,4'-dicarboxylate (**Me_2BPDC-(NH_2)$_2$**) was synthesized according to literature.[80]

Melting points are uncorrected and were measured on a Stuart SMP10 instrument. All NMR spectra were recorded using a Bruker DPX300, AVNEO400, AVIII400, AVI600 and a AVII600 NMR spectrometer, at 298K. All spectra were calibrated using the corresponding solvent residual peak according to literature (DMSO-*d_6* (2.50 ppm for ^{1}H NMR and 39.52 ppm for ^{13}C NMR), $CDCl_3$ (7.26 ppm for ^{1}H NMR and 77.16 ppm for ^{13}C NMR), D_2O (4.79 ppm for ^{1}H NMR)).[81] All resonances were assigned according to 2D NMR techniques.

For all MOF digestions for NMR, the selected MOF (20 mg) was shaken in 0.1M NaOD/D_2O solution (1 mL) for 10 minutes and aged overnight.

MS (ESI) measurements were recorded on a Bruker maXis II ETD spectrometer. UV-Visible measurements were performed on a Specord 200 Plus instrument for solutions, and on a UV-3600 UV-Vis-NIR Spectrophotometer from Shimadzu for solids. All molar extinction coefficients were calculated by linear regression of the absorbance vs concentration, using at least three different concentrations, and all linear regression had a R2 of over 0.993. Since MOFs are highly water adsorbent, all MOFs were stored in a desiccator to avoid decomposition.

Powder X-ray diffraction was measured with a Bruker D8 Discover diffractometer, using Cu Kα1 radiation selected by a Ge (111) Johanssen monochromator and a Bruker LYNXEYE detector. Thermogravimetric analysis was performed on a NETZSCH STA 449 F3 Jupiter, ramping from 30 to 900 °C with a 10 K/min ramping rate. The samples were under a stream of synthetic air, consisting of a 20 ml/min flowrate and 5 mL/min flowrate of N_2 and O_2, respectively. SEM images were taken on a Hitachi SU8230 Field Emission Scanning Electron Microscope (FE-SEM).

Nitrogen sorption measurements were conducted on a BelSorp mini II instrument, and all samples were subject to a pre-treatment at 120°C under vacuum for 90 min.

3.2 Synthesis of linkers

3.2.1 Dimethyl 2,2'-dinitrobiphenyl-4,4'-dicarboxylate (Me_2BPDC-$(NO_2)_2$)

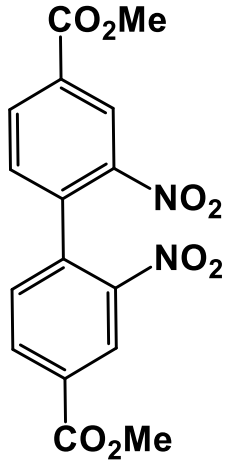

Me_2BPDC-$(NO_2)_2$

A three-necked round bottom flask containing conc. H_2SO_4 (120 mL) was cooled to around 2 °C in an ice bath. Dimethylbiphenyl-4,4'-dicarboxylate (10 g, 37 mmol, 1.0 equiv.) was added in portions over 25 min.

To the resulting solution, a mixture of conc. HNO_3 (5.9 mL, 133 mmol, 3.6 equiv.) and conc. H_2SO_4 (7.8 mL, 144 mmol, 3.9 equiv.) was added dropwise over 40-60 min, maintaining the temperature at around 5 °C. The ice bath was removed, and the reaction was left to stir for 30 min.

The reaction mixture was poured into 1.2 L of ice slush and the precipitate was filtered, washed with water, and dried overnight. The precipitate was dissolved in ethyl acetate (720 mL) and washed with sat. $NaHCO_3$ (2 x 200 mL) and sat. NaCl (2 x 200 mL) and dried with Na_2SO_4. The solvent was removed under reduced pressure and the crude product was recrystallized from MeCN (10.72 g, 29.75 mmol, 80%).

^{1}H NMR (400 MHz, $CDCl_3$) δ 8.86 (d, J = 1.6 Hz, 2H), 8.34 (dd, J = 1.7, 7.9 Hz, 2H), 7.37 (d, J = 8.0 Hz, 2H), 3.99 ppm (s, 6H); ^{13}C NMR (100 MHz, CDCl3) δ 164.4, 146.8, 137.6, 134.1, 131.8, 130.8, 126.0, 52.9 ppm; LRMS (ESI/Q-TOF): m/z (%): 383.049 (100) $[M + Na]^+$; HRMS (ESI/Q-TOF): $[M + Na]^+$ m/z calcd. for $C_{16}H_{12}N_2NaO_8$: 383.0486. Found 383.0486. The spectroscopic data are in accordance with those reported in the literature.[80]

3.2.2 Dimethyl 2,2'-diaminobiphenyl-4,4'-dicarboxylate (Me_2BPDC-$(NH_2)_2$)

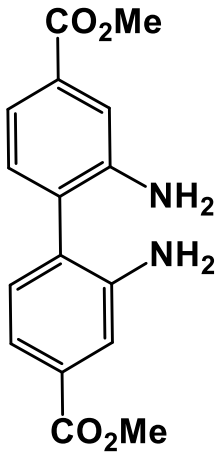

Me_2BPDC-$(NH_2)_2$

Dimethyl 2,2'-dinitrobiphenyl-4,4'-dicarboxylate (Me_2BPDC-$(NO_2)_2$) (18 g, 50 mmol, 1.0 equiv.) and subsequently Fe (45 g, 0.8 mol, 16 equiv.) were added to a flask containing acetic acid (500 mL).

The mixture stirred under a stream of Argon and after 3 hours an exothermic reaction occured. After 1.5 hours the reaction slowed down and the reaction mixture remained stirring under Argon for an additional 20 hours at room temperature.

The suspension was then transferred to a beaker containing water (4.0 L) and stirred for 15 min. The solids were filtered off and washed with water (3 x 360 mL). The solids were dissolved in ethyl acetate (1.0 L) and filtered through Celite, which was subsequently washed with ethyl acetate (3 x 180 mL). The filtrate was dried with Na_2SO_4, and the solvent was removed under reduced pressure and the crude product was recrystallized from toluene (12 g, 40 mmol, 80%).

^{1}H NMR (400 MHz, DMSO-d_6) δ 7.44 (d, J = 1.6 Hz, 1H), 7.23 (dd, J = 1.8, 7.8 Hz, 1H), 7.08 (d, J = 7.9 Hz, 1H), 4.99 (s, 4H), 3.83 ppm (s, 6H); ^{13}C NMR (100 MHz, DMSO-d_6) δ 166.6, 145.6, 130.8, 129.6, 127.6, 117.2, 115.8, 51.9 ppm; LRMS (ESI/Q-TOF): m/z (%): 323.100 (100) $[M + Na]^+$. UV-Visible (MeCN): λ_{max} 233.3 (36 300), 277.3 (sh, 4 592), 332.0 nm (7 480 $M^{-1}cm^{-1}$).

The spectroscopic data are in accordance with those reported in the literature.[80]

3.2.3 2,2'-diaminobiphenyl-4,4'dicarboxylic acid ($H_2BPDC-(NH_2)_2$)

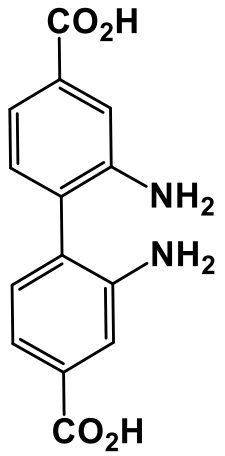

$H_2BPDC-(NH_2)_2$

Dimethyl 2,2'-diaminobiphenyl-4,4'-dicarboxylate ($Me_2BPDC-(NH_2)_2$) (7.0 g, 23 mmol, 1.0 equiv.) and subsequently LiOH (2.2 g, 93 mmol, 4.0 equiv.) were added to a flask containing a mixture of MeOH (50 mL), THF (100 mL) and distilled water (100 mL).

The mixture stirred at RT until the solids were dissolved and the solution stirred at RT for an additional 20 h.

The organic solvents were removed under reduced pressure, and distilled water (100 mL) was added to the solution. The product precipitated upon addition of acetic acid in excess (pH ≈ 4). The precipitate was filtered, washed with distilled water (3 x 100 mL) and dried in a vacuum oven at 80 °C overnight, yielding $H_2BPDC-(NH_2)_2$ as a pale yellow solid (6.2 g, 22.7 mmol, 98%).

^{1}H NMR (300 MHz, DMSO-d_6) δ 12.65 (br, 2H), 7.42 (d, J = 1.6 Hz, 2H), 7.23 (dd, J = 8.0, 1.6 Hz), 7.05 (d, 2H, J = 8.0Hz), 4.92 (s, 4H); LRMS (ESI/Q-TOF): m/z (%): 295.069 (63) $[M + Na]^+$, 317.051 (100) $[M + 2Na - H]^+$, 339.033 (60) $[M + 3Na – 2H]^+$. The spectroscopic data are in accordance with those reported in the literature.[82]

3.2.4 H_2BPDC-**3**

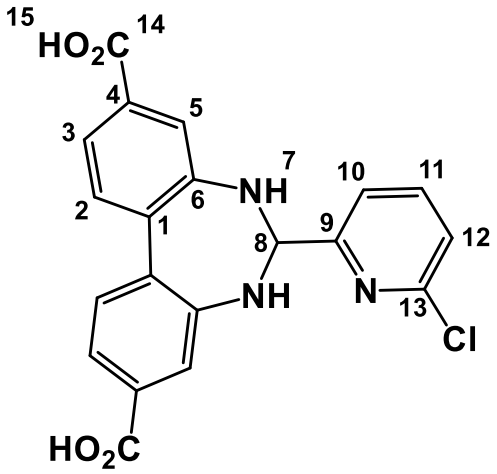

H_2BPDC-3

2,2'-diaminobiphenyl-4,4'-dicarboxylic acid (200 mg, 0.73 mmol, 1 equiv.) and 6-Chloro-2-formylpyridine (114 mg, 0.81 mmol, 1.1 equiv.) were mixed in methanol (4 mL) and left to stir at room temperature overnight. The precipitate was filtrated, and the crude product was left to dry in a vacuum oven at 70 °C for 2h yielding H2BPDC-pyrCl as a white solid (273 mg, 0.742 mmol, 94%).

M.p. >300 °C (decomp.). ^{1}H NMR (DMSO-d_6, 600 MHz) 12.77 (s, 2H, H15), 7.76 (t, J = 7.8 Hz, 1H, H11), 7.53 (d, J = 8.1 Hz, 2H, H2), 7.49 (d, J = 1.7 Hz, 2H, H5), 7.46 (dd, J = 1.7, 8.1 Hz, 2H, H3), 7.39 (d, J = 7.8 Hz, 1H, H12), 7.28 (d, J = 7.8 Hz, 1H, H10), 6.56 (d, J = 3.6 Hz, 2H, H7), 5.64 ppm (t, J = 3.5 Hz, 1H, H8); ^{13}C NMR (d_6-DMSO, 151 MHz) δ 167.2 (C14), 162.0 (C9), 149.3 (C13), 146.1 (C6), 140.1 (C11), 132.5 (C1), 130.1 (C4), 129.8 (C2), 123.3 (C12), 121.5 (C5), 121.3 (C3), 120.1 (C10), 78.3 ppm (C8); LRMS (ESI/Q-TOF): m/z (%): 418.056 (100) $[M + Na]^+$, 420.054 (32) $[(M + 2) + Na]^+$; HRMS (ESI/Q-TOF) m/z: $[M + Na]^+$ Calcd. for $C_{20}H_{14}ClN_3O_4Na$ 418.0565; Found 418.0564.

This compound has not been previously reported

3.3 MOF synthesis

The general mixed linker UiO-67-X$(NH_2)_2$ MOF synthesis procedure is as follows:

$ZrCl_4$ (1 equiv.) was added in portions to a beaker containing DMF (300 equiv.) and water (3 equiv.). The solution was heated, and benzoic acid (9 equiv.) was dissolved into the solution. 2,2'-diaminobiphenyl-4,4'dicarboxylic acid (X equiv.) was dissolved into the solution, which was then transferred to a round bottom flask containing biphenyl-4,4'dicarboxylic acid (1-X equiv.). The mixture was stirred at 138°C overnight. The product was filtered and washed with hot DMF and acetone, and dried in an oven at 140°C overnight.

3.3.1 UiO-67

$ZrCl_4$ (1.00 g, 4.29 mmol, 1.00 equiv.) was added in portions to a beaker containing DMF (99.7 mL, 1.29 mol, 300 equiv.) and water (230 µL, 12.9 mmol, 3.00 equiv.). The solution was heated, and benzoic acid (4.72 g, 38.6 mmol, 9.00 equiv.) was dissolved into the solution. The solution was transferred to a round bottom flask containing biphenyl-4,4'dicarboxylic acid (1.04 g, 4.29 mmol, 1.00 equiv.). The mixture was stirred at 138°C overnight. The product was filtered and washed with hot DMF (200 mL) and acetone (200 mL), and dried in an oven at 140°C overnight. Yield: 850 mg.

The product was analyzed by TGA, nitrogen adsorption, PXRD, SEM-EDX and liquid phase ^{1}H-NMR using 0.1M NaOD/D_2O as digestion solution.

The surface area was determined to be 2681 m^2/g by BET analysis.

The composition of the hydroxylated MOF was determined to be:

$Zr_6O_4(OH)_4(BPDC)_{5.43}(BA)_{0.45}(FA)_{0.04}(H_2O/OH^-)_{0.64}$

3.3.2 UiO-67-0.1$(NH_2)_2$

$ZrCl_4$ (1.00 g, 4.29 mmol, 1.00 equiv.) was added in portions to a beaker containing DMF (99.7 mL, 1.29 mol, 300 equiv.) and water (230 µL, 12.9 mmol, 3.00 equiv.). The solution was heated, and benzoic acid (4.72 g, 38.6 mmol, 9.00 equiv.) was dissolved into the solution. 2,2'-diaminobiphenyl-4,4'dicarboxylic acid (0.12 g, 0.44 mmol, 0.10 equiv.) was dissolved into the solution, which was then transferred to a round bottom flask containing biphenyl-4,4'dicarboxylic acid (0.94 g, 3.88 mmol, 0.90 equiv.). The mixture was stirred at 138°C overnight. The product was filtered and washed with hot DMF (200 mL) and acetone (200 mL), and dried in an oven at 140°C overnight. Yield: 1.31 g.

The product was analyzed by TGA, nitrogen adsorption, PXRD, SEM-EDX and liquid phase ^{1}H NMR using 0.1M NaOD/D_2O as digestion solution.

The surface area was determined to be 2390 m^2/g by BET analysis.

The composition of the hydroxylated MOF was determined to be:

$Zr_6O_4(OH)_4(BPDC)_{5.03}(BPDC\text{-}(NH_2)_2)_{0.41}(BA)_{0.43}(FA)_{0.38}(H_2O/OH^-)_{0.31}$

3.3.3 UiO-67-0.2$(NH_2)_2$

$ZrCl_4$ (2.00 g, 8.58 mmol, 1.00 equiv.) was added in portions to a beaker containing DMF (199.4 mL, 2.58 mol, 300 equiv.) and water (460 µL, 25.8 mmol, 3.00 equiv.). The solution was heated, and benzoic acid (9.43 g, 77.2 mmol, 9.00 equiv.) was dissolved into the solution. 2,2'-diaminobiphenyl-4,4'dicarboxylic acid (0.47 g, 1.73 mmol, 0.20 equiv.) was dissolved into the solution, which was then transferred to a round bottom flask containing biphenyl-4,4'dicarboxylic acid (1.66 g, 6.85 mmol, 0.80 equiv.). The mixture was stirred at 138°C overnight. The product was filtered and washed with hot DMF (250 mL) and acetone (250 mL), and dried in an oven at 140°C overnight. Yield: 2.99 g.

The product was analyzed by TGA, nitrogen adsorption, PXRD, SEM-EDX and liquid phase ^{1}H NMR using 0.1M NaOD/D_2O as digestion solution.

The surface area was determined to be 2386 m^2/g by BET analysis.

The composition of the hydroxylated MOF was determined to be:

$Zr_6O_4(OH)_4(BPDC)_{4.43}(BPDC\text{-}(NH_2)_2)_{0.54}(BA)_{1.59}(FA)_{0.10}(H_2O/OH^-)_{0.37}$

3.3.4 UiO-67-0.3$(NH_2)_2$

$ZrCl_4$ (2.00 g, 8.58 mmol, 1.00 equiv.) was added in portions to a beaker containing DMF (199.4 mL, 2.58 mol, 300 equiv.) and water (460 µL, 25.8 mmol, 3.00 equiv.). The solution was heated, and benzoic acid (9.43 g, 77.2 mmol, 9.00 equiv.) was dissolved into the solution. 2,2'-diaminobiphenyl-4,4'dicarboxylic acid (0.70 g, 2.57 mmol, 0.30 equiv.) was dissolved into the solution, which was then transferred to a round bottom flask containing biphenyl-4,4'dicarboxylic acid (1.46 g, 6.01 mmol, 0.70 equiv.). The mixture was stirred at 138°C overnight. The product was filtered and washed with hot DMF (250 mL) and acetone (250 mL), and dried in an oven at 140°C overnight. Yield: 3.04 g.

The product was analyzed by TGA, nitrogen adsorption, PXRD, SEM-EDX and liquid phase ^{1}H NMR using 0.1M NaOD/D_2O as digestion solution.

The surface area was determined to be 2336 m^2/g by BET analysis.

The composition of the hydroxylated MOF was determined to be:

$Zr_6O_4(OH)_4(BPDC)_{3.98}(BPDC\text{-}(NH_2)_2)_{1.35}(BA)_{0.59}(FA)_{0.75}$

3.3.5 UiO-67-0.5$(NH_2)_2$

$ZrCl_4$ (2.00 g, 8.58 mmol, 1.00 equiv.) was added in portions to a beaker containing DMF (199.4 mL, 2.58 mol, 300 equiv.) and water (460 µL, 25.8 mmol, 3.00 equiv.). The solution was heated, and benzoic acid (9.43 g, 77.2 mmol, 9.00 equiv.) was dissolved into the solution. 2,2'-diaminobiphenyl-4,4'dicarboxylic acid (1.17 g, 4.29 mmol, 0.50 equiv.) was dissolved into the solution, which was then transferred to a round bottom flask containing biphenyl-4,4'dicarboxylic acid (1.04 g, 4.29 mmol, 0.50 equiv.). The mixture was stirred at 138°C overnight. The product was filtered and washed with hot DMF (250 mL) and acetone (250 mL), and dried in an oven at 140°C overnight. Yield: 2.75 g.

The product was analyzed by TGA, nitrogen adsorption, PXRD, SEM-EDX and liquid phase ^1H NMR using 0.1M $NaOD/D_2O$ as digestion solution.

The surface area was determined to be 2353 m^2/g by BET analysis.

The composition of the hydroxylated MOF was determined to be:

$Zr_6O_4(OH)_4(BPDC)_{3.10}(BPDC\text{-}(NH_2)_2)_{2.04}(BA)_{0.69}(FA)_{1.01}(H_2O/OH^-)_{0.04}$

3.3.6 UiO-67-0.7$(NH_2)_2$

$ZrCl_4$ (1.00 g, 4.29 mmol, 1.00 equiv.) was added in portions to a beaker containing DMF (99.7 mL, 1.29 mol, 300 equiv.) and water (230 µL, 12.9 mmol, 3.00 equiv.). The solution was heated, and benzoic acid (4.72 g, 38.6 mmol, 9.00 equiv.) was dissolved into the solution. 2,2'-diaminobiphenyl-4,4'dicarboxylic acid (0.82 g, 2.99 mmol, 0.70 equiv.) was dissolved into the solution, which was then transferred to a round bottom flask containing biphenyl-4,4'dicarboxylic acid (0.31 g, 1.28 mmol, 0.30 equiv.). The mixture was stirred at 138°C overnight. The product was filtered and washed with hot DMF (200 mL) and acetone (200 mL), and dried in an oven at 140°C overnight. Yield: 1.38 g.

The product was analyzed by TGA, nitrogen adsorption, PXRD, SEM-EDX and liquid phase ^1H NMR using 0.1M $NaOD/D_2O$ as digestion solution.

The surface area was determined to be 1977 m^2/g by BET analysis.

The composition of the hydroxylated MOF was determined to be:

$Zr_6O_4(OH)_4(BPDC)_{2.12}(BPDC\text{-}(NH_2)_2)_{2.88}(BA)_{1.11}(FA)_{0.87}(H_2O/OH^-)_{0.03}$

3.3.7 UiO-67-0.9$(NH_2)_2$

$ZrCl_4$ (0.50 g, 2.15 mmol, 1.00 equiv.) was added in portions to a beaker containing DMF (49.8 mL, 0.64 mol, 300 equiv.) and water (120 µL, 6.44 mmol, 3.00 equiv.). The solution was heated, and benzoic acid (2.36 g, 19.3 mmol, 9.00 equiv.) was dissolved into the solution. 2,2'-diaminobiphenyl-4,4'dicarboxylic acid (0.52 g, 1.93 mmol, 0.90 equiv.) was dissolved into the solution, which was then transferred to a round bottom flask containing biphenyl-4,4'dicarboxylic acid (51.9 mg, 0.21 mmol, 0.10 equiv.). The mixture was stirred at 138°C overnight. The product was filtered and washed with hot DMF (100 mL) and acetone (100 mL), and dried in an oven at 140°C overnight. Yield: 0.62 g.

The product was analyzed by TGA, nitrogen adsorption, PXRD, SEM-EDX and liquid phase ^1H NMR using 0.1M $NaOD/D_2O$ as digestion solution.

The material was determined to be non-porous by nitrogen adsorption.

The composition of the hydroxylated MOF was determined to be:

$Zr_6O_4(OH)_4(BPDC)_{0.65}(BPDC\text{-}(NH_2)_2)_{3.60}(BA)_{1.40}(FA)_{1.59}(H_2O/OH^-)_{0.51}$

3.4 MOF post-synthetic functionalization

General functionalization procedure for mixed linker BPDC-$(NH_2)_2$ MOFs:

UiO-67-X$(NH_2)_2$ (1 equiv.) and 6-chloropicolinaldehyde (5 equiv.) were added transferred to a 15 mL centrifuge tube. Methanol was added to the 10 mL mark, and the tube was shaken (250 rpm) at room temperature overnight. The tube was centrifuged, and the supernatant was removed, the MOF was then washed 4 times with methanol (methanol was added to the 10 mL mark, shaken for 5 min, centrifuged and the supernatant was removed) and dried on an oven at 140°C overnight.

3.4.1 UiO-67-0.1(**3**)

UiO-67-0.1$(NH_2)_2$ (150 mg, 0.04 mmol diamino-functionalization, 1 equiv.) and 6-chloropicolinaldehyde (29.6 mg, 0.2 mmol, 5 equiv.) were added transferred to a 15 mL centrifuge tube. Methanol was added to the 10 mL mark, and the tube was shaken (250 rpm) at room temperature overnight. The tube was centrifuged, and the supernatant was removed, the MOF was then washed 4 times with methanol (methanol was added to the 10 mL mark, shaken for 5 min, centrifuged and the supernatant was removed). The MOF was dried on an oven at 140°C overnight, yielding 132 mg of UiO-67-0.1(**3**) as a pale yellow solid.

The product was analyzed by TGA, nitrogen adsorption, PXRD, SEM-EDX and liquid phase ^{1}H-NMR using 0.1M NaOD/D_2O as digestion solution.

The surface area was determined to be 1353 m^2/g by BET analysis.

The chlorine to zirconium ratio found by EDX was 0.14.

3.4.2 UiO-67-0.3(**3**)

UiO-67-0.1$(NH_2)_2$ (300 mg, 0.21 mmol diamino-functionalization, 1.00 equiv.) and 6-chloropicolinaldehyde (146 mg, 1.03 mmol, 5.00 equiv.) were added transferred to a 15 mL centrifuge tube. Methanol was added to the 10 mL mark, and the tube was shaken (250 rpm) at room temperature overnight. The tube was centrifuged, and the supernatant was removed, the MOF was then washed 4 times with methanol (methanol was added to the 10 mL mark, shaken for 5 min, centrifuged and the supernatant was removed). The MOF was dried on an oven at 140°C overnight, yielding 275 mg of UiO-67-0.3(**3**) as a pale yellow solid.

The product was analyzed by TGA, nitrogen adsorption, PXRD, SEM-EDX and liquid phase ^{1}H-NMR using 0.1M NaOD/D_2O as digestion solution.

The surface area was determined to be 1205 m^2/g by BET analysis.

The chlorine to zirconium cluster ratio (Cl/Zr_6) found by EDX was 2.08.

3.4.3 UiO-67-0.5(**3**)

UiO-67-0.1$(NH_2)_2$ (300 mg, 0.33 mmol diamino-functionalization, 1.00 equiv.) and 6-chloropicolinaldehyde (231 mg, 1.63 mmol, 5.00 equiv.) were added transferred to a 15 mL centrifuge tube. Methanol was added to the 10 mL mark, and the tube was shaken (250 rpm) at room temperature overnight. The tube was centrifuged, and the supernatant was removed, the MOF was then washed 4 times with methanol (methanol was added to the 10 mL mark, shaken for 5 min, centrifuged and the supernatant was removed). The MOF was dried on an oven at 140°C overnight, yielding 321 mg of UiO-67-0.5(**3**) as a pale yellow solid.

The product was analyzed by TGA, nitrogen adsorption, PXRD, SEM-EDX and liquid phase ^{1}H-NMR using 0.1M NaOD/D_2O as digestion solution.

The surface area was determined to be 1596 m^2/g by BET analysis.

The chlorine to zirconium cluster ratio (Cl/Zr_6) found by EDX was 4.56.

3.4.4 UiO-67-0.7(**3**)

UiO-67-0.1$(NH_2)_2$ (300 mg, 0.41 mmol diamino-functionalization, 1.00 equiv.) and 6-chloropicolinaldehyde (287 mg, 2.03 mmol, 5.00 equiv.) were added transferred to a 15 mL centrifuge tube. Methanol was added to the 10 mL mark, and the tube was shaken (250 rpm) at room temperature overnight. The tube was centrifuged, and the supernatant was removed, the MOF was then washed 4 times with methanol (methanol was added to the 10 mL mark, shaken for 5 min, centrifuged and the supernatant was removed). The MOF was dried on an oven at 140°C overnight, yielding 319 mg of UiO-67-0.7(**3**) as a pale yellow solid.

The product was analyzed by TGA, nitrogen adsorption, PXRD, SEM-EDX and liquid phase ^{1}H-NMR using 0.1M NaOD/D_2O as digestion solution.

The surface area was determined to be 1362 m^2/g by BET analysis.

The chlorine to zirconium cluster ratio (Cl/Zr_6) found by EDX was 6.09.

4 Results and Discussion

4.1 Aldehyde screening

As a part of the author's bachelor's project, the reaction of the dimethyl ester $Me_2BPDC\text{-}(NH_2)_2$ molecule with an aldehyde in the presence of the metal salt $Zn(OAc)_2{\cdot}2H_2O$ as a Lewis acid was studied (See **Paper I**). Besides the diazepine, two side products were observed, the mono- and diimine (Scheme 5). However, no trend was observed, and the outcome of the reaction was found to be aldehyde dependent.

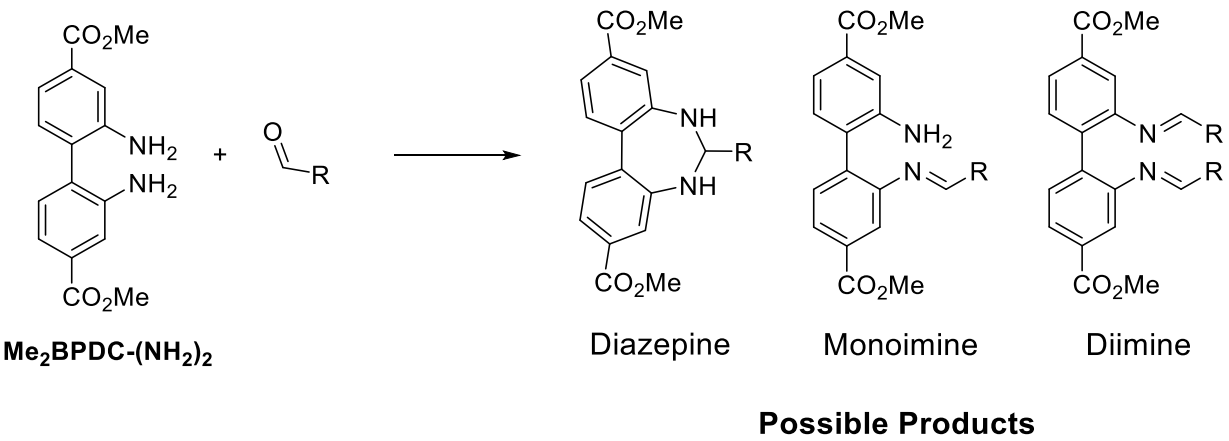

Scheme 5. Possible products found in the reaction of $Me_2BPDC\text{-}(NH_2)_2$ with an aldehyde.

When functionalizing the MOF, in order to maintain its porosity characteristics, is important to refrain from using bulky aldehydes. A bulkier diazepine will occupy more space inside of the pores, causing them to become smaller, and therefore the surface area of the MOF decreases. Employing aldehydes containing elements that are well distinguishable from the rest of the MOF in EDX, such as chlorine and iodine, allows to quantify the diazepine functionalisation with EDX.

In the bachelor's project, mostly aromatic heterocycles were used, and it is interesting to understand whether the diazepine formation can also be observed when aldehydes containing alkane chains, as well as substituted phenyl rings, are used. There has been reports on hydrophobic MOFs and their applications, and it is thought that the long alkane chain would help improve the MOFs hydrophobicity.[83,84] The aldehydes screened in this thesis are shown in Figure 13.

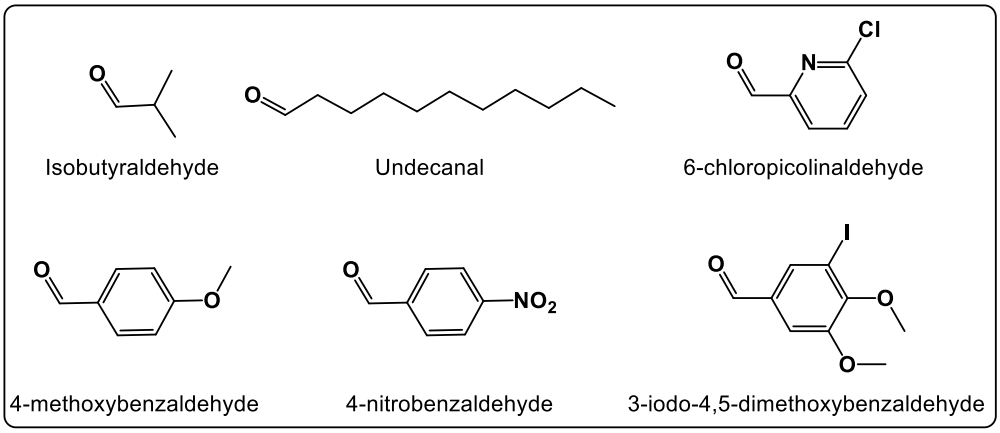

Figure 13. Aldehydes screened in this thesis.

From the six aldehydes screened, two (6-chloropicolinaldehyde and 3-iodo-4,5-dimethoxybenzaldehyde) contain chlorine and iodine, and therefore, the corresponding diazepines would be suitable for EDX analysis.

The reaction using 6-chloropicolinaldehyde proved to be successful even without the Lewis acid, but the yield obtained decreased from 92% to 79%. While the reaction using 3-iodo-4,5-dimethoxybenzaldehyde yielded the diazepine (**14**) as the major product, the diimine (**14D**) was also observed as a minor product.

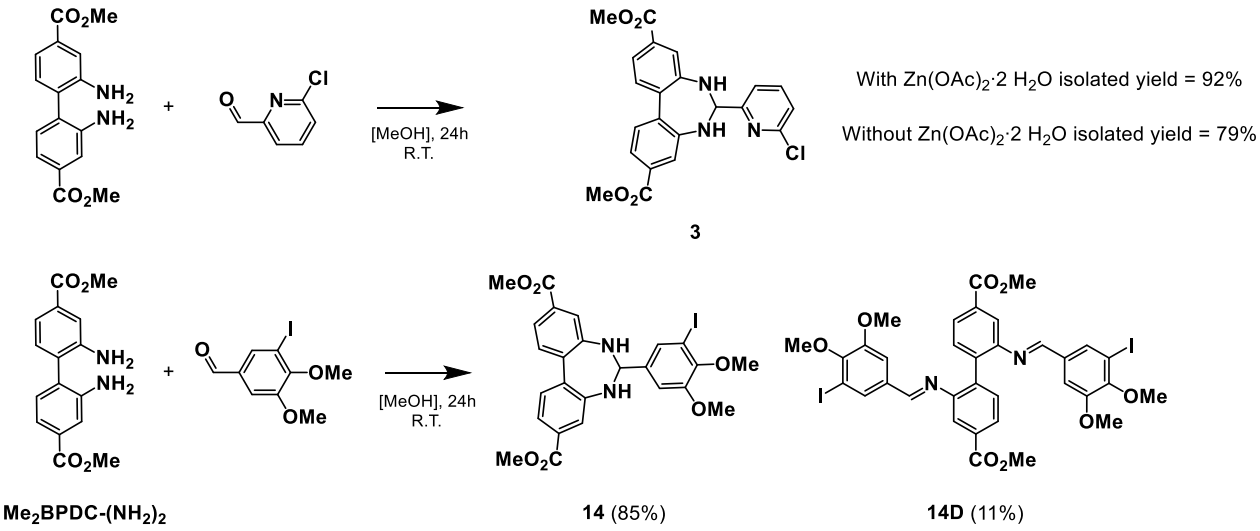

Scheme 6. Reaction outcomes for two aldehydes, conversion, found by ^{1}H-NMR, is shown for 3-iodo-4,5- dimethoxybenzaldehyde. Numbering as in the manuscript Paper I, which can be found in the appendix.

Interestingly enough, for a reaction at room temperature overnight, both isobutyraldehyde and undecanal yielded solely the diazepine, but for the reaction with undecanal the absence of $Zn(OAc)_2{\cdot}2H_2O$ showed unconverted $Me_2BPDC\text{-}(NH_2)_2$ in the collected solids. The diazepine yielded in the reaction with isobutyraldehyde showed to have a higher solubility in the solvent used (MeOH), and therefore the synthesis procedure was changed to accommodate this change.

Lastly, the reaction with the *para* substituted aldehydes yielded different results, showing that the nature of the *para* substituent influences the reaction. A reaction at room temperature overnight with the Zn salt for the 4-methoxybenzaldehyde showed 62% conversion of the $Me_2BPDC\text{-}(NH_2)_2$ to **5**, however, the same reaction conditions only led to 25% conversion for the 4-nitrobenzaldehyde to **15**.

It was possible to achieve a diazepine conversion of 93% for the nitro substituted aldehyde in the absence of the Lewis acid, but small amounts of mono- (**15M,** 3%) and diimine (**15D,** 5%) were found as minor products.

All aldehydes screened in **Paper I** were considered for the MOF incorporation, and the outcome of the reactions is shown in Table 1, the aldehydes screened as a part of this thesis are highlighted. An overview of the isolatable dibenzo[*d,f*]-1,2-dihydro-[1,3]diazepines synthesized in **Paper I** is shown in Figure 14.

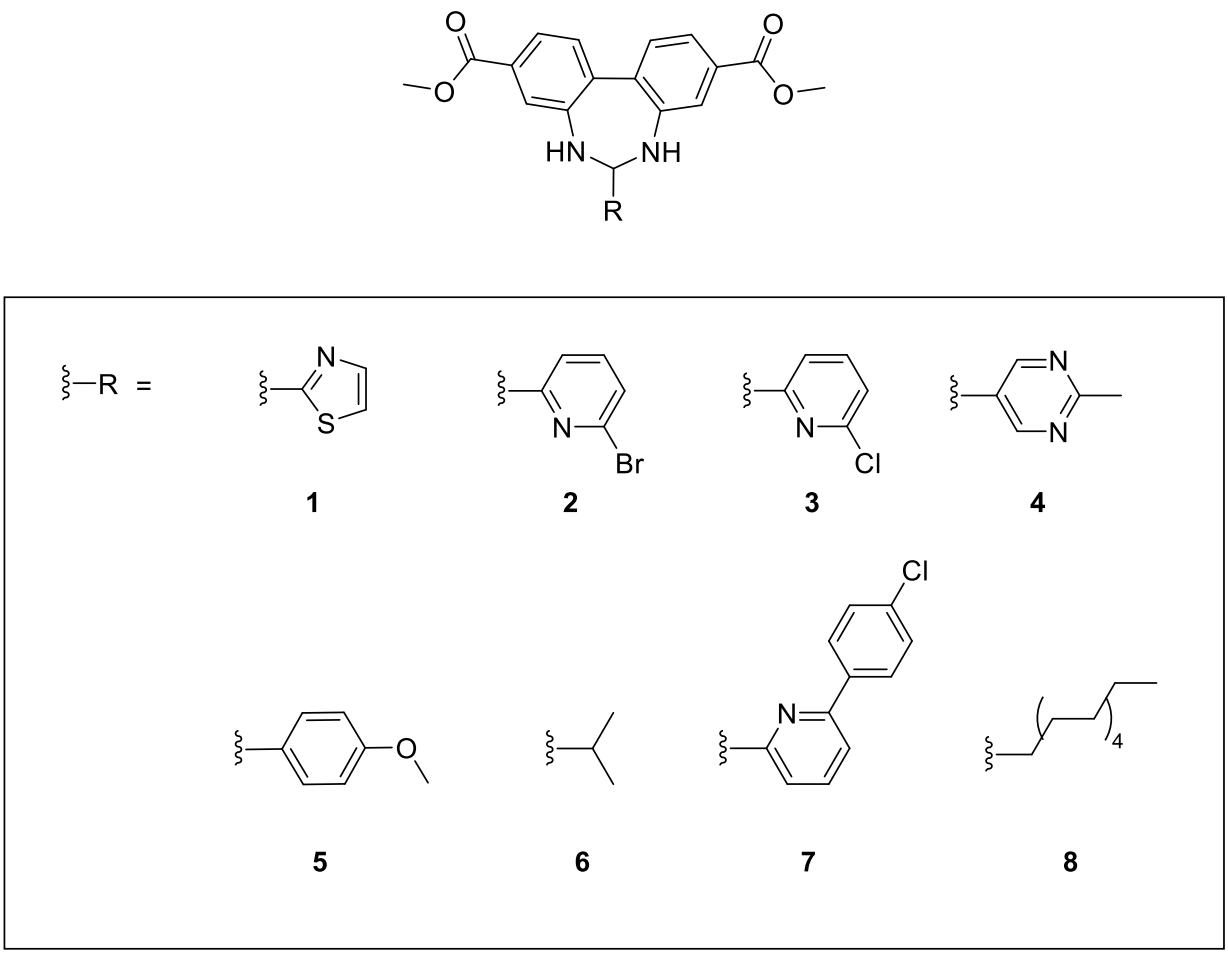

Figure 14 Overview of the dibenzo[*d,f*]-1,2-dihydro-[1,3]diazepines isolated in **Paper** I.

Table 1. Aldehydes screened on **Paper I** for dibenzo[*d,f*]-1,2-dihydro-[1,3]diazepine synthesis.Highlighted, the aldehydes screened as part of this thesis. If a mixture was obtained, the % of products and starting material in the isolated crude product are given as determined by ^{1}H NMR (M = monoimine and D = diimine). Reaction conditions as given in the general procedure (RT, overnight reaction, 1.1 equiv. aldehyde, solvent: MeOH), unless specified otherwise.

Aldehyde	Diazepine	Imine	Starting Material
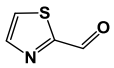	**1** 70% **1** (86% yield)† **1** 57%†*	n.d. n.d. n.d.	30% n.d. 43%
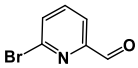	**2** (81% yield) **2** (64% yield)*	n.d. n.d.	n.d. n.d.
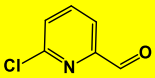	**3** (92% yield) **3** (79% yield)*	n.d. n.d.	n.d. n.d.
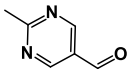	n.d. n.d.* **4** (36% yield)§ **4** (91%)*§	n.d. n.d. n.d. n.d.	recovered recovered n.d. 9%
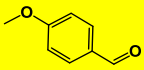	**5** (62%) **5** (86% yield)† **5** (87%)*†	**5M** (5%) n.d. **5M** (13%)	33% n.d. n.d.
	6 (86% yield) **6** (95% yield)*	n.d. n.d.	n.d. n.d.
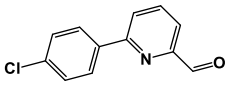	**7** (95% yield) **7** (85% yield)*	**7M** (traces) n.d.	traces n.d.
	8 (56% yield) **8** (62%)*	n.d. n.d.	n.d. 38%
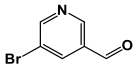	n.d. **9** (95%)*	n.d. n.d.	recovered 5%
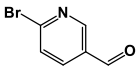	**10** (37%) **10** (75%)*	n.d. n.d.	63% 25%
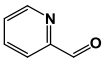	**11** (70%)	n.d.	30%
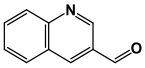	**12** (10%)	**12D** (21%)	69%
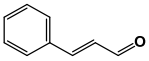	**13** (traces)	**13D** (90%)	10%
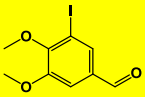	**14** (85%)	**14D** (11%)	4%
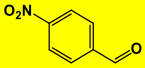	**15** (25%) **15** (93%)*	**15M** (Traces), **15D** (1%) **15M** (3%), **15D** (5%)	74% n.d.
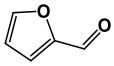	n.d.	**17D** (86% yield)	n.d.
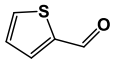	n.d.	**16D** (8%)	92%
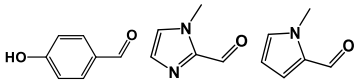	n.d.	n.d.	recovered

† 3 days reaction time; * Without $Zn(OAc)_2 \cdot 2H_2O$; § Reflux

From all aldehydes screened, in order to choose one aldehyde to incorporate into the MOF, it is important to choose an aldehyde that gives near to full conversion to the diazepine. To better monitor the aldehyde incorporation, EDX can be used whenever suitable atoms are present in the MOF, which for the aldehydes screened are: chlorine, iodine and sulphur. It is unknown how the Lewis acid Zn-salt would influence the reaction when the 1,4-diaryl compound is inside of the MOF, so its use is disregarded. Therefore, the most suitable aldehyde for the MOF incorporation is 6-chloropicolinaldehyde, due to its small size, the presence of a chlorine atom, its relative short reaction time (overnight) compared to other aldehydes and the full conversion without the Lewis acid ($Zn(OAc)_2{\cdot}2H_2O$).

Inside of the MOF, the 1,4-diaryldiamino compound found is however not the $Me_2BPDC\text{-}(NH_2)_2$ ester, but instead the carboxylate variant of the linker ($BPDC\text{-}(NH_2)_2$). Therefore, the reaction of the dicarboxylic acid compound, $H_2BPDC\text{-}(NH_2)_2$, with 6-chloropicolinaldehyde was attempted.

This reaction yielded solely the dicarboxylic acid of compound **3**, named **H_2-3**, as seen on the ^{1}H NMR (Figure 15). The isolated yield was 92%, indicating the high conversion of the $H_2BPDC\text{-}(NH_2)_2$ into the diazepine.

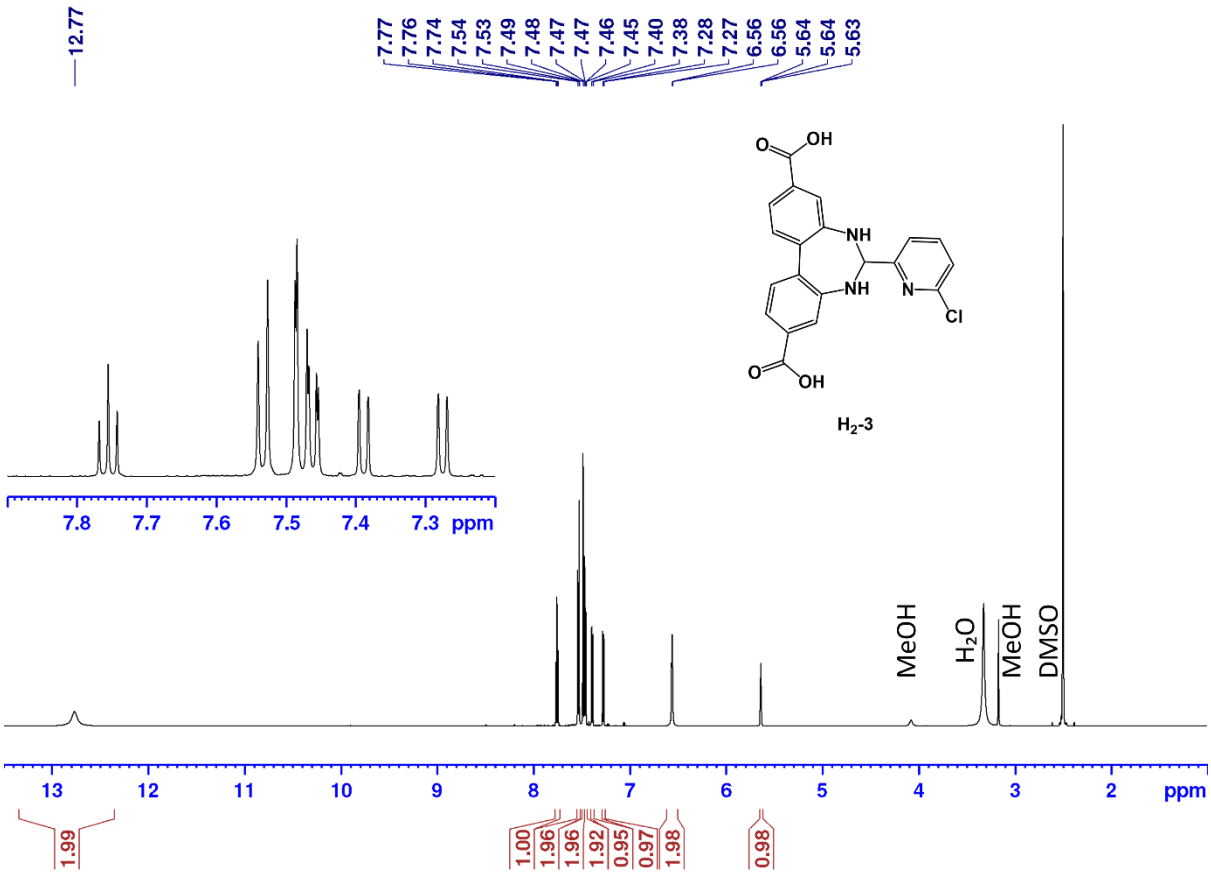

Figure 15. ^{1}H NMR for compound **H_2-3** (600 MHz, DMSO-d_6).

4.2 Exploring the photophysical properties

A key feature to identifying if the formation of the 1,3-dibenzodiazepines was successful, is the shift in colour and fluorescence of the molecule. While the diamino precursor (**Me_2BPDC-$(NH_2)_2$**) has no apparent colour in solution, it has a light blue fluorescence under UV light (368 nm). Nonetheless, for all NMR samples using DMSO-d_6 as the solvent, the solution exhibited an intense yellow colour, and a yellow fluorescence under UV light (368 nm), even for reactions with low conversion of the diazepine. On the other hand, the diazepines show that the colour of the solution is highly dependent on the solvent. An exception is found for the 4-nitrobenzene substituted diazepine, where even though the solution exhibited an intense yellow colour, no fluorescence was observed. This can be explained by the known fluorescence quenching ability of nitro compounds.[85]

It is therefore interesting to see how the absorption and emission of the diazepines change when changing the substituent. Their spectra are shown in Figure 16.

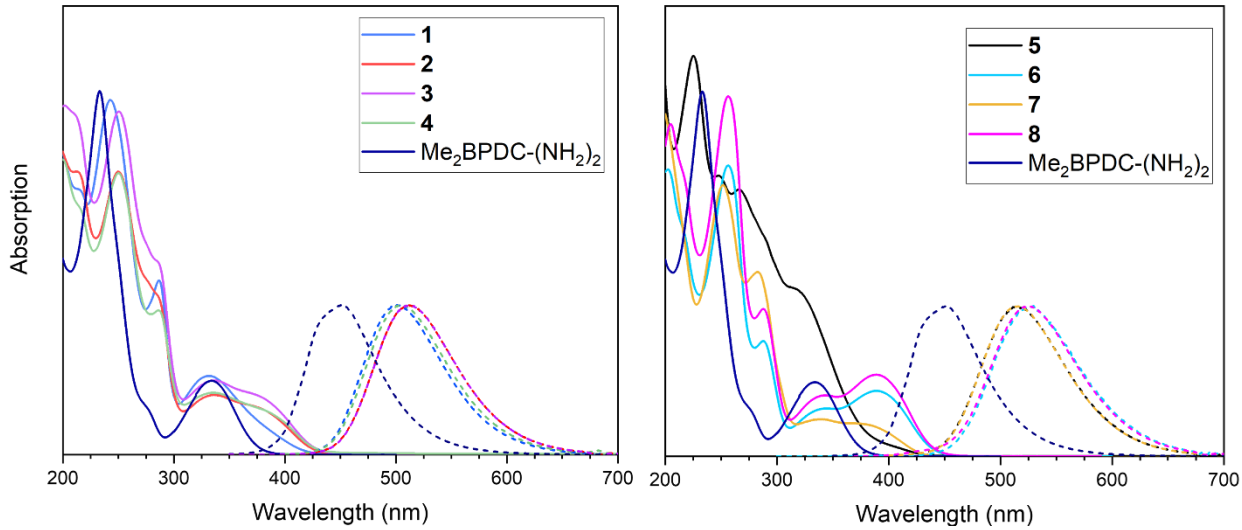

Figure 16. UV-Vis absorption (solid lines) and normalized emission spectra (dashed lines) of **1-8** and **Me_2BPDC-$(NH_2)_2$** in MeCN (ca. 30 µM for absorption).

Although the UV-Vis absorption spectra for all diazepines are very similar independently of the substituent, the spectrum for compound **5** is more similar to the spectrum for the starting material than to the other diazepines. It is important to note that the UV-Vis spectrum was obtained one year after the synthesis. Therefore, the year old sample was analysed by ^{1}H-NMR. The comparison of the ^{1}H-NMR spectra of the year old sample, compound **5** and sample and **Me_2BPDC-$(NH_2)_2$** is shown in Figure 17. It was found that the sample was now a mixture composed of **5** and **Me_2BPDC-$(NH_2)_2$**. The UV-Vis absorption obtained is therefore composed of a mixture of both the diazepine and the 1,4-diaryldiamino compound.

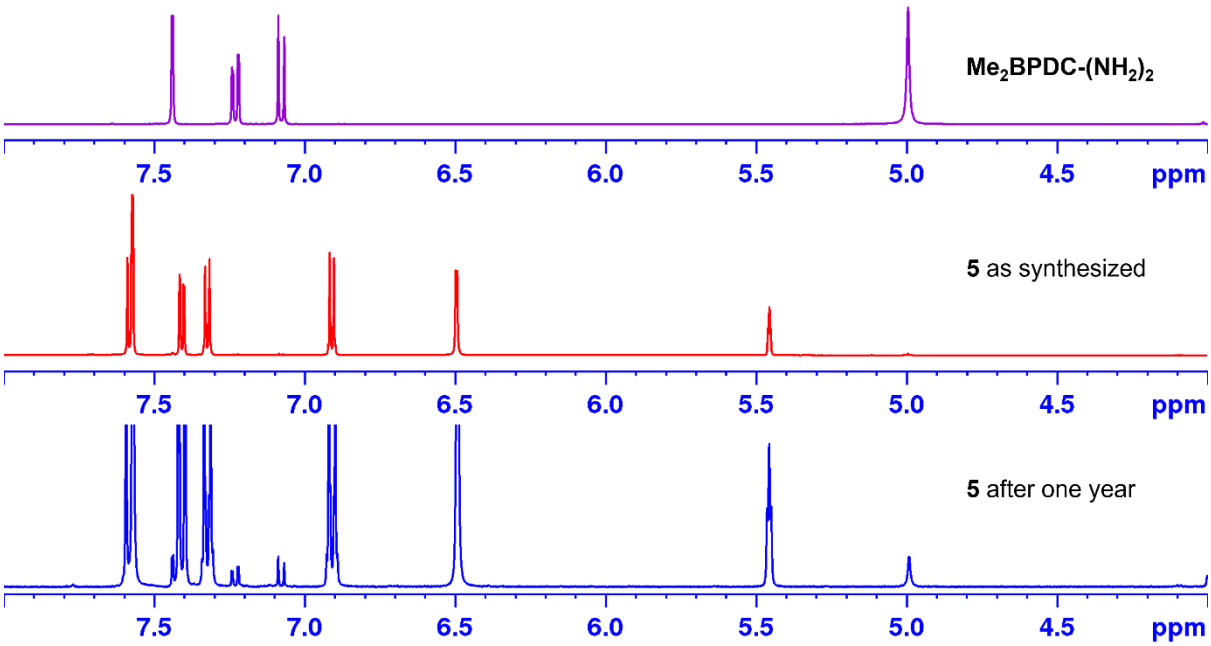

Figure 17 Partial ^{1}H-NMR (400 MHz, DMSO-d_6). Top: NMR obtained for **$Me_2BPDC-(NH_2)_2$** Middle: NMR obtained for sample as synthesized. Bottom: NMR obtained for sample one year after synthesis.

For most of the diazepines synthesized, it is possible to see four absorption bands, while for the $Me_2BPDC-(NH_2)_2$ starting material, it is only possible to see two well defined absorption bands. A summary of the absorption bands, emission wavelength and quantum yield found is shown in Table 2.

Table 2. Absorption maxima and their molar extinction coefficient, emission, and fluorescence quantum yield of **1-8** and **$Me_2BPDC-(NH_2)_2$** in MeCN. The fluorescence quantum yield was determined with quinine sulphate in 0.05M H_2SO_4 as reference.[86,87]

Compound	λ_1 [nm] (ε [$M^{-1}cm^{-1}$])	λ_2 [nm] (ε [$M^{-1}cm^{-1}$])	λ_3 [nm] (ε [$M^{-1}cm^{-1}$])	λ_4 [nm] (ε [$M^{-1}cm^{-1}$])	λ_{em} (nm)	Φ_F
1	243 (33 200)	287 (16 300)	332 (7 430)	N/A	502	0.57
2	250 (29 300)	287 (sh, 16 300)	336 (6 300)	381 (sh, 4 800)	512	0.59
3	250 (32 000)	287 (sh, 18 000)	339 (6 900)	378 (sh, 5 300)	513	0.59
4	250 (27 810)	286 (14 190)	335 (6 114)	386 (sh, 4 189)	505	0.58
5	225 (37 270)	248 (26 100)	266 (24 900)	319 (15 600)	515	0.60
6	257 (32 200)	288 (12 300)	345 (5 170)	389 (7 130)	530	0.61
7	252 (42 400)	283 (29 200)	339 (5 900)	382 (sh, 5 000)	513	0.59
8	256 (33 800)	287.8 (13 960)	343 (5 800)	389 (7 680)	526	0.62
$Me_2BPDC-(NH_2)_2$	233 (36 200)	277 (sh, 4 592)	334 (7 480)	N/A	451	0.51

It is possible to see that for most diazepines synthesized, with the exception of **1**, and **5**, there is an additional absorption band at around 400 nm, compared to the starting material (**$Me_2BPDC-(NH_2)_2$**). In addition, the two first absorption bands have been red-shifted for all diazepines. The emission spectra also had a red-shift, ranging 51 - 79 nm depending on the diazepine. The quantum yield for all diazepines show an improvement from the one for **$Me_2BPDC-(NH_2)_2$**. However, the quantum yield between compound **1-8** does not differ a lot, which shows that the substituent does not have an influence on the quantum yield.

In **Paper I** the solvatochromatic properties of compound **6** was investigated using the Lippert-Mataga equation, showing a good correlation between the stokes-shift and the solvent's orientation polarizability function for a series of solvents. This proves that the solvatochromatic properties are not primarily affected by solvent-specific interactions.[88]

To obtain a higher understanding of the orbitals involved in the photophysical processes described above, TD-DFT calculations were performed on compound **6** and **$Me_2BPDC-(NH_2)_2$** using the Gaussian16 program.[89] The PBE0 functional with the 6-311+G** basis-set were

used for the geometry optimization,[90,91] and the M06 functional with the def2svp basis-set were used for the TD-DFT calculations (See SI of **Paper I** for details on the benchmarking).[92,93] For both the geometry optimization and the TD-DFT calculations, implicit solvation using the SMD model was used.[94]

For each of the main electronic transitions found for **$Me_2BPDC-(NH_2)_2$** and **6**, the molecular orbitals involved are listed in Table 3. Figure 18 and Figure 19 show the energy and shapes of the molecular orbitals for **6** and **$Me_2BPDC-(NH_2)_2$** in MecN, respectively.

Table 3. Excitation wavelength (λ_{Exc}), the oscillator strength (*f*) and the molecular orbitals involved (MOs) for the main electronic excited states for different compounds in MeCN. Table retrieved from **Paper I**.

Compound	λ_{Exc} (nm)	*f*	MOs
$Me_2BPDC-(NH_2)_2$	229	0.1430	HOMO – 1 → LUMO + 3
	236	0.1884	HOMO – 1 → LUMO + 2
	261	0.2550	HOMO – 2 → LUMO
	324	0.1215	HOMO – 1 → LUMO
	335	0.2682	HOMO → LUMO
6	203	0.5172	HOMO – 2 → LUMO + 2
	248	0.2889	HOMO → LUMO + 3
	260	0.1225	HOMO → LUMO + 2
	284	0.2143	HOMO – 2 → LUMO
	330	0.0814	HOMO – 1 → LUMO
	388	0.3047	HOMO → LUMO

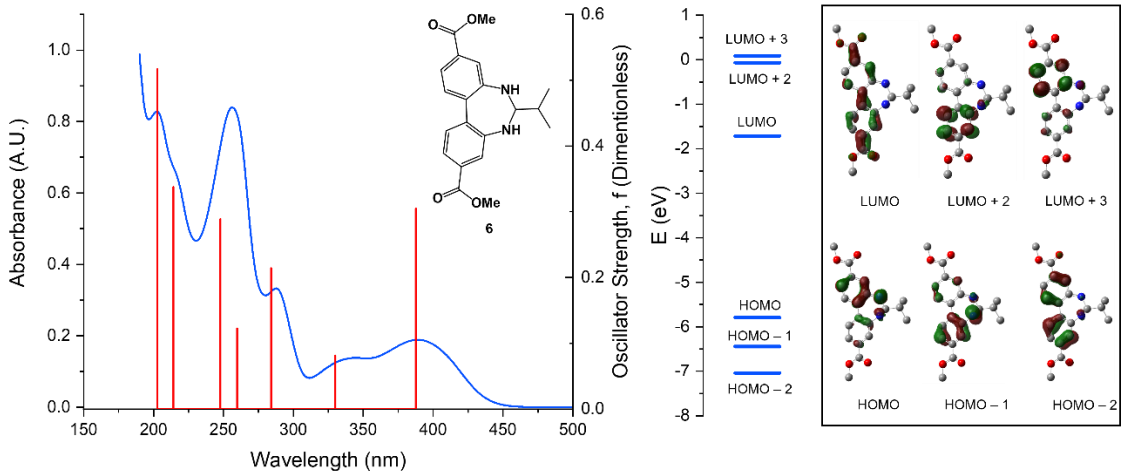

Figure 18 Left: Experimental UV-Visible spectrum of **6** in MeCN (blue curve) and the main TD-DFT(M06) electronic excitations (red lines). Right: Calculated molecular orbitals for **6** in MeCN and frontier orbitals involved in the main TD-DFT(M06) electronic transitions, see Table 4. Hydrogens were omitted for clarity. Frontier orbitals are shown with an isovalue of 0.05 a.u.

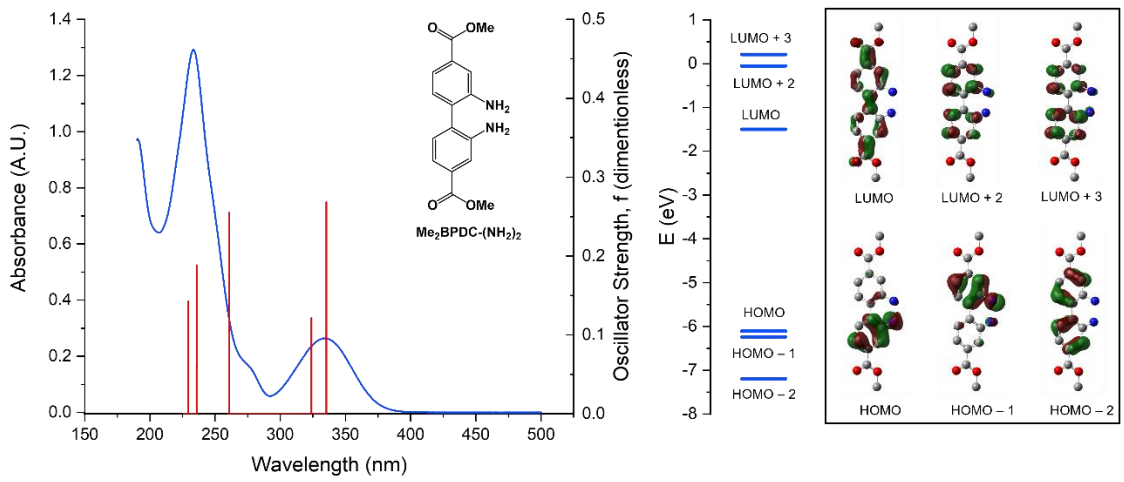

Figure 19 Left: Experimental UV-Visible spectrum of **$Me_2BPDC-(NH_2)_2$** in MeCN (blue curve) and the main TD-DFT(M06) electronic excitations (red lines). Right: Calculated molecular orbitals for **$Me_2BPDC-(NH_2)_2$** in MeCN and frontier orbitals involved in the main TD-DFT(M06) electronic transitions. Hydrogens were omitted for clarity. Frontier orbitals are shown with an isovalue of 0.05 a.u.

For **6**, the HOMO and HOMO– 1 orbitals are localised on the diazepine moiety, while the LUMO orbital is distributed over the whole diaryl backbone, including the esters. Similarly, for **$Me_2BPDC-(NH_2)_2$** the HOMO and HOMO– 1 orbitals are localised in each of the amines, while the LUMO is distributed over the backbone.

The HOMO → LUMO transition is responsible for the absorption at the highest wavelength (λ_4 for **6**), while the HOMO – 1 → LUMO transition is responsible to the absorption at the second highest wavelength (λ_3 for **6**). However, for **$Me_2BPDC-(NH_2)_2$** those transitions are close in energy giving rise to only one absorption band (λ_3). This is explained by the conjugation of the lone pair on one of the nitrogens in the diazepine ring with the phenyl ring, causing the transition from that nitrogen to the backbone less energetic, and therefore red-shifted.

This is seen on the distance between the carbon on the phenyl ring to the nitrogen in the diazepine/amine on the optimized geometries (Figure 20). While the distance between the phenyl ring and the amines found in **$Me_2BPDC-(NH_2)_2$** is almost equal (1.385 Å and 1.387 Å), the distance between the phenyl rings and the diazepine nitrogens have a higher difference (1.368 Å and 1.395 Å).

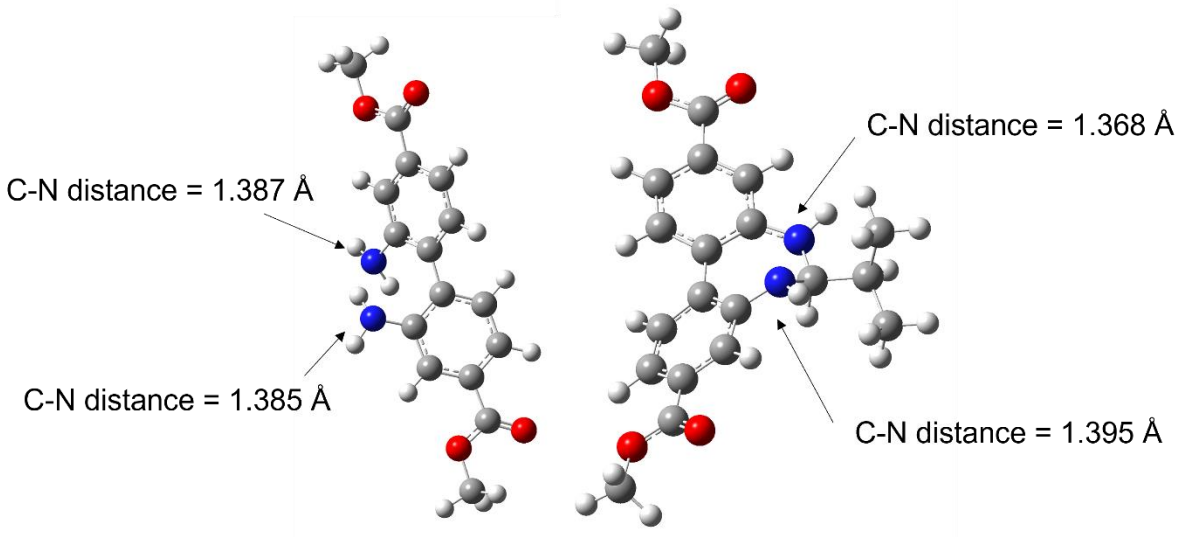

Figure 20 C-N distances found in the optimized geometries for **$Me_2BPDC-(NH_2)_2$**, on the left, and **6** on the right.

4.3 Synthesis of mixed linker UiO-67 MOFs

Due to the use of $ZrCl_4$ as the Zr(IV) source, the synthesis of the UiO-67 MOF will occur in a very acidic medium, as hydrochloric acid is formed in the synthesis. The synthesis equation for the formation of UiO-67 is shown below.

$$6ZrCl_4(s) + 8\,H_2O\,(l) + 6\,H_2BPDC\,(s) \underset{\Delta}{\rightarrow} Zr_6O_4(OH)_4(BPDC)_6(s) + 24HCl\,(g)$$

It is then necessary to use linkers that not only are soluble in DMF, but also can survive the high temperature and acidic reaction conditions. This is not the case for the 1,3-dibenzodiazepines explored in this thesis. Based on experimental observations, the diazepine ring is cleaved in the presence of an acid, being converted back into the $H_2BPDC-(NH_2)_2$ and the aldehyde. Therefore, a post synthetic method had to be used in order to incorporate the diazepine moiety into the UiO-67 MOF.

One method of incorporating the diazepines into the MOF is via post synthetic functionalization (PSF). This way, a UiO-67 MOF containing $BPDC-(NH_2)_2$ can be reacted with an aldehyde yielding then the diazepine MOF. This general synthesis route is shown in Scheme 7.

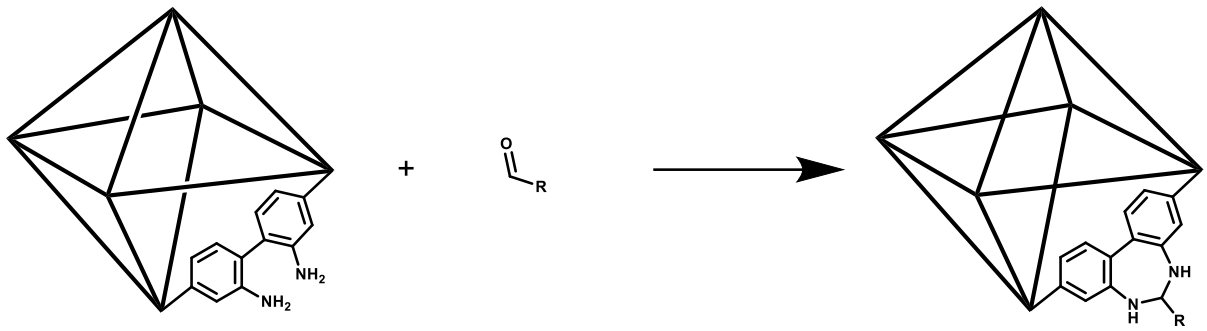

Scheme 7. General synthesis procedure for post synthetic functionalization (PSF) of 1,3-dibenzodiazepines in the UiO-67 MOF.

To investigate how the fluorescence changes when the diazepine is incorporated into the MOF, a series of UiO-67 MOFs containing different amounts of BPDC-$(NH_2)_2$ was synthesized and characterized.

In literature, a series of mixed linker UiO-67 using 2,2'-bipyridine-5,5'-dicarboxylic acid (BPYDC) linkers was synthesized, and it was observed that the molar percentage of BPYDC added was not the same molar percentage incorporated.[44] It is therefore necessary to fully investigate the final BPDC-$(NH_2)_2$ incorporation.

This can be done primarily with the use of liquid phase digestion ^{1}H-NMR and TGA. The names for the MOFs synthesized are given according to their attempted BPDC-$(NH_2)_2$ incorporation, so, for the attempted 10% diamino MOF, its name becomes UiO-67-0.1$(NH_2)_2$.

Literature shows the UiO-67 MOF, when synthesized with only the BPDC-$(NH_2)_2$ linker, has low crystallinity and very low surface area (A_{BET} ca. 300 m^2/g),[51] the surface area decreases even more after post synthetic functionalization with Lithium tert-butoxide on the oxohydrometallic clusters (A_{BET} ca. 20 m^2/g). Therefore, the attempted percentages were: 10%; 20%; 30%; 50%; 70% and 90%. In addition, a regular UiO-67 was also synthesized for comparing purposes.

For the mixed linker UiO-67-x$(NH_2)_2$ MOF, additional peaks for the BPDC-$(NH_2)_2$ linker will appear. Due to the use of D_2O as the solvent used for the digestion, the high deuterium exchange causes the amino groups to become NMR silent. There are therefore only three signals visible as shown in Figure 21. Those will be two doublets and one doublet of doublet. Even though the proton closest to the amino group does not have any neighbouring protons, a $^4J_{H,H}$ coupling between proton D-3, in red, and D-2, in pink, is observed.

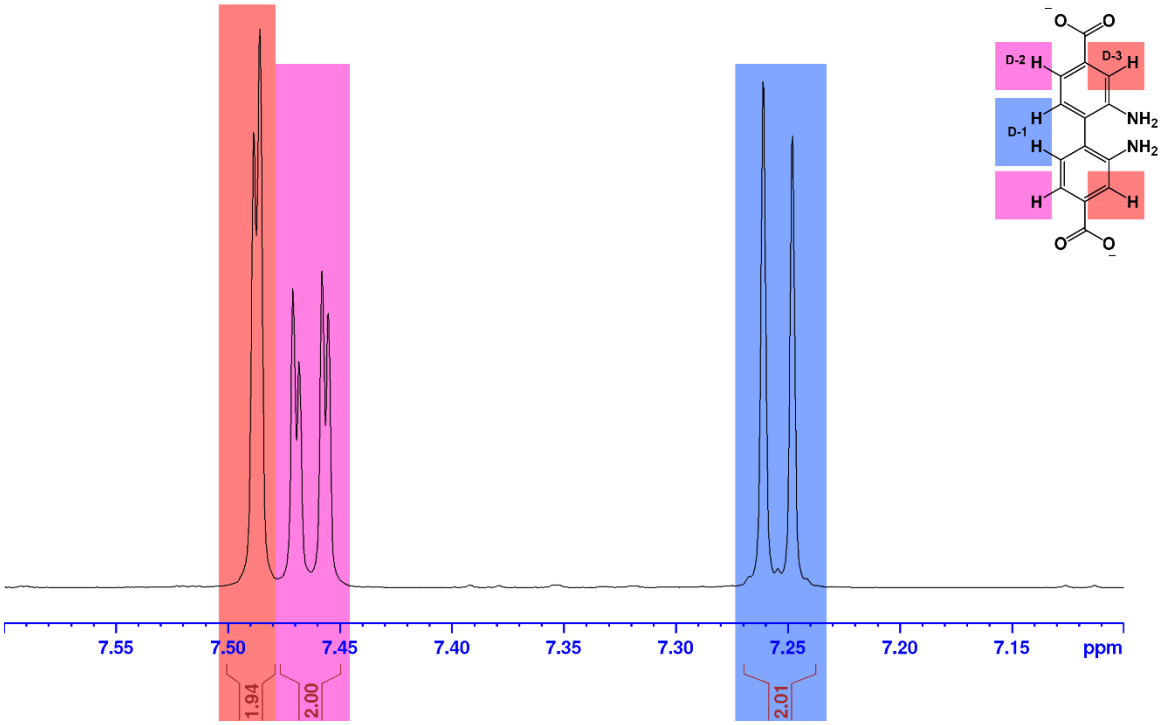

Figure 21. ^{1}H NMR of the diamino linker under digestion conditions (600 MHz, 0.1M NaOD/D_2O), showing an amplified vision of the aromatic region.

The presence of formate during the synthesis can result in formylation of the diamino linkers, as shown in Scheme 8. This reaction is an equilibrium reaction, and therefore, the synthesized MOF could contain a mixture of the non-, mono- and biformylated linkers. Those formylated linkers can also be formed through a transamidation reaction directly with DMF, this is although a slow reaction, and not thought as the main source of formylated linkers.

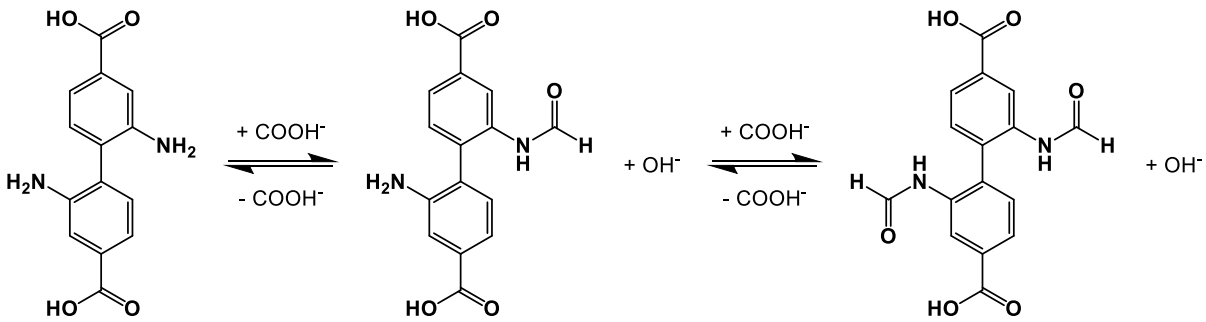

Scheme 8 General formylation equilibrium reaction of the diamino linker in an acidic medium.

The integrals found can be converted to integrated relative molar amounts ($I_{rel,BPDC}$) by dividing the integral to the number of corresponding equivalent hydrogens the signal arises from. For example, in Figure 9, the integral for the BPDC peak is 1, therefore its relative molar amount will be $I_{rel,BPDC}$ = ¼ = 0.25. Correspondingly, the relative molar amount for benzoate is $I_{rel,BA}$ = 0.04/2 = 0.02.

When the MOF is digested with NaOD, the formate present in the pores will be dissolved into the solution. As previously discussed, the presence of DMF in the MOF, adsorbed into the pores, for example, will cause a basic hydrolysis reaction to occur (Scheme 3). This will then increase the number of formate molecules as well as DMA. The presence of formylated linkers in the basic digestion solution will cause a non-reversible hydrolysis reaction (shown in , in which the linkers will slowly get deformylated. Therefore, it is important to conduct the digestion overnight, so that the hydrolysis can be, or come close to a completion.

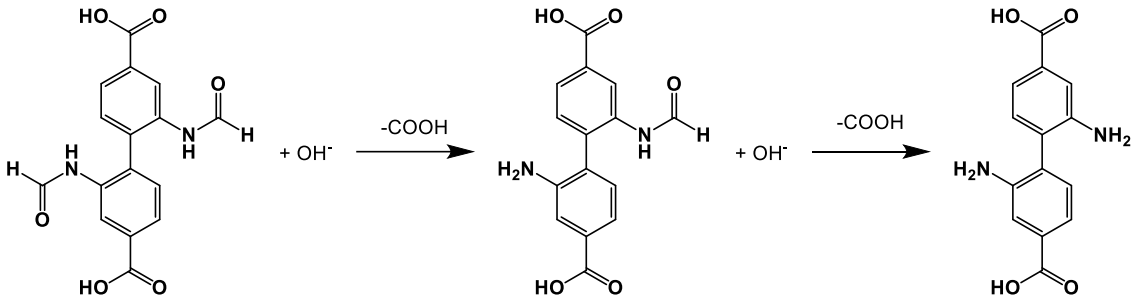

Scheme 9. General hydrolysis reaction of the **BPDC-$(NH_2)_2$** linker in a basic medium.

For the biformylated linker, 3 signals are expected due to its symmetry, while for the monoformylated 6 signals are expected. This results in an uncertainty in the quantification of linker incorporation into the MOF. Figure 22 shows the ^{1}H digestion NMR of the UiO-67-0.1$(NH_2)_2$ MOF, a ^{1}H NMR spectrum was taken 30 minutes after the digestion started, and another after 24 hours. The most reliable signal to use for the quantification of the BPDC-$(NH_2)_2$ linker is the one with the lowest chemical shift (D-1, see Figure 21), since there are no peaks overlapping with those of benzoic acid or H_2BPDC.

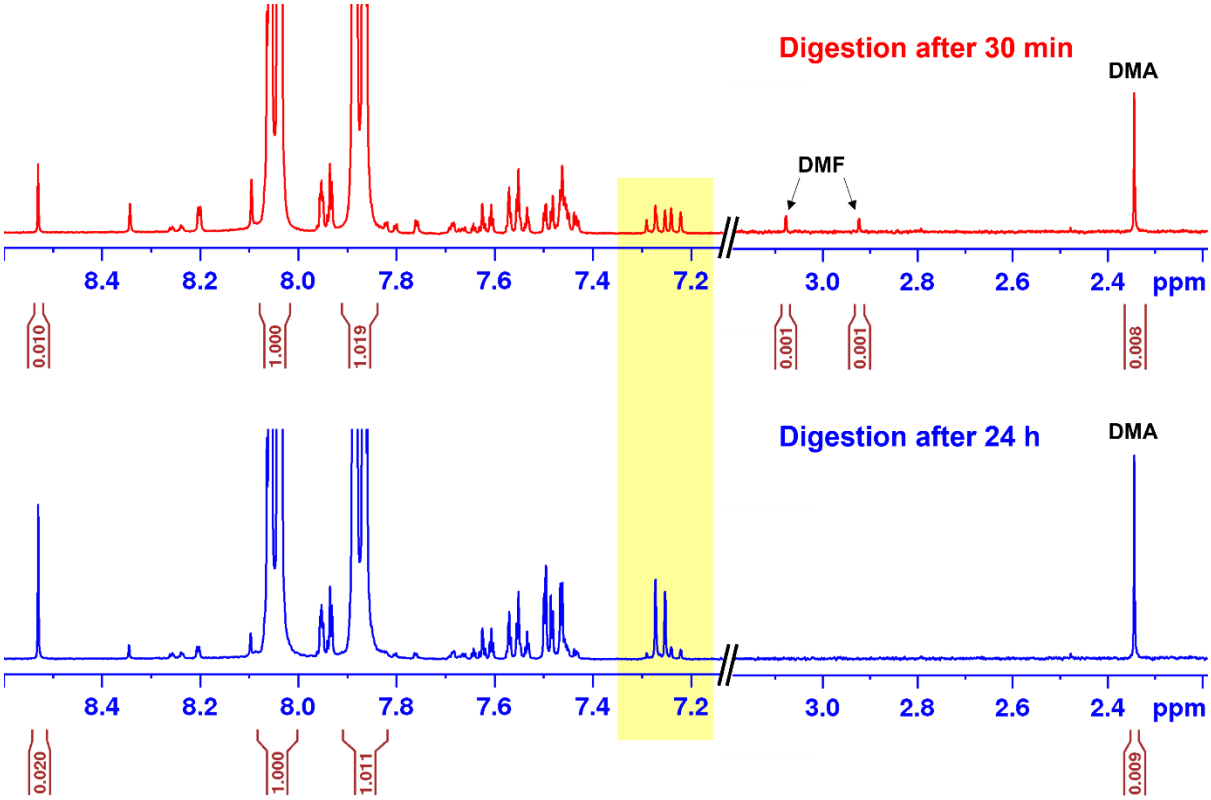

Figure 22. Partial ^{1}H NMR of the UiO-67-0.1$(NH_2)_2$ MOF (400 MHz, 0.1M NaOD/D_2O), Top: NMR obtained 30 min after digestion start. Bottom: NMR obtained 24 h after digestion start.

After only 30 minutes, it is possible to detect traces of DMF in the sample. At the same time, the peaks for D-1 and the corresponding protons in the formylated forms, seem to be equal. After 24 hours, it is possible to see that the formate peak's integral has increased at the expense of the DMF peaks, which are gone. The BPDC-$(NH_2)_2$ linker has now been converted back into its non-formylated form, although it is still possible to see traces of the formylated BPDC-$(NH_2)_2$ linker. Even though the formate signal has doubled its integral (+ 100%), the DMA signal has merely changed, and for each formate formed from the DMF hydrolysis, a DMA molecule is formed. That means that for every integrated proton on the formate signal, six integrated protons should be integrated for the DMA peak.

This further confirms the presence of formylated linkers, and the formate peak will be a mixture of the three formate sources: formate found as a capping agent in the MOF; formate obtained from the hydrolysis of DMF; and formate obtained from the hydrolysis of formylated BPDC-$(NH_2)_2$ linkers. It is possible to find how much formate comes from the DMF, by subtracting the integrated relative molar amounts of formate ($I_{rel,FA}$) found by the value encountered for DMA ($I_{rel,DMA}$) . The formate coming from the hydrolysis of the formylated linkers are harder to be reliably calculated. The formate content found by ^{1}H-NMR will then be higher than the one encountered in the MOF, showing a higher degree of missing linker defect.

The calculations on the linkers incorporated into the MOF are therefore slightly smaller than what it has been incorporated, showing a higher percentage of formate present than it should.

As mentioned before, six mixed-linker BPDC-$(NH_2)_2$ MOFs were synthesized, and their integrated relative molar amounts ($I_{rel,\ x}$) of the components found by liquid phase digestion ^{1}H-NMR are shown in Table 4. Their respective spectra are found in the appendix.

Table 4. ^{1}H-NMR integrated relative molar amounts ($I_{rel,\ x}$) for the linkers, modulator, formate, and DMA found in the different MOFs synthesized. The results are normalized so that the relative molar amount of BPDC is equal to 1.

MOF	BPDC-$(NH_2)_2$	BA	Formate	DMA	Formate - DMA
UiO-67	N/A	0.083	0.0072	0.0002	0.007
UiO-67-0.1$(NH_2)_2$	0.0822	0.0856	0.0752	0.0066	0.0686
UiO-67-0.2$(NH_2)_2$	0.122	0.358	0.0224	0.001	0.0214
UiO-67-0.3$(NH_2)_2$	0.3388	0.1484	0.1880	0.0069	0.1811
UiO-67-0.5$(NH_2)_2$	0.657	0.2216	0.3252	0.0245	0.3007
UiO-67-0.7$(NH_2)_2$	1.355	0.5218	0.4108	0.0587	0.3521
UiO-67-0.9$(NH_2)_2$	5.5582	2.1698	2.4576	0.5478	1.9098

The ideal TGA plateau for the dehydroxylated MOFs synthesized (W_t) and the ones found experimentally (W_e) are shown in Table 5.

Table 5. Theoretical and experimental TGA plateaus, their difference, and TGA mass loss for MOFs synthesized. Weight relative to 6 ZrO_2 (s).

MOF	W_t (%)	W_e (%)	W_t - W_e (%)	TGA mass loss (°C)
UiO-67	282.0	271.3	10.7	490 – 582
UiO-67-0.1$(NH_2)_2$	284.4	276.3	8.1	440 – 520
UiO-67-0.2$(NH_2)_2$	286.8	277.6	9.2	425 – 518
UiO-67-0.3$(NH_2)_2$	289.3	282.0	7.3	415 – 500
UiO-67-0.5$(NH_2)_2$	294.2	283.0	11.2	395 – 476
UiO-67-0.7$(NH_2)_2$	299.0	288.8	10.2	380 – 476
UiO-67-0.9$(NH_2)_2$	303.9	287.0	16.9	380 – 476

From the table it is possible to see an increase of the experimentally found TGA plateaus, with the increase of H_2BPDC-$(NH_2)_2$ equivalents in the synthesis of the MOFs. That is, with the exception of UiO-67-$(NH_2)_{0.9}$ which should have an increase in W_e from UiO-67-$(NH_2)_{0.7}$ but instead had a decrease. Even though it is possible to see the decrease in mass from the theoretical to the experimental value, it is not possible to fully quantify the missing linker defects. When a BPDC linker gets replaced by two benzoates, the molar mass of the MOF is almost equal to the one of an ideal MOF, the difference would be only marginal. It is, however,

possible to see that if instead of a BPDC-$(NH_2)_2$ linker, two benzoates are present, the mass will decrease. Figure 23 shows an overview of the TGA curves for all MOFs.

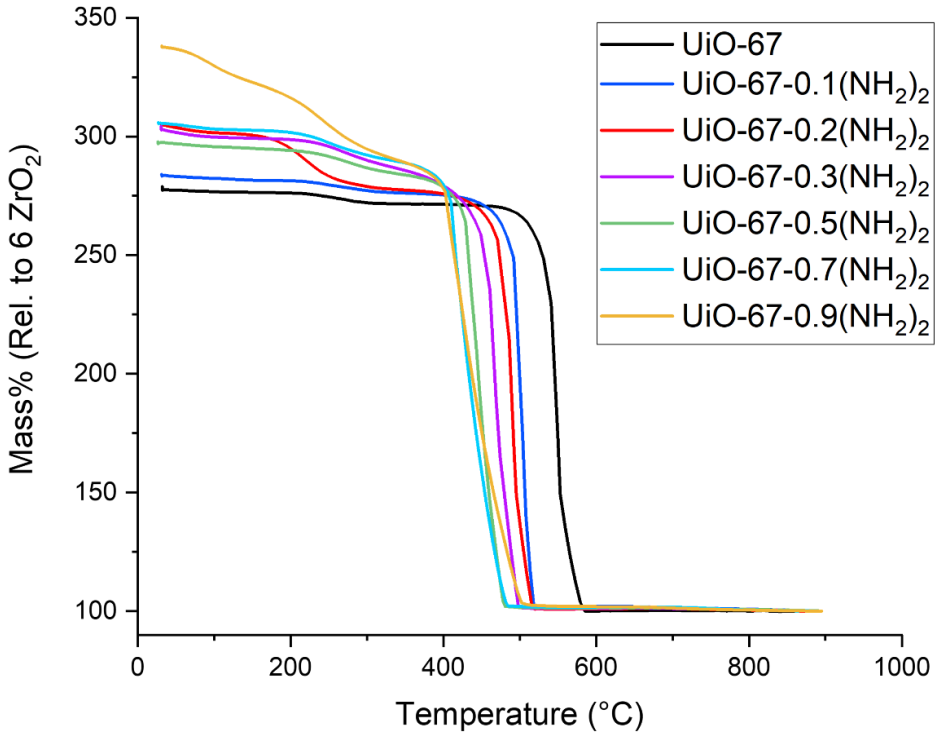

Figure 23. TGA curves for all BPDC-$(NH_2)_2$ MOFs synthesized.

Comparing the TGA curves with the digestion NMR results, it is possible to see that the MOFs UiO-67 and UiO-67-0.1$(NH_2)_2$ plateaus do not differ much between the hydroxylated and the dehydroxylated form. It is therefore possible to state that the amount of formate, water and solvent trapped in the pores is small. This is confirmed by digestion NMR, where the relative molar amount of formate and DMA is less than 0.07 and 0.007, respectively.

For the UiO-67-0.2$(NH_2)_2$ however, there is a leap of ca. 23%, a value almost 5 times as expected for the dehydration process. A high presence of solvents such as DMF, is a possible explanation for this deviation. However, the digestion NMR suggests otherwise, and the relative molar amounts found for formate and DMA of 0.0214 and 0.001, respectively, a value almost neglectable. This is better explained by the presence of water in the pores. It is also possible to see that this process occurs earlier, at around 200°C, for this particular MOF compared to the others synthesized, at around 250°C.

The MOF where the largest percentage of BPDC-$(NH_2)_2$ linker incorporation was attempted, UiO-67-0.9$(NH_2)_2$, has a different TGA curve than the other MOFs. This is a MOF with a much higher quantity of formate, as well as DMF trapped in the pores. It is therefore almost impossible to see where the experimental TGA plateau for the hydroxylated MOF is, since the dehydration of the MOF happens simultaneously as the decomposition of formate and

desorption of DMF from the pores. This leads to the hypothesis that this MOF is highly defective and unstable.

Another information possible to obtain from TGA, is the thermal stability of the MOF. In general, UiO-67 type MOFs are stable at high temperatures, due to the strong coordination bond between the cluster and the linker. The addition of diamino component into the biphenyl moiety will create weaker C-NH_2 bonds, according to their dissociation energy, decreasing its thermic stability.[95] With the increase of BPDC-$(NH_2)_2$ linker, the second mass loss starts at an earlier temperature, with temperatures as low as 380°C for the higher amounts, and a visual plot of the TGA mass loss is shown in Figure 24.

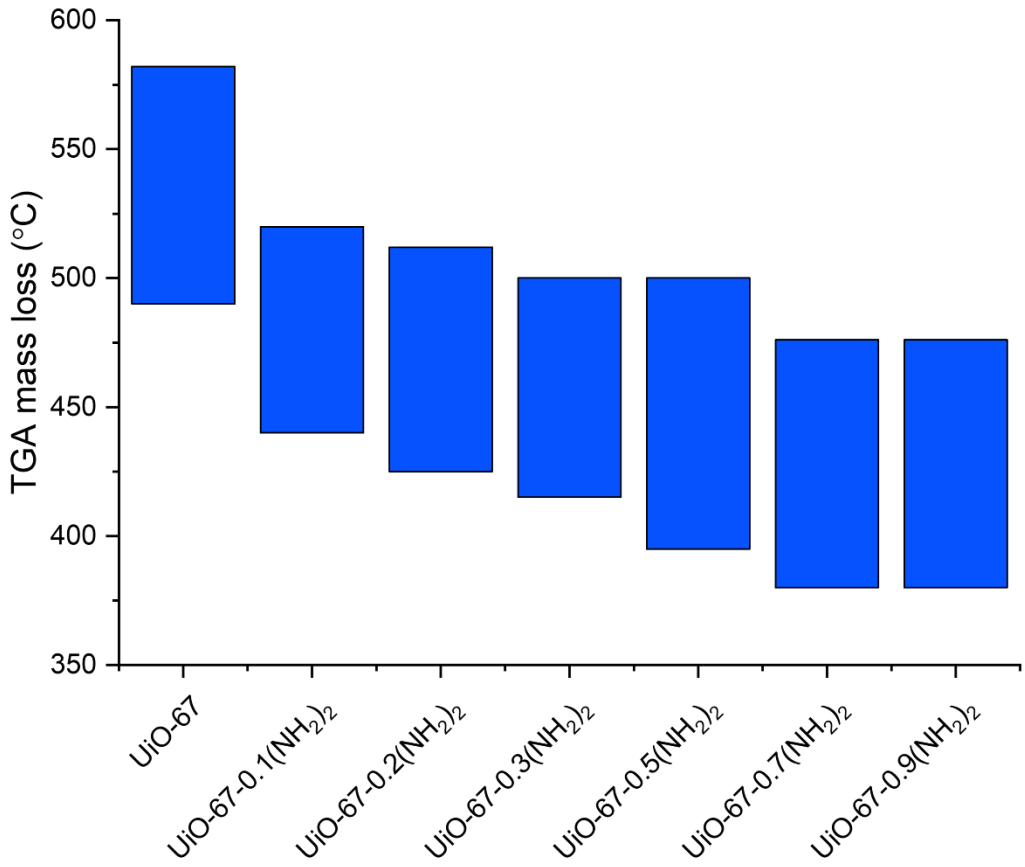

Figure 24. Visual representation of the TGA mass loss for all BPDC-$(NH_2)_2$ MOFs synthesized.

It is, however, important to notice that the thermal stability found by TGA is only an approximation, since it does not tell anything about the crystallinity and structural integrity of the MOF during the analysis. In literature, UiO-66 MOFs have been investigated with PXRD after leaving on air at increasing temperatures for 12h.[96] the results show that the MOF loses its crystallinity at temperatures as low as 300°C, while their TGA curve show that the linkers on the MOF don't start combusting before 450°C.

All MOFs were subjected to PXRD, and their diffractograms can be found in the appendix. Those diffractograms were further refined using the Pawley method with the TOPAS software.[97] Thereby, the lattice parameter *a* can be obtained, which is the only constant that can vary for the space group *Fm-3m*. An example of the refinement is shown for the UiO-67-0.5$(NH_2)_2$ MOF is shown in Figure 25, and the value for a found for all MOFs is shown in Table 6.

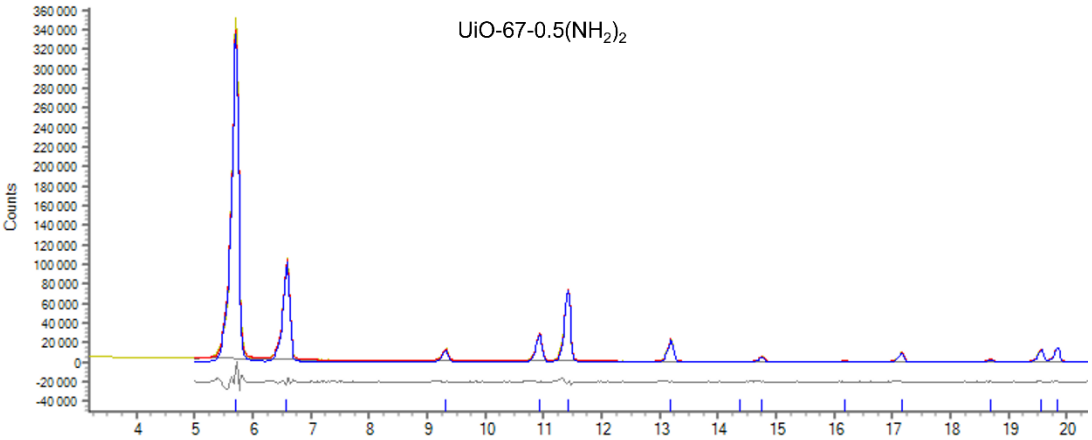

Figure 25. Pawley refinement of the UiO-67-0.5$(NH_2)_2$ MOF. In blue, the obtained PXRD diffractogram, in red, the refined diffractogram. In grey, the difference between the refined and obtained diffractograms. R_{wp} = 0.06.

Table 6. Space group and lattice parameter *a* found after Pawley refinement as well as the weighted profile R-factor (R_{wp}) found after the refinement.

MOF	Lattice parameter *a*	R_{wp}
UiO-67	26.89	0.13
UiO-67-0.1$(NH_2)_2$	26.88	0.15
UiO-67-0.2$(NH_2)_2$	26.84	0.06
UiO-67-0.3$(NH_2)_2$	26.85	0.08
UiO-67-0.5$(NH_2)_2$	26.82	0.06
UiO-67-0.7$(NH_2)_2$	26.81	0.05
UiO-67-0.9$(NH_2)_2$	26.88	0.09

Looking away from the UiO-67-0.9$(NH_2)_2$ MOF, the lattice parameter *a* decreases as the equivalency of BPDC-$(NH_2)_2$ increases. This means that the unit cell volume decreases, and therefore also the pore size, when a higher quantity of BPDC-$(NH_2)_2$ linker is present.

The characteristic morphology of UiO-67 is of octahedral nature, and that was observed for all MOFs synthesized, as shown in Figure 26. The low deformities found in the MOFs synthesized shows that they are grown slowly and of well-defined morphology.

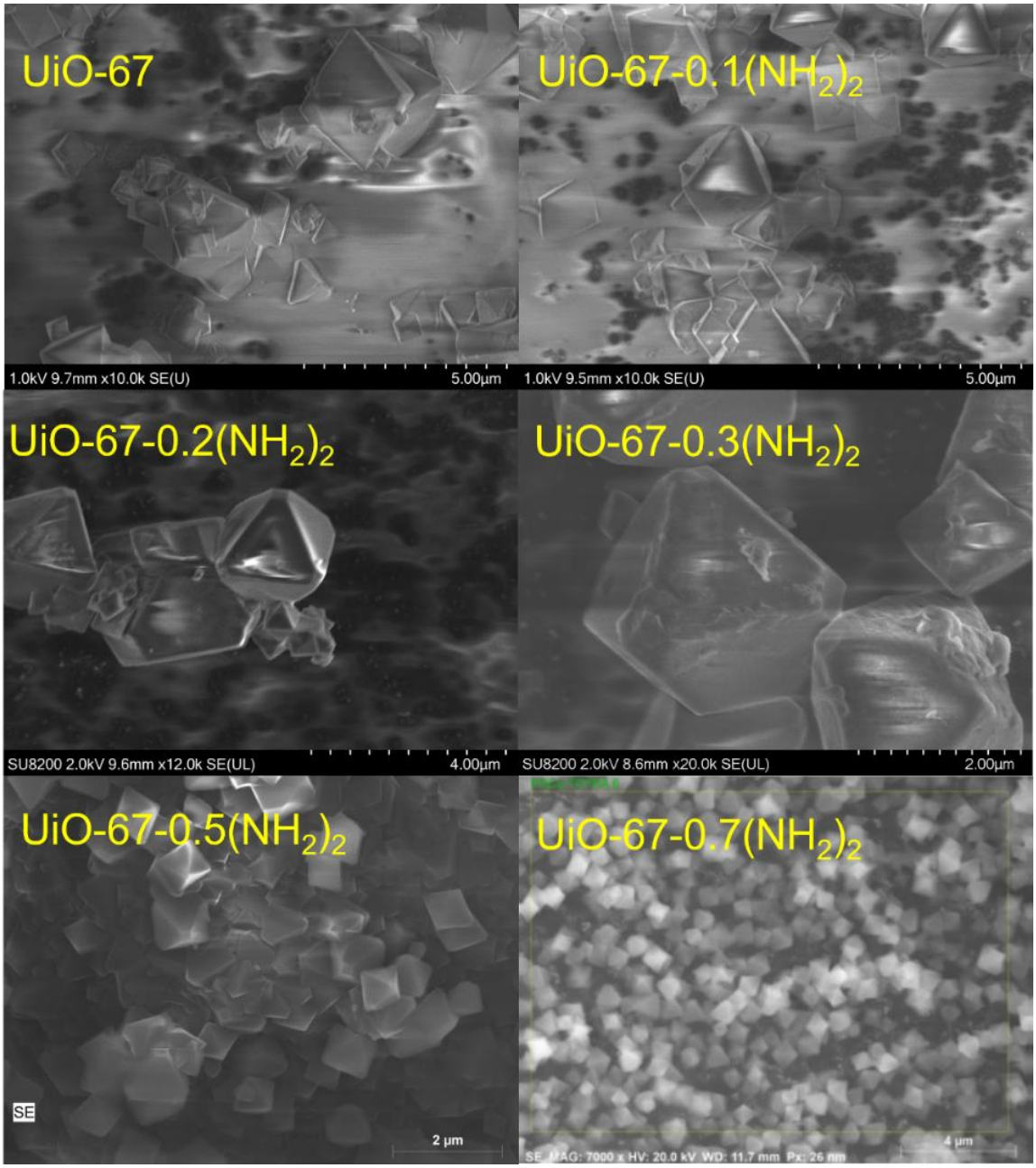

Figure 26. SEM images for all crystalline MOFs synthesized.

On EDX, the chlorine Kα speak is found at 2.621 keV right after the zirconium Lα peak at 2.042 keV, but for all mixed linker BPDC-$(NH_2)_2$ no such signals were found. An example of the EDX analysis is shown in Figure 27 for the UiO-67-0.7$(NH_2)_2$ MOF. This means that no chloride ions are found on the linker vacancy sites of the diamino-functionalised MOF. Thereby, the chlorine content determined for the MOF after diazepine functionalisation must necessarily originate from aldehyde incorporation.

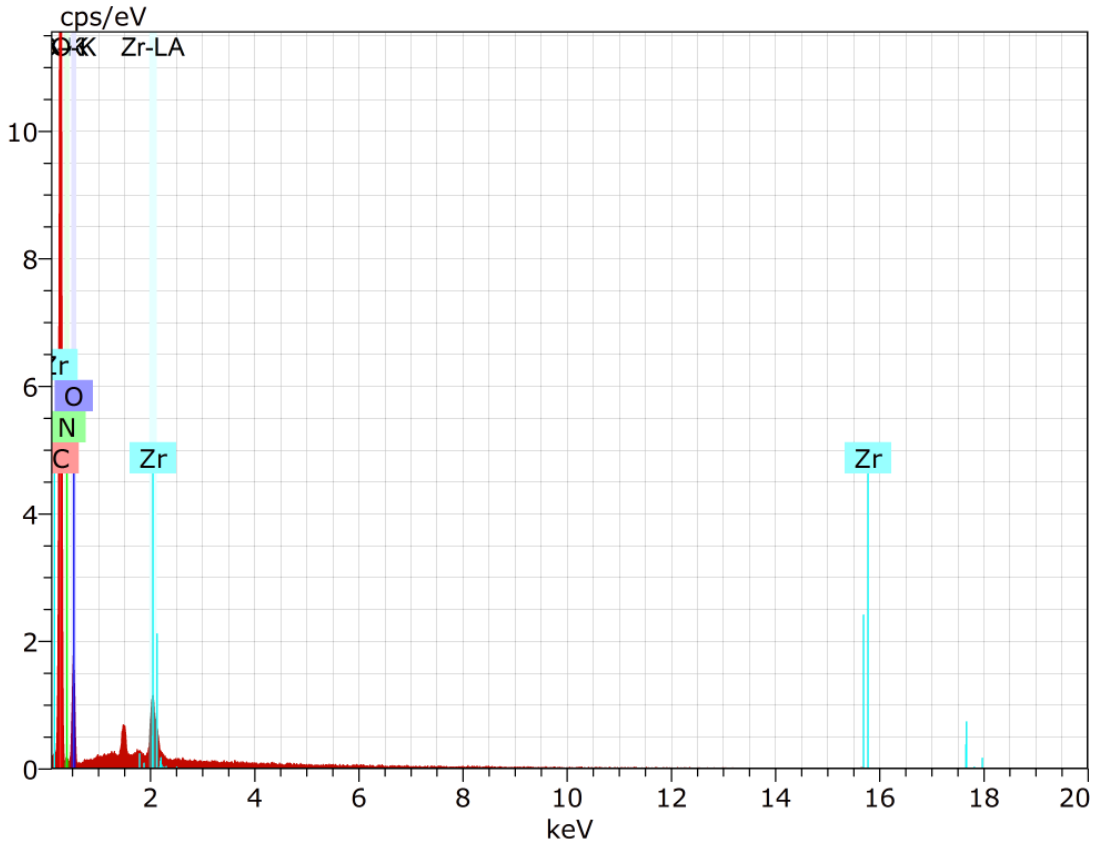

Figure 27. Energy-dispersion x-ray spectroscopy (EDX) spectrum for the UiO-67-0.7$(NH_2)_2$ MOF. A 20 keV acceleration voltage was used.

It is now possible to find the composition of the MOF by employing the calculations discussed in Section 2.6. The results found are shown in Table 7, and a visual representation of the linker content on the MOFs is shown in Figure 28. It is important to remember that the value found is an overestimation since the formate will not only come from the formate found in the MOF as a capping agent, but also from the formylated BPDC-$(NH_2)_2$ linkers.

Table 7. Linker composition for all BPDC-$(NH_2)_2$ mixed linker MOFs synthesized, found by liquid digestion ^{1}H-NMR and TGA.

MOF	BPDC	BPDC-$(NH_2)_2$	Benzoate	Formate	H_2O/OH^-	Linker vacancies
UiO-67	5.43	0	0.45	0.04	0.64	9.4%
UiO-67-0.1$(NH_2)_2$	5.03	0.41	0.43	0.38	0.31	9.3%
UiO-67-0.2$(NH_2)_2$	4.43	0.54	1.59	0.10	0.37	17.1%
UiO-67-0.3$(NH_2)_2$	3.98	1.35	0.59	0.75	0	11.1%
UiO-67-0.5$(NH_2)_2$	3.10	2.04	0.69	1.01	0.04	14.4%
UiO-67-0.7$(NH_2)_2$	2.12	2.88	1.11	0.87	0.03	16.7%
UiO-67-0.9$(NH_2)_2$	0.65	3.60	1.40	1.59	0.51	29.2%

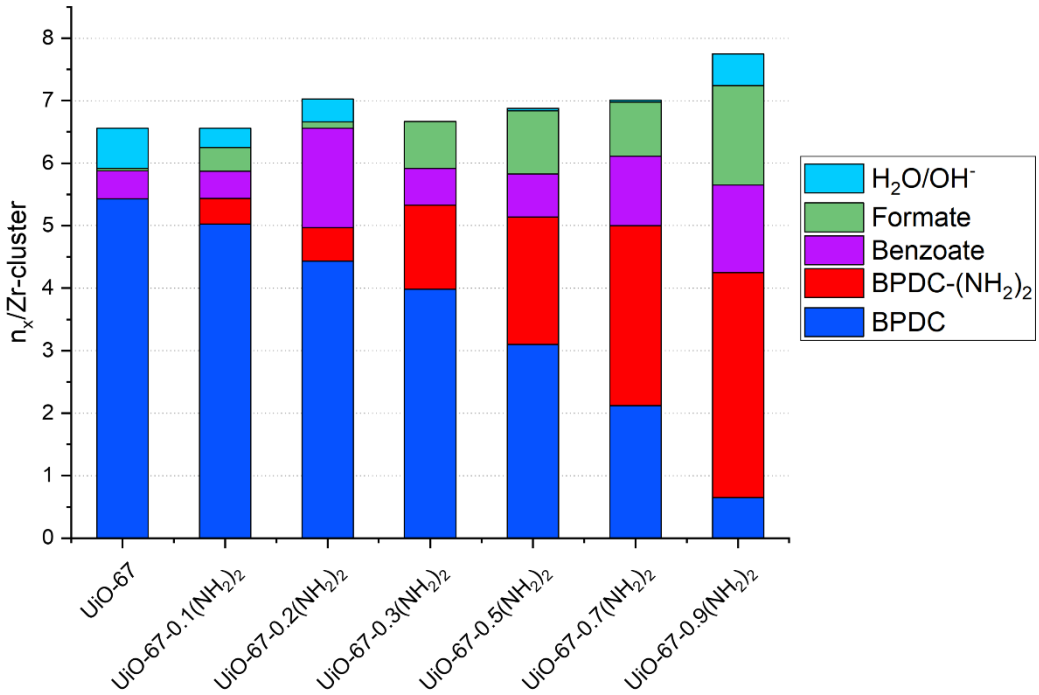

Figure 28. Visual representation of the linker composition for all BPDC-$(NH_2)_2$ mixed linker MOFs synthesized.

From the composition of the MOFs synthesized, it is possible to see, with the exception of UiO-67-0.2$(NH_2)_2$, that the amount of linker vacancies increases with the equivalents of BPDC-$(NH_2)_2$ in the synthesis. The amount of BPDC-$(NH_2)_2$ linker incorporated also increased with the amount of equivalency found in the reaction mixture. The quantity of BPDC-$(NH_2)_2$ linker incorporated into the MOFs are also smaller than the percentages initially found in the reaction mixture, and the highest BPDC-$(NH_2)_2$ linker percentage found was at 60% for the UiO-67-0.9$(NH_2)_2$ MOF. However, as this MOF contains almost 30% linker vacancies it is no surprise that it is not stable. It is possible to see on Figure 29 that the BPDC-$(NH_2)_2$ incorporation increased linearly with the added equivalency into the reaction mixture, however, the amount of actually incorporated linker was only ca. 70% of the intended amount.

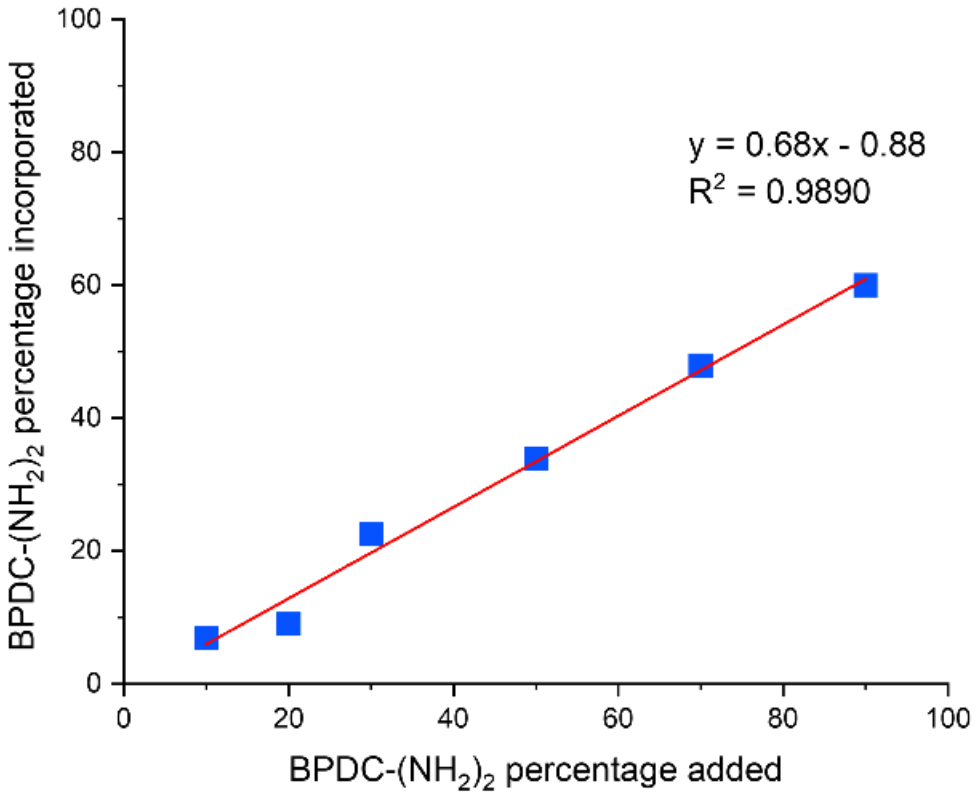

Figure 29. The percentage of actually incorporated BPDC-$(NH_2)_2$ linker compared to percentage of BPDC-$(NH_2)_2$ added during the synthesis of the MOF.

The surface areas of the BPDC-$(NH_2)_2$ mixed linker MOFs synthesized were found by BET analysis of the nitrogen adsorption isotherms. The isotherms measured (shown in Figure 30) are of type I and shows that all MOFs contain only micropores, as is expected for a UiO-67 type MOF. The instability of the UiO-67-0.9$(NH_2)_2$ MOF can also be seen in the nitrogen sorption isotherms, measured one month after synthesis, where it does not show any adsorption, meaning that this MOF has become non-porous.

The surface areas of the MOFs synthesized are found together with other selected characteristics in Table 8. It is possible to see a decrease in the BET surface area with the increase in BPDC-$(NH_2)_2$ linker, which is also expected. The bulkier diamino linker will occupy a larger space in the pores, causing the surface area to decrease. However, due to the increase in linker vacancies, this surface area does not differ by a lot, ranging from 2390 m^2/g for the UiO-67-0.1$(NH_2)_2$ MOF to 1977 m^2/g for the UiO-67-0.7$(NH_2)_2$ MOF.

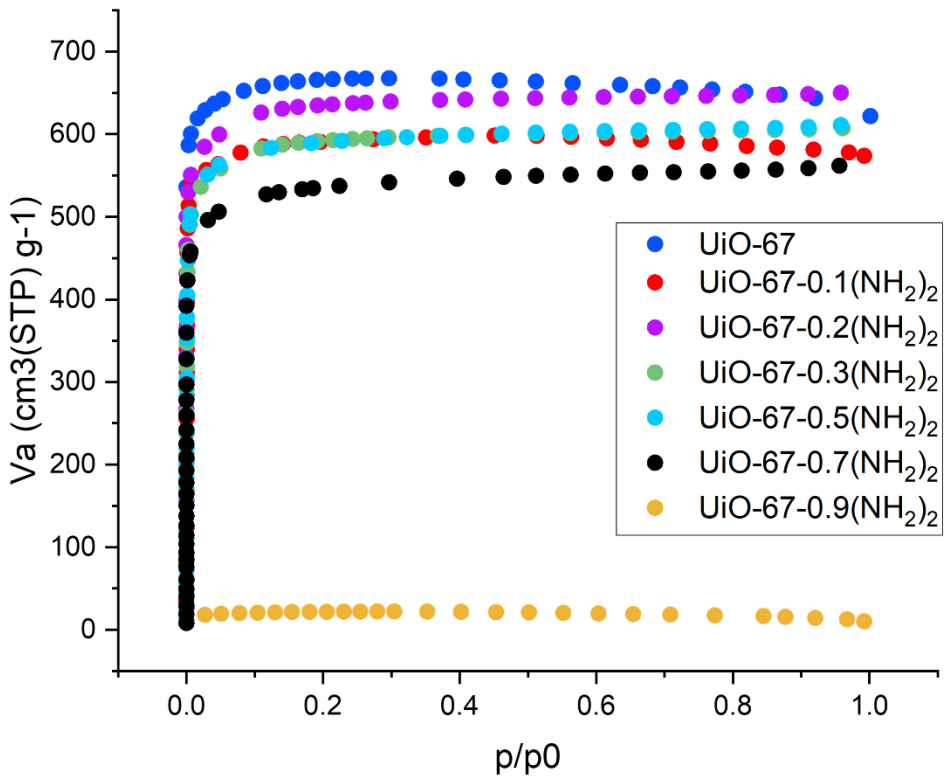

Figure 30. Nitrogen adsorption curves for all BPDC-$(NH_2)_2$ mixed linker MOFs synthesized.

Table 8. Selected characteristics of the BPDC-$(NH_2)_2$ mixed linker MOFs synthesized.

MOF	A_{BET} (m^2/g)	TGA mass loss (°C)	Percentage of BPDC-$(NH_2)_2$	Linker vacancies	Unit cell size a (Rwp)
UiO-67	2681	490 – 582	-	9.4%	26.89 (0.13)
UiO-67-0.1$(NH_2)_2$	2390	440 – 520	6.9%	9.3%	26.88 (0.15)
UiO-67-0.2$(NH_2)_2$	2386	425 – 518	9.0%	17.1%	26.84 (0.06)
UiO-67-0.3$(NH_2)_2$	2336	415 – 500	22.5%	11.1%	26.85 (0.08)
UiO-67-0.5$(NH_2)_2$	2353	395 – 476	33.9%	14.4%	26.82 (0.06)
UiO-67-0.7$(NH_2)_2$	1977	380 – 476	47.9%	16.7%	26.81 (0.05)
UiO-67-0.9$(NH_2)_2$	N/A	380 – 476	60.0%	29.2%	26.88 (0.09)

After the nitrogen adsorption experiment showed no porosity, the integrity of the UiO-67-0.9$(NH_2)_2$ MOF was questioned. Therefore, a PXRD of the MOF was collected in order to investigate the crystallinity of the sample. The PXRD taken after synthesis and after 8 months is shown in Figure 31. There, it is possible to see that not only were less peaks found, but also peak broadening is observed. This leads to the conclusion that this MOF is not stable over time, even when stored in a desiccator.

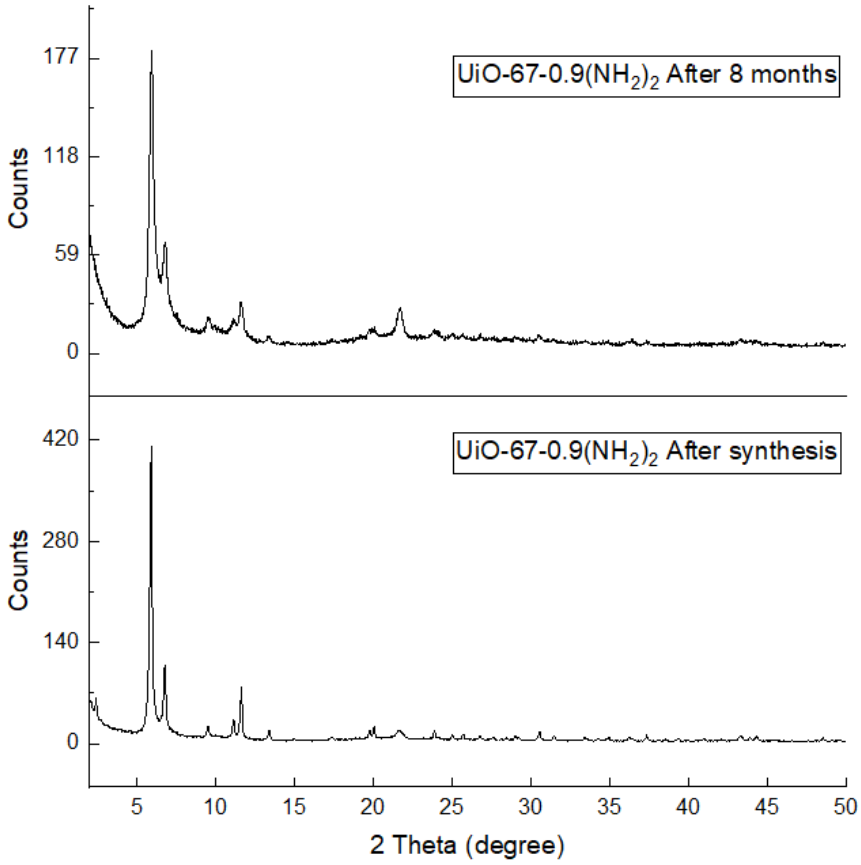

Figure 31. PXRD diffractograms for UiO-67-0.9$(NH_2)_2$ obtained at different timeframes. Bottom: Diffractrogram after synthesis. Top: Diffractogram after 8 months in storage.

4.4 Diazepine incorporation into UiO-67 MOFs

Due to the high linker vacancies found in the UiO-67-0.2$(NH_2)_2$ and its low content of BPDC- $(NH_2)_2$, this MOF was not further functionalized to yield the diazepine MOF. The instability of the UiO-67-0.9$(NH_2)_2$ also caused the non-functionalization of this MOF as well. However, the diazepine post synthetic functionalization was attempted for the remaining four mixed linker BPDC-$(NH_2)_2$ MOFs.

As discussed in Section 4.1, the most suitable aldehyde for the diazepine incorporation into the MOF is 6-chloropicolinaldehyde, yielding compound **3** inside of the MOF. The nomenclature of the now functionalized MOFs will then be UiO-67-X-(**3**), where X is the percentage of BPDC-$(NH_2)_2$ added in the synthesis.

After functionalization, the MOF was washed thoroughly with MeOH, and after each washing step, thin layer chromatography was used to identify if the aldehyde was still present in the supernatant. After the third wash, it was no longer possible to see spots for the aldehyde, therefore the aldehyde had been washed from the reaction mixture.

The now functionalized MOFs were subjected to PXRD, shown in Figure 32. The diffractograms show no lost in crystallinity, in addition, no forbidden peaks were found, meaning that the functionalized MOFs are free of crystalline impurities.

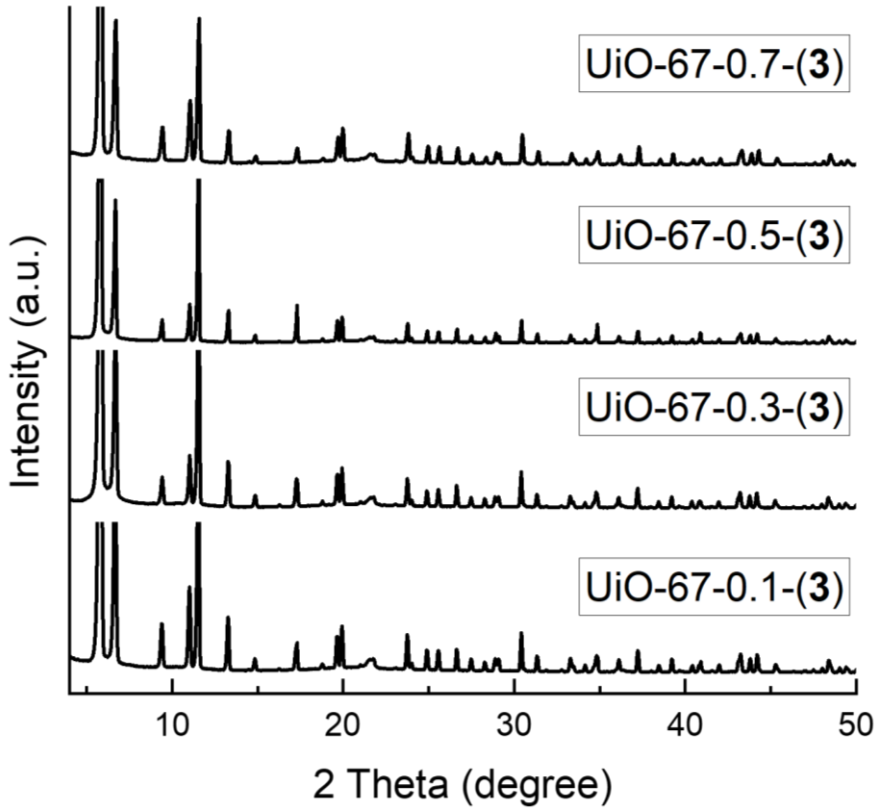

Figure 32. PXRD diffractogram for all functionalized MOFs

The functionalized MOFs were characterized by TGA (Figure 33). As expected, the plateaus of the functionalized MOF have increased compared to the original BPDC-$(NH_2)_2$ MOF. This suggests that the BPDC-$(NH_2)_2$ linkers have been converted to the BPDC-(**3**) diazepine linker.

The TGA mass loss for the functionalized MOFs have also increased compared to the corresponding original BPDC-$(NH_2)_2$ MOF. It is therefore possible to speculate that the BPDC-$(NH_2)_2$ linkers have reacted into a stronger bond, increasing the thermal stability of the MOF, possibly indicating the cyclization of the linker into the 1,3-dibenzodiazepines.

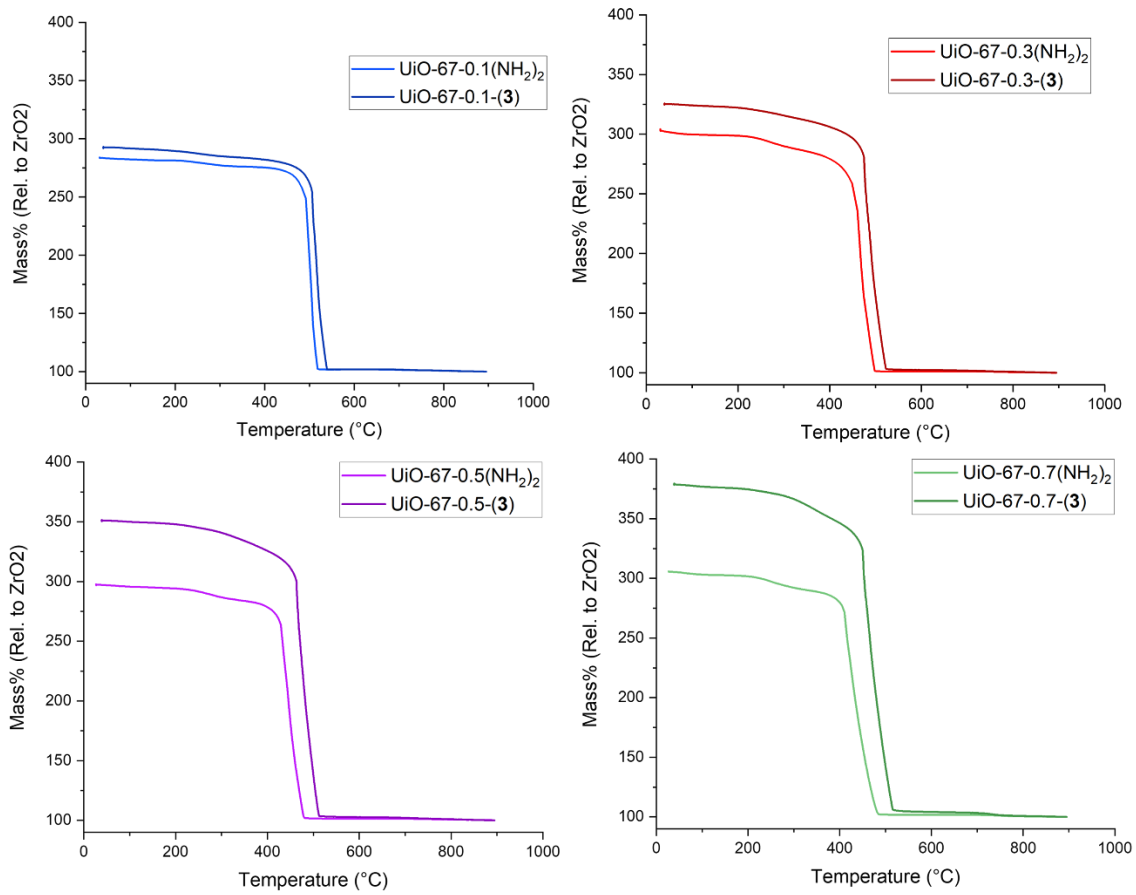

Figure 33. TGA plots for MOFs before and after functionalization.

Considering that the diazepine conversion was successful and the MOF composition found in Section 4.3, it is possible to calculate a theoretical plateau in the TGA. This theoretical plateau, together with the experimental and the difference found is shown in Table 9.

Table 9. Theoretical and experimental TGA plateaus, their difference, and TGA mass loss for MOFs synthesized. Weight relative to 6 ZrO_2 (s).

MOF	W_t (%)	W_e (%)	W_t - W_e (%)	TGA mass loss (°C)
UiO-67-0.1-(**3**)	283.3	278.4	4.9	475 – 540
UiO-67-0.3-(**3**)	302.9	302.7	0.2	460 – 530
UiO-67-0.5-(**3**)	314.3	317.4	-3.1	440 – 515
UiO-67-0.7-(**3**)	333.5	337.7	-4.2	435 – 520

For the UiO-67-0.5-(**3**) and UiO-67-0.7-(**3**) MOFs, the plateau found experimentally was slightly higher than the theoretical one. It can be justified by remembering that the increased amount of BPDC-$(NH_2)_2$ linker in the synthesis of the original MOFs also increases the amount of formylated BPDC-$(NH_2)_2$ linkers. That means that the increased formylated linkers will also increase the amount of formate miscalculated as capping agents in the MOF, decreasing the amount of all other linkers in the MOF.

The composition analysis using liquid phase digestion ^{1}H-NMR of the functionalized MOFs proved to be far too complex due to the many overlapping peaks in the aromatic region. Even with the use of a high resolution NMR spectrometer, the signals corresponding to the different components could not be reliably integrated. As an example, Figure 34 shows a comparison between the digested UiO-67-0.7-(3) MOF and the dicarboxylic acid version of compound **3**, H_2-**3**. It is possible to see that the diazepine formation was successful, due to presence of a singlet at 5.85 ppm, corresponding to the CH proton on the diazepine ring. This singlet was observed on the liquid phase ^{1}H-NMR digestion for all MOFs functionalized, and the spectra can be found in the appendix.

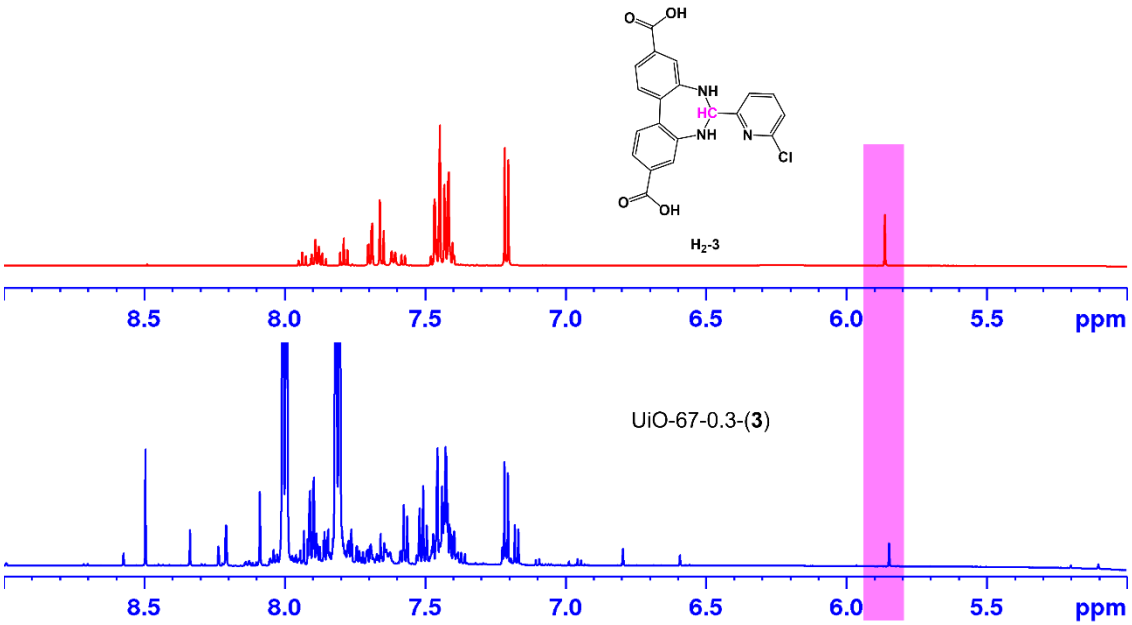

Figure 34. Partial ^{1}H-NMR comparing the H_2-**3** compound, on top and the digested UiO-67-0.3-(**3**) MOF, on bottom (600 MHz, 0.1M NaOD/D_2O).

PXRD showed that the MOF maintained its crystallinity, and this was confirmed again by SEM, as shown in Figure 35.

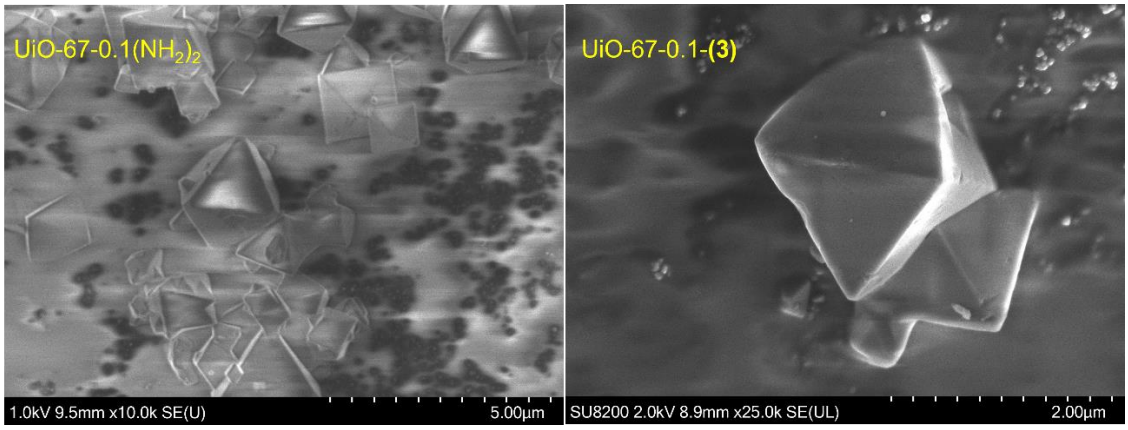

Figure 35. SEM Images for a BPDC-$(NH_2)_2$ mixed-linker MOF before (UiO-67-0.1$(NH_2)_2$) and after functionalization (UiO-67-0.1-(**3**)).

The post functionalization MOFs were also subjected to EDX analysis, where not only the zirconium, but also the chlorine can be detected and quantified. The findings by EDX are summed in Table 10.

Table 10. Atomic percent of zirconium and chlorine atoms found by EDX. The Cl/Zr_6 ratio and the BPDC-$(NH_2)_2$ linker/Zr_6 ratio found in the non-functionalized MOF is also shown.

MOF	Cl (at. %)	Zr (at. %)	Cl/Zr_6 ratio	BPDC-$(NH_2)_2$ linker/Zr_6 ratio
UiO-67-0.1-(**3**)	6.05	41.78	0.87	0.41
UiO-67-0.3-(**3**)	10.59	30.46	2.08	1.35
UiO-67-0.5-(**3**)	13.44	17.70	4.56	2.04
UiO-67-0.7-(**3**)	9.89	9.75	6.09	2.88

It is possible to see that the Cl/Zr_6 ratio increases linearly as the amount of incorporated BPDC-$(NH_2)_2$ increases, which is in accordance with the trend expected. This is shown in Figure 36, where even with the EDX's low precision, the linear fit had a R^2 of 0.9674, which is acceptable. However, in the diazepine it is expected one Cl atom per BPDC-$(NH_2)_2$ linker, and the values found are more than the double of what was expected. Even though TGA and Liquid digestion ^{1}H-NMR suggest the formation of the diazepine **3** in the MOF, EDX does not support that hypothesis.

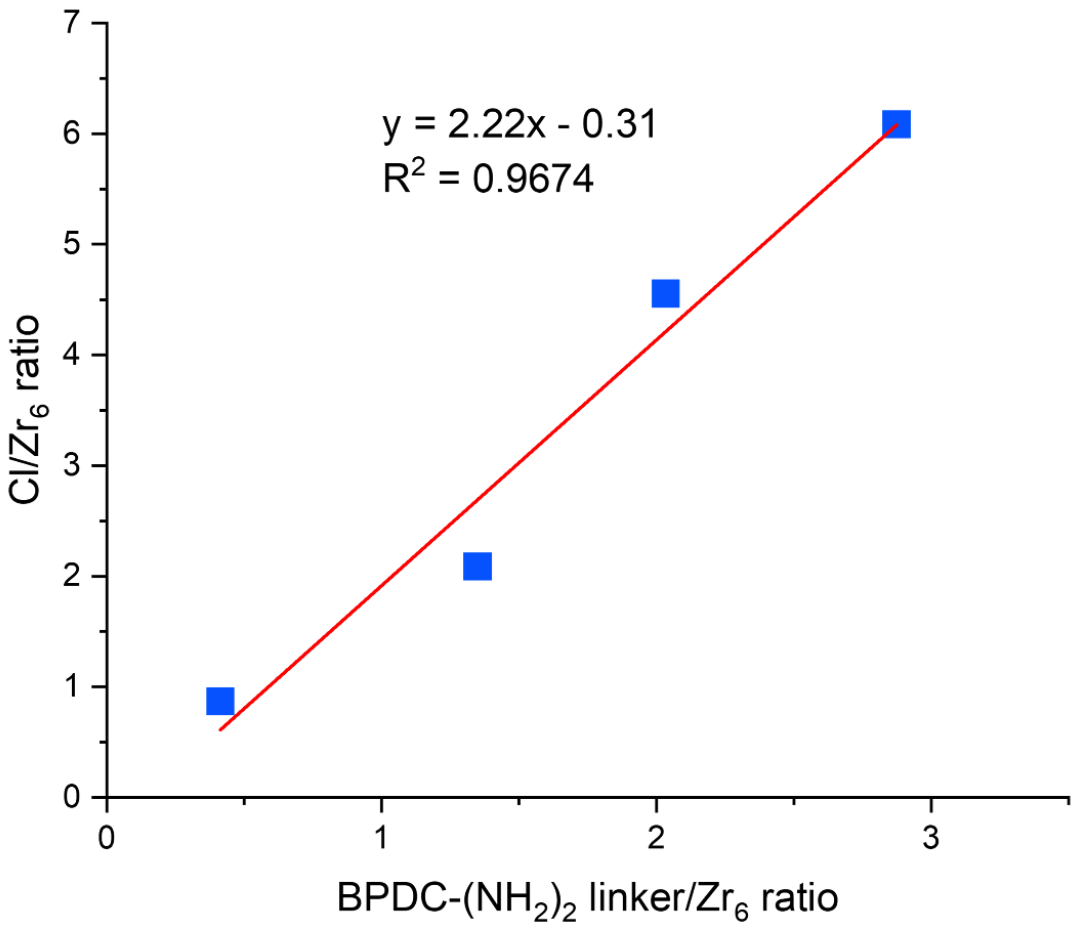

Figure 36. Scatter plot, in blue, and linear fit, in red, of the BPDC-$(NH_2)_2$ linker/Zr_6 ratio found in the original MOF and the Cl/Zr_6 ratio found by EDX.

Another possibility using EDX is to use the elemental mapping function, it is possible to visualize where from the sample each characteristic X-ray is coming from. The elemental mapping for zirconium and chlorine on all functionalized MOFs is shown in Figure 37. Since no aldehyde was found in liquid phase digestion ^{1}H-NMR, all X-ray signals found in the elemental mapping must come from the functionalized diamino linker, as the diazepine.

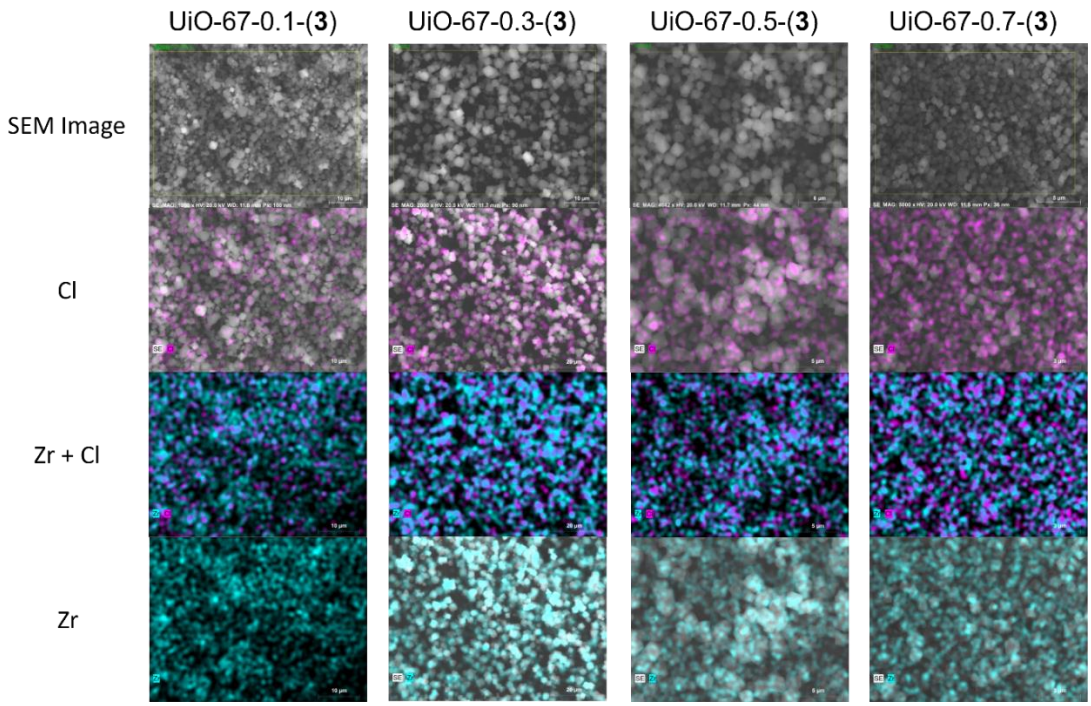

Figure 37. SEM-EDX elemental mapping of Cl (in purple), Zr (in cyan) and SEM image for all functionalized MOFs.

The mapping shows even distribution of the bromine throughout the image, indicating a successful incorporation of the 1,3-benzodiazepine into the MOF.

It is interesting to investigate how the porosity of the MOF has changed with the diazepine incorporation. The surface area for the functionalized MOFs were found by BET analysis of nitrogen adsorption isotherms. The measured isotherms for all MOFs pre- and post-functionalization are shown in Figure 38. The surface areas found are shown in Table 11 together with other characteristics for the functionalized MOFs.

It is possible to see that even for the lower percentages of diazepine, the surface areas have decreased by ca. 40% of the surface are before functionalization. However, the values found are still comparable to other porous materials, ranging from 1205 m^2/g for the UiO-67-0.3-(**3**) MOF, to 1596 m^2/g for the UiO-67-0.5-(**3**) MOF.

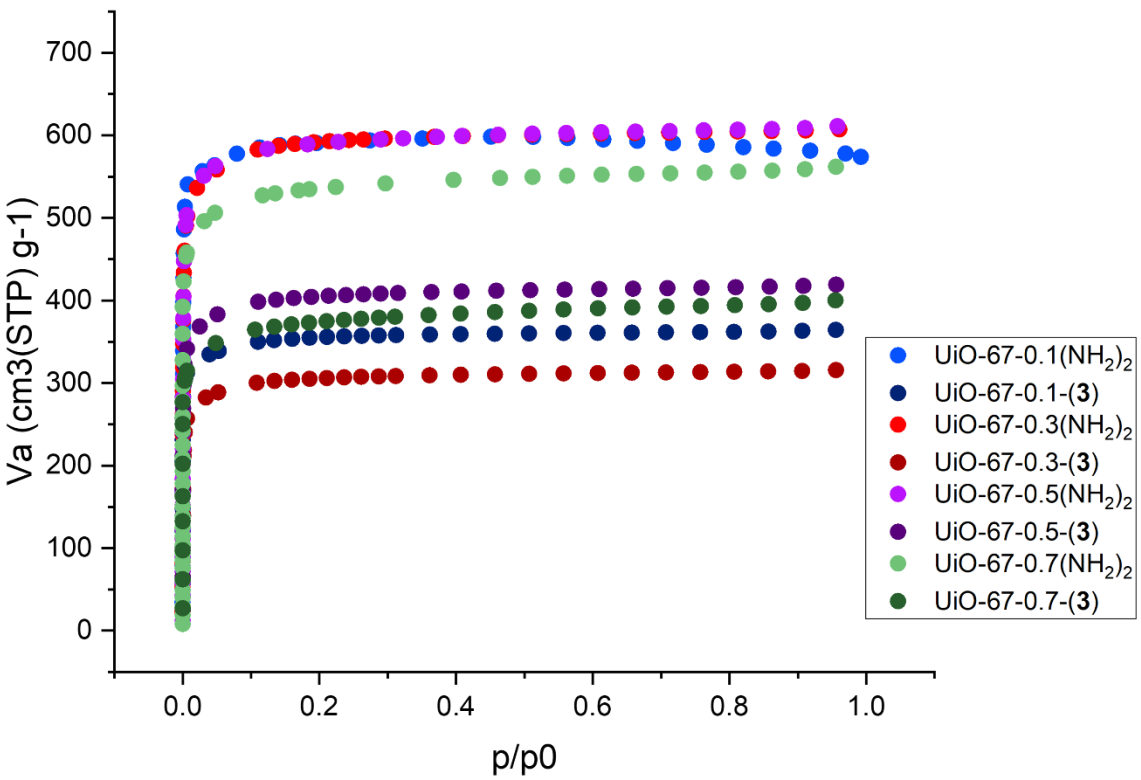

Figure 38. Nitrogen adsorption isotherms for MOFs before and after functionalization.

Table 11. Selected characteristics of the mixed linker diazepine MOFs functionalized.

MOF	A_{BET} (m^2/g)	TGA mass loss (°C)	Cl/Zr_6 ratio
UiO-67-0.1-(**3**)	1353	475 – 540	0.87
UiO-67-0.3-(**3**)	1205	460 – 530	2.08
UiO-67-0.5-(**3**)	1596	440 – 515	4.56
UiO-67-0.7-(**3**)	1362	435 – 520	6.09

The pristine and functionalized MOFs were characterized by UV-Vis diffuse reflectance spectroscopy, and the spectra for UiO-67-0.3$(NH_2)_2$ and UiO-67-0.3(**3**) are shown in Figure 39. It is possible to see how the reflectance gets more intense for the functionalized MOF in higher wavelengths, and this is in accordance with the observations of **3** in solution.

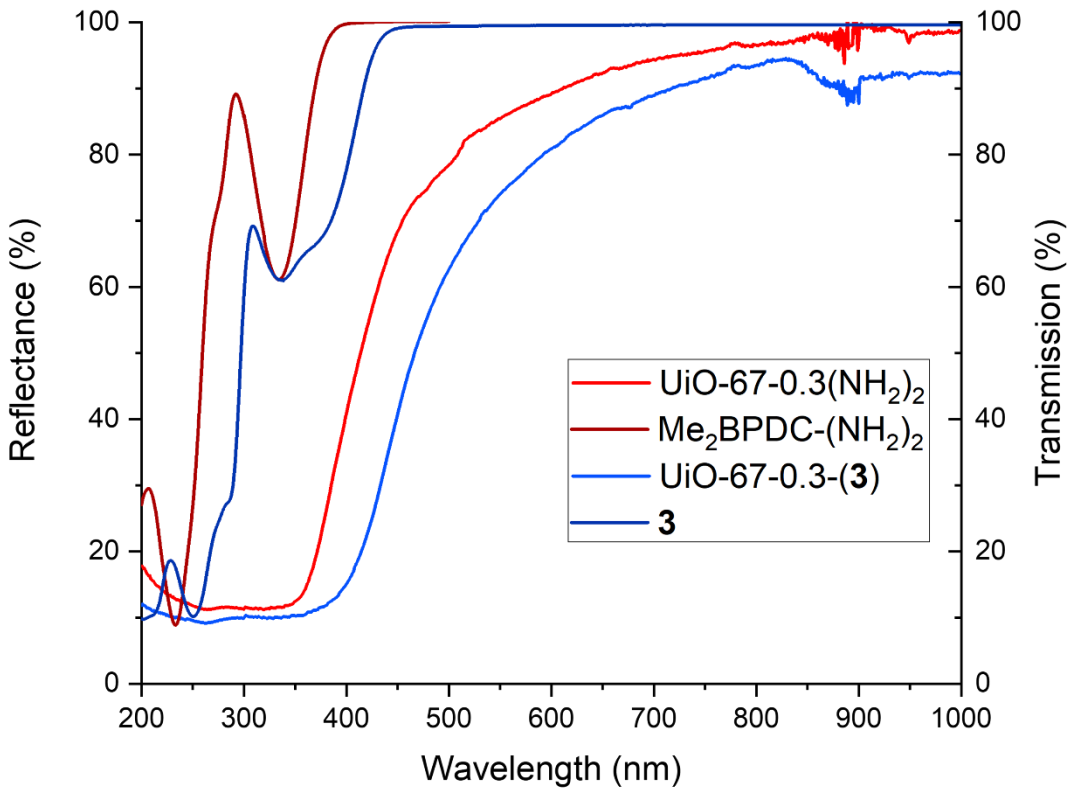

Figure 39. UV/Vis spectroscopy: diffuse reflectance of the mixed linker MOFs pre- (UiO-67-0.3(NH_2)$_2$; red) and post-functionalization (UiO-67-0.3-(**3**)). The plot is overlaid with the transmission spectrum of both Me_2BPDC-(NH_2)$_2$ (dark red) and **3** (dark blue) in solution (30µM).

5 Conclusion and outlook

In this thesis, the reaction of **Me_2BPDC-$(NH_2)_2$** with six different aldehydes was investigated, continuing and building upon studies previously worked on. Four novel 1,3-dibenzodiazepines were isolated, and the search for a suitable diazepine to be incorporated into the UiO-67 MOF proved successful.

The photophysical properties of the isolated diazepines found in **Paper I** were thoroughly investigated and the use of TD-DFT provided an insight into the experimentally observed shifts observed.

A series of mixed-linker BPDC-$(NH_2)_2$ UiO-67 MOFs were synthesized, and missing linker defects were observed and characterized.

Missing linker defects in all BPDC-$(NH_2)_2$ UiO-67 MOFs were characterized by the use of liquid phase digestion ^{1}H-NMR, TGA and EDX. It has been observed that the increase in molar percentages of the BPDC-$(NH_2)_2$ linker in the synthesis also results in an increase in the amount of missing linker defects. For further work, the use of solvent assisted ligand exchange to decrease the missing linker defects and increasing the incorporation of the BPDC-$(NH_2)_2$ linker should be investigated. It was observed that higher percentages of BPDC-$(NH_2)_2$ linker decrease the MOFs stability.

The postsynthetic functionalization of a series of BPDC-$(NH_2)_2$ mixed linker UiO-67 MOFs for the incorporation of compound **3** was successful. A linear correlation between the relative amount of chlorine atoms per Zr_6 was observed, and found by EDX, as well as the amount of BPDC-$(NH_2)_2$ incorporated in the MOF. The MOFs fluorescence should be investigated, for both the pristine MOFs and the diazepine functionalized MOFs. The use of those MOFs for the sensing of nitroaromatic compounds should also be investigated in future work.

6 References

1 S. R. Batten, N. R. Champness, X.-M. Chen, J. Garcia-Martinez, S. Kitagawa, L. Öhrström, M. O'Keeffe, M. P. Suh and J. Reedijk, *Pure Appl. Chem.*, 2013, **85**, 1715–1724.

2 M. Eddaoudi, D. B. Moler, H. Li, B. Chen, T. M. Reineke, M. O'Keeffe and O. M. Yaghi, *Acc. Chem. Res.*, 2001, **34**, 319–330.

3 O. M. Yaghi and H. Li, *J. Am. Chem. Soc.*, 1995, **117**, 10401–10402.

4 H. Li, M. Eddaoudi, M. O'Keeffe and O. M. Yaghi, *Nature*, 1999, **402**, 276–279.

5 P. Z. Moghadam, A. Li, S. B. Wiggin, A. Tao, A. G. P. Maloney, P. A. Wood, S. C. Ward and D. Fairen-Jimenez, *Chem. Mater.*, 2017, **29**, 2618–2625.

6 Case: How many MOFs are there in the CSD? - The Cambridge Crystallographic Data Centre (CCDC), https://www.ccdc.cam.ac.uk/support-and-resources/support/case/?caseid=9833bd2c-27f9-4ff7-8186-71a9b415f012, (accessed June 4, 2022).

7 S. Dai, A. Tissot and C. Serre, *Bull. Chem. Soc. Jpn.*, 2021, **94**, 2623–2636.

8 O. M. Yaghi, M. O'Keeffe, N. W. Ockwig, H. K. Chae, M. Eddaoudi and J. Kim, *Nature*, 2003, **423**, 705–714.

9 M. Eddaoudi, J. Kim, N. Rosi, D. Vodak, J. Wachter, M. O'Keeffe and O. M. Yaghi, *Science*, 2002, **295**, 469–472.

10 J. H. Cavka, S. Jakobsen, U. Olsbye, N. Guillou, C. Lamberti, S. Bordiga and K. P. Lillerud, *J. Am. Chem. Soc.*, 2008, **130**, 13850–13851.

11 D. Feng, Z.-Y. Gu, Y.-P. Chen, J. Park, Z. Wei, Y. Sun, M. Bosch, S. Yuan and H.-C. Zhou, *J. Am. Chem. Soc.*, 2014, **136**, 17714–17717.

12 D. Feng, Z.-Y. Gu, J.-R. Li, H.-L. Jiang, Z. Wei and H.-C. Zhou, *Angew. Chem. Int. Ed.*, 2012, **51**, 10307–10310.

13 S. B. Kalidindi, S. Nayak, M. E. Briggs, S. Jansat, A. P. Katsoulidis, G. J. Miller, J. E. Warren, D. Antypov, F. Corà, B. Slater, M. R. Prestly, C. Martí-Gastaldo and M. J. Rosseinsky, *Angew. Chem. Int. Ed.*, 2015, **54**, 221–226.

14 D. Feng, K. Wang, J. Su, T.-F. Liu, J. Park, Z. Wei, M. Bosch, A. Yakovenko, X. Zou and H.-C. Zhou, *Angew. Chem. Int. Ed.*, 2015, **54**, 149–154.

15 A. Schaate, P. Roy, T. Preuße, S. J. Lohmeier, A. Godt and P. Behrens, *Chem. – Eur. J.*, 2011, **17**, 9320–9325.

16 P. Deria, D. A. Gómez-Gualdrón, W. Bury, H. T. Schaef, T. C. Wang, P. K. Thallapally, A. A. Sarjeant, R. Q. Snurr, J. T. Hupp and O. K. Farha, *J. Am. Chem. Soc.*, 2015, **137**, 13183–13190.

17 T. C. Wang, W. Bury, D. A. Gómez-Gualdrón, N. A. Vermeulen, J. E. Mondloch, P. Deria, K. Zhang, P. Z. Moghadam, A. A. Sarjeant, R. Q. Snurr, J. F. Stoddart, J. T. Hupp and O. K. Farha, *J. Am. Chem. Soc.*, 2015, **137**, 3585–3591.

18 R. D'Amato, R. Bondi, I. Moghdad, F. Marmottini, M. J. McPherson, H. Naïli, M. Taddei and F. Costantino, *Inorg. Chem.*, 2021, **60**, 14294–14301.

19 A. H. Vahabi, F. Norouzi, E. Sheibani and M. Rahimi-Nasrabadi, *Coord. Chem. Rev.*, 2021, **445**, 214050.

20 J. Lee, O. K. Farha, J. Roberts, K. A. Scheidt, S. T. Nguyen and J. T. Hupp, *Chem. Soc. Rev.*, 2009, **38**, 1450–1459.

21 S. Ma and H.-C. Zhou, *Chem. Commun.*, 2010, **46**, 44–53.

22 J. A. Mason, M. Veenstra and J. R. Long, *Chem. Sci.*, 2013, **5**, 32–51.

23 B. V. de Voorde, B. Bueken, J. Denayer and D. D. Vos, *Chem. Soc. Rev.*, 2014, **43**, 5766–5788.

24 J.-R. Li, R. J. Kuppler and H.-C. Zhou, *Chem. Soc. Rev.*, 2009, **38**, 1477–1504.

25 X.-Y. Wang, Z.-M. Wang and S. Gao, *Chem. Commun.*, 2007, 1127–1129.

26 J.-H. Dou, M. Q. Arguilla, Y. Luo, J. Li, W. Zhang, L. Sun, J. L. Mancuso, L. Yang, T. Chen, L. R. Parent, G. Skorupskii, N. J. Libretto, C. Sun, M. C. Yang, P. V. Dip, E. J. Brignole, J. T. Miller, J. Kong, C. H. Hendon, J. Sun and M. Dincă, *Nat. Mater.*, 2021, **20**, 222–228.

27 R. C. Huxford, J. Della Rocca and W. Lin, *Curr. Opin. Chem. Biol.*, 2010, **14**, 262–268.

28 M. D. Allendorf, C. A. Bauer, R. K. Bhakta and R. J. T. Houk, *Chem. Soc. Rev.*, 2009, **38**, 1330–1352.

29 Z.-Z. Lu, R. Zhang, Y.-Z. Li, Z.-J. Guo and H.-G. Zheng, *J. Am. Chem. Soc.*, 2011, **133**, 4172–4174.

30 E. J. Mittemeijer, in *Fundamentals of Materials Science: The Microstructure–Property Relationship Using Metals as Model Systems*, ed. E. J. Mittemeijer, Springer International Publishing, Cham, 2021, pp. 231–282.

31 O. Halbherr and R. A. Fischer, in *The Chemistry of Metal–Organic Frameworks*, John Wiley & Sons, Ltd, 2016, pp. 795–822.

32 O. V. Gutov, M. G. Hevia, E. C. Escudero-Adán and A. Shafir, *Inorg. Chem.*, 2015, **54**, 8396–8400.

33 L. Valenzano, B. Civalleri, S. Chavan, S. Bordiga, M. H. Nilsen, S. Jakobsen, K. P. Lillerud and C. Lamberti, *Chem. Mater.*, 2011, **23**, 1700–1718.

34 M. J. Katz, Z. J. Brown, Y. J. Colón, P. W. Siu, K. A. Scheidt, R. Q. Snurr, J. T. Hupp and O. K. Farha, *Chem. Commun.*, 2013, **49**, 9449–9451.

35 Y. Han, M. Liu, K. Li, Y. Zuo, Y. Wei, S. Xu, G. Zhang, C. Song, Z. Zhang and X. Guo, *CrystEngComm*, 2015, **17**, 6434–6440.

36 C. A. Trickett, K. J. Gagnon, S. Lee, F. Gándara, H.-B. Bürgi and O. M. Yaghi, *Angew. Chem. Int. Ed.*, 2015, **54**, 11162–11167.

37 G. C. Shearer, S. Chavan, S. Bordiga, S. Svelle, U. Olsbye and K. P. Lillerud, *Chem. Mater.*, 2016, **28**, 3749–3761.

38 M. J. Cliffe, W. Wan, X. Zou, P. A. Chater, A. K. Kleppe, M. G. Tucker, H. Wilhelm, N. P. Funnell, F.-X. Coudert and A. L. Goodwin, *Nat. Commun.*, 2014, **5**, 4176.

39 S. Waitschat, M. T. Wharmby and N. Stock, *Dalton Trans.*, 2015, **44**, 11235–11240.

40 S. Øien, D. Wragg, H. Reinsch, S. Svelle, S. Bordiga, C. Lamberti and K. P. Lillerud, *Cryst. Growth Des.*, 2014, **14**, 5370–5372.

41 P. Xydias, I. Spanopoulos, E. Klontzas, G. E. Froudakis and P. N. Trikalitis, *Inorg. Chem.*, 2014, **53**, 679–681.

42 F. Norouzi and H. R. Khavasi, *New J. Chem.*, 2020, **44**, 8937–8943.

43 E. Mydske Thoresen, S. Øien-Ødegaard, G. Kaur, M. Tilset, K. Petter Lillerud and M. Amedjkouh, *RSC Adv.*, 2020, **10**, 9052–9062.

44 R. Thür, N. Van Velthoven, S. Slootmaekers, J. Didden, R. Verbeke, S. Smolders, M. Dickmann, W. Egger, D. De Vos and I. F. J. Vankelecom, *J. Membr. Sci.*, 2019, **576**, 78–87.

45 G. Kaur, Department of Chemistry, Faculty of Mathematics and Natural Sciences, University of Oslo, 2020.

46 R. Sun, B. Liu, B.-G. Li and S. Jie, *ChemCatChem*, 2016, **8**, 3261–3271.

47 C. Wang, Z. Xie, K. E. deKrafft and W. Lin, *J. Am. Chem. Soc.*, 2011, **133**, 13445–13454.

48 C.-C. Hou, T.-T. Li, S. Cao, Y. Chen and W.-F. Fu, *J. Mater. Chem. A*, 2015, **3**, 10386–10394.

49 R. Huang, Y. Peng, C. Wang, Z. Shi and W. Lin, *Eur. J. Inorg. Chem.*, 2016, **2016**, 4358–4362.

50 I. Gerz, S. A. V. Jannuzzi, K. T. Hylland, C. Negri, D. S. Wragg, S. Øien-Ødegaard, M. Tilset, U. Olsbye, S. DeBeer and M. Amedjkouh, *Eur. J. Inorg. Chem.*, 2021, **2021**, 4762–4775.

51 R. Gil-San-Millan, E. López-Maya, M. Hall, N. M. Padial, G. W. Peterson, J. B. DeCoste, L. M. Rodríguez-Albelo, J. E. Oltra, E. Barea and J. A. R. Navarro, *ACS Appl. Mater. Interfaces*, 2017, **9**, 23967–23973.

52 F. A. Son, A. Atilgan, K. B. Idrees, T. Islamoglu and O. K. Farha, *Inorg. Chem. Front.*, 2020, **7**, 984–990.

53 M. Kim, J. F. Cahill, Y. Su, K. A. Prather and S. M. Cohen, *Chem. Sci.*, 2011, **3**, 126–130.

54 H. Fei and S. M. Cohen, *Chem. Commun.*, 2014, **50**, 4810–4812.

55 B.-K. Choi and T. Yamamoto, *Electrochem. Commun.*, 2003, **5**, 566–570.

56 S. Glomb, D. Woschko, G. Makhloufi and C. Janiak, *ACS Appl. Mater. Interfaces*, 2017, **9**, 37419–37434.

57 L.-Q. Wei and B.-H. Ye, *Inorg. Chem.*, 2019, **58**, 4385–4393.

58 A. Das, N. Anbu, M. SK, A. Dhakshinamoorthy and S. Biswas, *Inorg. Chem.*, 2019, **58**, 5163–5172.

59 L. E. Hollister, B. Müller-Oerlinghausen, K. Rickels and R. I. Shader, *J. Clin. Psychopharmacol.*, 1993, **13**, 169–169.

60 H. Ashton, *Drugs*, 1994, **48**, 25–40.

61 Y. Malki, L. T. Maillard and N. Masurier, *Eur. J. Org. Chem.*, 2022, **2022**, e202100492.

62 T. A. Tikhonova, K. A. Lyssenko, I. V. Zavarzin and Y. A. Volkova, *J Org Chem*, 2019, **84**, 15817–15826.

63 S. Montanaro, I. A. Wright, A. S. Batsanov and M. R. Bryce, *J. Org. Chem.*, 2018, **83**, 12320–12326.

64 L. Yan, H. Wang, Y. Chen, Z. Li and Y. Pei, *Mol. Divers.*, 2018, **22**, 323–333.

65 Y. Ning, X. He, Y. Zuo, J. Wang, Q. Tang, M. Xie, R. Li and Y. Shang, *Org. Biomol. Chem.*, 2020, **18**, 2893–2901.

66 A. S. A. Youssef, F. A. El-Mariah, F. T. Abd-Elmottaleb and H. E. Hashem, *J. Heterocycl. Chem.*, 2019, **56**, 456–463.

67 M. Tomar, N. T. Lucas, K. Müllen and J. Jacob, *Tetrahedron Lett.*, 2013, **54**, 5883–5885.

68 R. Weiss and L. Chledowski, *Monatshefte Für Chem. Verwandte Teile Anderer Wiss.*, 1934, **65**, 357–366.

69 H. Schiff, *Justus Liebigs Ann. Chem.*, 1864, **131**, 118–119.

70 A. Schaate, P. Roy, A. Godt, J. Lippke, F. Waltz, M. Wiebcke and P. Behrens, *Chem. – Eur. J.*, 2011, **17**, 6643–6651.

71 S. Diring, S. Furukawa, Y. Takashima, T. Tsuruoka and S. Kitagawa, *Chem. Mater.*, 2010, **22**, 4531–4538.

72 T. Tsuruoka, S. Furukawa, Y. Takashima, K. Yoshida, S. Isoda and S. Kitagawa, *Angew. Chem.*, 2009, **121**, 4833–4837.

73 G. C. Shearer, PhD Thesis, Department of Chemistry, Faculty of Mathematics and Natural Sciences, University of Oslo, 2015.

74 In *Materials Characterization*, John Wiley & Sons, Ltd, 2013, pp. 47–82.

75 Y. Waseda, E. Matsubara and K. Shinoda, in *X-Ray Diffraction Crystallography: Introduction, Examples and Solved Problems*, eds. Y. Waseda, E. Matsubara and K. Shinoda, Springer, Berlin, Heidelberg, 2011, pp. 107–167.

76 G. C. Shearer, J. G. Vitillo, S. Bordiga, S. Svelle, U. Olsbye and K. P. Lillerud, *Chem. Mater.*, 2016, **28**, 7190–7193.

77 In *Physics and Chemistry of Interfaces*, John Wiley & Sons, Ltd, 2003, pp. 177–205.

78 I. Langmuir, *J. Am. Chem. Soc.*, 1918, **40**, 1361–1403.

79 S. Brunauer, P. H. Emmett and E. Teller, *J. Am. Chem. Soc.*, 1938, **60**, 309–319.

80 K. T. Hylland, S. Øien-Ødegaard, R. H. Heyn and M. Tilset, *Eur. J. Inorg. Chem.*, 2020, **2020**, 3627–3643.

81 G. R. Fulmer, A. J. M. Miller, N. H. Sherden, H. E. Gottlieb, A. Nudelman, B. M. Stoltz, J. E. Bercaw and K. I. Goldberg, *Organometallics*, 2010, **29**, 2176–2179.

82 N. Ko, J. Hong, S. Sung, K. E. Cordova, H. J. Park, J. K. Yang and J. Kim, *Dalton Trans.*, 2015, **44**, 2047–2051.

83 R. Antwi-Baah and H. Liu, *Materials*, 2018, **11**, 2250.

84 L. Liu, Z.-P. Tao, H.-R. Chi, B. Wang, S.-M. Wang and Z.-B. Han, *Dalton Trans.*, 2021, **50**, 39–58.

85 M.-C. Chen, D.-G. Chen and P.-T. Chou, *ChemPlusChem*, 2021, **86**, 11–27.

86 S. R. Meech and D. Phillips, *J. Photochem.*, 1983, **23**, 193–217.

87 A. M. Brouwer, *Pure Appl. Chem.*, 2011, **83**, 2213–2228.

88 J. R. Lakowicz, Ed., in *Principles of Fluorescence Spectroscopy*, Springer US, Boston, MA, 2006, pp. 205–235.

89 M. J. Frisch, G. W. Trucks, H. B. Schlegel, G. E. Scuseria, M. A. Robb, J. R. Cheeseman, G. Scalmani, V. Barone, G. A. Petersson, H. Nakatsuji, X. Li, M. Caricato, A. V. Marenich, J. Bloino, B. G. Janesko, R. Gomperts, B. Mennucci, H. P. Hratchian, J. V. Ortiz, A. F. Izmaylov, J. L. Sonnenberg, D. Williams-Young, F. Ding, F. Lipparini, F. Egidi, J. Goings, B. Peng, A. Petrone, T. Henderson, D. Ranasinghe, V. G. Zakrzewski, J. Gao, N. Rega, G. Zheng, W. Liang, M. Hada, M. Ehara, K. Toyota, R. Fukuda, J. Hasegawa, M. Ishida, T. Nakajima, Y. Honda, O. Kitao, H. Nakai, T. Vreven, K. Throssell, J. A. Montgomery Jr., J. E. Peralta, F. Ogliaro, M. J. Bearpark, J. J. Heyd, E. N. Brothers, K. N. Kudin, V. N. Staroverov, T. A. Keith, R. Kobayashi, J. Normand, K. Raghavachari, A. P. Rendell, J. C. Burant, S. S. Iyengar, J. Tomasi, M. Cossi, J. M. Millam, M. Klene, C. Adamo, R. Cammi, J. W. Ochterski, R. L. Martin, K. Morokuma, O. Farkas, J. B. Foresman and D. J. Fox, *Gaussian 16, Revision C.01*, Gaussian Inc., Wallingford CT, 2016.

90 C. Adamo and V. Barone, *J. Chem. Phys.*, 1999, **110**, 6158–6170.

91 R. Krishnan, J. S. Binkley, R. Seeger and J. A. Pople, *J. Chem. Phys.*, 1980, **72**, 650–654.

92 Y. Zhao and D. G. Truhlar, *Theor. Chem. Acc.*, 2008, **120**, 215–241.

93 F. Weigend and R. Ahlrichs, *Phys. Chem. Chem. Phys.*, 2005, **7**, 3297–3305.

94 A. V. Marenich, C. J. Cramer and D. G. Truhlar, *J. Phys. Chem. B*, 2009, **113**, 6378–6396.

95 *Comprehensive Handbook of Chemical Bond Energies*, CRC Press, 2007.

96 G. C. Shearer, S. Chavan, J. Ethiraj, J. G. Vitillo, S. Svelle, U. Olsbye, C. Lamberti, S. Bordiga and K. P. Lillerud, *Chem. Mater.*, 2014, **26**, 4068–4071.

97 A. A. Coelho, *J. Appl. Crystallogr.*, 2018, **51**, 210–218.

7 Appendices I-VI

I. Additional Data

II. Paper I

Appendix I

Additional Data

7.1 NMR data

The ^{13}C-NMR spectrum of compound **H_2-3** is shown in Figure 40. The liquid phase digestion ^{1}H-NMR for the synthesized UiO-67, and all mixed-linker BPDC-$(NH_2)_2$ UiO-67 MOFs are shown in Figures 41-47. The liquid phase digestion ^{1}H-NMR for all functionalized MOFs are shown in Figures 48-51.

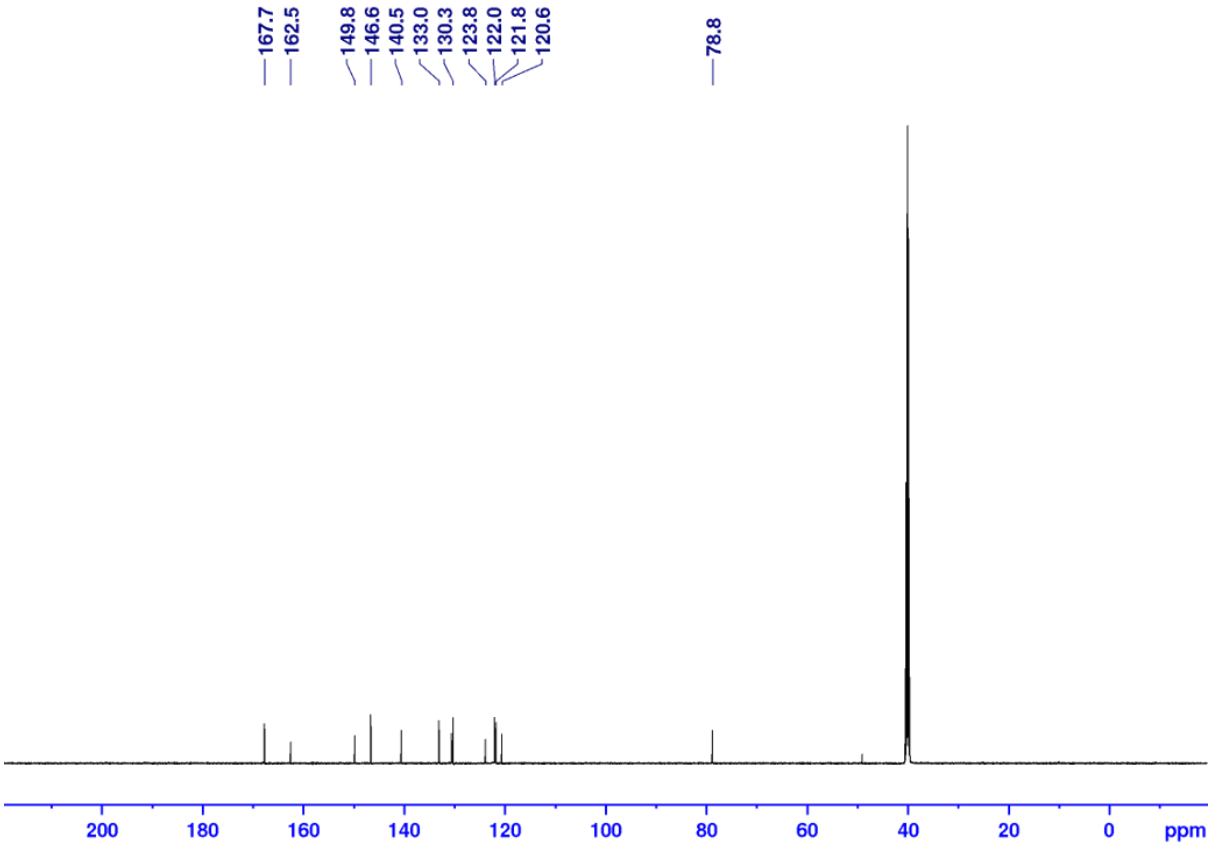

Figure 40. ^{13}C NMR spectrum of compound **H_2-3** (151 MHz, 0.1M NaOD/D_2O).

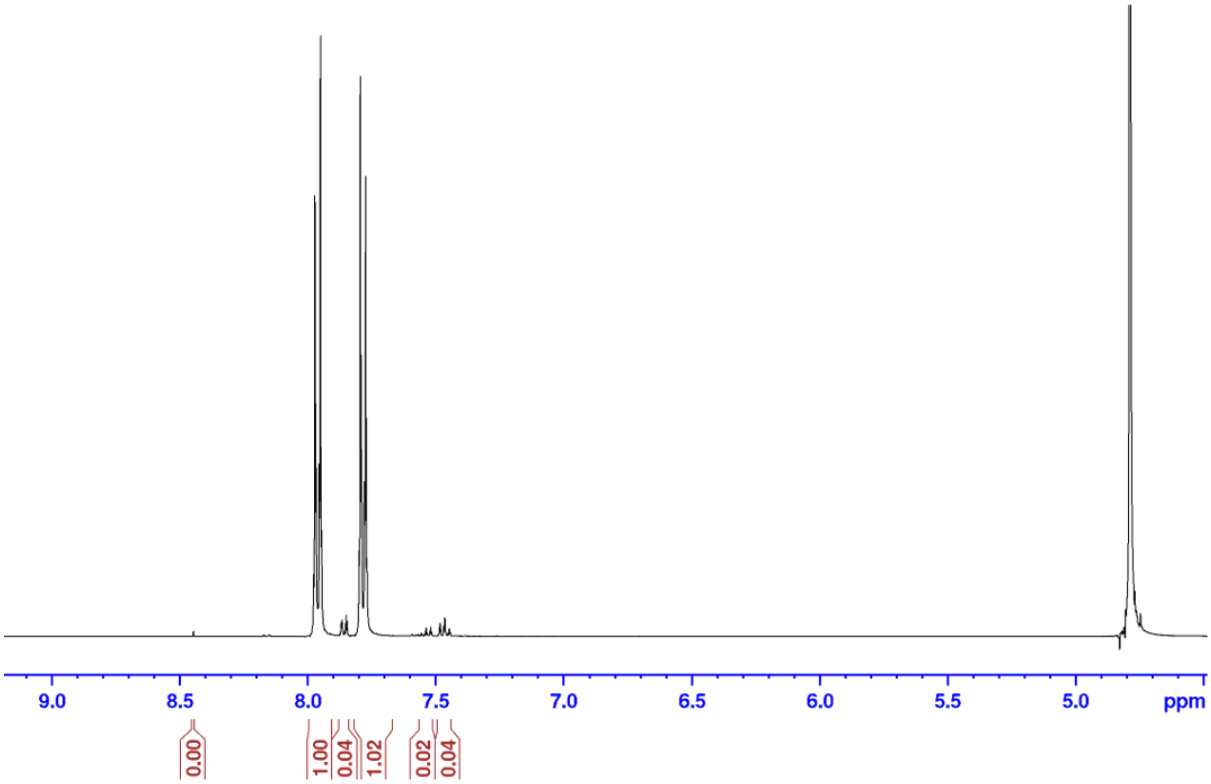

Figure 41. Liquid phase digestion ^{1}H NMR spectrum of UiO-67 MOF (600 MHz, 0.1M NaOD/D_2O).

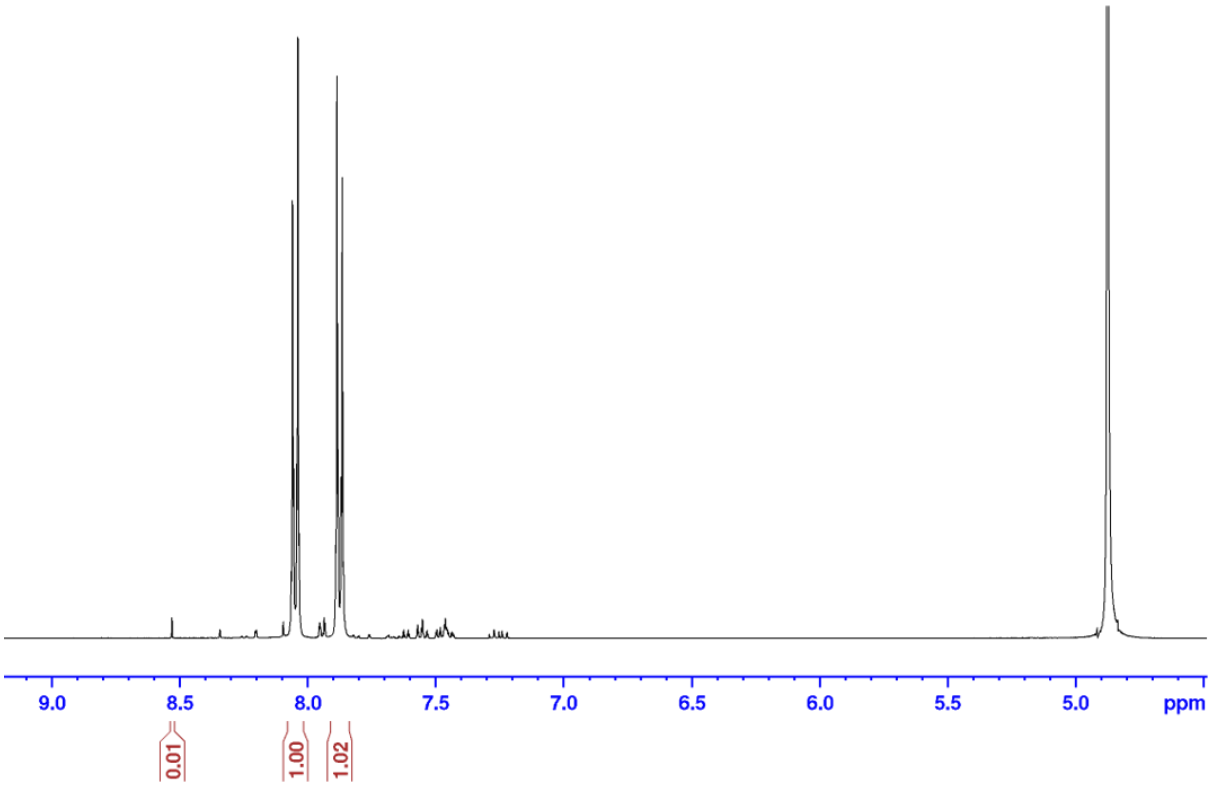

Figure 42. Liquid phase digestion ^{1}H NMR spectrum of **UiO-67-0.1(NH_2)$_2$** (600 MHz, 0.1M NaOD/D_2O).

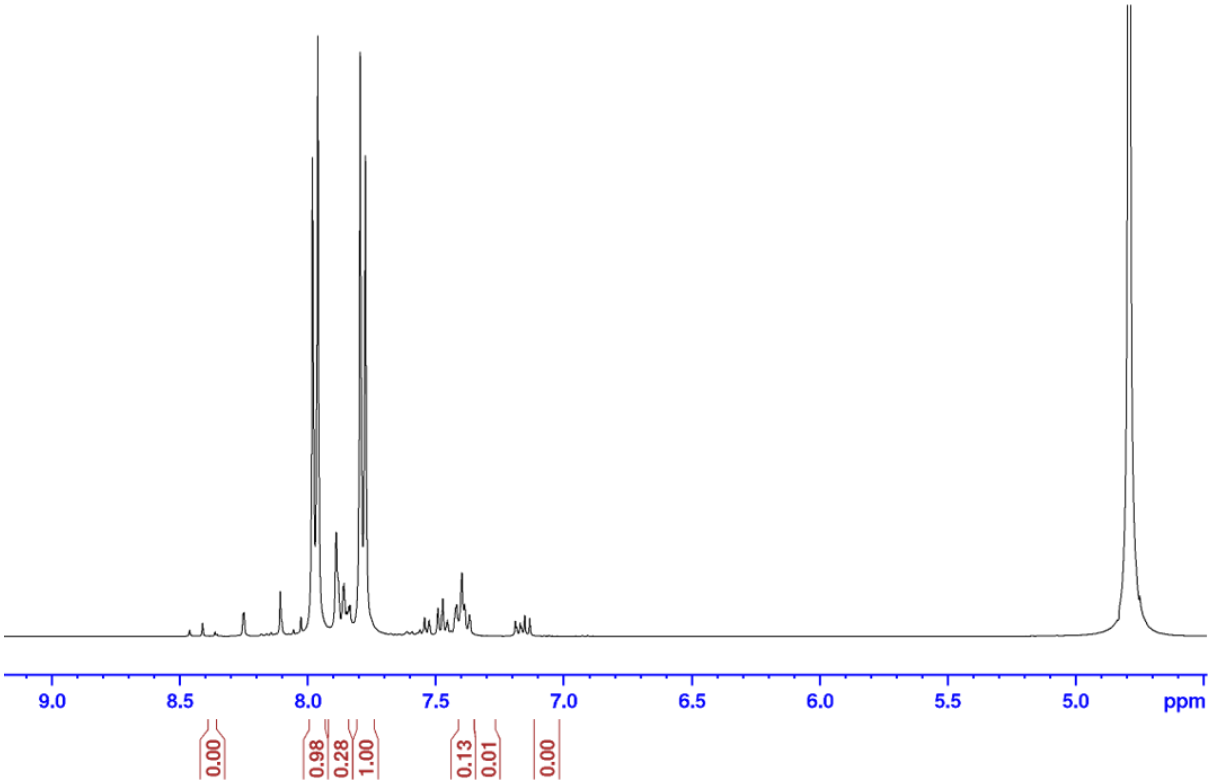

Figure 43. Liquid phase digestion ^{1}H NMR spectrum of **UiO-67-0.2(NH$_2$)$_2$** (600 MHz, 0.1M NaOD/D_2O).

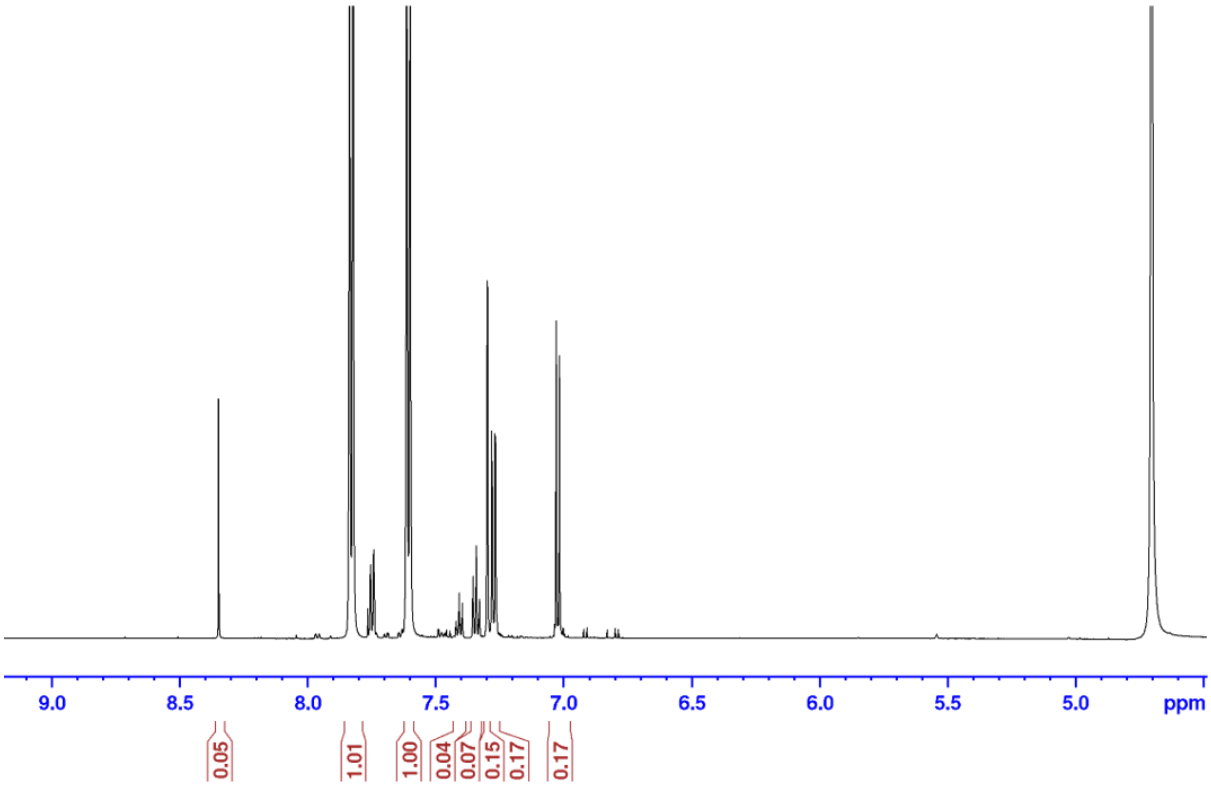

Figure 44. Liquid phase digestion ^{1}H NMR spectrum of **UiO-67-0.3(NH$_2$)$_2$** (600 MHz, 0.1M NaOD/D_2O).

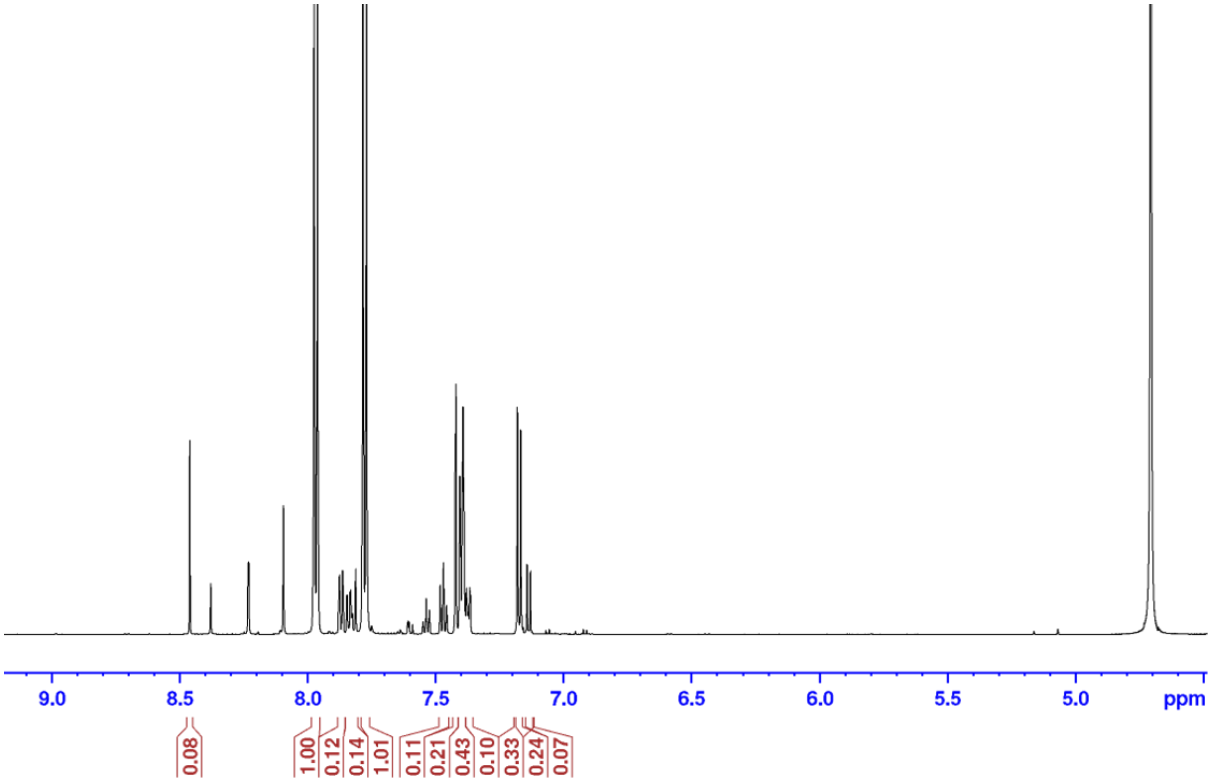

Figure 45. Liquid phase digestion ^{1}H NMR spectrum of **UiO-67-0.5(NH_2)$_2$** (600 MHz, 0.1M NaOD/D_2O).

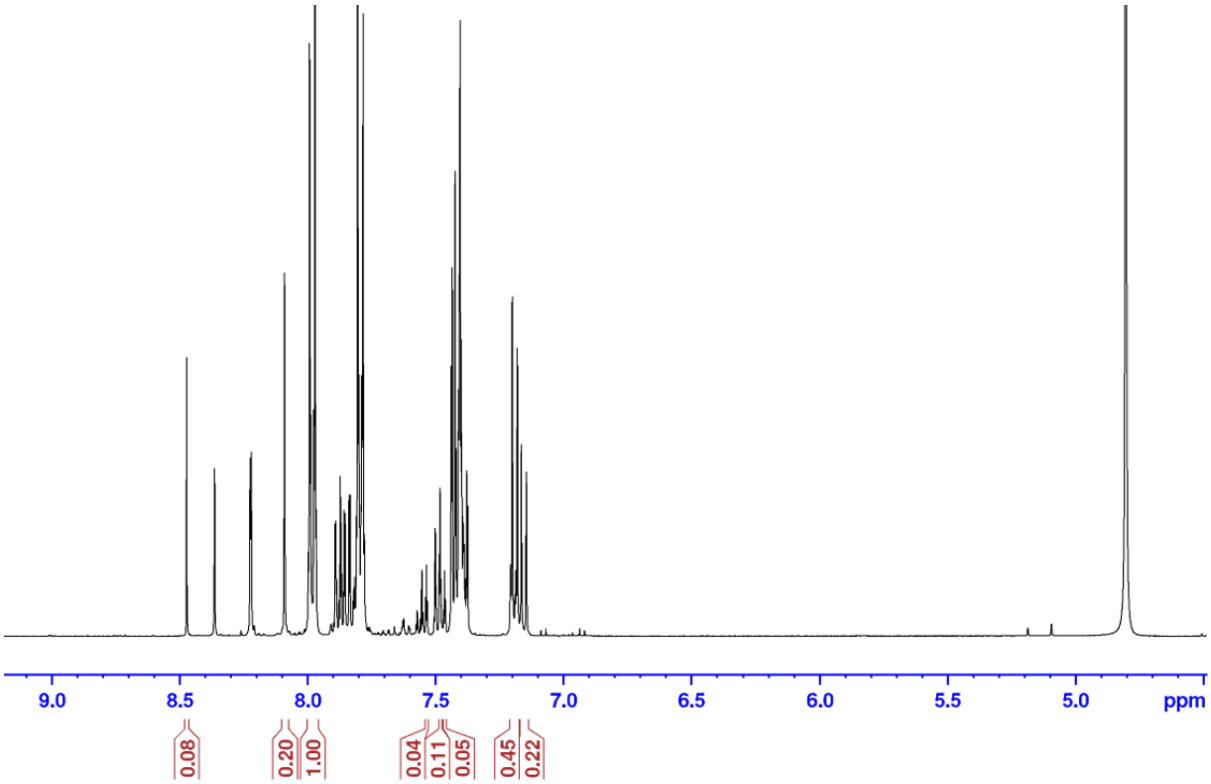

Figure 46. Liquid phase digestion ^{1}H NMR spectrum of **UiO-67-0.7(NH_2)$_2$** (600 MHz, 0.1M NaOD/D_2O).

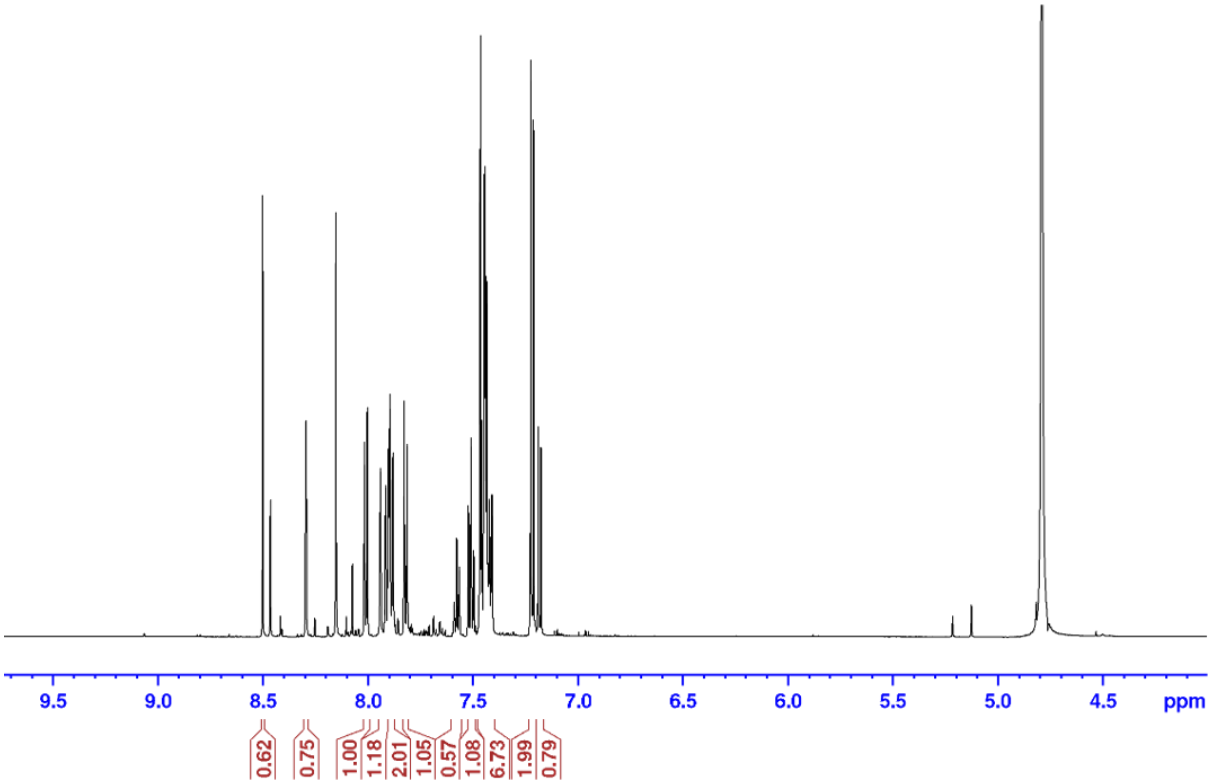

Figure 47 Liquid phase digestion ^{1}H NMR spectrum of **UiO-67-0.9(NH_2)$_2$** (600 MHz, 0.1M NaOD/D_2O).

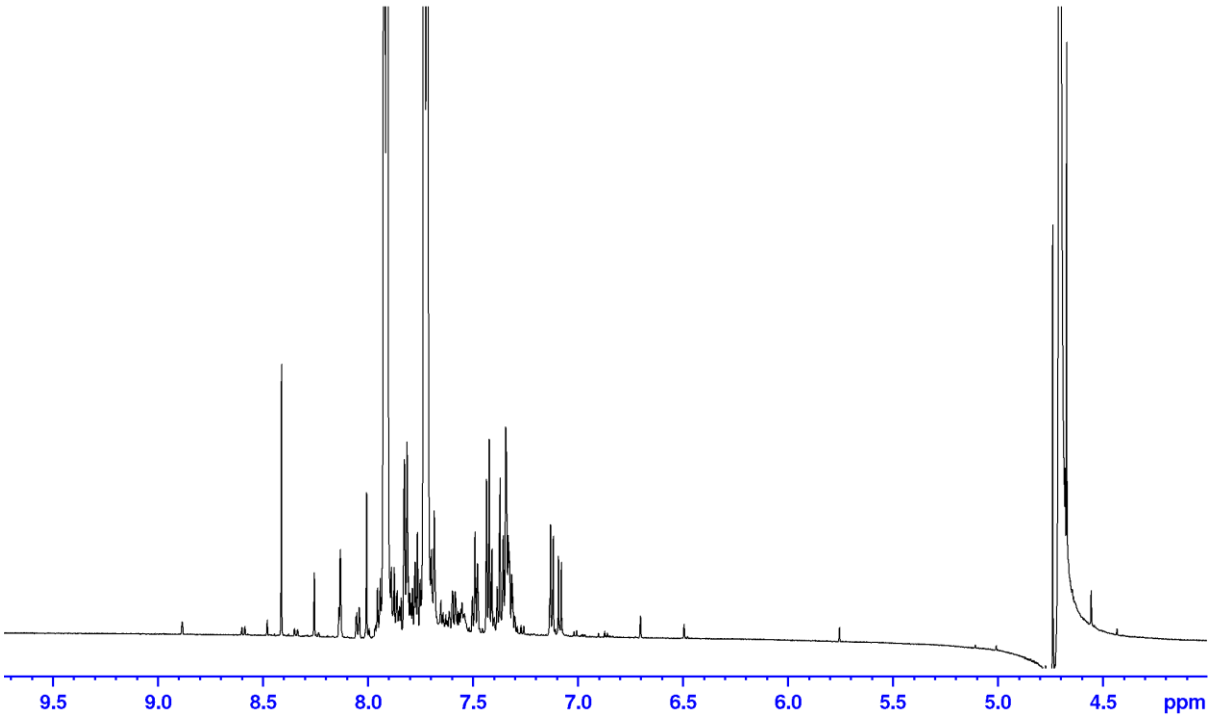

Figure 48 Liquid phase digestion ^{1}H NMR spectrum of **UiO-67-0.1(3)** (600 MHz, 0.1M NaOD/D_2O).

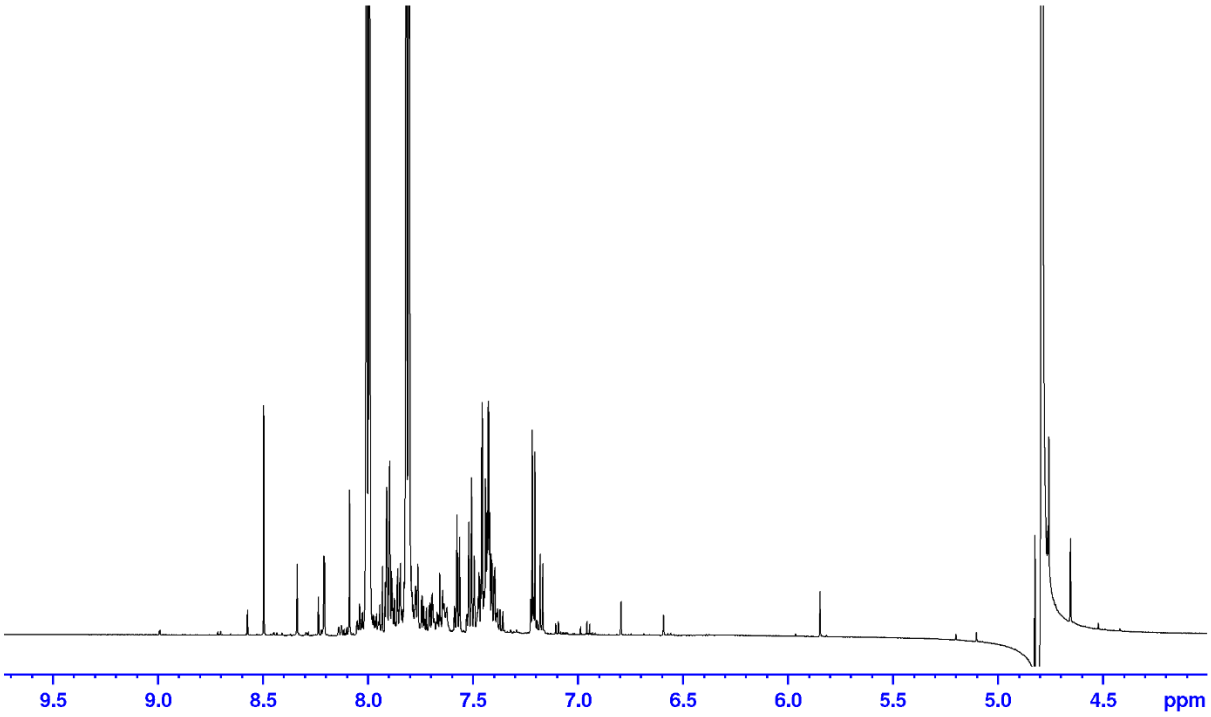

Figure 49 Liquid phase digestion ^{1}H NMR spectrum of **UiO-67-0.3(3)** (600 MHz, 0.1M NaOD/D_2O).

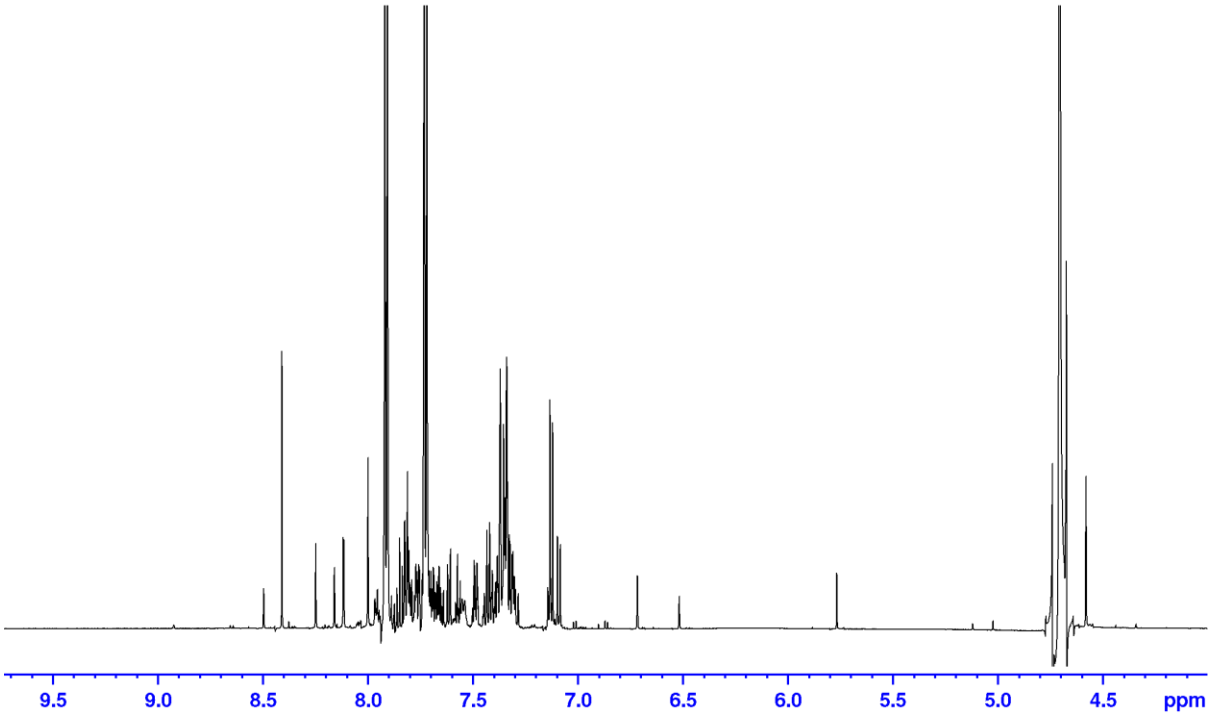

Figure 50 Liquid phase digestion ^{1}H NMR spectrum of **UiO-67-0.5(3)** (600 MHz, 0.1M NaOD/D_2O).

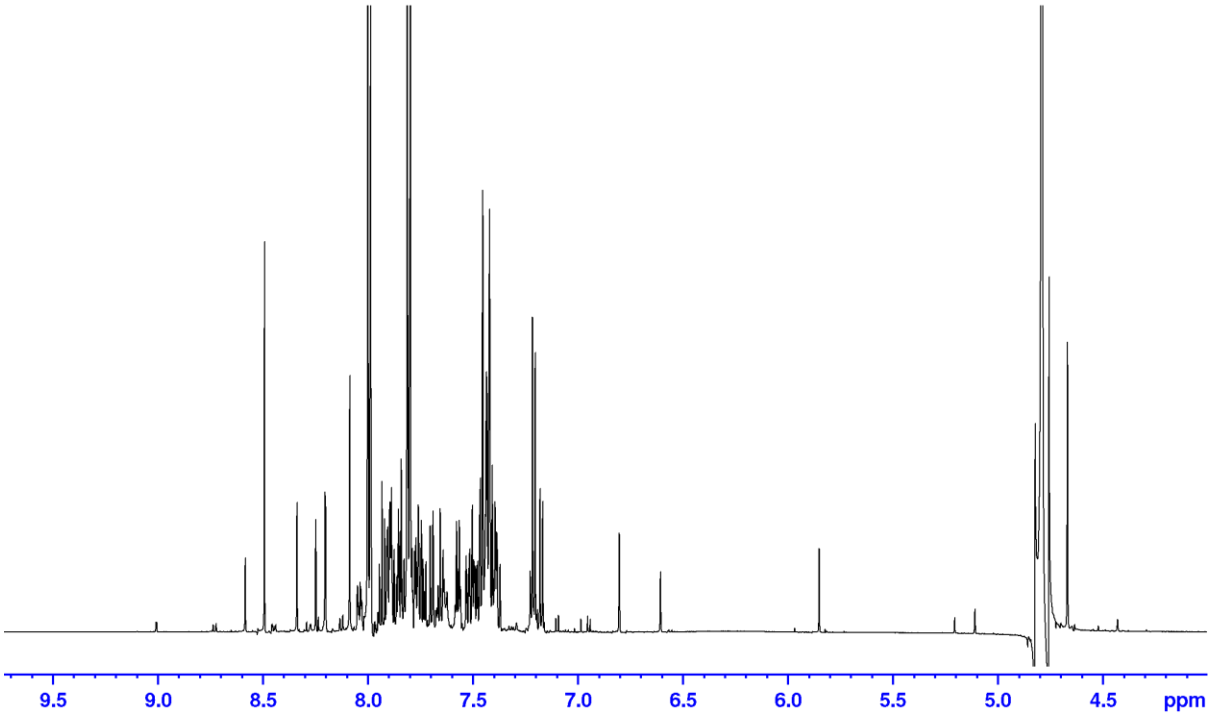

Figure 51 Liquid phase digestion ^{1}H NMR spectrum of **UiO-67-0.7(3)** (600 MHz, 0.1M NaOD/D_2O).

7.2 PXRD data

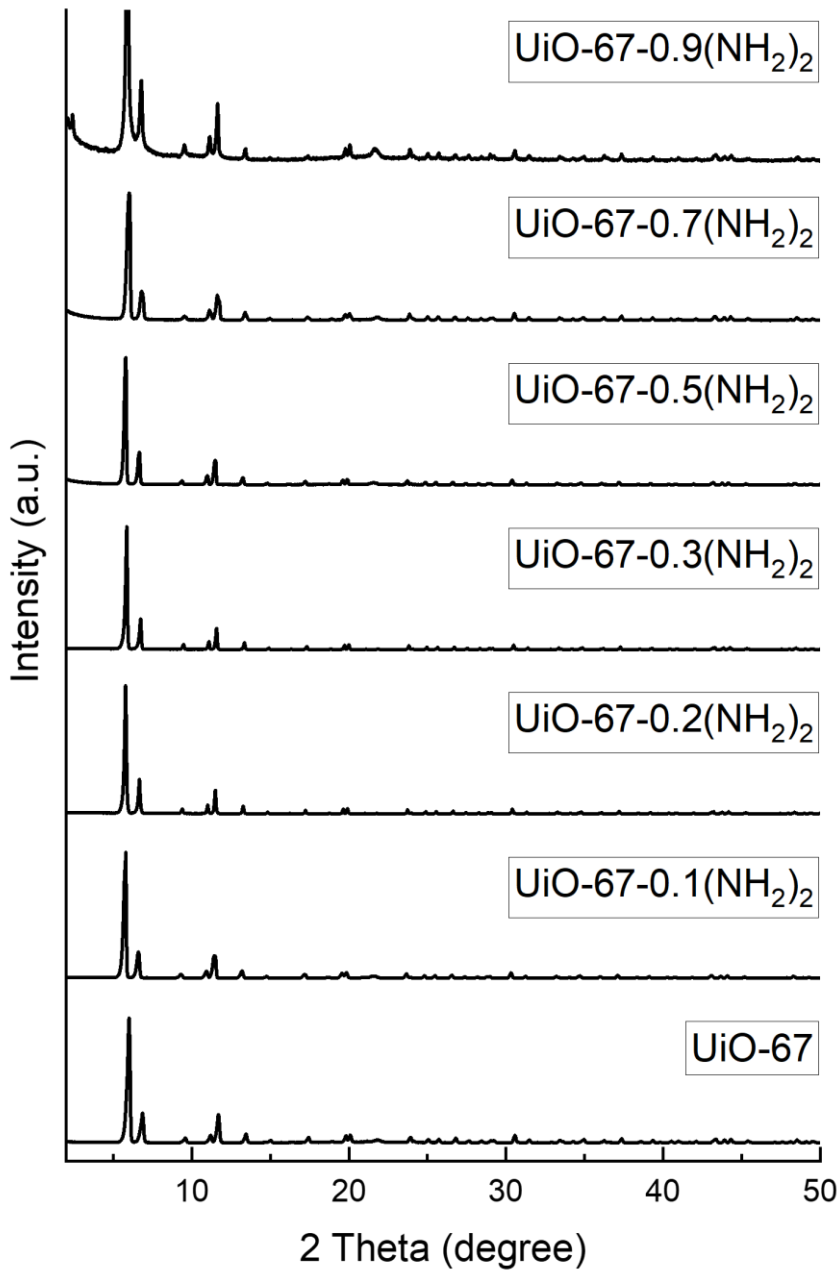

Figure 52 PXRD diffractograms for all pristine MOFs.

Appendix II

Synthesis and Luminescence of Dibenzo[*d,f*]-1,2-dihydro-[1,3]diazepines

*Isabelle Gerz,[a,b] Rafael Cortez Sgroi Pupo,[a,b] David S. Wragg,[a,b] Ainara Nova,[a,b,c,d] Mohamed Amedjkouh[*a,b], manuscript under preparation.*

[a] Department of Chemistry, University of Oslo, P. O. Box 1033 Blindern, 0315 Oslo, Norway

[b] Centre for Materials Science and Nanotechnology, University of Oslo, P.O. Box 1126 Blindern, 0316 Oslo, Norway

[c] Hylleraas Centre for Quantum Molecular Sciences, Department of Chemistry, University of Oslo, N-0315 Oslo, Norway

[d] UiT-The Arctic University of Norway, 9037 Tromsø, Norway

UiO : University of Oslo
Faculty of mathematics and natural sciences

Co-author declaration for the following joint paper:

This declaration should describe the research contribution of the candidate, the main supervisor (where he/she is an associate author) and the other two most central authors (the corresponding author must be among them). If applicable, the contributions from other PhD candidates who has or intend to include the paper in a thesis should be described. Contributions from master students should be described.

Authors: Isabelle Gerz, Rafael Cortez Sgroi Pupo, David S. Wragg, Ainara Nova, Mohamed Amedjkouh
Title: Synthesis and Luminescence of Dibenzo[d,f]-1,2-dihydro-[1,3]diazepines
Journal: ***Manuscript under preparation***

Isabelle Gerz's independent contribution:
☒ First author ☐ Corresponding author ☐ Other
IG synthesised and fully characterised three compounds, denominated 1, 2, and 10 in the manuscript. IG measured all 15N NMR. IG measured and analysed UV/Vis and fluorescence spectra together with RCSP. IG co-supervised RCSP. IG wrote the manuscript, apart from the part written by RCSP.

Rafael Cortez Sgroi Pupo
☐ First author ☐ Main supervisor ☐ Corresponding author ☐ PhD candidate ☒ Other
RCSP synthesised and characterised all compounds other than those listed for IG. RCSP measured and analysed UV/Vis and Fluorescence spectra together with IG. RCSP performed all computational experiments under the supervision of AN. RCSP wrote the sections about solvatochromism and the computations in the manuscript. RCSP revised the manuscript.

Ainara Nova
☐ First author ☐ Main supervisor ☐ Corresponding author ☐ PhD candidate ☒ Other
AN supervised RCSP on the execution, analysis and writing of the computational part of the manuscript. AN revised the manuscript.

Mohamed Amedjkouh
☐ First author ☒ Main supervisor ☒ Corresponding author ☐ PhD candidate ☐ Other
MA supervised IG and RCSP. MA revised the manuscript.

Has this paper been, or will this paper be part of another doctoral degree thesis?

Yes: ☐ No: ☒

If yes, elaborate:

Contributions from master students: See RCSP above

Synthesis and Luminescence of Dibenzo[*d,f*]-1,2-dihydro-[1,3]diazepines

Isabelle Gerz,[a,b] Rafael Cortez Sgroi Pupo,[a,b] David S. Wragg,[a,b] Ainara Nova,[a,b,c,d] Mohamed Amedjkouh[a,b]*

[a] Department of Chemistry, University of Oslo, P. O. Box 1033 Blindern, 0315 Oslo, Norway
[b] Centre for Materials Science and Nanotechnology, University of Oslo, P.O. Box 1126 Blindern, 0316 Oslo, Norway
[c] Hylleraas Centre for Quantum Molecular Sciences, Department of Chemistry, University of Oslo, N-0315 Oslo, Norway
[d] UiT-The Arctic University of Norway, 9037 Tromsø, Norway

Abstract

A series of 2-substituted dibenzo[*d,f*]-1,2-dihydro-[1,3]diazepines was synthesised from a 2,2'-diaminobiphenyl and different aldehydes. The product formation and selectivity were found to be highly dependent on the aldehyde. Addition of a Lewis acid (Zn^{2+}, Cu^{+}) to the reaction mixture influenced conversion of starting material and selectivity for the diazepine. Additionally, the photophysical properties of the compounds in solution were explored by UV/Vis spectroscopy and DFT computations. The diazepine motif extended the absorption into the visible light range for most substituents. We found the fluorescent emission to be solvatochromatic, a property not previously reported for dibenzo[*d,f*]-1,2-dihydro-[1,3]diazepines.

Introduction

Diazepines are seven-membered heterocycles with two nitrogen atoms (Figure 1). Depending on the relative position of the nitrogen atoms and substituents in the ring, several routes are viable for diazepine synthesis.[1] While 1,4-benzodiazepines are extensively researched drugs that are sold commercially world-wide,[2] 1,3-benzodiazepines are less researched.

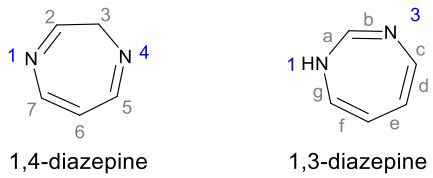

Figure 1. Nomenclature of diazepines: The atoms in the ring are numbered according to their position relative to two nitrogen atoms in the ring. For not fully unsaturated diazepines, the formally reduced positions are labelled 'hydro'. For rings fused to the nitrogen, letters are used to denote the shared bond.

The synthesis of 1,3-diazepines has gained increased attention in the last years.[3–5] For diaryl-1,3-diazepines, an easily accessible route is the reaction between a suitable 1,4-diamine and a carbonyl compound.[3,5–7] Tomar *et al.* reported the synthesis of a dibenzo[*d,f*][1,3]-diazepine from a substituted 2,2'-diaminobiphenyl and arylaldehydes (Scheme 1, A).[7] The formation of the fully unsaturated diazepine requires oxidation of the former carbonyl carbon and one nitrogen, which was effectuated by the I_2 under basic conditions.[7] An oxidant is not necessary when diaryl[*d,f*]-1,2-dihydro-[1,3]diazepines are the desired products. Montanaro *et al.* reported a one-pot reduction of nitro groups and the formation of 1,3-diazepines with $SnCl_2{\cdot}2H_2O$ and various carbonyl compounds (Scheme 1, B).[5] As these and other 1,3-diazepines have potential

medicinal applications,[5,8,9] tin reagents are best to be avoided. Additionally, tin reagents have been reported to lead to formation of benzo[*c*]cinnolines as a side-product in the reduction of 2,2'-dinitrobiphenyls/biaryls.[10] Remarkably, the same combination of starting materials, carbonyl compounds and amines, are also commonly employed to generate Schiff bases.[11–13] Despite both reactions, Schiff base formation and diazepine formation, being reported a long time ago (1864[11] and 1934[6] respectively), there is no straightforward procedure to selectively yield either diazepines or diimines. Pilkington and co-workers have found that metalation of their Schiff base ligands resulted in multifaceted ligand reactivity, including the formation of diazepines.[14–16] They found that a pyridine substituted Schiff base ligand formed the corresponding dipyrido[*d,f*]-1,2-dihydro-[1,3]diazepine when reacted with $Cu(hfac)_2$ (Scheme 1, C), but $Zn(hfac)_2$ yielded the fully unsaturated, amide substituted, dipyrido[*d,f*]-[1,3]diazepine.[16] Reaction of the salicylaldehyde derived Schiff base with a variety of metals gave either the dipyrido[*d,f*]-1,2-dihydro-[1,3]diazepine ($Cu(ClO_4)_2$, $SnCl_2$, $MnCl_2$) or hydrolysis to the monoimine ($FeCl_3/NEt_3$).[14]

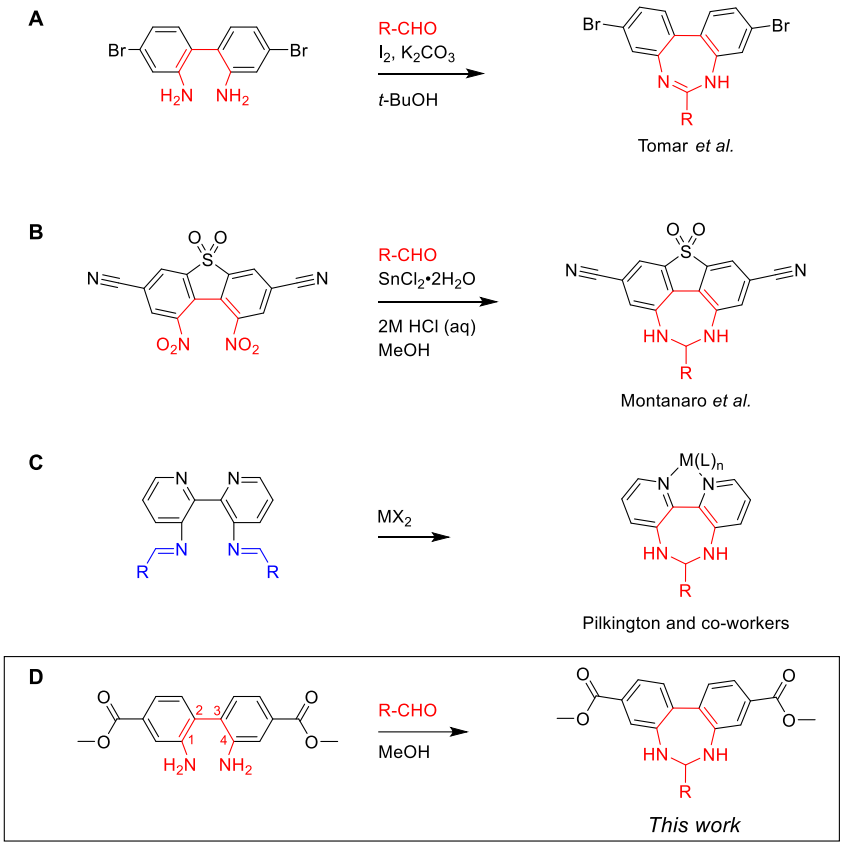

Scheme 1. A-C: Reported synthesis of diaryl-1,3-diazepines with.[5,7,14,16] Dibenzo[*d,f*][1,3]-diazepines are reported in literature either in the fully unsaturated form[7,14,17] or the dihydro analogue.[5,14] D: This work.

In this work, the diazepines were synthesized from dimethyl-2,2'-diaminobiphenyl-4,4'diacarboxylate. This diamine was reported to yield the Schiff base product exclusively in the acid-catalysed reaction with two equivalents of salicylaldehydes.[18] Dibenzodiazepines have been reported to be fluorescent.[5,7]

Cornelio *et al*. have functionalised a metal-organic framework (MOF) with a diazepine derivative to create a luminescent MOF.[19] Literature examples of diazepine functionalisation of either (semi)conducting polymers[7,20] or MOFs[21,22] have also targeted electrochemical properties[7,20] and gas absorption.[21] This work reports a series of methyl ester substituted dibenzo[*d,f*]-1,2-dihydro-[1,3]diazepines with varying R groups (Scheme 1 D). The scope and limitations of the synthesis protocol were explored, screening 20 aldehydes as starting material. The effect of $Zn(OAc)_2{\cdot}2H_2O$ as a reagent was investigated, highlighting the ambiguous role of a Lewis acid for the product formation. The photophysical properties of dibenzo[*d,f*]-1,2-dihydro-[1,3]diazepines were explored and the compounds were found to be solvatochromatic fluorophores. The transitions at the origin of the absorption and fluorescence were investigated through TD-DFT. The positive solvatochromatism that was found experimentally, could be reproduced computationally with an implicit solvent model.

Results and discussion

Synthesis of Diazepines

Starting from commercially available dimethyl biphenyl-4,4'-dicarboxylate, the dibenzodiazepines were synthesized in three steps – nitration, reduction and condensation (see Scheme 2 and SI). The nitration and subsequent reduction with iron were carried out according to the procedure of Hylland *et al*. that avoids the benzo[*c*]cinnolines side-product and yields dimethyl-2,2'-diaminobiphenyl-4,4'diacarboxylate,[18] which will be denominated starting material **SM** for simplicity. Thereafter, the aldehyde was condensed onto the diamine at room temperature (see Scheme 2 and SI). The product was collected through filtration. Initial screening of the dibenzo[*d,f*]-1,2-dihydro-[1,3]diazepine formation indicated a beneficial effect of a Lewis acid. Therefore, one equivalent of $Zn(OAc)_2{\cdot}2H_2O$, which can be detected by ^{1}H NMR, was employed in the synthesis. A more in-depth discussion of the effect of the salt can be found below.

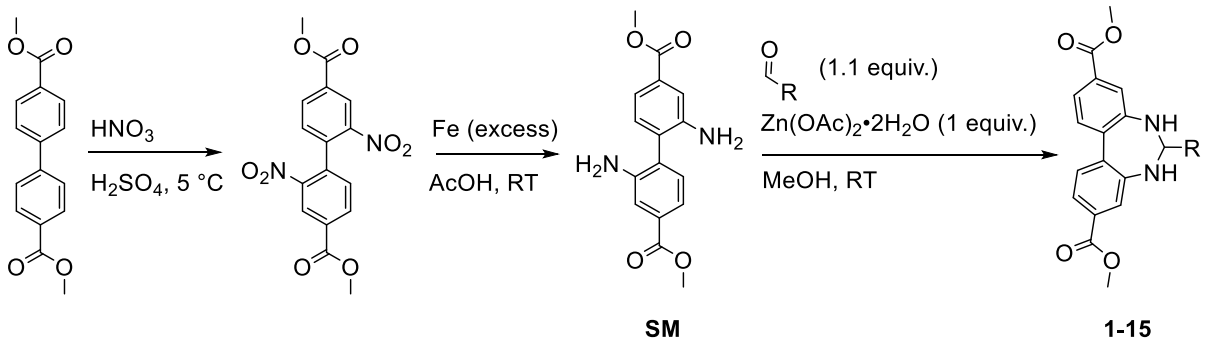

Scheme 2. Synthetic route to the dibenzo[*d,f*]-1,2-dihydro-[1,3]diazepines reported in this work.

To investigate the scope of the diazepine synthesis, several aldehydes were screened (Table 1). Compounds **1**-**7** were obtained in good to excellent yields. Their characterisation will be discussed in the respective section. We observed three possible products – apart from the diazepine, also mono- (**M**) and diimines (**D**) were formed (see Scheme 3). Even among structurally related aldehydes, the reaction outcome was strongly dependent on the exact substitution. Of the six pyridine aldehydes employed, the simplest substrate (unsubstituted picolinaldehyde) gave a mixture of diazepine **11** and **SM**, while those with additional 6-substitution yielded the diazepine exclusively. The 6-bromo-substituted nicotinaldehyde gave a 2:1 ratio of starting material and diazepine **10**, while no conversion was observed for the 5-bromo-substituted nicotinaldehyde. The condensation of the diamine with 2-methylpyrimidine-5-carbaldehyde to form **4** also failed at room temperature. We found that running the reaction at reflux instead enabled the synthesis of **4**. Other heterocycles in π-conjugation to the aldehyde seemed to struggle to form the diazepine. Both non-aromatic aldehydes in the series, isobutyraldehyde and undecanal, yielded the diazepines **6** and **8** exclusively, but adjustments to the procedure were necessary to accommodate for the higher solubility of the diazepine products in MeOH.

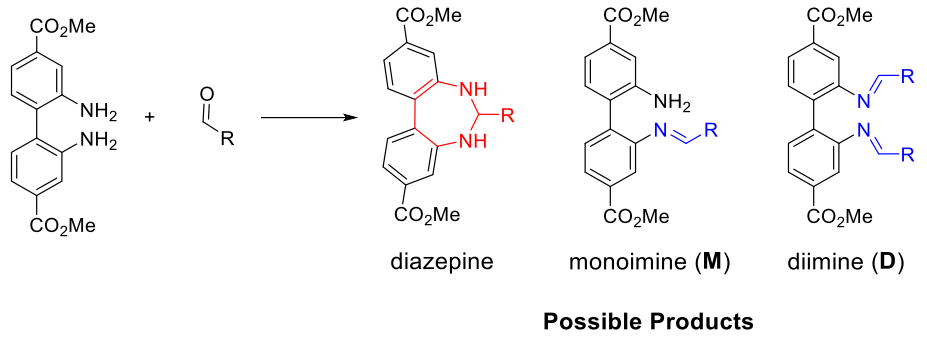

Scheme 3. Products formed when reacting 2,2'-diaminobiphenyls and aldehydes.

Table 1. Aldehydes screened for dibenzo[*d,f*]-1,2-dihydro-[1,3]diazepine synthesis. If a mixture was obtained, the % of products and starting material in the isolated crude product are given as determined by ^{1}H NMR (M = monoimine and D = diimine). Reaction conditions as given in the general procedure (RT, overnight reaction, 1.1 equiv. aldehyde, solvent: MeOH), unless specified otherwise.

Aldehyde	Diazepine	Imine	Starting Material
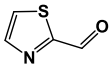	**1** 70% **1** (86% yield)† **1** 57%†*	n.d. n.d. n.d.	30% n.d. 43%
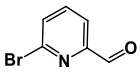	**2** (81% yield) **2** (64% yield)*	n.d. n.d.	n.d. n.d.
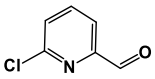	**3** (92% yield) **3** (79% yield)*	n.d. n.d.	n.d. n.d.
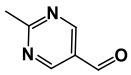	n.d. n.d.* **4** (36% yield)§ **4** (91%)*§	n.d. n.d. n.d. n.d.	recovered recovered n.d. 9%
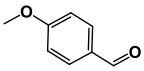	**5** (62%) **5** (86% yield)† **5** (87%)*†	**5M** (5%) n.d. **5M** (13%)	33% n.d. n.d.
	6 (86% yield) **6** (95% yield)*	n.d. n.d.	n.d. n.d.
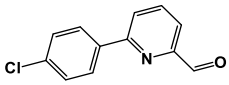	**7** (95% yield) **7** (85% yield)*	**7M** (traces) n.d.	traces n.d.
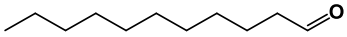	**8** (56% yield) **8** (62%)*	n.d. n.d.	n.d. 38%
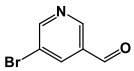	n.d. **9** (95%)*	n.d. n.d.	recovered 5%
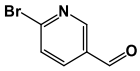	**10** (37%) **10** (75%)*	n.d. n.d.	63% 25%
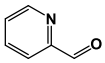	**11** (70%)	n.d.	30%
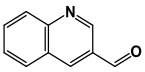	**12** (10%)	**12D** (21%)	69%
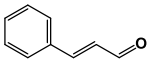	**13** (traces)	**13D** (90%)	10%
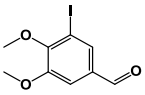	**14** (85%)	**14D** (11%)	4%
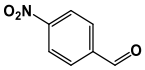	**15** (25%) **15** (93%)*	**15M** (Traces), **15D** (1%) **15M** (3%), **15D** (5%)	74% n.d.
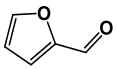	n.d.	**17D** (86% yield)	n.d.
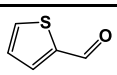	n.d.	**16D** (8%)	92%
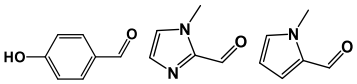	n.d.	n.d.	recovered

† 3 days reaction time; * Without $Zn(OAc)_2 \cdot 2H_2O$; § Reflux

Interestingly, we observed disproportionation of the diazepine to the Schiff base **1D** during hot recrystallization of **1** from an acetonitrile/toluene mixture (Scheme 4). The collected solids were identified as **1D**, while the diamine, which must have formed as byproduct, was not observed in the precipitate. The conversion of the diazepine product to the diimine represents the inverse reaction to what was observed by Pilkington and co-workers,[14,16] suggesting that the Schiff base product and the diazepine product are interconvertible.

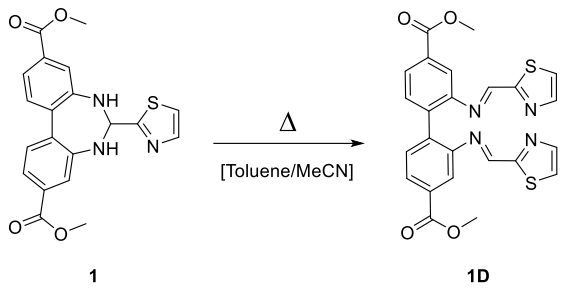

Scheme 4. Conversion of **1** to **1D** upon heating.

The results obtained for the synthesis of diazepines with and without $Zn(OAc)_2{\cdot}2H_2O$ showed the intriguing role of the metal salt in these reactions (table 1). The syntheses of **1**, **4**, and **5** necessitated $Zn(OAc)_2{\cdot}2H_2O$ to drive the reaction to completion. Adding one equivalent of $Zn(OAc)_2{\cdot}2H_2O$ improved the yield for **2** from 64% to 81%. For its constitutional isomers however, the addition of $Zn(OAc)_2{\cdot}2H_2O$ was detrimental, reducing the percentage of **10** in the crude product from 75% to 37% and inhibiting the formation of **9**. As reported by Pilkington and co-workers (see introduction),[14–16] the nature of the cation strongly affects the preference for either Schiff base or diazepine. Accordingly, the selectivity switched when using CuOTf instead of $Zn(OAc)_2{\cdot}2H_2O$. With the $Zn(OAc)_2{\cdot}2H_2O$ protocol reported herein, we found diazepine **11** to be the only product from the reaction of picolinaldehyde and the diamine. Contrary to that, the reaction with copper(I) triflate afforded exclusively the diimine copper complex, reported elsewhere.[23] Copper salts do however not preclude the formation of diazepines *per se*. A reaction mixture of CuI, the diamine and two equivalents of thiazole aldehyde did not yield the diimine copper complex. Instead, the copper complex of the diazepine was observed in single-crystal XRD (see single crystal XRD section).

Overall, the screening of reaction conditions and aldehyde substrates shows that conversion and selectivity are susceptible to changes in the protocol and the substrate structure. The possible products (diazepine and imine) are interconvertible, and the outcome depends on an interplay of aldehyde structure, Lewis acid and temperature. For these systems, no clear preference for structural motifs could be deciphered, albeit pyridines with the aldehyde in 2-position seem to form the diazepine readily. These findings suggest that the reaction conditions need to be adjusted to the aldehyde in question, as demonstrated for **4**.

Characterisation of the Diazepine Products

Dibenzo[*d,f*]-1,2-dihydro-[1,3]-diazepines **1**-**7** (Figure 2) were obtained in high purity and therefore further investigated. The compounds were characterised by NMR (^{1}H, ^{13}C, ^{15}N), elemental analysis, UV/Vis spectroscopy, and HRMS (see SI for details). Additionally, the crystal structures of **2**, **6** (Figure 3) and of a copper complex of **1** were obtained (Figure 4).

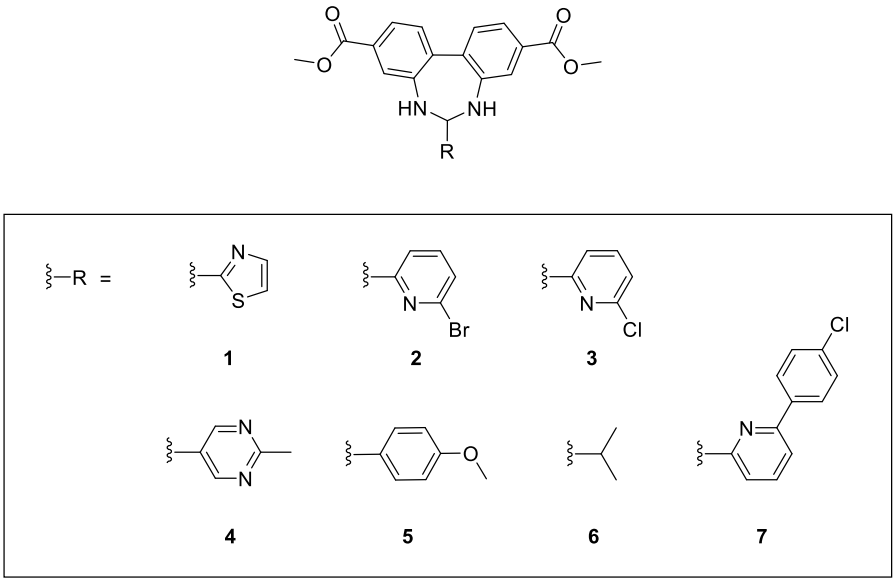

Figure 2. Overview of the dibenzo[*d,f*]-1,2-dihydro-[1,3]diazepines synthesized in this work.

The ^{1}H NMR spectra of dibenzo[*d,f*]-1,2-dihydro-[1,3]diazepines showed resonances characteristic for the dihydrodiazepine motif. Two ^{1}H NMR resonances upfield of the aromatic region originate from this motif, a triplet integrating for one proton and a doublet integrating for two. The doublet correlates to the triplet in COSY, but no carbon in HSQC, identifying it as the resonance of the NH protons in the diazepine ring. The ^{15}N NMR shifts of the dihydrodiazepines were ranged from –301.6 ppm to –290.2 ppm (referenced to nitromethane, Table 2), which is within the region associated with amines.[24]

Table 2. ^{15}N NMR shifts in ppm of compounds **1**-**7** (*vs*. external nitromethane standard).

Compound	**1**	**2**	**3**	**4**	**5**	**6**	**7**
Diazepine-N [ppm]	–301.6	–299.6	–299.5	–296.3	–290.2	–293.3	–296.7
Other nitrogen atom [ppm]	thiazole –64.0	pyridine –69.8	pyridine –78.2	pyrimidine –89.0	/	/	pyridine –76.9

Additional structural information can be gained from single crystal XRD structures of the diazepines. The diazepine is non-planar in all three crystal structures (Figure 3 and Figure 4). The angle between the backbone phenyls is 25°-40°, values comparable to those found in the structures reported by Tomar *et al.* (see Scheme 1A).[7]

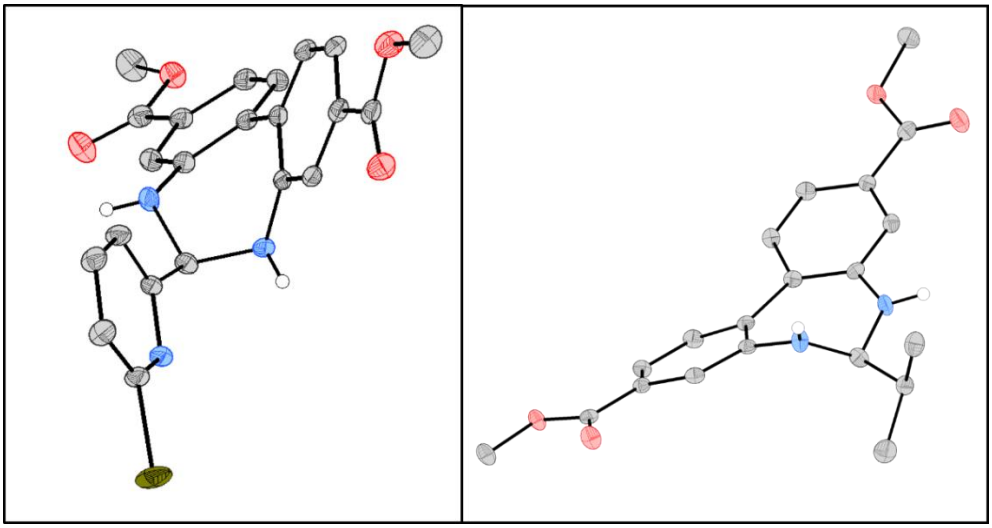

Figure 3. Single crystal XRD structures of **2** and **6** with ellipsoids at 50% probability. Hydrogen atoms other than the ones attached to nitrogen atoms were omitted for clarity.

The pyridine is oriented almost orthogonally to the biphenyl backbone in the single crystal XRD structure of **2** (Figure 3, left). Contrary to that, the crystal structures reported by Tomar *et al.*,[7] show little deviation from planarity between R and the R'-substituted phenyl ring that it is connected to via the imine-type nitrogen. This is consistent with an aromatic system spanning from the backbone to the attached aromatic ring in fully unsaturated dibenzo[*d,*f][1,3]diazepines. In the dibenzo[*d,f*]-1,2-dihydro-[1,3]diazepines however, the conjugation is broken, as the aromatic backbone is connected via sp^3 hybridized atoms to the R group.

A copper complex bearing **1** as a ligand (**1-CuI**) was obtained when reacting thiazole aldehyde with the diamine and CuI. Recrystallization of **1-CuI** from acetonitrile yielded single crystals suitable for single crystal X-Ray diffraction. The obtained structure shows **1** coordinating copper through the nitrogen atom in the thiazole. The tetrahedral coordination environment (τ_4= 0.89)[25] around copper is completed by two molecules of acetonitrile and two bridging iodides, creating a dimeric structure (see Figure 4).

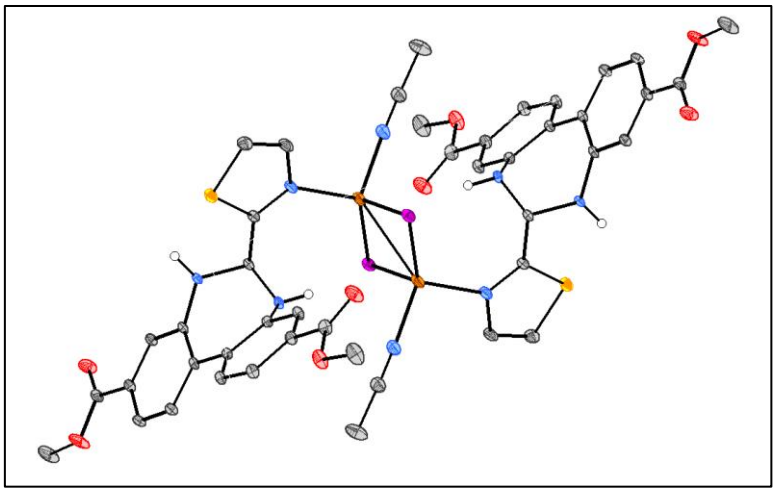

Figure 4. Single Crystal XRD structure of a dimeric structure composed of dibenzodiazepine **1**, CuI and acetonitrile. Each copper atom is ligated by bridging iodines, the nitrogen atom of the thiazole and one solvent molecule. The hydrogen atoms (with exception of the N**H**) and two non-coordinating acetonitrile molecules are removed for clarity. Selected bond lengths [Å]: Cu–Cu: 2.8281(4); Cu1–N3: 2.0618(14); Cu1–N4(MeCN): 2.0199(16); I1–Cu1: 2.5795(2); I1–Cu1: 2.7038(3).

This finding shows that the R-group can enable the coordination to a metal. Given the ease of diazepine formation and their reported application in macromolecule functionalisation,[19–22] it can be envisioned to use the diazepine moiety as an anchoring point for metal-binding sites in macromolecules.

Photophysical Properties

As dibenzo[d,f]-1,2 dihydro-[1,3]diazepines and dibenzo[d,f][1,3]diazepines have been reported to be fluorescent,[5,7,19] we wanted to further investigate the photophysical properties of compounds **1**-**7**. The UV/Vis spectra of the diazepines and the 2,2'-diaminobiphenyl starting material in acetonitrile are shown in Figure 5. While all compounds showed strong absorption in the UV region, the diazepines' absorption bands also trail into the visible region, resulting in coloured solutions. In addition to one band at ca. 340 nm, compounds **2**, **3**, **4**, **6**, and **7** display a band around 380 nm. Intriguingly, the UV/Vis spectrum of the only diazepine with an aliphatic 2-substitution, the isopropyl bearing diazepine **6**, resembles the spectra of diazepines **2, 3, 4,** and **7**, which all bear six-membered heterocycles as R-groups. The only apparent difference is the higher intensity of the near-visible band for **6** compared to the others.

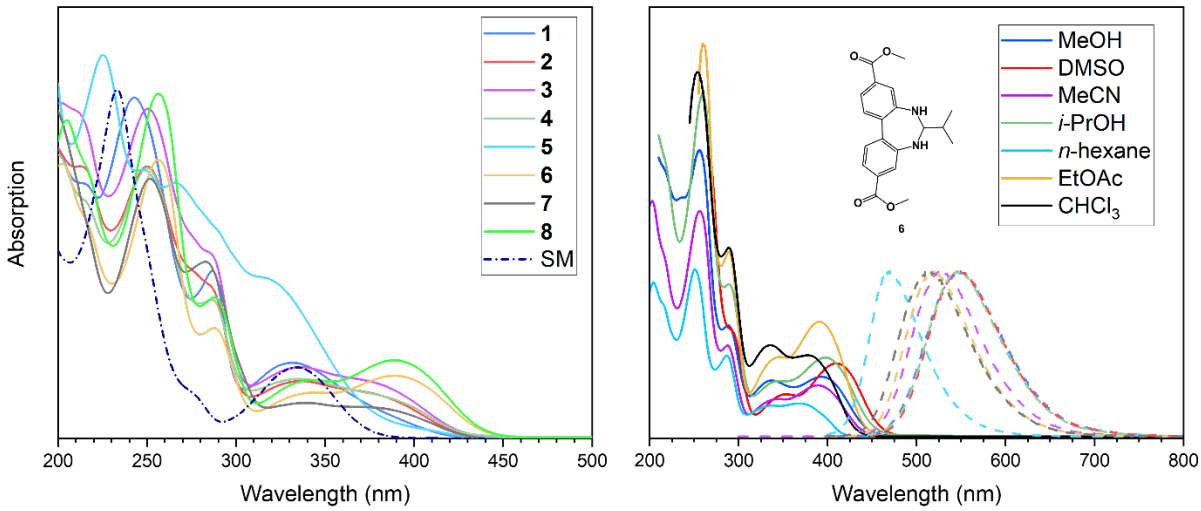

Figure 5. Left: UV/Vis absorption spectra of **1**-**8** in MeCN (ca. 30 µM). Right: UV/Vis absorption (solid lines) and emission spectra (dashed lines) of **6** in a series of solvents.

We found all solutions containing diazepines to be fluorescent, except **15**, bearing a nitro substituent. This can be explained by the known ability of nitro-groups to quench fluorescence.[26] The emission colour of compounds **1**-**7** depends on the solvent. We selected compound **6** to further investigate this property, as it showed the best solubility in most solvents. The absorbance and emission spectra of **6** in a series of solvents are shown in Figure 5. The absorption and emission maxima, as well as the resulting Stoke shifts ($\Delta\bar{\upsilon}$), can be found in

Table 3. As expected for a polar fluorophore, the Stoke shift increases with the polarity of the solvent.[27]

Table 3. Absorption maxima, emission, stokes shifts and fluorescence quantum yield of **6** in different solvents.

Solvent	λ_1 (nm)	λ_2 (nm)	λ_3(nm)	λ_4 (nm)	λ_5 (nm)	λ_{em}(nm)	$\Delta\bar{\nu}$ (cm^{-1})	Φ_F
n-Hexane	204	251	287	332	375	468	5299	0.48
$CHCl_3$	n/a	254	289	338	384	513	6548	0.72
EtOAc	n/a	261	289	341	391	520	6328	0.61
DMSO	n/a	n/a	296	349	408	549	6295	0.79
i-PrOH	n/a	260	290	345	398	547	6844	0.69
MeCN	203	254	289	341	387	530	6972	0.61
MeOH	n/a	256	289	337	395	547	7020	0.66

This solvatochromatic fluorescence was further analysed through the Lippert-Mataga equation (Eq.1), where Δf is the solvent's orientation polarizability function, μ_e and μ_g are the dipole moments of the excited and ground state of the fluorophore, h is the Planck's constant, c is the speed of light in vacuum and a is the radius of the solvent cavity occupied by the fluorophore.

$$\Delta\bar{\upsilon} = \frac{2(\mu_e-\mu_g)^2}{hca^3}\Delta f + const \qquad \text{Eq.1}$$

The Lippert-Mataga-plot shown in Figure 6 shows a good correlation between Δf and $\Delta\bar{\upsilon}$ for the series of solvents (Figure 6). The Lippert-Mataga equation does not account for solvent-specific interactions.[27]

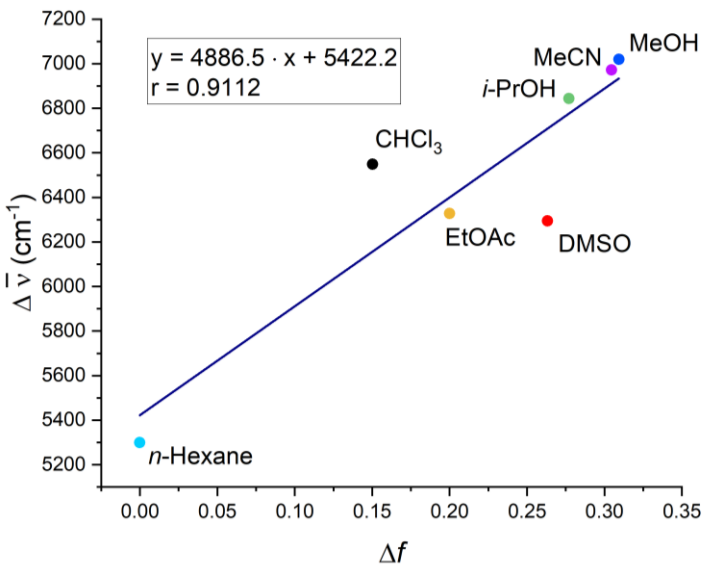

Figure 6. Lippert-Mataga plot displaying the correlation between Stoke shift of **6** (λ_5 to λ_{em}) in different solvents and the solvents' respective Δf, the orientation polarizability function.

DFT calculations were used to determine the orbitals involved in the described photophysical processes. These calculations were executed with the Gaussian16 program[28] by using the PBE0 functional and a 6-311+G** basis-set for the geometry optimization,[29,30] and the M06 functional and a def2svp basis-set for the TD-DFT calculations (see SI for further details).[31,32] Implicit solvation using the SMD method was added in both geometry optimization and TD-DFT calculations.[33] The optimized geometry of **6** was in excellent agreement with the crystal structure. An RMSD for all carbon-carbon and carbon-hetero atom bond distances of 0.009 Å was obtained. The twist of the backbone was found to be 26° compared to 32° in the crystal structure. The TD-DFT calculations are in excellent agreement with the bands observed experimentally in both UV and visible regions, shown in Figure 7. The MAE for the solvents range from the lowest deviation of 4 nm for *n*-hexane, to the highest deviation of 17 nm for DMSO (See SI for further details). All calculated bands are blue shifted compared to the ones observed experimentally.

Figure 8 shows the energy and shapes of the molecular orbitals, as well as the values for the HOMO-LUMO gap for **6** in different solvents. The HOMO–2, HOMO–1 and HOMO orbitals are localised on the

diazepine moiety, while the LUMO and LUMO+1 are distributed over the whole backbone, including the esters. Furthermore, the LUMO+2 and LUMO+3 are located on either phenyl ring on the backbone. The HOMO-LUMO gap for **6** spans from 4.16 eV in *n*-hexane to 4.03 eV in MeOH. Positive solvatochromism originates from the decreased HOMO-LUMO gap as the dipole moment of the ground state is smaller than that of the excited state.[34] Therefore, the DFT calculations are in line with the experimental finding of the bathochromic shift of λ_{max} in polar solvents (Table 3).

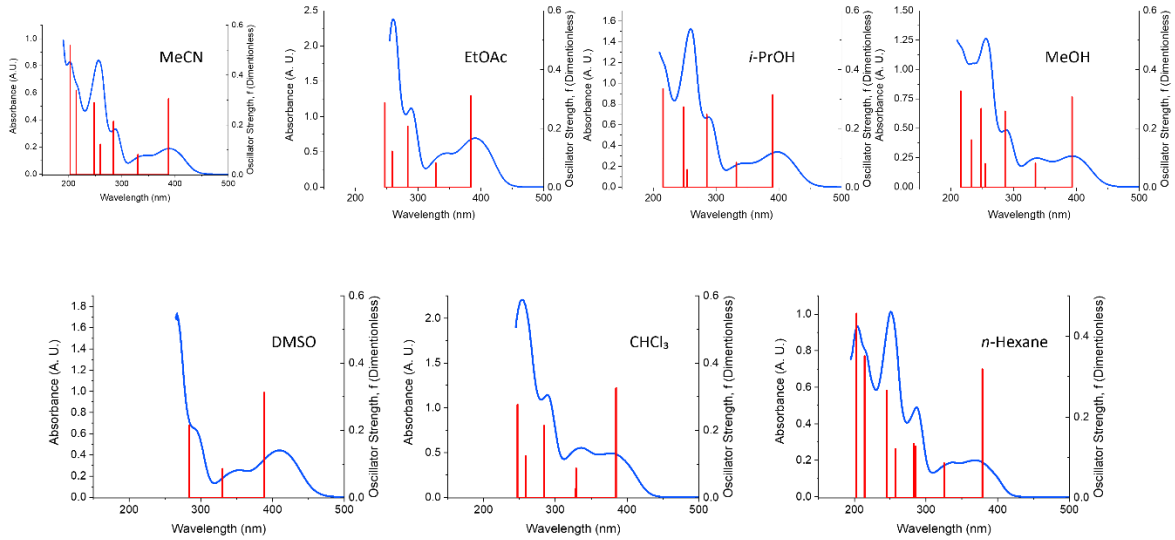

Figure 7. Experimental spectra of **6** in different solvents (blue curve) and the main TD-DFT(M06) electronic excitations (red bars).

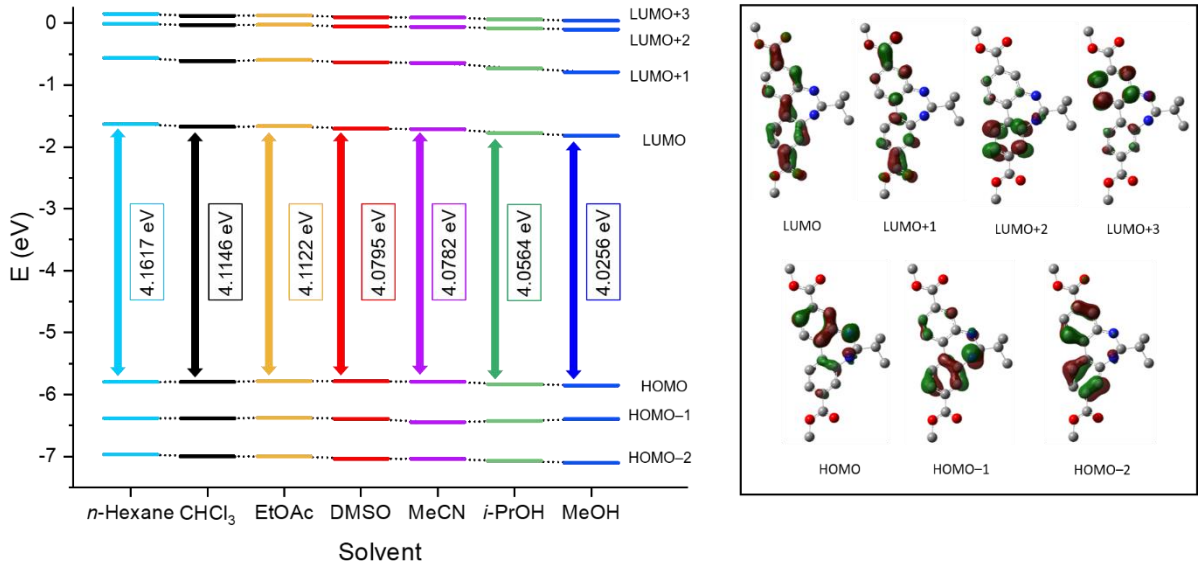

Figure 8. Left: calculated molecular orbitals for **6** in different solvents with their respective HOMO-LUMO gap values. Right: Frontier orbitals involved in the main TD-DFT(M06) electronic transitions, see Table 4 for more details. Hydrogens were omitted for clarity. The isovalue is 0.05 a.u.

For each of the main electronic transitions of **6**, the involved molecular orbitals are listed in Table 4. The λ_2 excitation is an overlap of two transitions, each transferring electron density from the diazepine moiety to the phenyl rings. The absorption at the longest wavelength (λ_5 = 375 - 408 nm) is caused by the HOMO → LUMO transition. As a result, the orbitals shift from localized in the diazepine moiety to the whole biphenyl ester backbone. The contribution of the ester in the excited state is interesting for the use of these compounds in the synthesis of conducting materials.[7,20] The excitation at λ_4 = 332 - 349 nm stems from the HOMO–1 → LUMO transition, which also involves an increase in delocalization from the nitrogen and the phenyl rings, to the whole biphenyl backbone.

Table 4. Excitation wavelength (λ_{Exc}), the oscillator strength (*f*) and the molecular orbitals involved (MOs) for the main electronic excited states for different compounds in MeCN.

Compound	λ_{Exc} (nm)	*f*	MOs
SM	229	0.1430	HOMO – 1 → LUMO + 3
	236	0.1884	HOMO – 1 → LUMO + 2
	261	0.2550	HOMO – 2 → LUMO
	324	0.1215	HOMO – 1 → LUMO
	335	0.2682	HOMO → LUMO
6	203	0.5172	HOMO – 2 → LUMO + 2
	248	0.2889	HOMO → LUMO + 3
	260	0.1225	HOMO → LUMO + 2
	284	0.2143	HOMO – 2 → LUMO
	330	0.0814	HOMO – 1 → LUMO
	388	0.3047	HOMO → LUMO

In the starting material (**SM**), the HOMO → LUMO and the HOMO–1 → LUMO transitions are close in energy, giving rise to the band at λ = 334 nm (see SI, Figure S39). In the diazepine however, the lone pair of one nitrogen is in conjugation with the phenyl ring. This results in a less energetic transition from that nitrogen to the backbone. Thereby, an additional band is found that causes the absorption in the visible range (Figure 5).

Conclusions

A series of aldehydes was screened for the preparation of dibenzo[*d,f*]-1,2-dihydro-[1,3]diazepines. The results highlight an intricate balance of imine and diazepine formation that is sensitive to the aldehyde structure, the nature of the Lewis acid and temperature. For the first time, we have shown that dibenzo[*d,f*]-1,2-dihydro-[1,3]diazepines present solvatochromatic fluorescence. TD-DFT calculations showed that the orbital involved in the excited state has a strong contribution of the biphenyl ester backbone. These results are promising for using diazepines in applications where luminescence is implemented to indicate changes in the molecular environment.

Experimental

Synthesis

All aldehydes, solvents and $Zn(OAc)_2{\cdot}2H_2O$ were purchased from commercial sources and used without further purification. Dimethyl 2,2'-diaminobiphenyl-4,4'-dicarboxylate was synthesized according to literature.[18] Experimental procedures,

spectral data, and details concerning instruments, single crystal XRD data and computations can be found in the SI.

Example **6**.

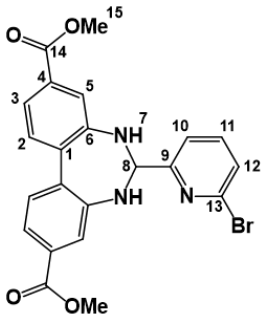

2

Dimethyl 2,2'-diaminobiphenyl-4,4'-dicarboxylate (100 mg, 0.33 mmol, 1 equiv.) and 6-bromopicolinaldehyde (68 mg, 0.36 mmol, 1.1 equiv.) were mixed in methanol (4 mL) and left to stir at room temperature overnight. The precipitate was filtrated, and the crude product was left to dry overnight yielding **2** as a white solid (99 mg, 0.213 mmol, 64%). M.p. 200-202 °C. ^{1}H-NMR (*d*$_6$-DMSO, 600 MHz) δ 7.65 (t, *J* = 7.7 Hz, 1H, H11), 7.56 (d, *J* = 8.2 Hz, 2H, H2), 7.53 (d, *J* = 1.7 Hz, 3H, H5), 7.52 (d, *J* = 7.7 Hz, 2H, H12), 7.47 (dd, *J* = 1.8, 8.2 Hz, 2H, H3), 7.31 (d, *J* = 7.7 Hz, 1H, H10), 6.67 (d, *J* = 4.0 Hz, 2H, H7), 5.63 (t, *J* = 4.0 Hz, 1H, H8), 3.83 ppm (s, 6H, H15); ^{13}C-NMR (*d*$_6$-DMSO, 151 MHz) δ 166.1 (C14), 162.2 (C9), 146.4 (C1), 140.4 (C13), 139.8 (C11), 132.4 (C6), 130.0 (C2), 128.9 (C4), 127.1 (C12), 121.2 (C5), 120.8 (C3), 120.5 (C10), 77.8 (C8), 51.9 ppm (C15);^{15}N{^{1}H} NMR (*d*$_6$-DMSO, 600 MHz): –69.8 (N_{py}), –301.8 (NH^7); LRMS (ESI/Q-TOF): m/z (%): 490.037 (100) $[M + Na]^+$, 492.035 (98) $[(M + 2) + Na]^+$; HRMS (ESI/Q-TOF) m/z: $[M + Na]^+$ Calcd. for $C_{22}H_{18}BrN_3O_4Na$ 490.0373; Found 490.0373. Anal. Calcd for $C_{22}H_{18}BrN_3O_4$: C, 56.42; H, 3.87; N, 8.97. Found: C, 56.40; H, 3.86; N, 8.95 %. UV/Vis (MeCN): λ_{max} 212.0 (29 000), 249.5 (29 300), 286.5 (sh, 16 300), 336.0 (6 300), 381.0 nm (sh, 4 800 $M^{-1}cm^{-1}$).

Acknowledgements

The authors are grateful to NMBU and Ole Golten for help and access to their instrument for fluorescence measurements. The authors thank Marita Clausen for generous access to the UV/Vis instrument. The authors thank Knut Hylland for the helpful discussions. This work was supported by the Research Council of Norway through the Norwegian NMR Package in 1994, through the Norwegian NMR Platform, NNP (226244/F50) and through the Hylleraas Centre for Quantum Molecular Sciences (project number 262695) and the Norwegian Metacenter for Computational Science (NOTUR, nn4654k).

References

1 J. H. Ryan, J. L. Green, C. Hyland, J. A. Smith and C. C. Williams, in *Progress in Heterocyclic Chemistry*, eds. G. W. Gribble and J. A. Joule, Elsevier, 2011, vol. 23, pp. 465–504.
2 C. E. Griffin, A. M. Kaye, F. R. Bueno and A. D. Kaye, *Ochsner J*, 2013, **13**, 214–223.
3 Y. Malki, L. T. Maillard and N. Masurier, *Eur. J. Org. Chem.*, , DOI:10.1002/ejoc.202100492.
4 T. A. Tikhonova, K. A. Lyssenko, I. V. Zavarzin and Y. A. Volkova, *J. Org. Chem.*, 2019, **84**, 15817–15826.
5 S. Montanaro, I. A. Wright, A. S. Batsanov and M. R. Bryce, *J. Org. Chem.*, 2018, **83**, 12320–12326.
6 R. Weiss and L. Chledowski, *Monatsh. Chem.*, 1934, **65**, 357–366.
7 M. Tomar, N. T. Lucas, K. Müllen and J. Jacob, *Tetrahedron Lett.*, 2013, **54**, 5883–5885.
8 Y. Malki, J. Martinez and N. Masurier, *Med. Res. Rev.*, 2021, **41**, 2247–2315.
9 F. M. Leonik, I. Ghiviriga and N. A. Horenstein, *Tetrahedron*, 2010, **66**, 5566–5572.

10 L. Racané, H. Čičak, Z. Mihalić, G. Karminski-Zamola and V. Tralić-Kulenović, *Tetrahedron*, 2011, **67**, 2760–2767.
11 H. Schiff, *Justus Liebigs Ann. Chem.*, 1864, **131**, 118–119.
12 P. G. Cozzi, *Chem. Soc. Rev.*, 2004, **33**, 410–421.
13 S. M. Nelson, *Pure and Applied Chemistry*, 1980, **52**, 2461–2476.
14 R. Gumbau-Brisa, J. J. Hayward, J. D. Wallis, J. M. Rawson and M. Pilkington, *CrystEngComm*, 2016, **18**, 1892–1903.
15 J. Wang, S. Onions, M. Pilkington, H. Stoeckli-Evans, J. C. Halfpenny and J. D. Wallis, *Chem. Commun.*, 2007, 3628–3630.
16 J. Wang, J. J. Hayward, R. Gumbau-Brisa, J. D. Wallis, H. Stoeckli-Evans and M. Pilkington, *CrystEngComm*, 2015, **17**, 1159–1167.
17 W. Ried and A. Sinharay, *Chem. Ber.*, 1965, **98**, 3523–3531.
18 K. T. Hylland, S. Øien-Ødegaard, R. H. Heyn and M. Tilset, *Eur. J. Inorg. Chem.*, 2020, 3627–3643.
19 J. Cornelio, T.-Y. Zhou, A. Alkaş and S. G. Telfer, *J. Am. Chem. Soc.*, 2018, **140**, 15470–15476.
20 B.-K. Choi and T. Yamamoto, *Electrochem. Commun.*, 2003, **5**, 566–570.
21 S. Glomb, D. Woschko, G. Makhloufi and C. Janiak, *ACS Appl. Mater. Interfaces*, 2017, **9**, 37419–37434.
22 L.-Q. Wei and B.-H. Ye, *Inorg. Chem.*, 2019, **58**, 4385–4393.
23 I. Gerz, S. A. V. Jannuzzi, K. T. Hylland, C. Negri, D. S. Wragg, S. Øien-Ødegaard, M. Tilset, U. Olsbye, S. DeBeer and M. Amedjkouh, *Eur. J. Inorg. Chem.*, 2021, 4762–4775.
24 J. Mason, *Chem. Rev.*, 1981, **81**, 205–227.
25 L. Yang, D. R. Powell and R. P. Houser, *Dalton Trans.*, 2007, 955–964.
26 M.-C. Chen, D.-G. Chen and P.-T. Chou, *ChemPlusChem*, 2021, **86**, 11–27.
27 J. R. Lakowicz, Ed., in *Principles of Fluorescence Spectroscopy*, Springer US, Boston, MA, 2006, pp. 205–235.
28 M. J. Frisch, G. W. Trucks, H. B. Schlegel, G. E. Scuseria, M. A. Robb, J. R. Cheeseman, G. Scalmani, V. Barone, G. A. Petersson, H. Nakatsuji, X. Li, M. Caricato, A. V. Marenich, J. Bloino, B. G. Janesko, R. Gomperts, B. Mennucci, H. P. Hratchian, J. V. Ortiz, A. F. Izmaylov, J. L. Sonnenberg, D. Williams-Young, F. Ding, F. Lipparini, F. Egidi, J. Goings, B. Peng, A. Petrone, T. Henderson, D. Ranasinghe, V. G. Zakrzewski, J. Gao, N. Rega, G. Zheng, W. Liang, M. Hada, M. Ehara, K. Toyota, R. Fukuda, J. Hasegawa, M. Ishida, T. Nakajima, Y. Honda, O. Kitao, H. Nakai, T. Vreven, K. Throssell, J. A. Montgomery Jr., J. E. Peralta, F. Ogliaro, M. J. Bearpark, J. J. Heyd, E. N. Brothers, K. N. Kudin, V. N. Staroverov, T. A. Keith, R. Kobayashi, J. Normand, K. Raghavachari, A. P. Rendell, J. C. Burant, S. S. Iyengar, J. Tomasi, M. Cossi, J. M. Millam, M. Klene, C. Adamo, R. Cammi, J. W. Ochterski, R. L. Martin, K. Morokuma, O. Farkas, J. B. Foresman and D. J. Fox, *Gaussian 16, Revision C.01*, Gaussian Inc., Wallingford CT, 2016.
29 C. Adamo and V. Barone, *J. Chem. Phys.*, 1999, **110**, 6158–6170.
30 R. Krishnan, J. S. Binkley, R. Seeger and J. A. Pople, *J. Chem. Phys.*, 1980, **72**, 650–654.
31 Y. Zhao and D. G. Truhlar, *Theor Chem Account*, 2008, **120**, 215–241.
32 F. Weigend and R. Ahlrichs, *Phys. Chem. Chem. Phys.*, 2005, **7**, 3297–3305.
33 A. V. Marenich, C. J. Cramer and D. G. Truhlar, *J. Phys. Chem. B*, 2009, **113**, 6378–6396.
34 Principles and Applications of Solvatochromism - Shalini Nigam, Sarah Rutan, 2001, https://journals.sagepub.com/doi/10.1

366/0003702011953702, (accessed April 26, 2022).

Table of Contents (TOC) Graphic

Supporting information for

Synthesis and Luminescence of Dibenzo[*d,f*]-1,2-dihydro-[1,3]diazepines

Isabelle Gerz, Rafael Cortez Sgroi Pupo, David S. Wragg, Ainara Nova, Mohamed Amedjkouh

Contents

Synthesis and Luminescence of Dibenzo[*d,f*]-1,2-dihydro-[1,3]diazepines 1
General considerations 2
Synthesis and characterization of compounds 3
Compound 1 3
Compound 2 6
Compound 3 9
Compound 4 12
Compound 5 15
Compound 6 18
Compound 7 21
Compound 8 24
Compound 1D 27
Compound 17D 29
Crystallographic data 31
Computational details 32
Geometry optimization benchmarking 32
Functional benchmarking 35
TD-DFT calculations 38
Optimized geometries and energies (Hartree) 39
References 41

General considerations

Dimethyl 2,2'-diaminobiphenyl-4,4'-dicarboxylate was synthesized from dimethyl biphenyl-4,4'-dicarboxylate following the procedure developed by Hylland *et al*.[1]

Melting points are uncorrected and were measured on a Stuart SMP10 instrument. All spectra were recorded using a Bruker AVI600 NMR spectrometer and a AVII600 NMR spectrometer, at 298K using d_6-DMSO as a solvent. All spectra were calibrated using the solvent residual peak at 2.50 ppm for ^{1}H-NMR and at 39.52 ppm for ^{13}C-NMR according to literature.[2] ^{15}N NMR spectra are referenced to an external nitromethane standard. All resonances were assigned according to 2D NMR techniques.

MS (ESI) measurements were recorded on a Bruker maXis II ETD spectrometer. Elemental analysis was performed by Mikroanalytisches Laboratorium Kolbe, Oberhausen, Germany. UV-Visible measurements were performed on a Specord 200 Plus instrument. All molar extinction coefficients were calculated by linear regression of the absorbance vs concentration, using at least three different concentrations, and all linear regression had a R^2 of over 0.993.

Single crystal diffraction data were acquired on a Bruker D8 Venture equipped with a Photon 100 detector, using Mo Kα radiation (λ = 0.71073 Å) from an Incoatec iμS microsource. Data reduction was performed with the Bruker Apex3 Suite, the structures were solved with ShelXT and refined with ShelXL.[3,4] Olex2 was used as user interface.[5] The cif files were edited with enCIFer v. 1.4.6 and molecular graphics were produced with Diamond v. 4.6.2.

Synthesis and characterization of compounds

Compound 1

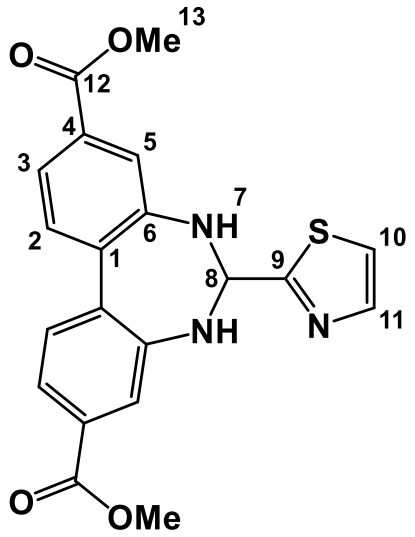

1

Dimethyl 2,2'-diaminobiphenyl-4,4'-dicarboxylate (100 mg, 0.33 mmol, 1 equiv.), zinc acetate dihydrate (73 mg, 0.33 mmol, 1 equiv.) and thiazole-2-carbaldehyde (40 mg, 0.36 mmol, 1.1 equiv.) were stirred in methanol (4 mL) at room temperature for 2 days. The precipitate was filtered and dried in a vacuum oven at 60 °C for three hours yielding **1** as a white solid (113 mg, 0.285 mmol, 86%). M.p. 206 - 207 °C; ^{1}H-NMR (*d*$_6$-DMSO, 600 MHz) δ 7.77 (d, J = 3.2 Hz, 1H, H11), 7.56 - 7.52 (m, 4H, H2 and H5), 7.51 - 7.49 (m, 3H, H10 and H3), 6.72 (d, J = 4.2 Hz, 2H,H7), 6.05 (t, J = 4.3 Hz, 1H, H8), 3.83 ppm (s, 6H, H13); ^{13}C-NMR (*d*$_6$-DMSO, 151 MHz) δ 174.1 (C9), 166.1 (C12), 145.0 (C1), 142.5 (C11), 134.4 (C4), 129.7 (C2), 129.2 (C6), 122.0 (C5), 121.9 (C3), 120.1 (C10), 76.8 (C8), 52.1 ppm (C13); ^{15}N{^{1}H} NMR (*d*$_6$-DMSO, 600 MHz): -64.0 (N_{th}), -301.8 ppm (NH^7); LRMS (ESI/Q-TOF) m/z (%): 418.083 (100) $[M + Na]^+$; HRMS (ESI/Q-TOF) m/z: $[M + Na]^+$ Calcd. for $C_{20}H_{17}N_3O_4Na$ 418.0832; Found 418.0832. Anal. Calcd for $C_{20}H_{17}N_3O_4$: C, 60.75; H, 4.33; N, 10.63. Found: C, 60.66; H, 4.31; N, 10.56 %. UV-Visible (MeCN): λ_{max} 243.0 (33 200), 286.5 (16 300), 332.0 nm (7 430 $M^{-1}cm^{-1}$).

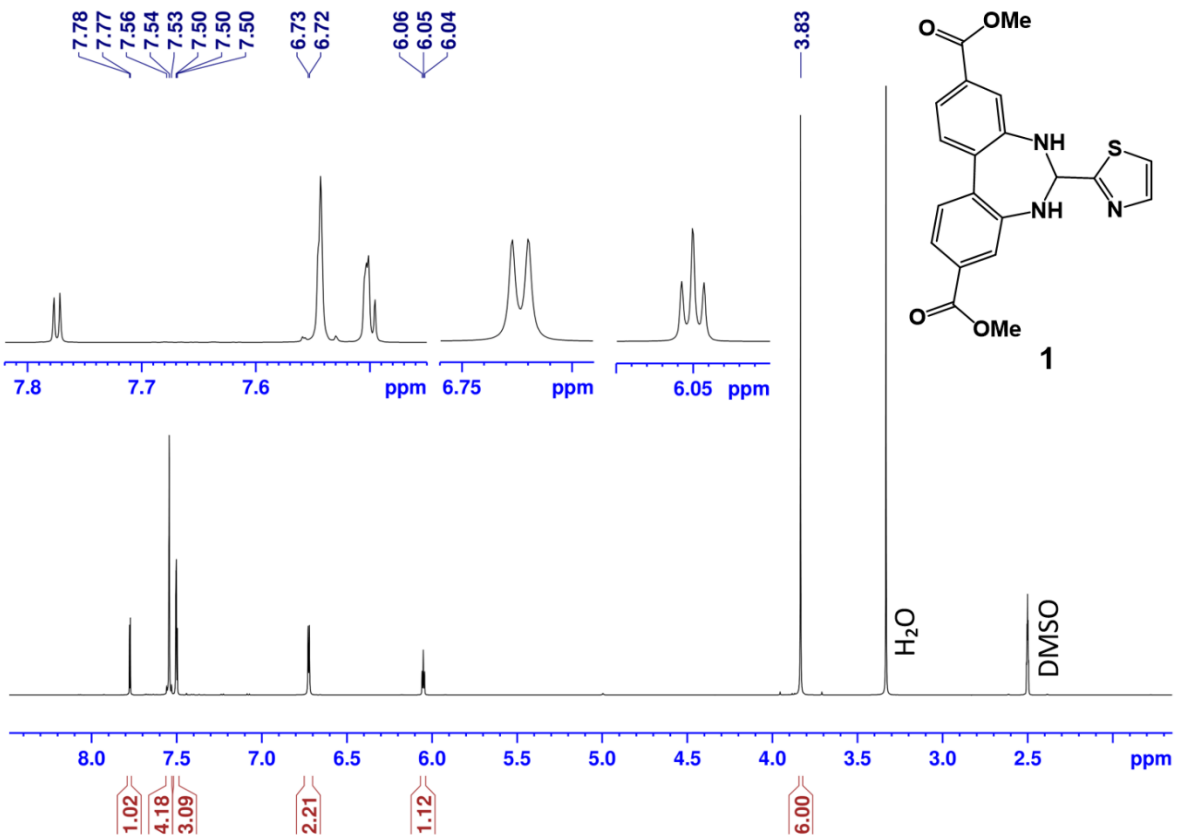

Figure S1 ^{1}H-NMR spectrum for compound **1** (600 MHz, d_6-DMSO).

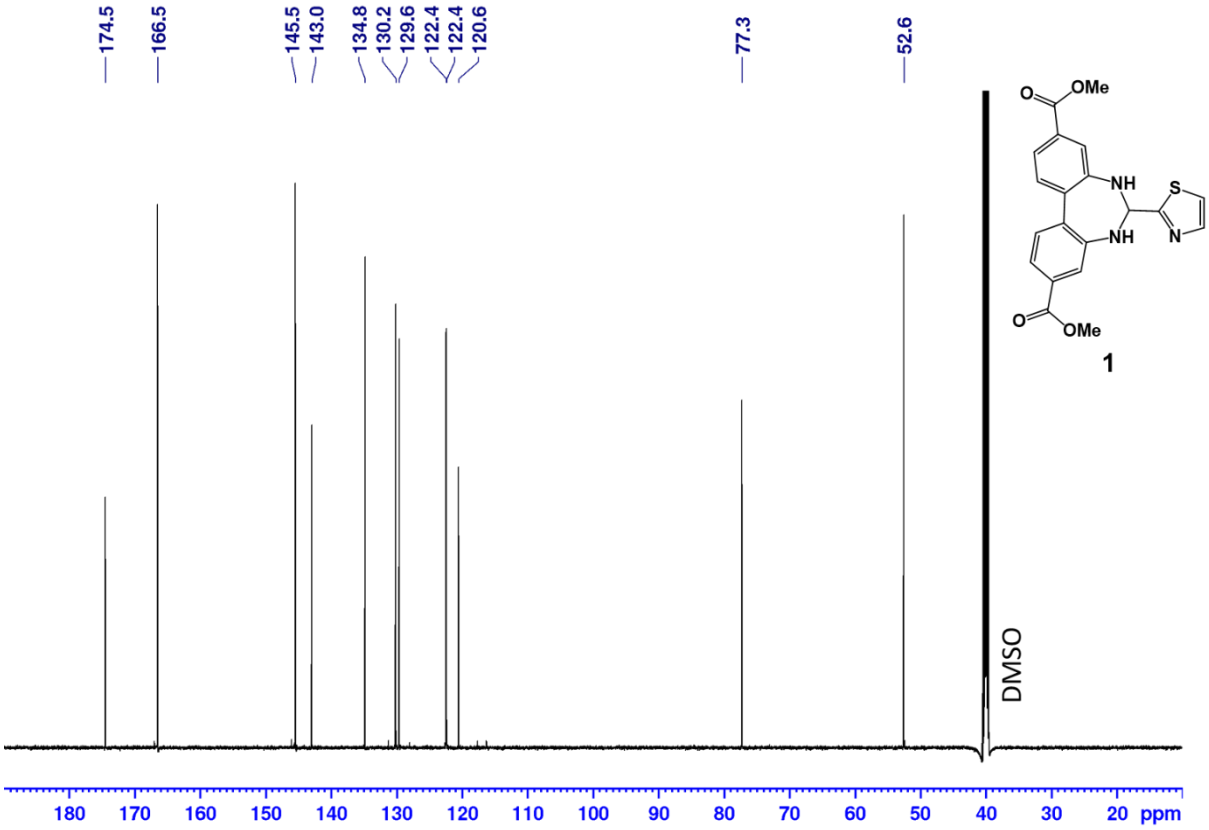

Figure S2 ^{13}C-NMR spectrum for compound **1** (600 MHz, d_6-DMSO).

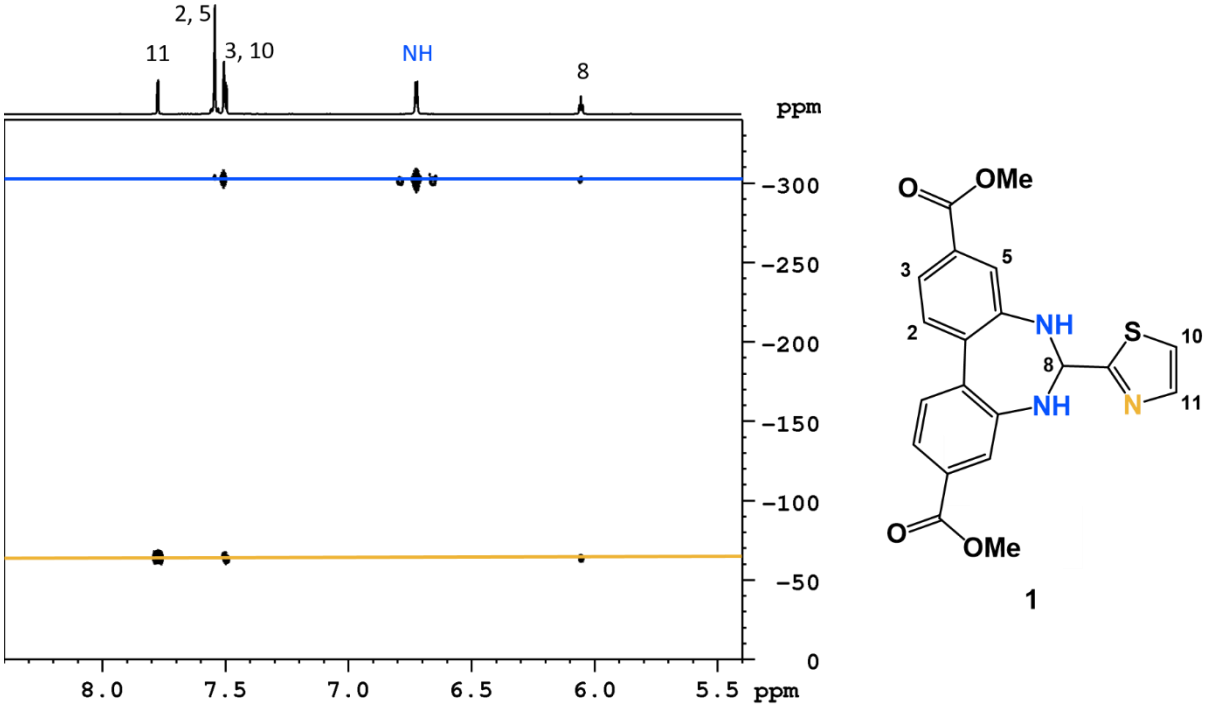

Figure S3 ^{1}H-^{15}N HMBC for compound **1** (600 MHz, d_6-DMSO).

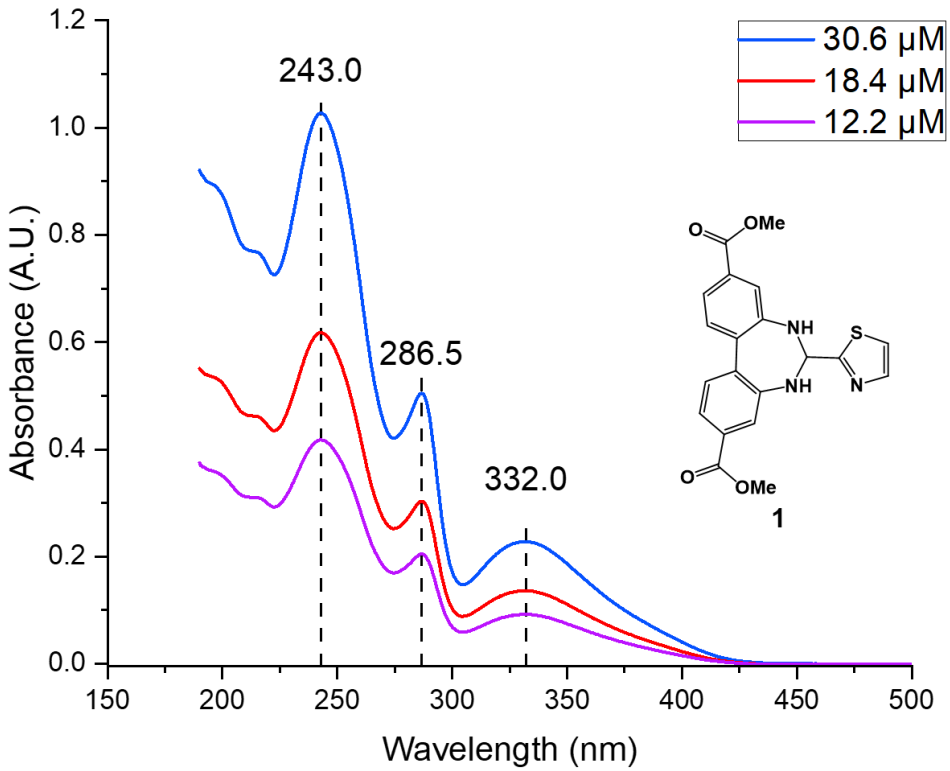

Figure S4 UV-Visible spectra of **1** at different concentrations in acetonitrile.

Compound 2

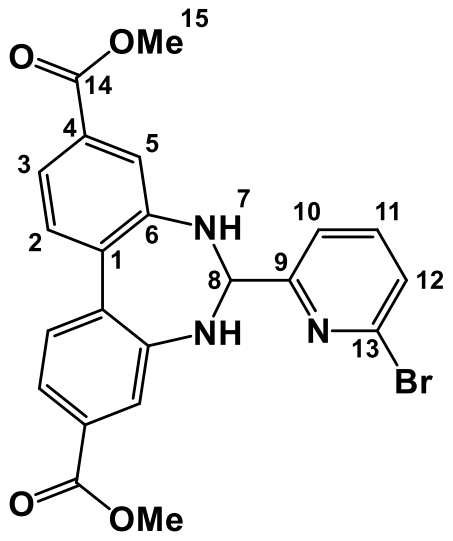

2

Dimethyl 2,2'-diaminobiphenyl-4,4'-dicarboxylate (100 mg, 0.33 mmol, 1 equiv.) and 6-bromopicolinaldehyde (68 mg, 0.36 mmol, 1.1 equiv.) were mixed in methanol (4 mL) and left to stir at room temperature overnight. The precipitate was filtrated, and the crude product was left to dry overnight yielding **2** as a white solid (99 mg, 0.213 mmol, 64%). M.p. 200 – 202 °C. ^{1}H-NMR (*d*$_6$-DMSO, 600 MHz) δ 7.65 (t, *J* = 7.7 Hz, 1H, H11), 7.56 (d, *J* = 8.2 Hz, 2H, H2), 7.53 (d, *J* = 1.7 Hz, 3H, H5), 7.52 (d, *J* = 7.7 Hz, 2H, H12), 7.47 (dd, *J* = 1.8, 8.2 Hz, 2H, H3), 7.31 (d, *J* = 7.7 Hz, 1H, H10), 6.67 (d, *J* = 4.0 Hz, 2H, H7), 5.63 (t, *J* = 4.0 Hz, 1H, H8), 3.83 ppm (s, 6H, H15); ^{13}C-NMR (*d*$_6$-DMSO, 151 MHz) δ 166.1 (C14), 162.2 (C9), 146.4 (C6), 140.4 (C13), 139.8 (C11), 132.4 (C1), 130.0 (C2), 128.9 (C4), 127.1 (C12), 121.2 (C5), 120.8 (C3), 120.5 (C10), 77.8 (C8), 51.9 ppm (C15);^{15}N{^{1}H} NMR (*d*$_6$-DMSO, 600 MHz): -69.8 (N_{py}), -301.8 (NH^7); LRMS (ESI/Q-TOF): m/z (%): 490.037 (100) $[M + Na]^+$, 492.035 (98) $[(M + 2) + Na]^+$; HRMS (ESI/Q-TOF) m/z: $[M + Na]^+$ Calcd. for $C_{22}H_{18}BrN_3O_4Na$ 490.0373; Found 490.0373. Anal. Calcd for $C_{22}H_{18}BrN_3O_4$: C, 56.42; H, 3.87; N, 8.97. Found: C, 56.40; H, 3.86; N, 8.95 %. UV-Visible (MeCN): λ_{max} 212.0 (29 000), 249.5 (29 300), 286.5 (sh, 16 300), 336.0 (6 300), 381.0 nm (sh, 4 800 $M^{-1}cm^{-1}$).

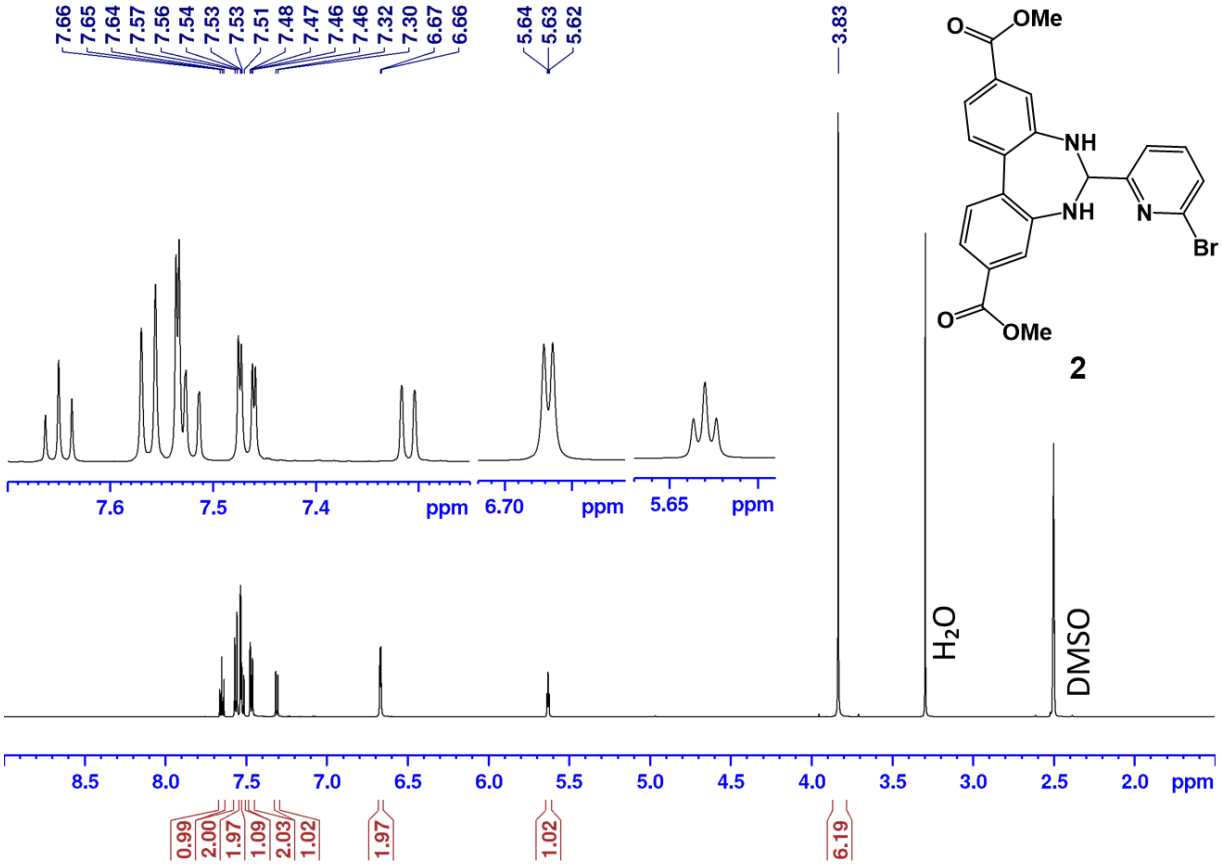

Figure S5 ^{1}H-NMR spectrum for compound **2** (600 MHz, d_6-DMSO).

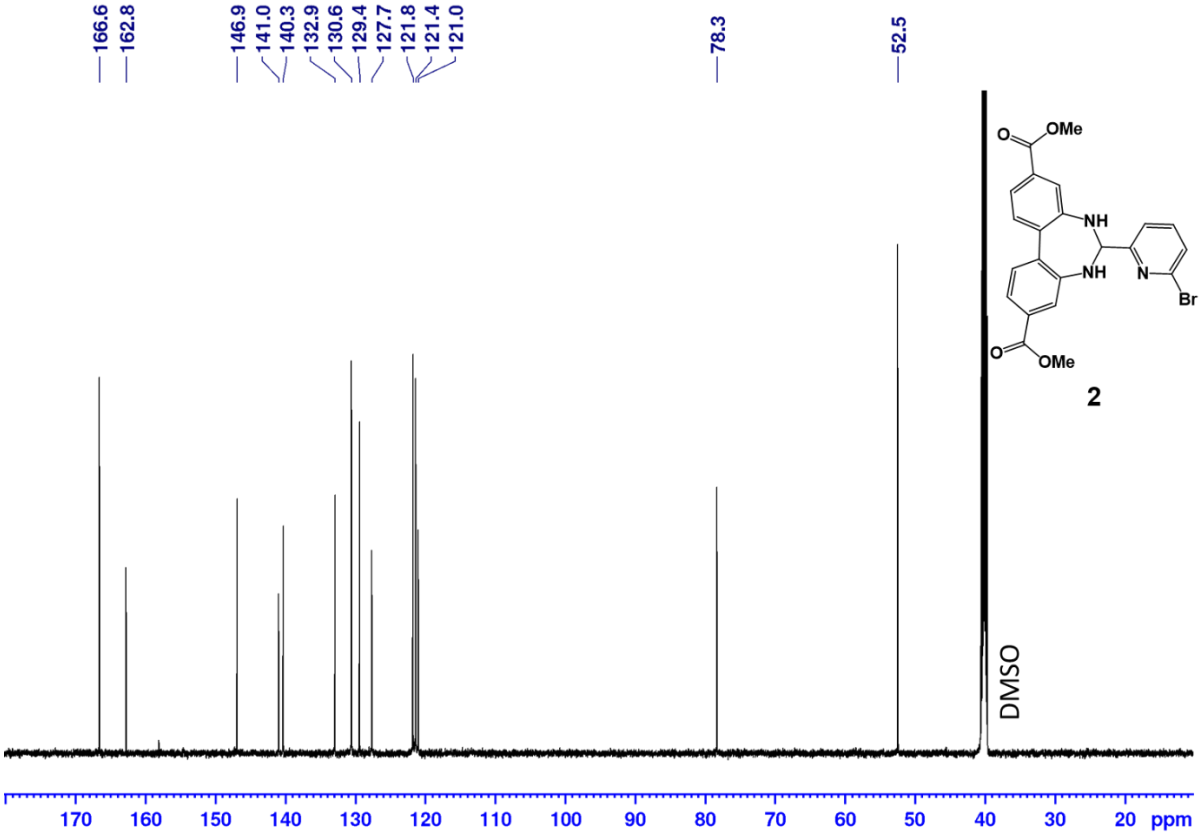

Figure S6 ^{13}C-NMR spectrum for compound **2** (600 MHz, d_6-DMSO).

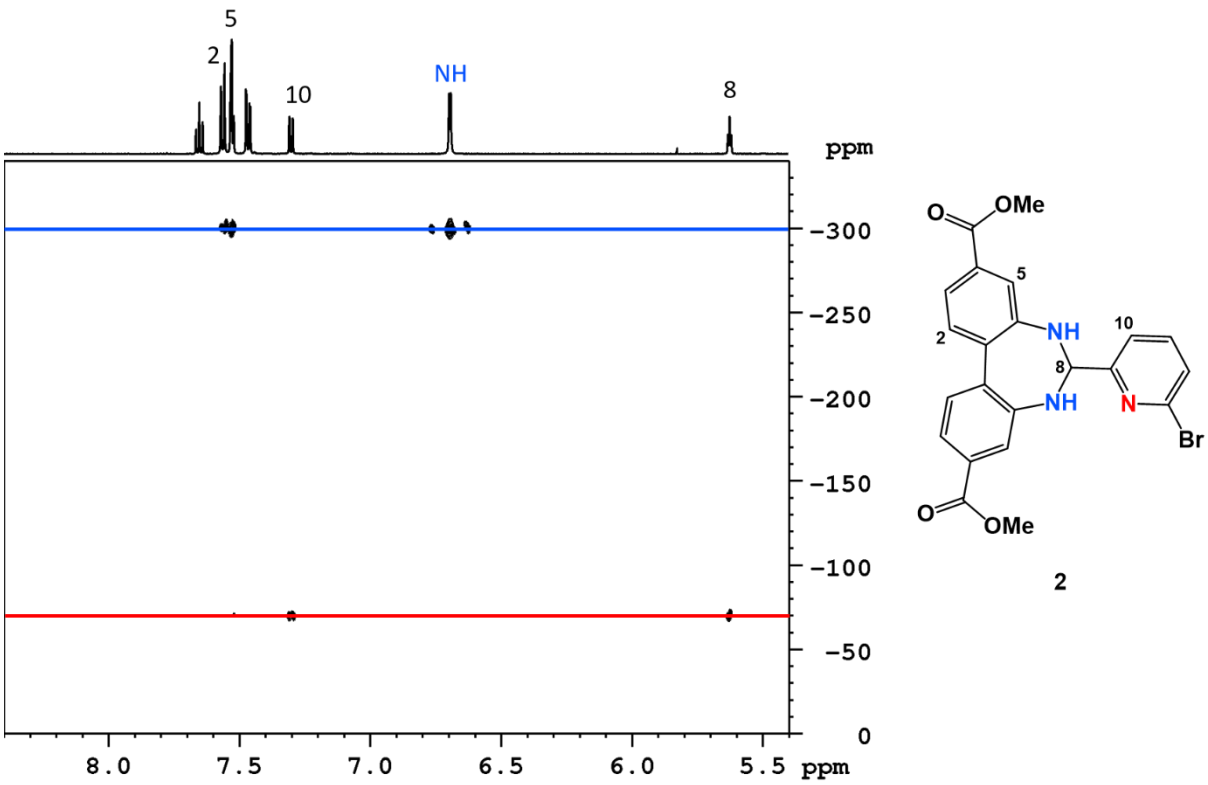

Figure S7 ^{1}H-^{15}N HMBC for compound **3** (600 MHz, d_6-DMSO).

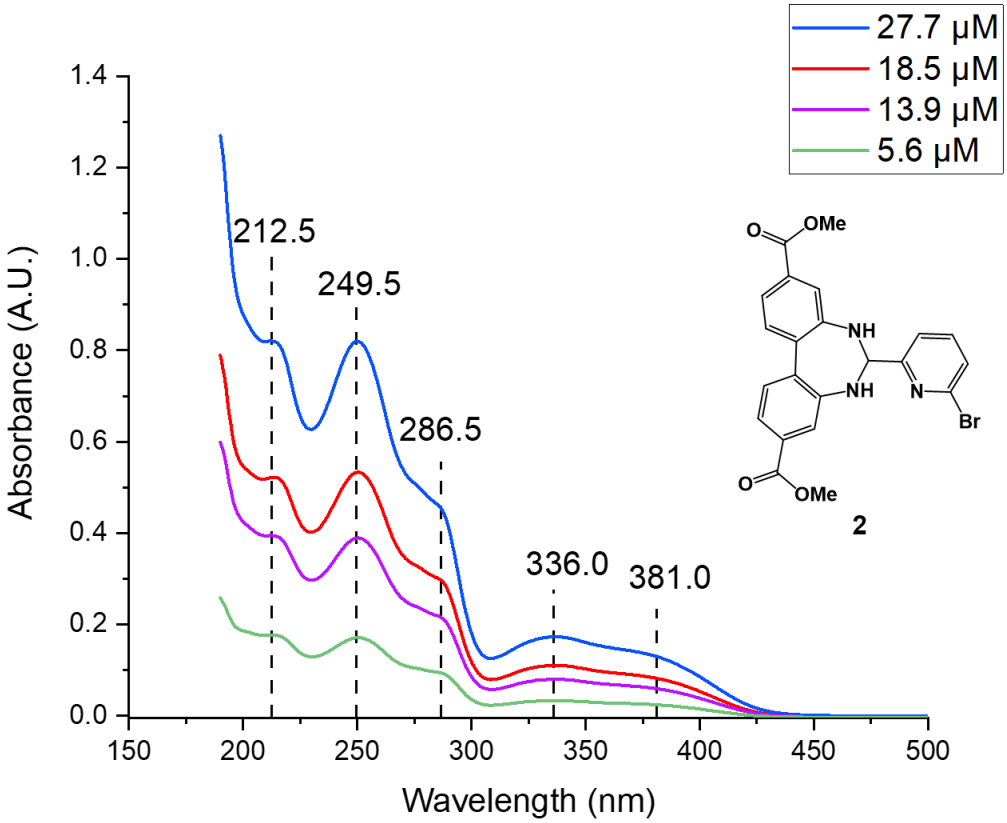

Figure S8 UV-Visible spectra of **2** at different concentrations in acetonitrile.

Compound 3

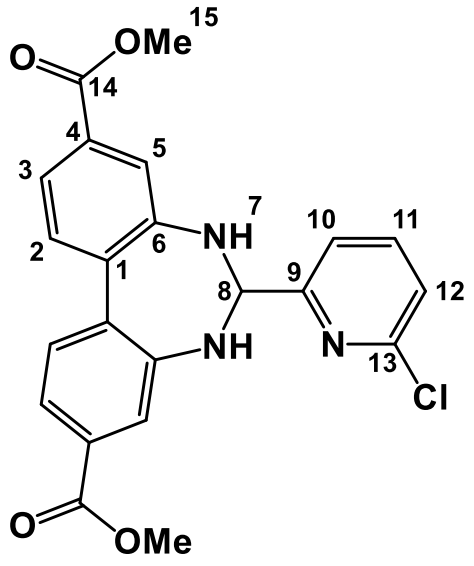

3

Dimethyl 2,2'-diaminobiphenyl-4,4'-dicarboxylate (100 mg, 0.33 mmol, 1 equiv.) and 6-Chloro-2-formylpyridine (52 mg, 0.36 mmol, 1.1 equiv.) were mixed in methanol (4 mL) and left to stir at room temperature overnight. The precipitate was filtrated, and the crude product was left to dry in a vacuum oven at 70 °C for 2h yielding **3** as a white solid (110 mg, 0.262 mmol, 79%). M.p. 202-203 °C. ^{1}H-NMR (d_6-DMSO, 600 MHz) δ 7.76 (t, *J* = 7.8 Hz, 1H,H11), 7.57 (d, *J* = 8.2 Hz, 2H,H2), 7.53 (d, *J* = 1.9 Hz, 2H,H5), 7.46 (dd, *J* = 1.8, 8.2 Hz, 2H,H3), 7.40 (d, *J* = 7.9 Hz, 1H,H12), 7.28 (d, *J* = 7.4 Hz, 1H,H10), 6.71 (d, *J* = 3.8 Hz, 2H, H7), 5.63 (t, *J* = 4.0 Hz, 1H, H8), 3.83 ppm (s, 6H, H15); ^{13}C-NMR (d_6-DMSO, 151 MHz) δ 166.1 (C14), 161.8 (C9), 149.4 (C13), 146.4 (C6), 140.2 (C11), 132.4 (C1), 130.1 (C2), 128.9 (C4), 123.4 (C12), 121.2 (C5), 120.9 (C3), 120.2 (C10), 77.8 (C8), 52.0 ppm (C15);^{15}N{^{1}H} NMR (d_6-DMSO, 600 MHz): -78.2 (N_{py}), -299.5 (NH^7); LRMS (ESI/Q-TOF): m/z (%): 446.088 (100) $[M + Na]^+$, 448.085 (32) $[(M + 2) + Na]^+$; HRMS (ESI/Q-TOF) m/z: $[M + Na]^+$ Calcd. for $C_{22}H_{18}ClN_3O_4Na$ 446.0878; Found 446.0878. Anal. Calcd for $C_{22}H_{18}ClN_3O_4$: C, 62.34; H, 4.28; N, 9.91; Cl, 8.36. Found: C, 62.33; H, 4.28; N, 9.90; Cl, 8.32 %. UV-Visible (MeCN): λ_{max} 202.0 (31 000), 250.5 (32 000), 286.5 (sh, 18 000), 338.5 (6 900), 378.0 nm (sh, 5 300 $M^{-1}cm^{-1}$).

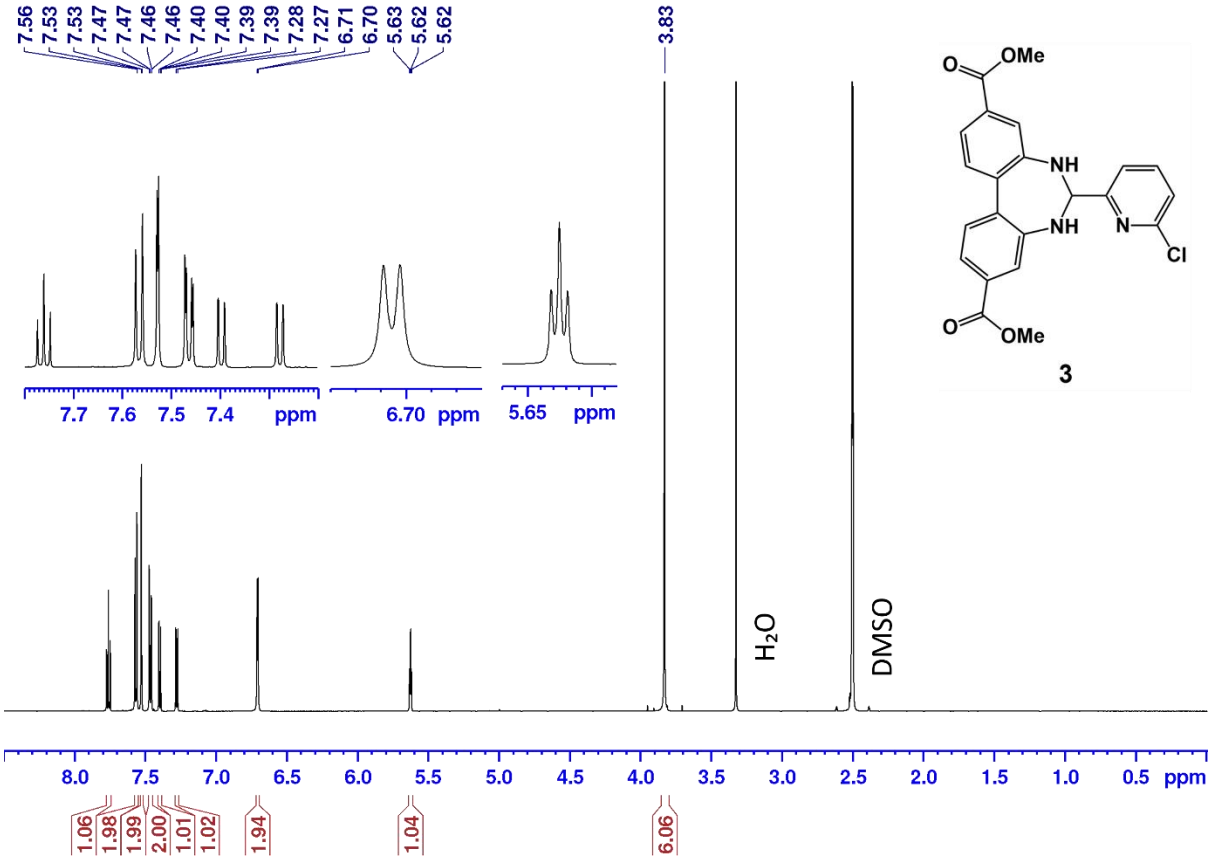

Figure S9 ^{1}H-NMR spectrum for compound **3** (600 MHz, d_6-DMSO).

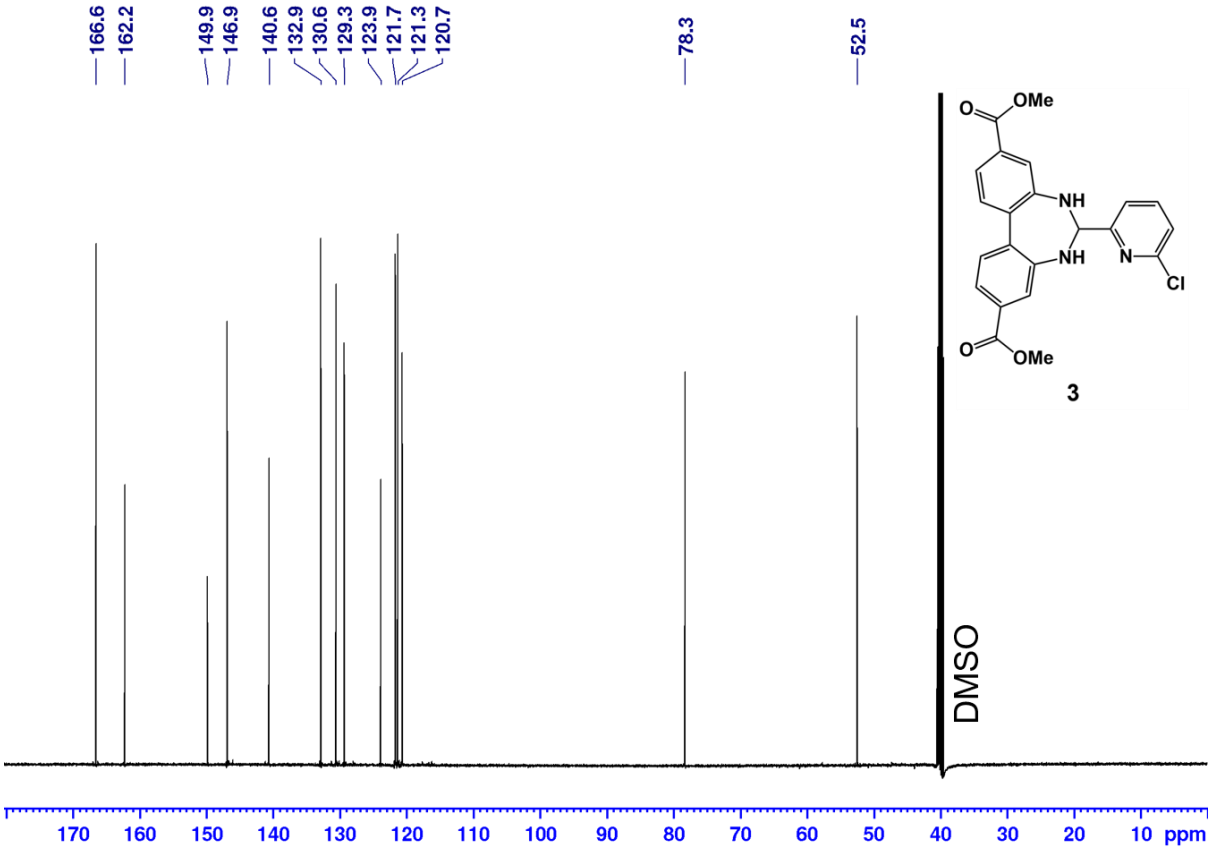

Figure S10 ^{13}C-NMR spectrum for compound **3** (600 MHz, d_6-DMSO).

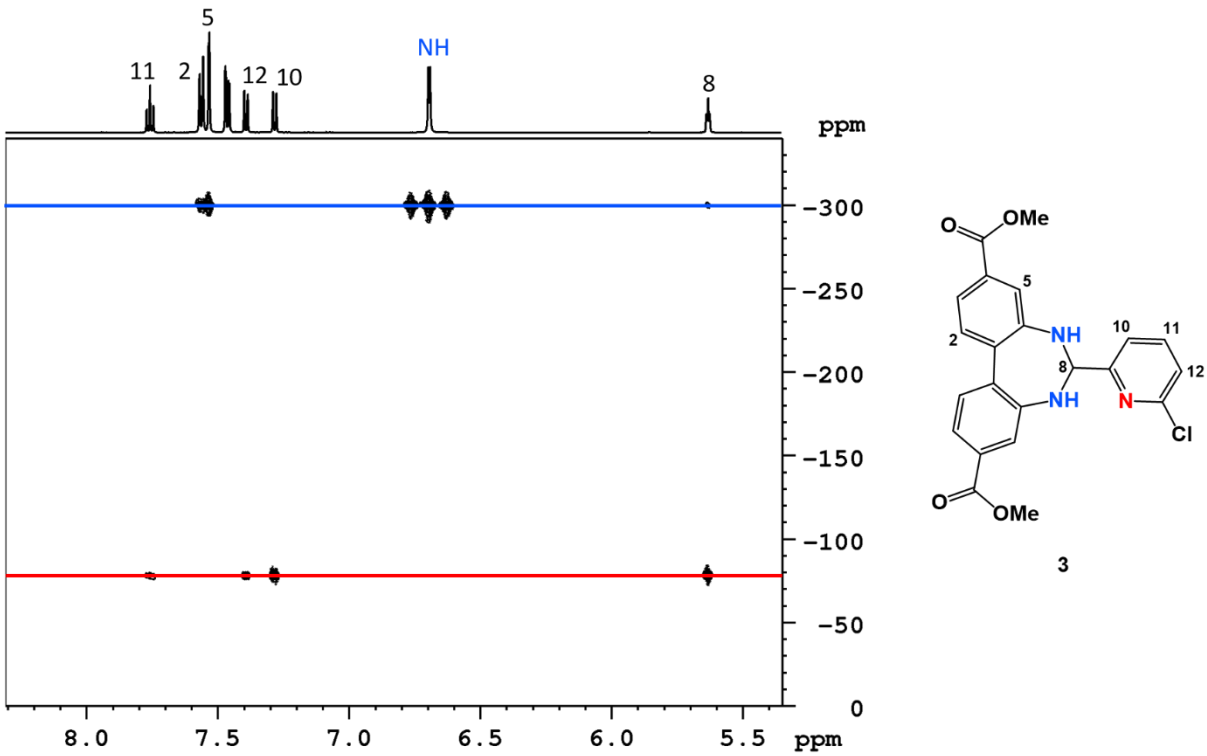

Figure S11 ^{1}H-^{15}N HMBC for compound **3** (600 MHz, d_6-DMSO).

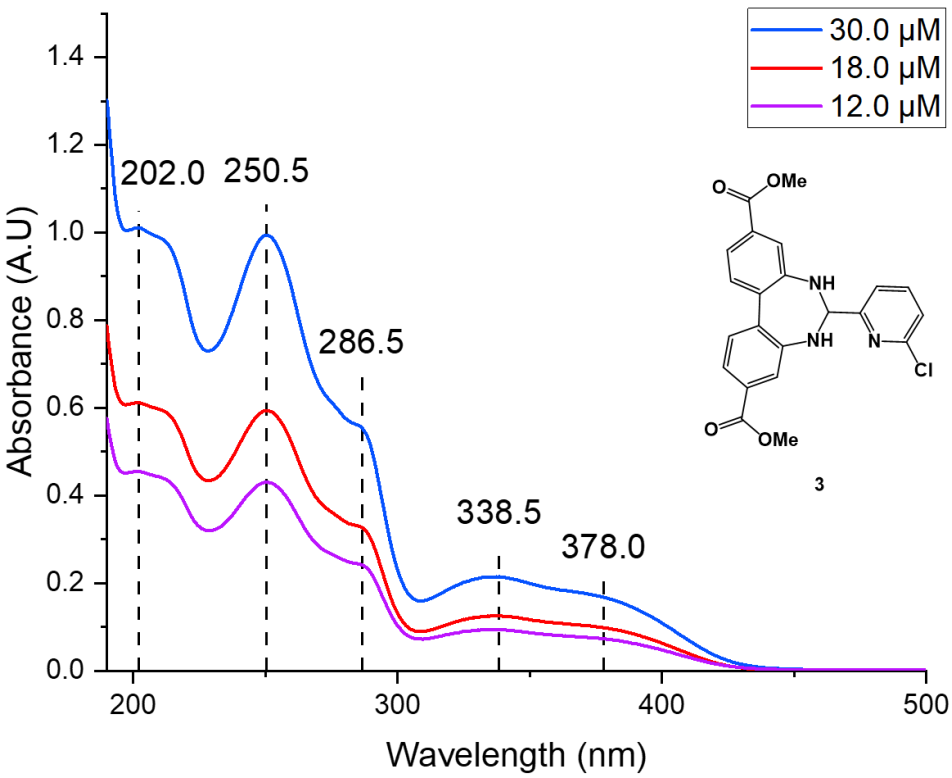

Figure S12 UV-Visible spectra of **3** at different concentrations in acetonitrile.

Compound 4

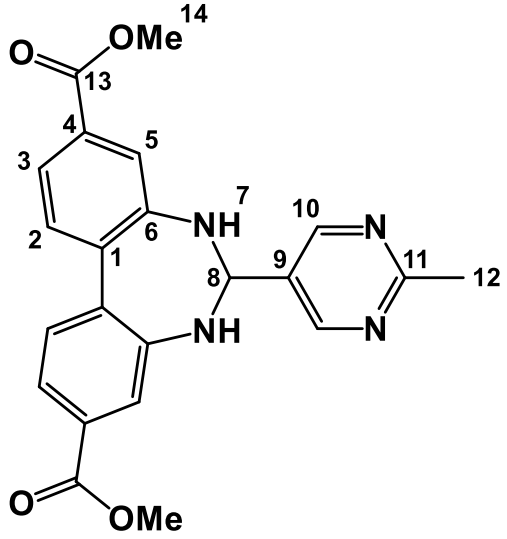

4

Dimethyl 2,2'-diaminobiphenyl-4,4'-dicarboxylate (200 mg, 0.67 mmol, 1 equiv.), zinc acetate dihydrate (146 mg, 0.67 mmol, 1 equiv.) and 2-methylpyrimidine-5-carbaldehyde (89 mg, 0.73 mmol, 1.1 equiv.) were mixed in methanol (4 mL) and left to stir on reflux overnight. The precipitate was filtered, and dried in a vacuum oven at 50 °C for two hours, yielding **4** as a pale orange solid (97.0 mg, 0.240 mmol, 36%). M.p. 206-208 °C. ^{1}H-NMR (*d*$_6$-DMSO, 600 MHz) δ 8.62 (s, 2H, H10), 7.61 (d, J = 8.3 Hz, 1H, H2), 7.54 (d, J = 1.7 Hz, 1H, H5), 7.47 (dd, J = 1.7, 8.2 Hz, 1H, H3), 6.66 (d, J = 3.2 Hz, 1H, H7), 5.67 (t, J = 3.1 Hz, 1H, H8), 3.83 (s, 6H , H14), 2.60 ppm (s,3H, H12); ^{13}C-NMR (*d*$_6$-DMSO, 151 MHz) δ 166.8 (C11), 166.1 (C13), 155.7 (C10), 146.7 (C6), 132.1 (C9), 131.8 (C1), 130.4 (C2), 128.9 (C4), 120.93 (C5), 120.87 (C3), 73.1 (C8), 52.1 (C14), 25.4 ppm (C12); ^{15}N{^{1}H} NMR (*d*$_6$-DMSO, 600 MHz): -89.0 (N_{py}), -296.3 (NH^7); LRMS (ESI/Q-TOF): m/z (%): 427.138 (100) $[M + Na]^+$; HRMS (ESI/Q-TOF) m/z: $[M + Na]^+$ Calcd. for $C_{22}H_{20}N_4O_4Na$ 427.1377; Found 427.1377. Anal. Calcd for $C_{22}H_{20}N_4O_4$: C, 65.34; H, 4.98; N, 13.85. Found: C, 65.31; H, 4.91; N, 13.81. UV-Visible (MeCN): λ_{max} 200.0 (26 100), 217.0 (sh, 23 300), 250.0 (27 810), 286.0 (14 190), 334.5 (6 114), 386.5 nm (sh, 4 189 $M^{-1}cm^{-1}$).

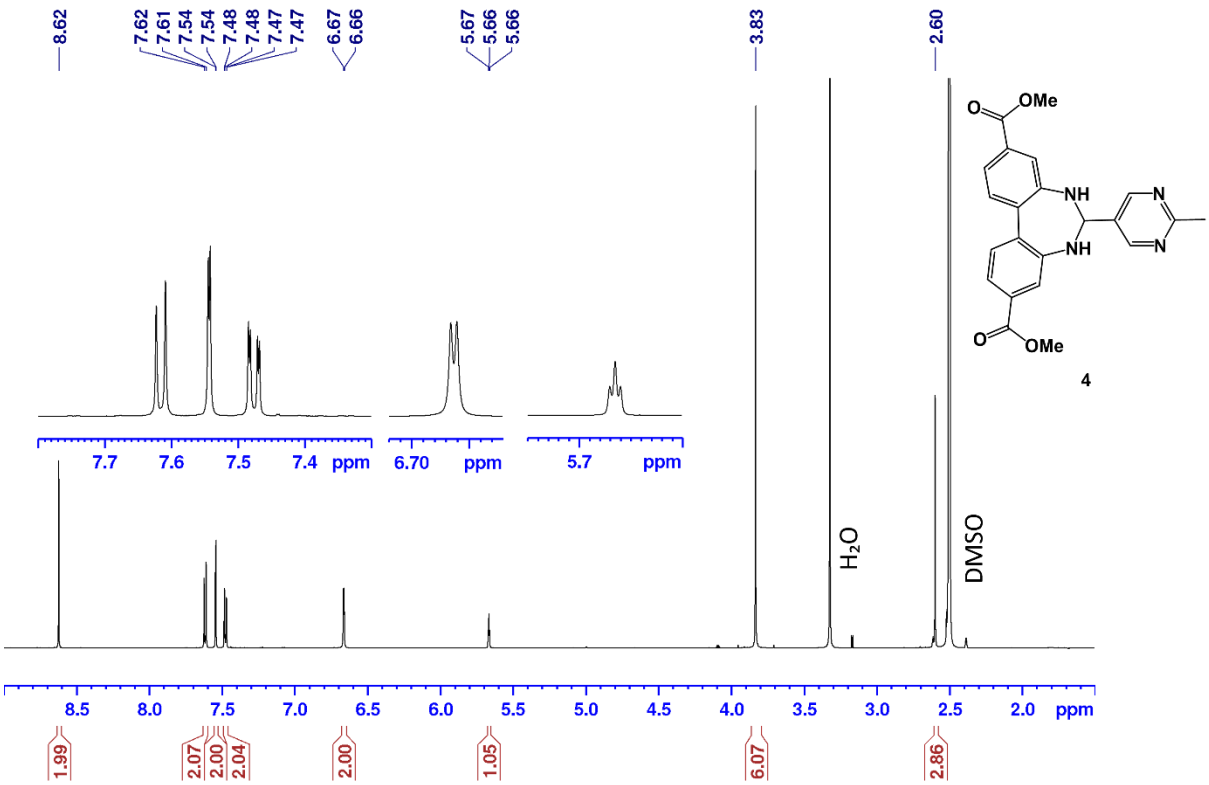

Figure S13 ^{1}H-NMR spectrum for compound **4** (600 MHz, d_6-DMSO).

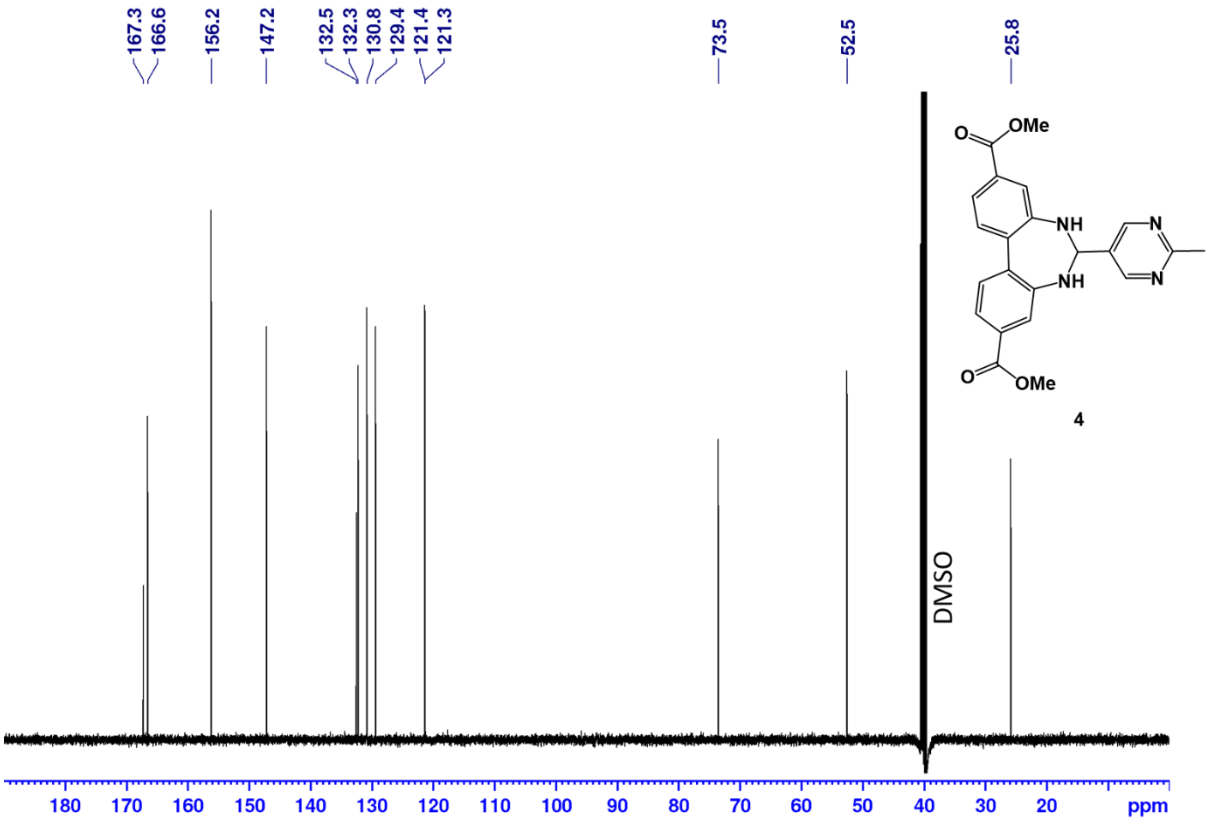

Figure S14 ^{13}C-NMR spectrum for compound **4** (600 MHz, d_6-DMSO).

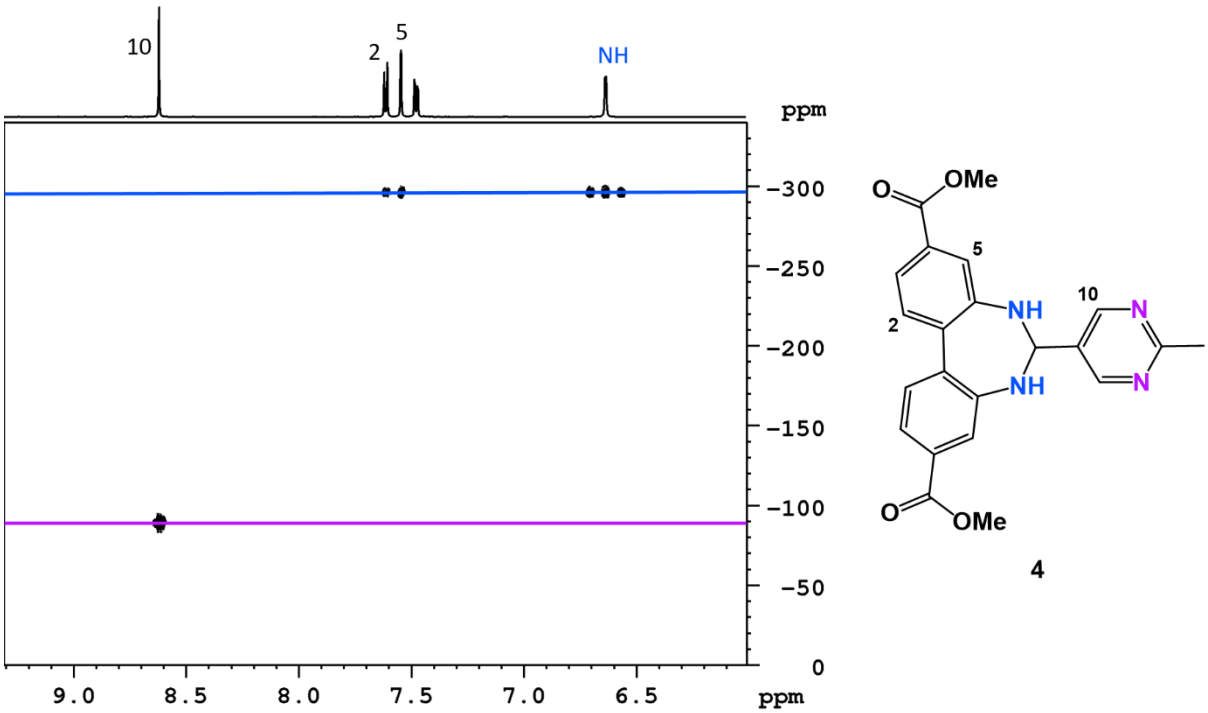

Figure S15 ^{1}H-^{15}N HMBC for compound **4** (600 MHz, d_6-DMSO).

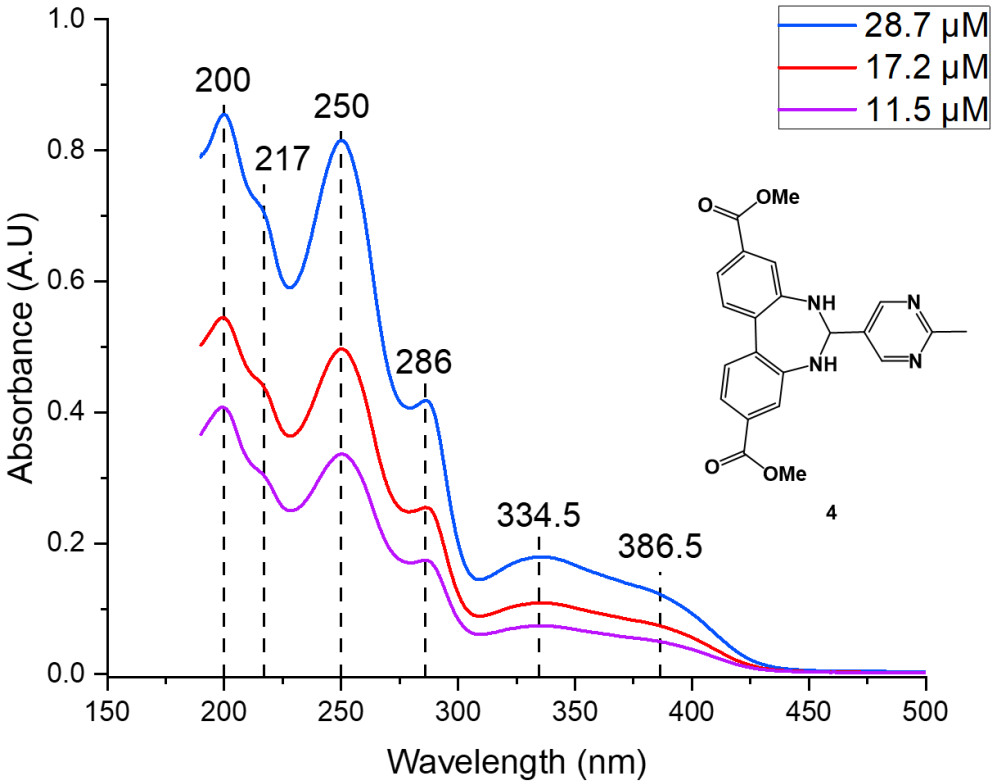

Figure S16 UV-Visible spectra of **4** at different concentrations in acetonitrile.

Compound 5

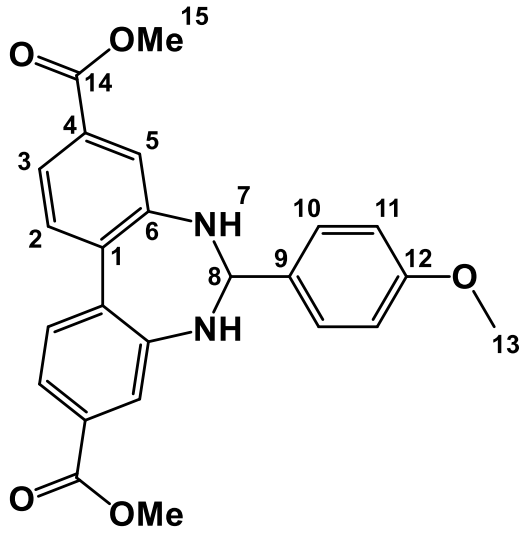

5

Dimethyl 2,2'-diaminobiphenyl-4,4'-dicarboxylate (100 mg, 0.33 mmol, 1 equiv.), zinc acetate dihydrate (73 mg, 0.33 mmol, 1 equiv.) and 4-anisaldehyde (50 mg, 0.36 mmol, 1.1 equiv.) were mixed in methanol (3 mL) and left to stir at room temperature over 3 days. The precipitate was filtered and left to air dry overnight yielding **5** as a pale yellow solid (120 mg, 0.286 mmol, 86%). M.p. 174-175 °C; ^{1}H-NMR (*d*$_6$-DMSO, 600 MHz) δ 7.58 (d, *J* = 8.4 Hz, 2H, H2), 7.57 (d, *J* = 1.8 Hz, 2H, H5), 7.41 (dd, *J* = 1.8, 8.4 Hz, 2H, H3), 7.32 (d, *J* = 8.7 Hz, 2H, H10), 6.91 (d, *J* = 8.6 Hz, 2H, H11), 6.50 (d, *J* = 2.8 Hz, 2H, H7), 5.46 (t, *J* = 2.7 Hz, 1H, H8), 3.82 (s, 6H, H15), 3.74 ppm (s, 3H, H13); ^{13}C-NMR (*d*$_6$-DMSO, 151 MHz) δ 166.2 (C14), 159.0 (C12), 147.7 (C6), 134.5 (C9), 131.0 (C1), 130.3 (C2), 128.6 (C4), 128.3 (C10), 120.7 (C5), 120.0 (C3), 113.5 (C11), 76.2 (C8), 55.1 (C13), 52.0 ppm (C15); ^{15}N{^{1}H} NMR (*d*$_6$-DMSO, 600 MHz): -290.2 ppm (NH^{7}); LRMS (ESI/Q-TOF) m/z (%): 441.142 (100) [M + Na]$^{+}$; HRMS (ESI/Q-TOF) m/z: [M + Na]$^{+}$ Calcd. for $C_{20}H_{22}N_2O_5Na$ 441.1421; Found 418.1420. Anal. Calcd for $C_{24}H_{22}N_2O_5$: C, 68.89; H, 5.30; N, 6.69. Found: C, 68.81; H, 5.31; N, 6.70 %. UV-Visible (MeCN): λ_{max} 192.5 (43 000), 225.0 (37 270), 248.0 (26 100), 266.0 (24 900), 319.0 nm (sh, 15 600 M^{-1}cm^{-1}).

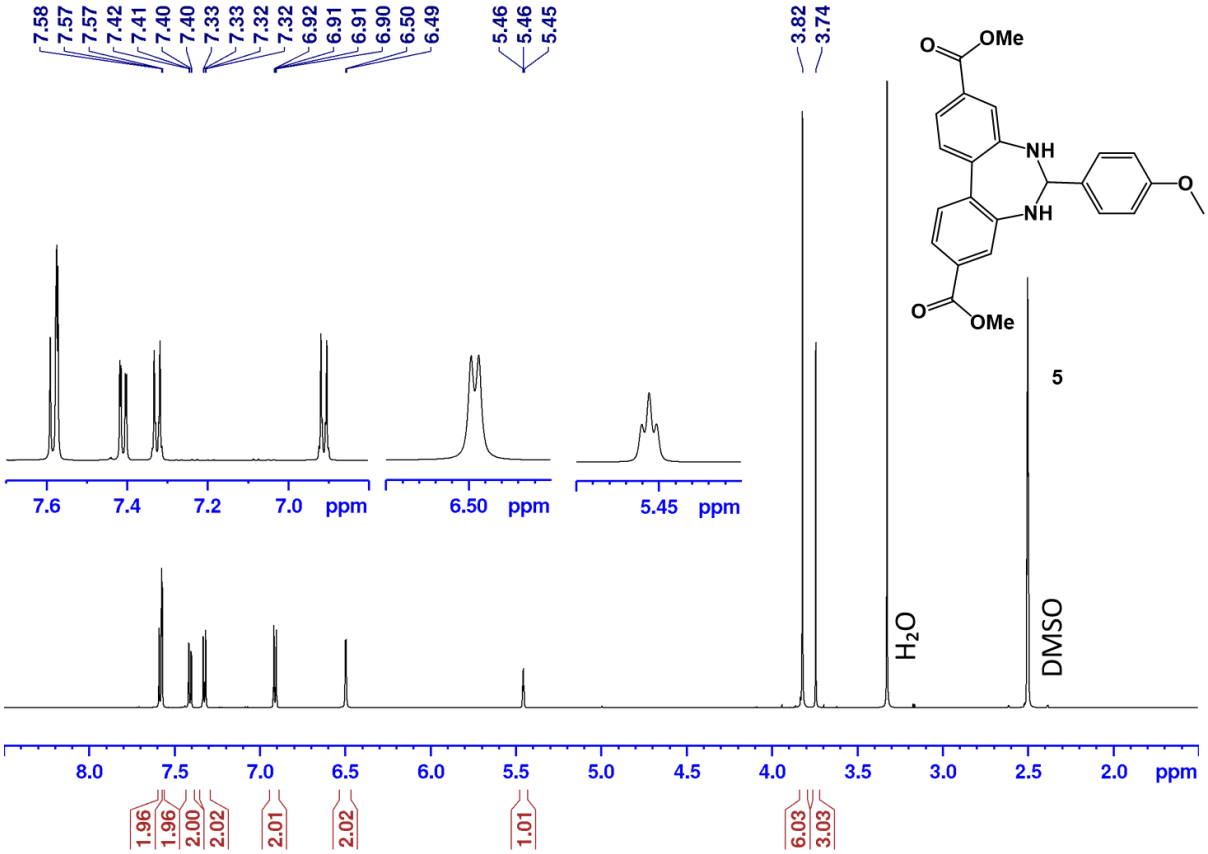

Figure S17 ^{1}H-NMR spectrum for compound **5** (600 MHz, d_6-DMSO).

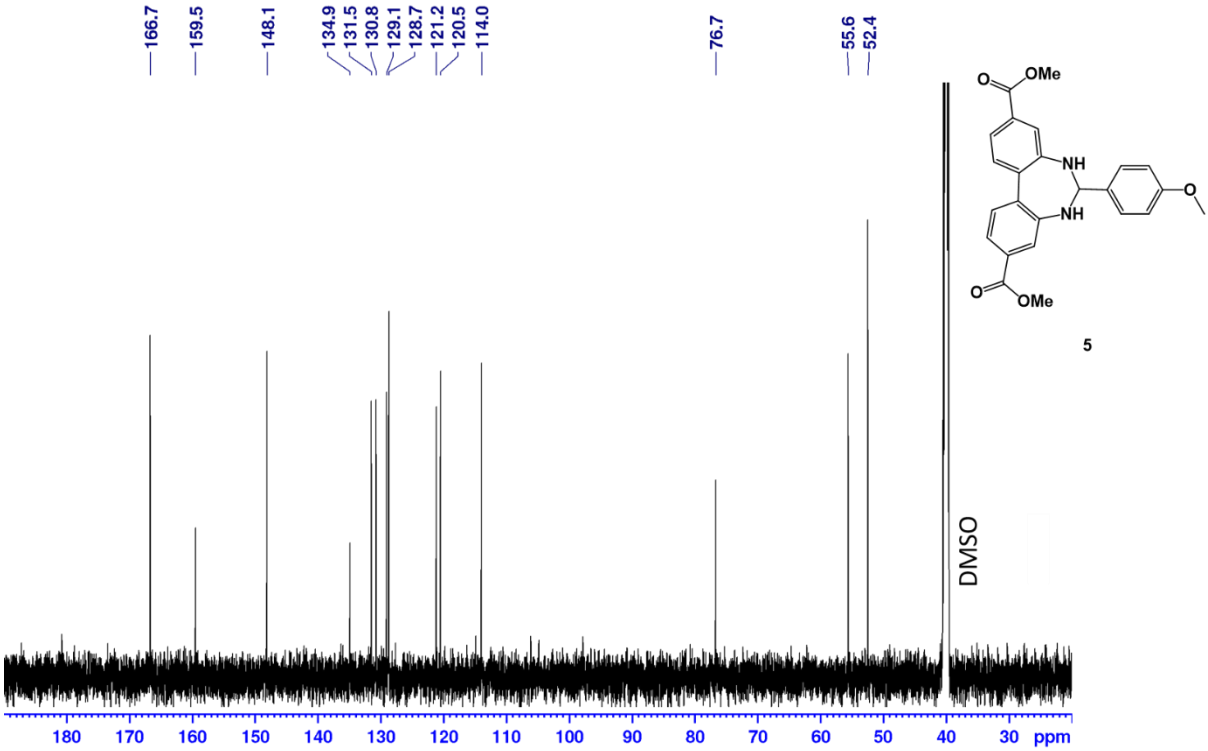

Figure S18 ^{13}C-NMR spectrum for compound **5** (600 MHz, d_6-DMSO).

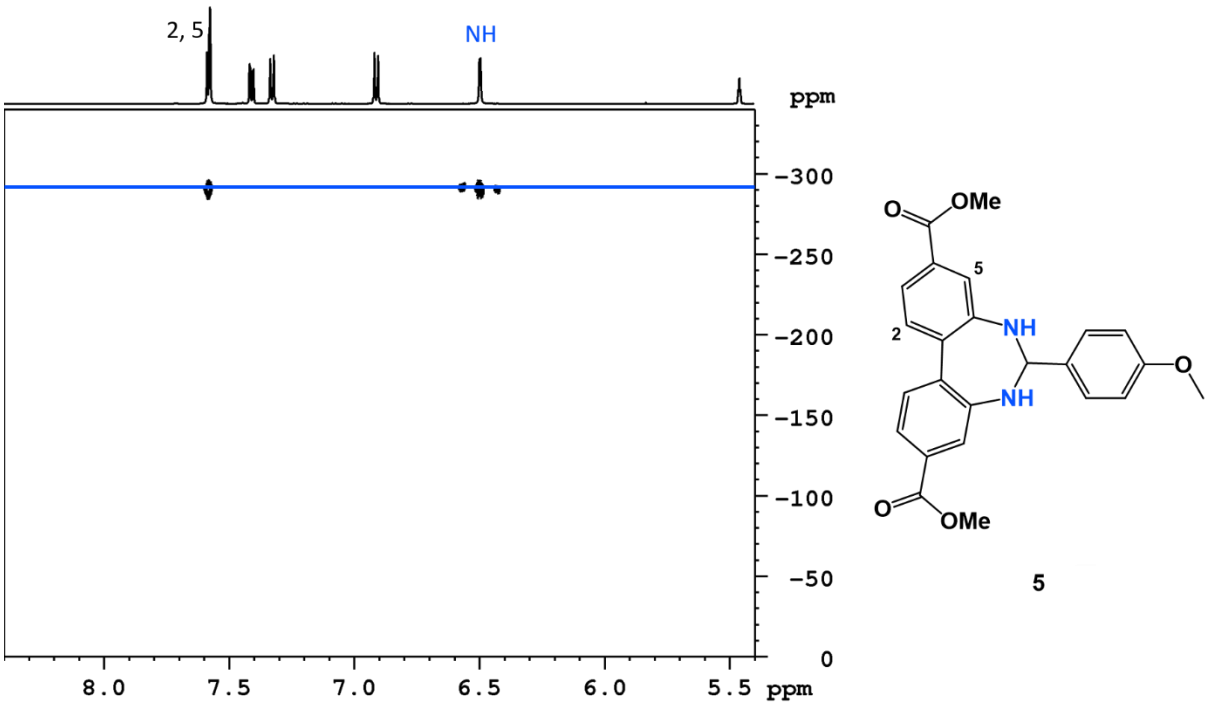

Figure S19 ^{1}H-^{15}N HMBC for compound **5** (600 MHz, d_6-DMSO).

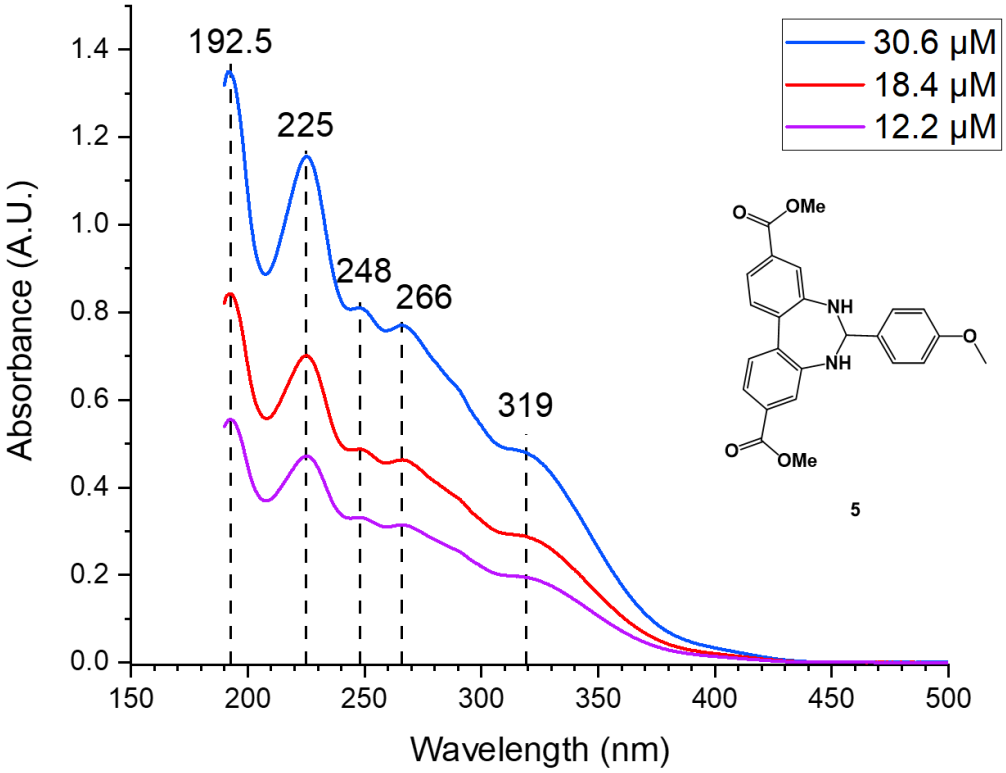

Figure S20 UV-Visible spectra of **5** at different concentrations in acetonitrile.

Compound 6

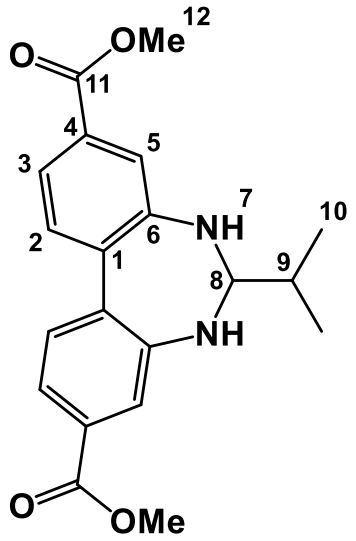

6

Dimethyl 2,2'-diaminobiphenyl-4,4'-dicarboxylate (100 mg, 0.33 mmol, 1 equiv.) and isobutyraldehyde (26 mg, 0.36 mmol, 1.1 equiv.) were mixed in methanol (4 mL) and left to stir at room temperature overnight. The solvent and aldehyde excess were removed under reduced pressure, yielding **6** as a yellow solid (112 mg, 0.316 mmol, 95%). M.p. 141-142 °C. ^{1}H-NMR (600 MHz, *d*$_6$-DMSO) δ 7.62 (d, J = 1.6 Hz, 1H, H5), 7.57 (d, J = 8.3 Hz, 1H, H2), 7.33 (dd, J = 1.7, 8.3 Hz, 1H, H3), 6.29 (d, J = 2.7 Hz, 1H, H7), 4.09 (q, J = 3.4 Hz, 1H, H8), 3.83 (s, 6H, H12), 1.95 (m, 1H, H9), 1.01 ppm (d, J = 7.0 Hz, 1H, H10); ^{13}C-NMR (151 MHz, *d*$_6$-DMSO) δ 166.3 (C11), 148.8 (C6), 130.5 (C2), 129.7 (C1), 128.3 (C4), 119.9 (C5), 119.2 (C3), 77.6 (C8), 52.0 (C12), 32.7 (C9), 17.4 ppm (C10); ^{15}N{^{1}H} NMR (*d*$_6$-DMSO, 600 MHz): -293.3 (NH^{7}); LRMS (ESI/Q-TOF): m/z (%): 377.147 (100) [M + Na]$^{+}$; HRMS (ESI/Q-TOF) : [M + Na]$^{+}$ m/z calcd. For $C_{20}H_{22}N_2O_4Na$: 377.1472; Found 377.1472; Anal. Calcd for $C_{20}H_{22}N_2O_4$: C, 67.78; H, 6.26; N, 7.90. Found: C, 67.50; H, 6.22; N, 7.87 %. UV-Visible (MeCN): λ_{max} 202.2 (30 500), 256.6 (32 200), 287.8 (12 300), 344.6 (5 170), 388.9 nm (7 130 $M^{-1}cm^{-1}$).

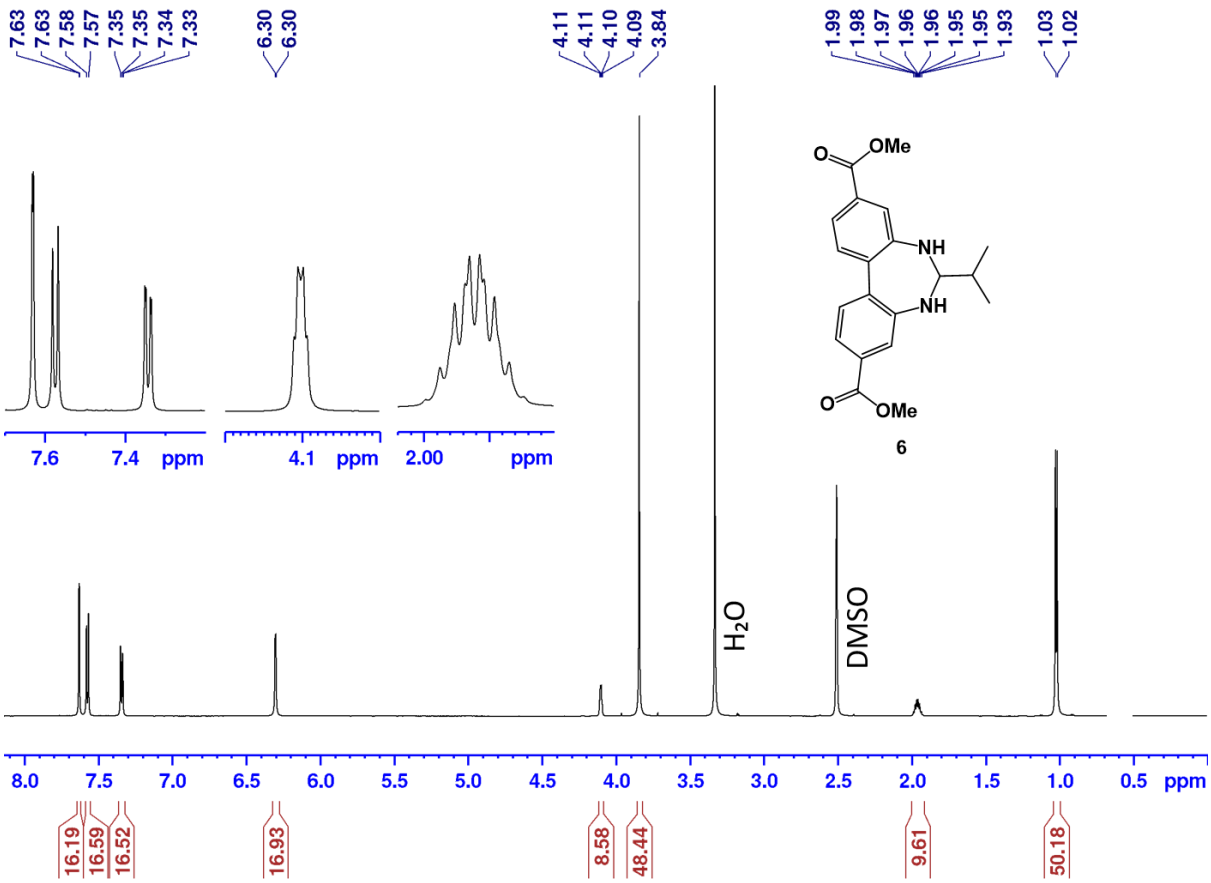

Figure S21 ^{1}H-NMR spectrum for compound **6** (600 MHz, d_6-DMSO).

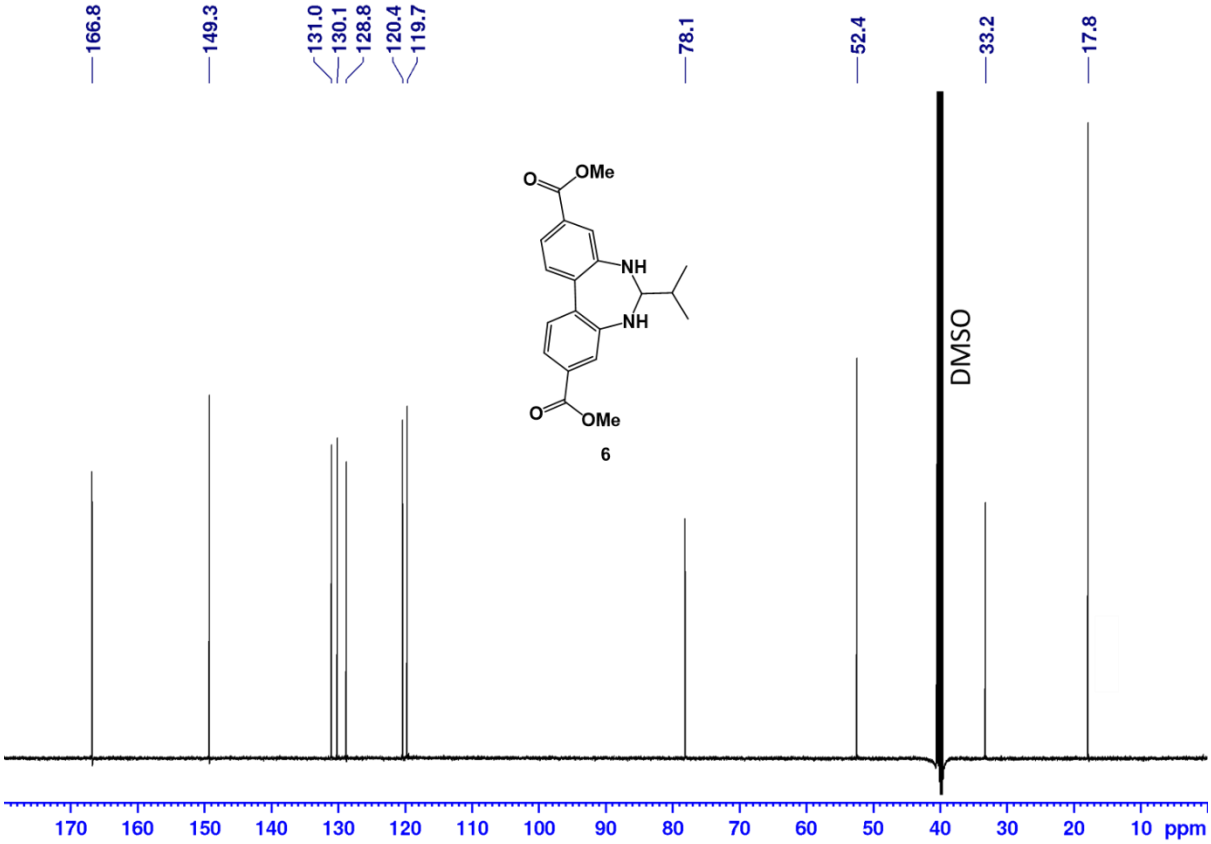

Figure S22 ^{13}C-NMR spectrum for compound **6** (600 MHz, d_6-DMSO).

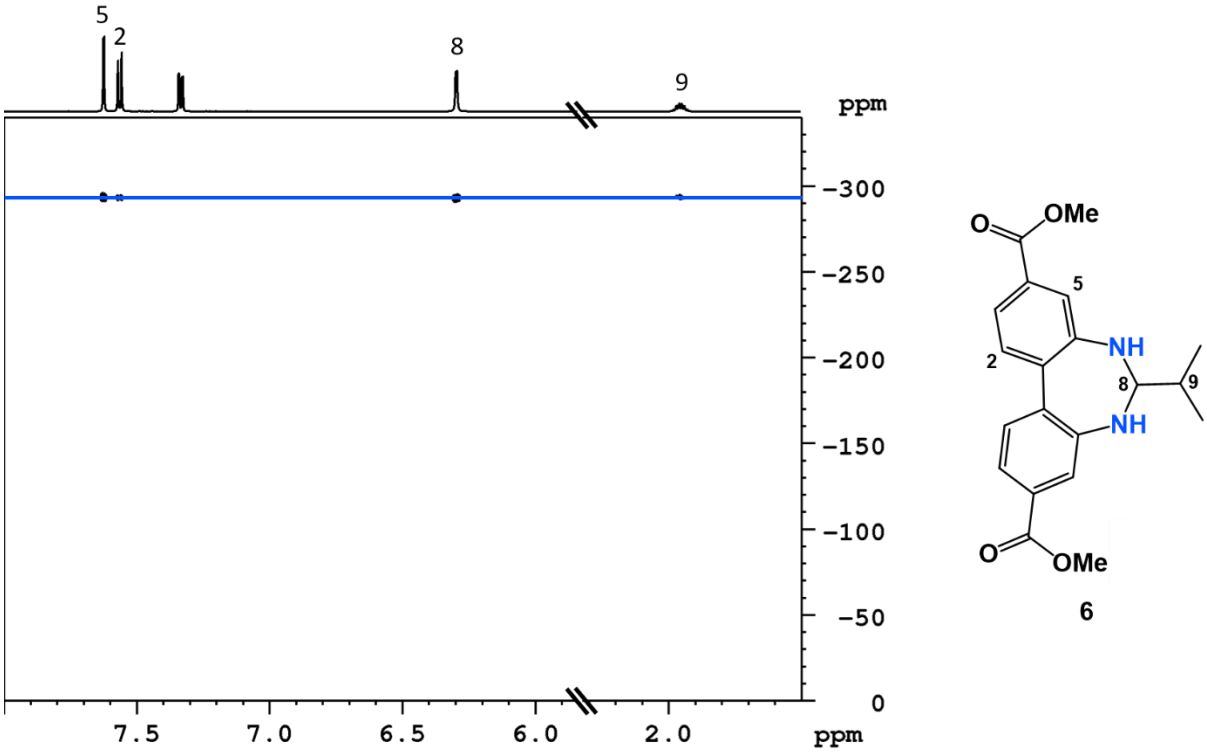

Figure S23 ^{1}H-^{15}N HMBC for compound **6** (600 MHz, d_6-DMSO).

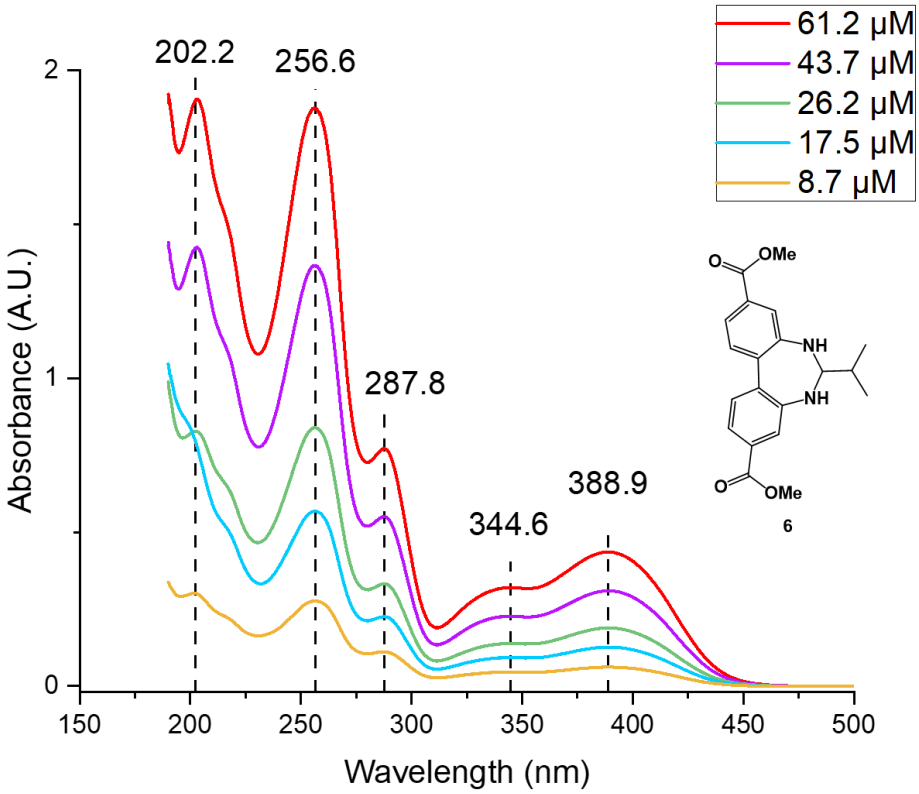

Figure S24 UV-Visible spectra of **6** at different concentrations in acetonitrile.

Compound 7

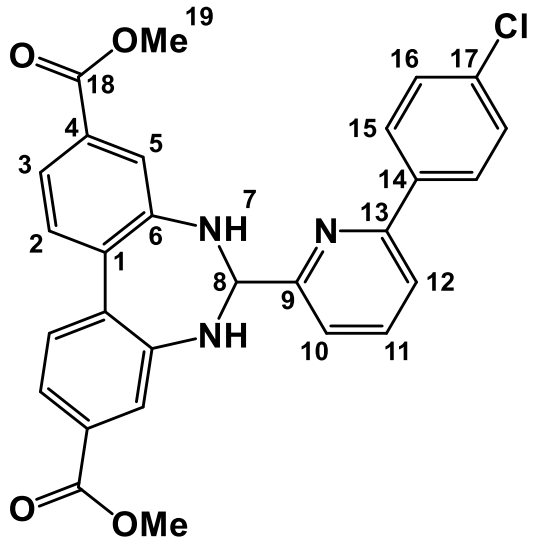

7

Dimethyl 2,2'-diaminobiphenyl-4,4'-dicarboxylate (100 mg, 0.33 mmol, 1 equiv.), zinc acetate dihydrate (73 mg, 0.33 mmol, 1 equiv.) and 6-(4-chlorophenyl)picolinaldehyde (78 mg, 0.36 mmol, 1.1 equiv.) were mixed in methanol (4 mL) and left to stir at room temperature for 45min. The precipitate was filtered and dried in a vacuum oven at 60°C for two hours yielding **7** as an off-white solid (144 mg, 0.289 mmol, 87%). M.p. 180-181 °C. ^{1}H-NMR (600 MHz, *d*$_6$-DMSO) δ 8.17 (d, J = 8.5 Hz, 2H, H15), 7.86 (dd, J = 7.7 and 0.8 Hz, 1H, H12), 7.82 (t, J = 7.7 Hz, 1H, H11), 7.60 (d, J = 1.7 Hz, 2H, H2), 7.58 (d, J = 8.3 Hz, 2H, H5), 7.55 (d, J = 8.5 Hz, 2H, H16), 7.43 (dd, J = 1.7, 8.2 Hz, 2H, H3), 7.33 (dd, J = 7.7 and 0.8 Hz, 1H, H10), 6.81 (d, J = 3.9 Hz, 2H, H7), 5.71 (t, J = 3.9 Hz, 1H, H8), 3.81 (s, 6H, H19); ^{13}C-NMR (151 MHz, *d*$_6$-DMSO) δ 166.2 (C18), 160.2 (C9), 154.0 (C13), 147.2 (C6), 137.9 (C11), 137.3 (C14), 134.0 (C17), 131.9 (C1), 130.2 (C5), 128.72 (C4), 128.66 (C16), 128.60 (C15), 121.2 (C2), 120.5 (C3), 120.4 (C10), 119.3 (C12), 77.6 (C8), 51.9 (C19); ^{15}N{^{1}H} NMR (*d*$_6$-DMSO, 600 MHz): -76.9 (N_{py}), -296.7 (NH^7);LRMS (ESI/Q-TOF): m/z (%): 500.137 (100) $[M + H]^+$; HRMS (ESI/Q-TOF): $[M + H]^+$ m/z calcd. for $C_{28}H_{23}ClN_3O_4$: 500.1372. Found 500.1370; Anal. Calcd for $C_{28}H_{22}ClN_3O_4$: C 67.27, H, 4.44, N 8.41, Cl 7.09; Found C, 67.05, H, 4.41, N 8.33, Cl 7.05 %. UV-Visible (MeCN): λ_{max} 196 (52 400), 251.5 (42 400), 283.0 (29 200), 339.0 (5 900), 382 nm (sh, 5 000 $M^{-1}cm^{-1}$).

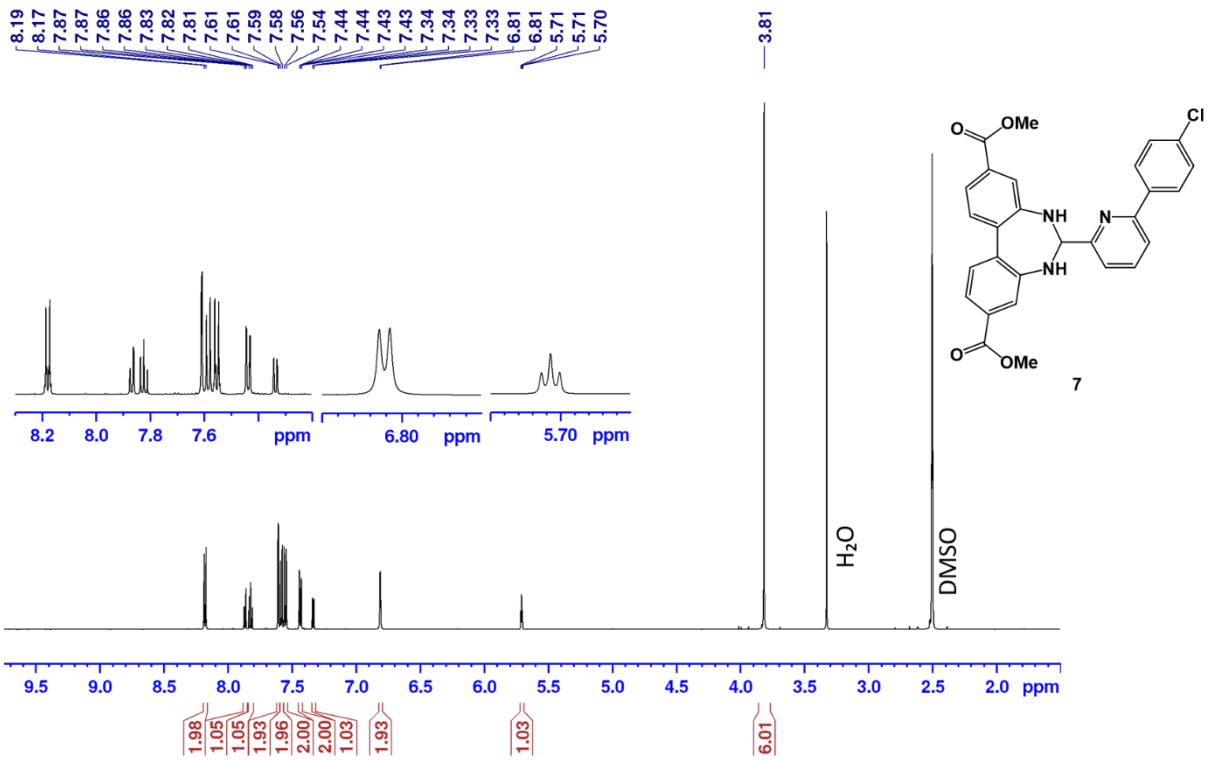

Figure S25 ^{1}H-NMR spectrum for compound **7** (600 MHz, d_6-DMSO).

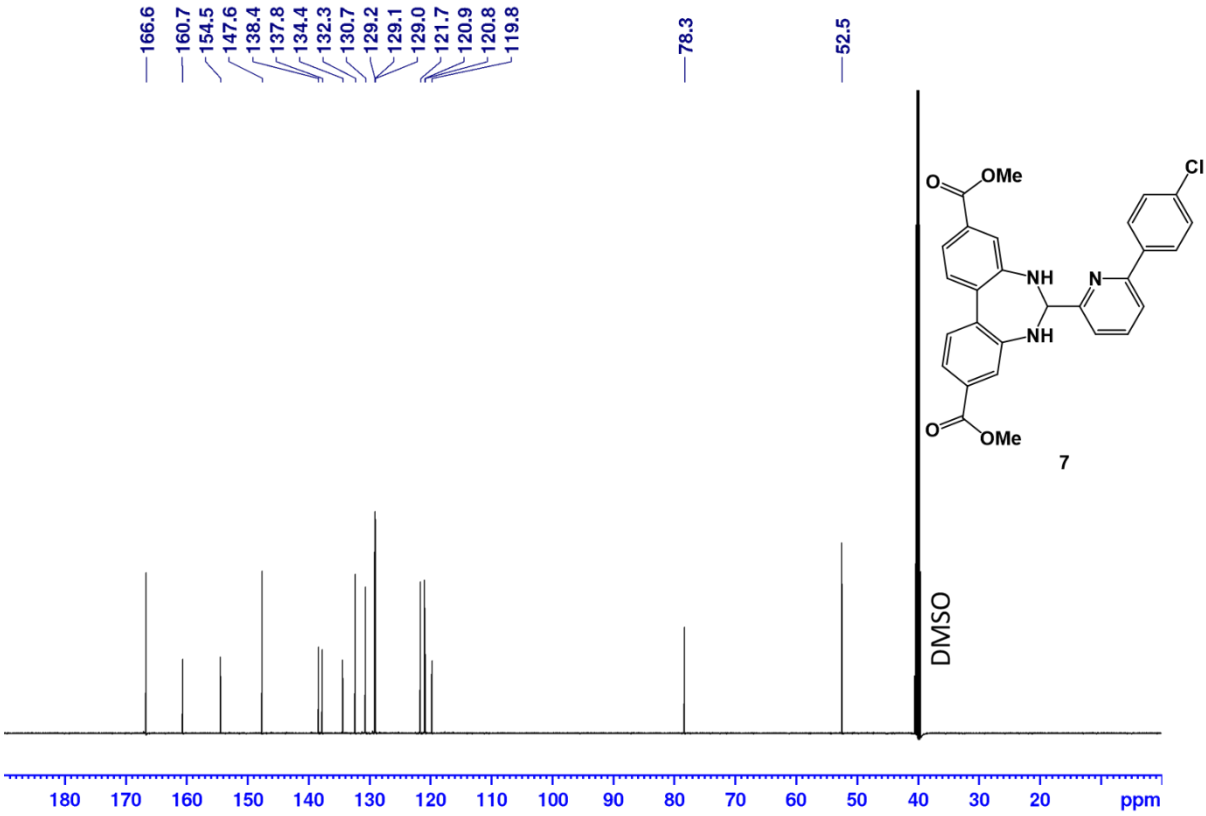

Figure S26 ^{13}C-NMR spectrum for compound **7** (600 MHz, d_6-DMSO).

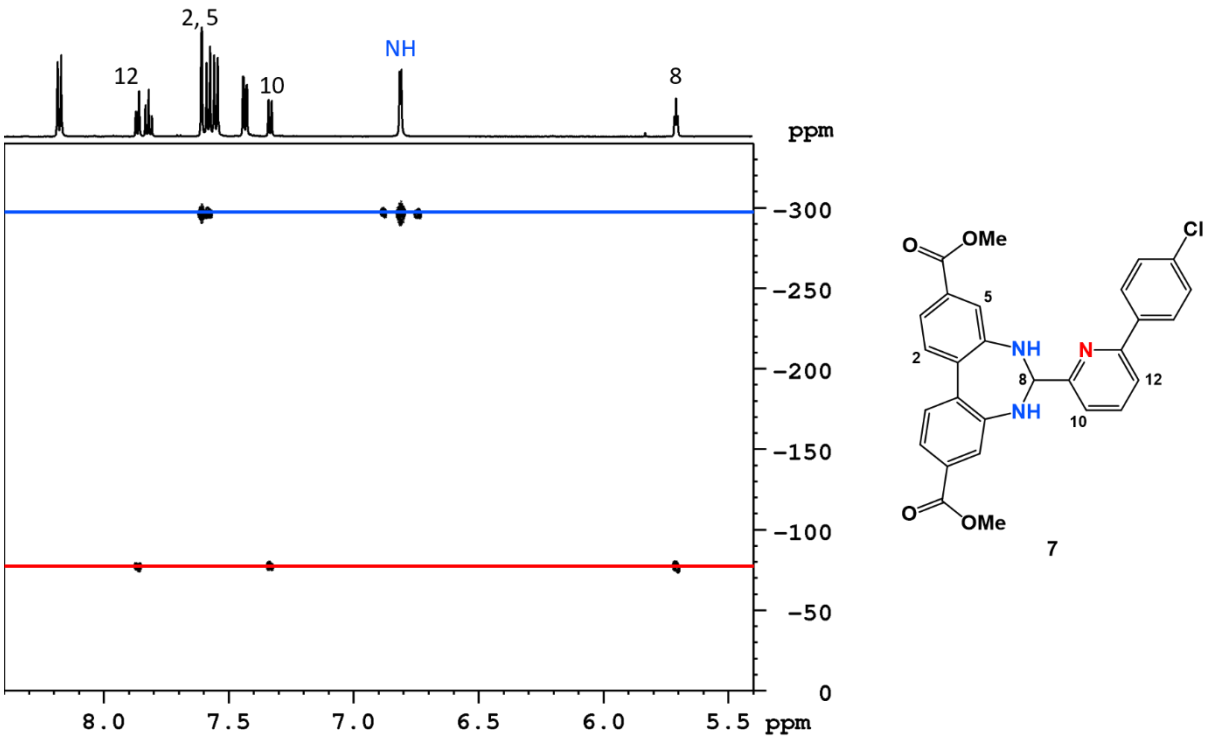

Figure S27 ^{1}H-^{15}N HMBC for compound **7** (600 MHz, d_6-DMSO).

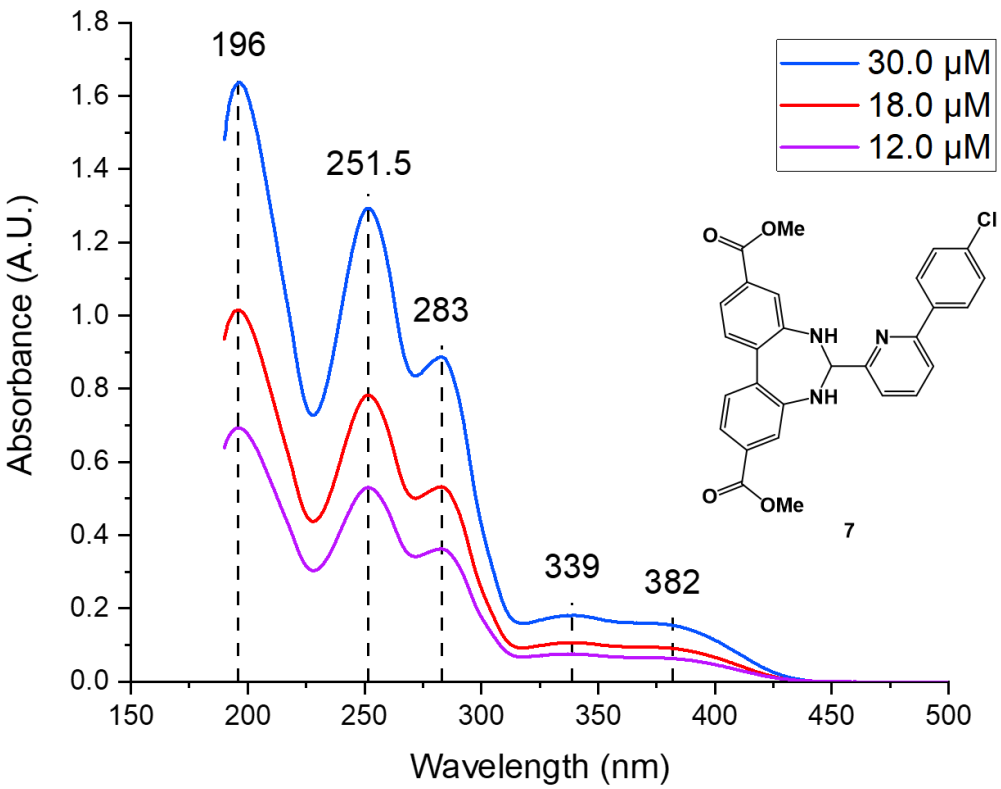

Figure S28 UV-Visible spectra of **7** at different concentrations in acetonitrile.

Compound 8

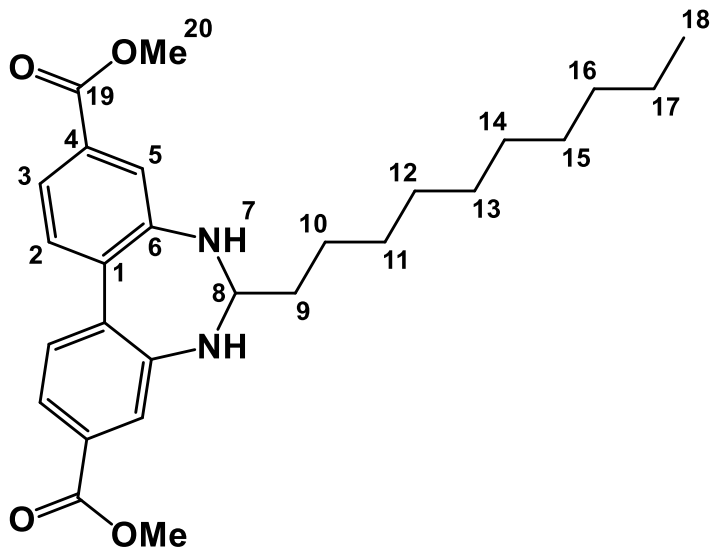

8

Dimethyl 2,2'-diaminobiphenyl-4,4'-dicarboxylate (100 mg, 0.33 mmol, 1 equiv.), zinc acetate dihydrate (73 mg, 0.33 mmol, 1 equiv.) and undecanal (62 mg, 0.36 mmol, 1.1 equiv.) were mixed in methanol (3 mL) and left to stir at room temperature overnight. The precipitate was filtered and dried in a vacuum oven at 60°C for two hours yielding **8** as a pale yellow solid (144 mg, 0.289 mmol, 87%). M.p. 127-129 °C. ^{1}H-NMR (600 MHz, d_6-DMSO) δ 7.58 (d, *J* = 8.3 Hz, 2H, H2), 7.56 (d, *J* = 1.9 Hz, 2H, H5), 7.34 (dd, *J* = 1.9, 8.3 Hz, 2H, H3), 6.35 (d, *J* = 2.9 Hz, 2H, H7), 4.24 (sept, *J* = 2.9 Hz, 1H, H8), 3.83 (s, 6H, H20), 1.68-1.63 (m, 2H, H9), 1.51-1.44 (m, 2H, H10), 1.30-1.21 (m, 14H, H11-H17), 0.85 (t, *J* = 7.0 Hz, 3H, H18); ^{13}C-NMR (151 MHz, d_6-DMSO) δ 166.3 (C19), 148.7 (C6), 130.6 (C2), 129.6 (C1), 128.3 (C4), 119.8 (C5), 119.3 (C3), 73.1 (C8), 51.9 (C20), 35.5 (C9), 31.3 (C^{alk}), 29.0 (C^{alk}), 28.96 (C^{alk}), 28.94 (C^{alk}), 28.7 (C^{alk}), 24.4 (C10), 22.1 (C^{alk}), 13.9 (C18); ^{15}N{^{1}H} NMR (d_6-DMSO, 600 MHz): -288.3 (NH^7); LRMS (ESI/Q-TOF): m/z (%): 475.257 (100) $[M + Na]^+$; HRMS (ESI/Q-TOF): $[M + Na]^+$ m/z calcd. for $C_{27}H_{36}NaN_2O_4$: 475.2567. Found 475.2566; Anal. Calcd for $C_{27}H_{36}N_2O_4$: C, 71.65, H, 8.02, N 6.19; Found C, 71.91, H, 8.11, N 5.94 %. UV-Visible (MeCN): λ_{max} 204.8 (30 600), 256.4 (33 800), 287.8 (13 960), 343.0 (5 800), 388.8 nm (7 680 $M^{-1}cm^{-1}$).

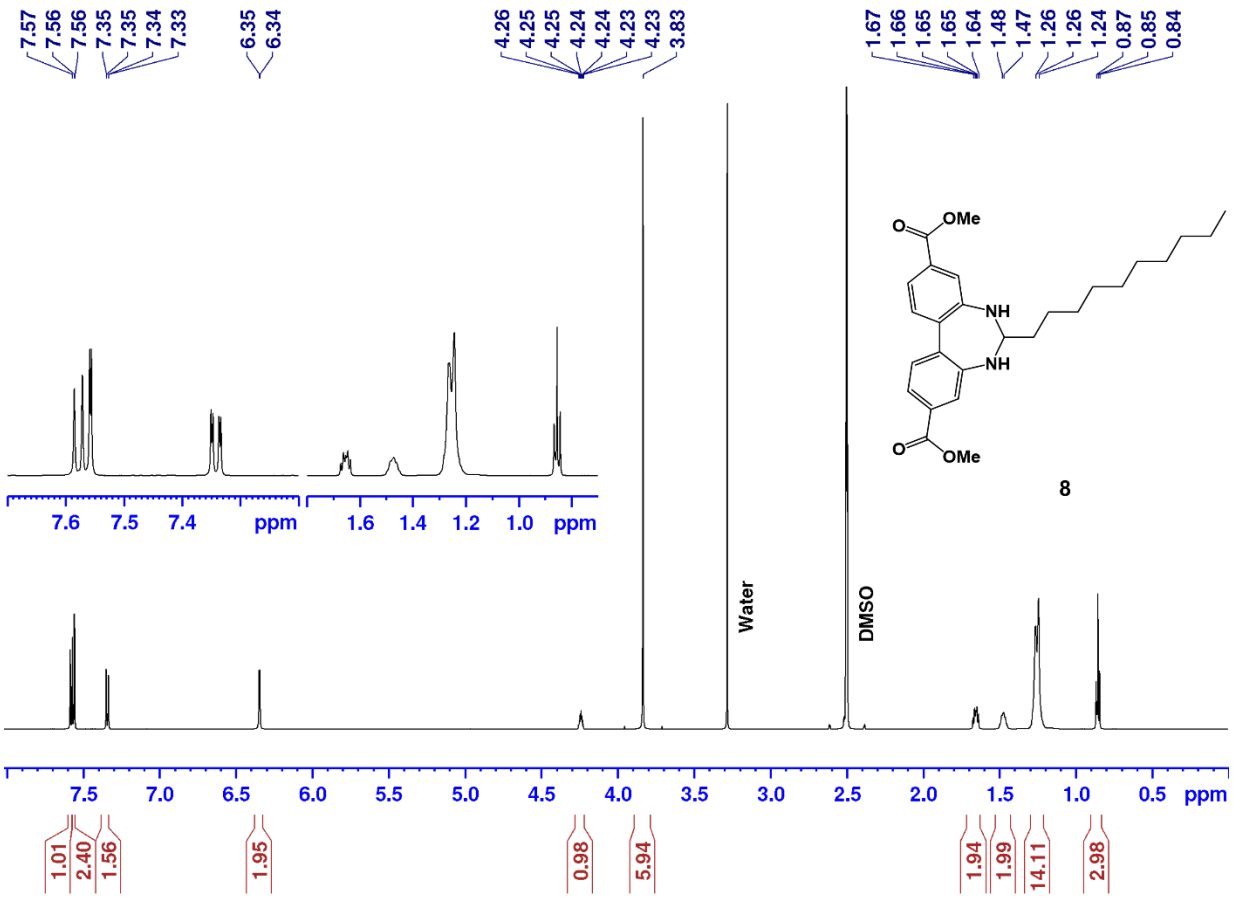

Figure S29 ^{1}H-NMR spectrum for compound **8** (600 MHz, d_6-DMSO).

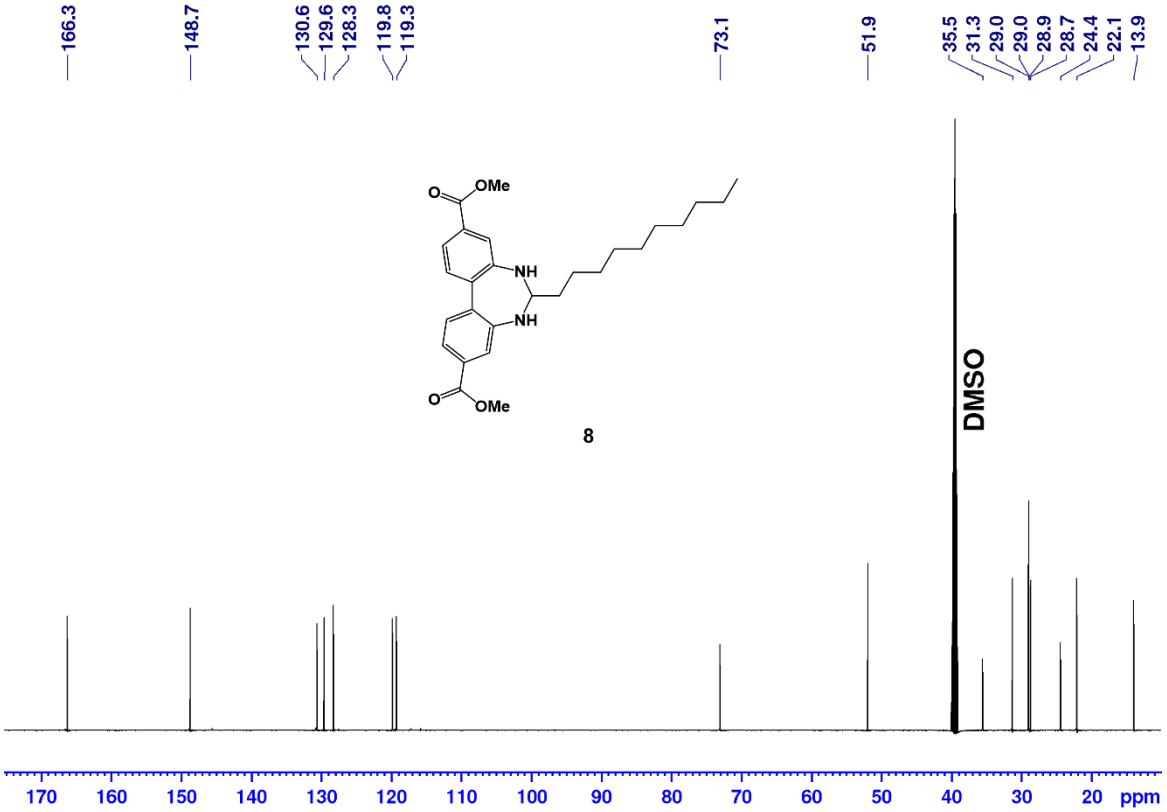

Figure S30 ^{13}C-NMR spectrum for compound **8** (600 MHz, d_6-DMSO).

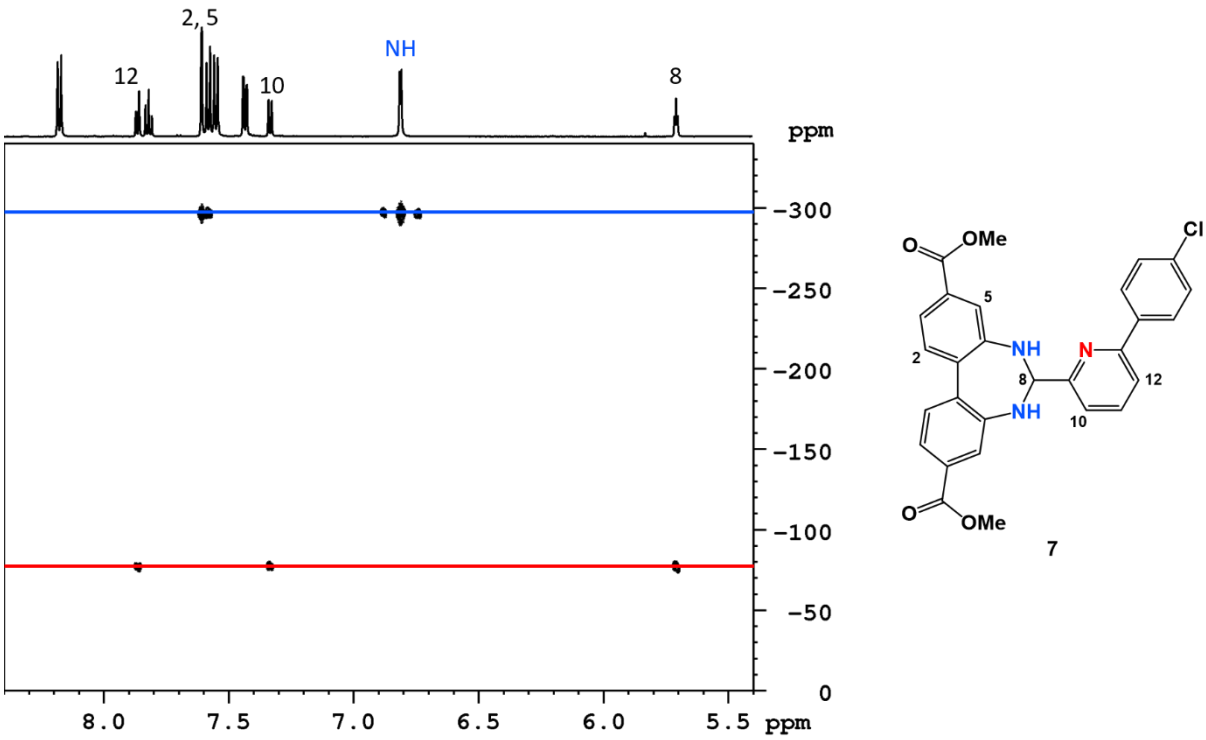

Figure S31 ^{1}H-^{15}N HMBC for compound **7** (600 MHz, d_6-DMSO).

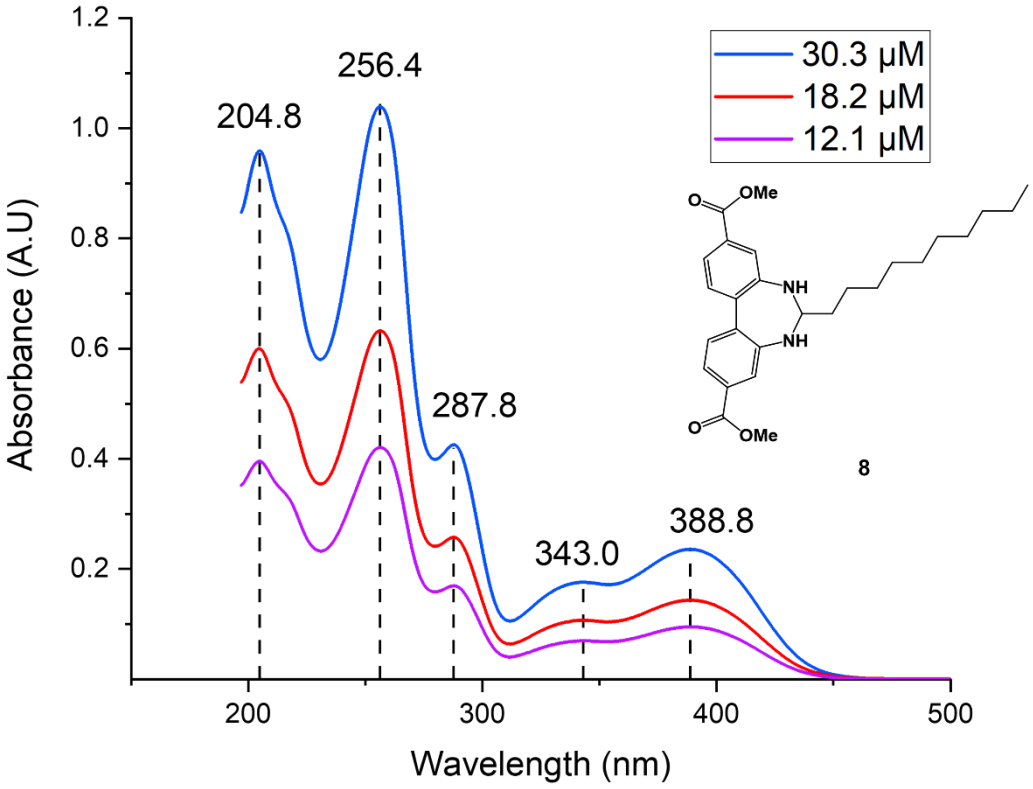

Figure S32 UV-Visible spectra of **8** at different concentrations in acetonitrile.

Compound 1D

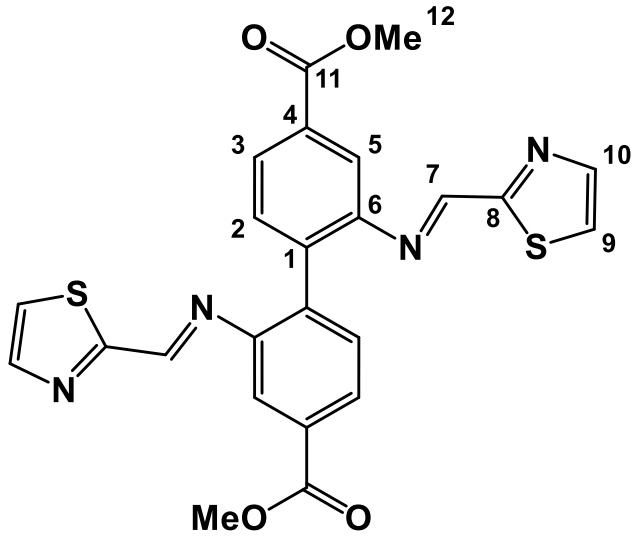

1D

Hot recrystallisation of **1** from an acetonitrile/toluene mixture precipitate small amounts of **1D**. ^{1}H-NMR (600 MHz, $CDCl_3$) δ 8.57 (s, 2H, H7), 8.04 (dd, J = 7.9 and 1.2 Hz, 2H, H3), 7.88 (m, 2H, H10), 7.84 (d, J = 1.0 Hz, 2H, H5), 7.52 (d, J 7.9 Hz, 2H, H2), 7.41 (d, J = 2.9 Hz, 2H, H9), 3.97 (s, 6H, H11); ^{13}C-NMR (151 MHz, $CDCl_3$) δ 166.9 (C8), 166.6 (C11), 153.9 (C7), 149 (C6) 144.8 (C10), 138.6 (C1), 131.5 (C2), 131.3 (C4), 127.8 (C3), 123.0 (C9), 119.1 (C5), 52.5 (C12); LRMS (ESI/Q-TOF): m/z (%): 513.066 (100) $[M + Na]^+$; HRMS (ESI/Q-TOF): $[M + Na]^+$ m/z calcd. for $C_{24}H_{18}N_4NaO_4S_2$: 513.0662. Found 513.0661.

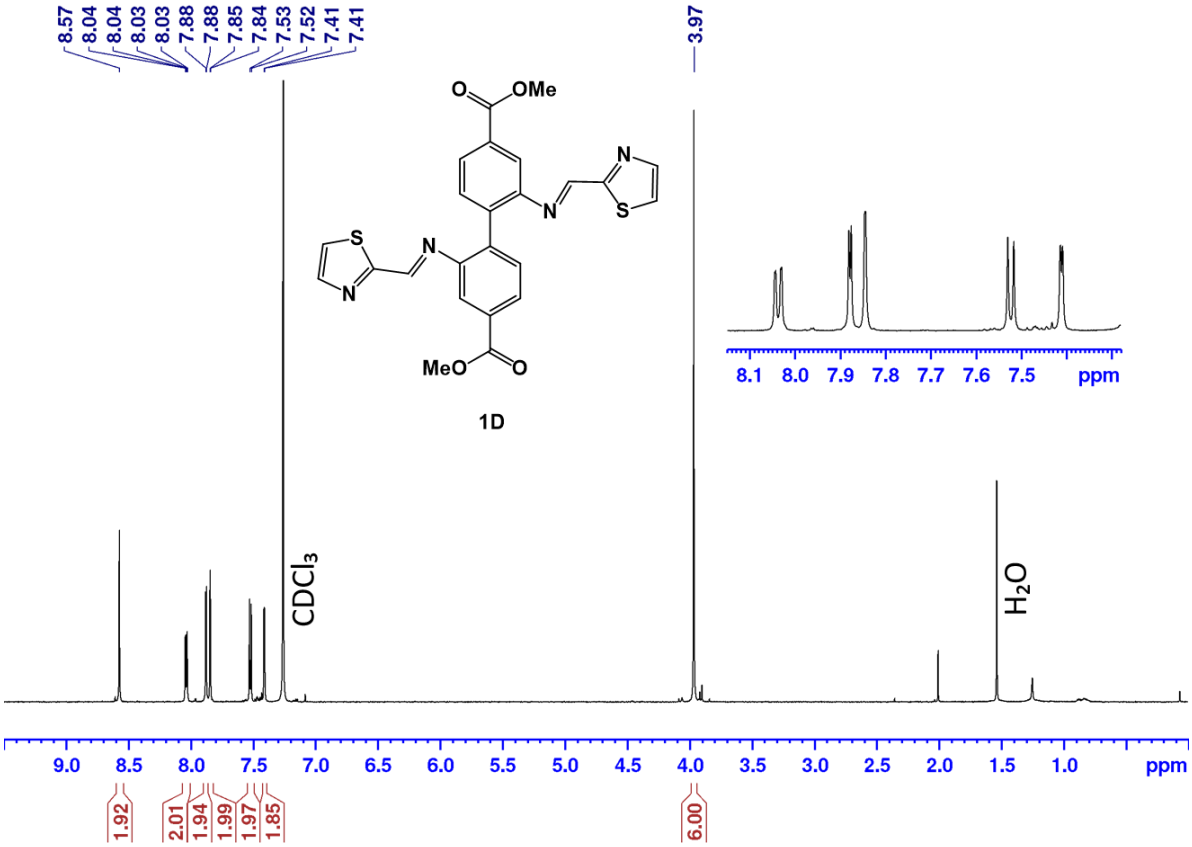

Figure S33 ^{1}H-NMR spectrum for compound **1D** (600 MHz, $CDCl_3$).

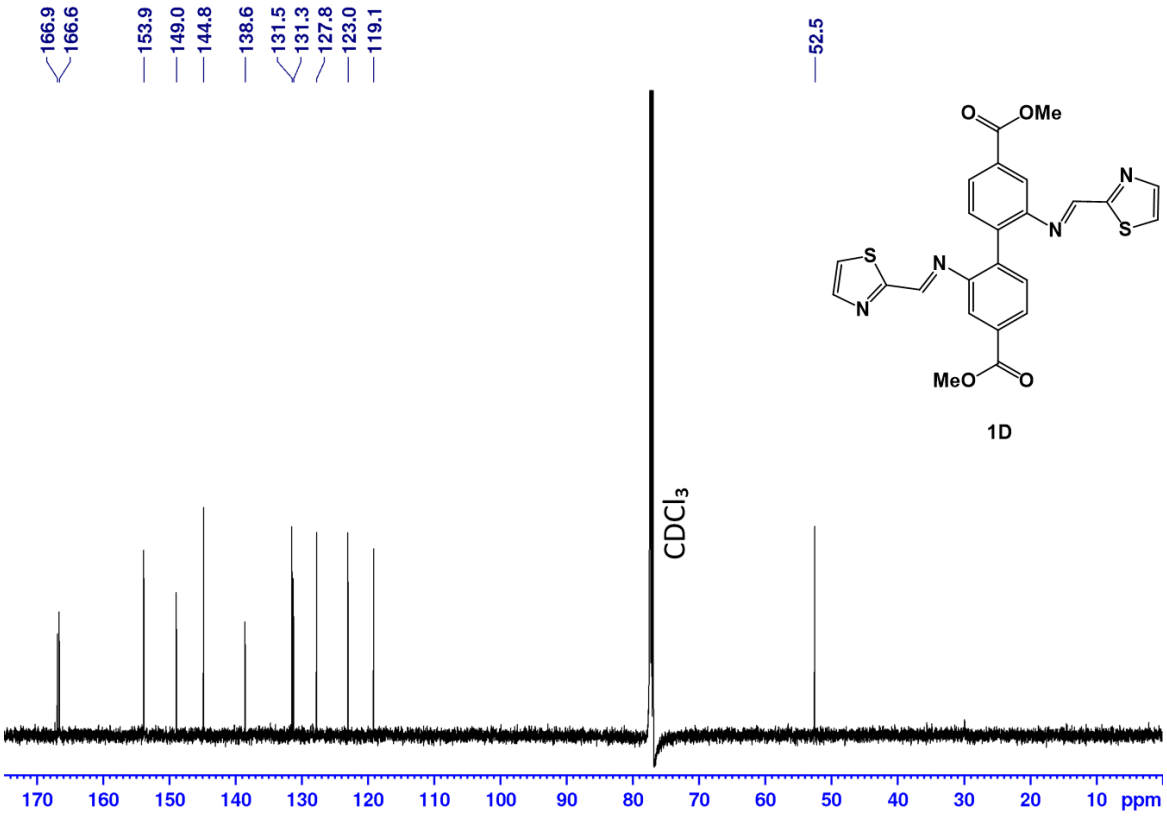

Figure S34 ^{13}C-NMR spectrum for compound **1D** (600 MHz, $CDCl_3$).

Compound 17D

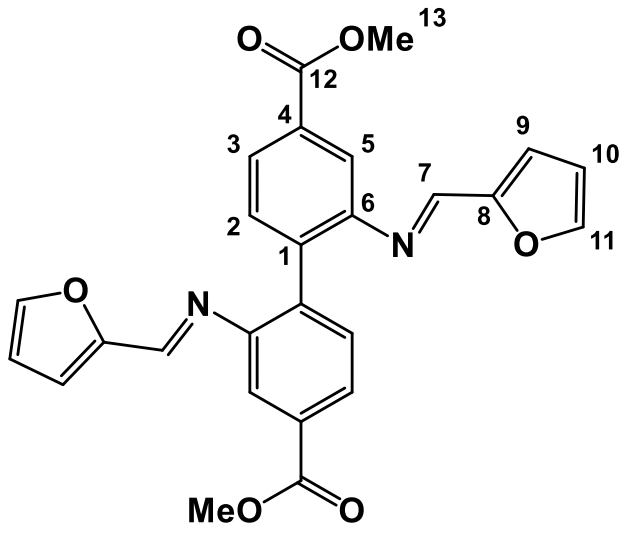

17D

Dimethyl 2,2'-diaminobiphenyl-4,4'-dicarboxylate (100 mg, 0.33 mmol, 1.0 equiv.), zinc acetate dihydrate (73 mg, 0.33 mmol, 1.0 equiv.) and furfural (35 mg, 0.36 mmol, 1.1 equiv.) were mixed in methanol (4 mL) and left to stir at room temperature overnight. The precipitate was filtered and dried in a vacuum oven at 60°C for two hours yielding **17D** as a light green solid (130 mg, 0.28 mmol, 86% of theoretical, based on aldehyde). ^{1}H-NMR (600 MHz, d_6-DMSO) δ 8.18 (s, 2H, H7), 7.87 (dd, J = 7.9 and 1.7 Hz, 2H, H3), 7.83 (m, 2H, H11), 7.61 (d, J = 1.6 Hz, 2H, H5), 7.50 (d, J 7.9 Hz, 2H, H2), 6.87 (dd, J = 3.4 Hz, J = 0.5 Hz, 2H, H9), 6.61 (dd, J = 3.4, 1.7 Hz, 2H, H10), 3.89 (s, 6H, H13); ^{13}C-NMR (151 MHz, d_6-DMSO) δ 166.4 (C12), 152.0 (C8), 151.3 (C6), 150.1 (C7), 147.1 (C11), 138.5 (C1), 131.7 (C2), 130.9 (C4), 126.2 (C3), 119.1 (C5), 118.2 (C9), 112.9 (C10), 52.8 (C13); LRMS (ESI/Q-TOF): m/z (%): 479.121 (100) $[M + Na]^+$; HRMS (ESI/Q-TOF): $[M + Na]^+$ m/z calcd. for $C_{26}H_{20}N_2NaO_6$: 479.1214. Found 479.1213; Anal. Calcd for $C_{26}H_{20}N_2O_6$: C 68.42, H, 4.42, N 6.14; Found C, 67.80, H, 5.21, N 6.09 %.

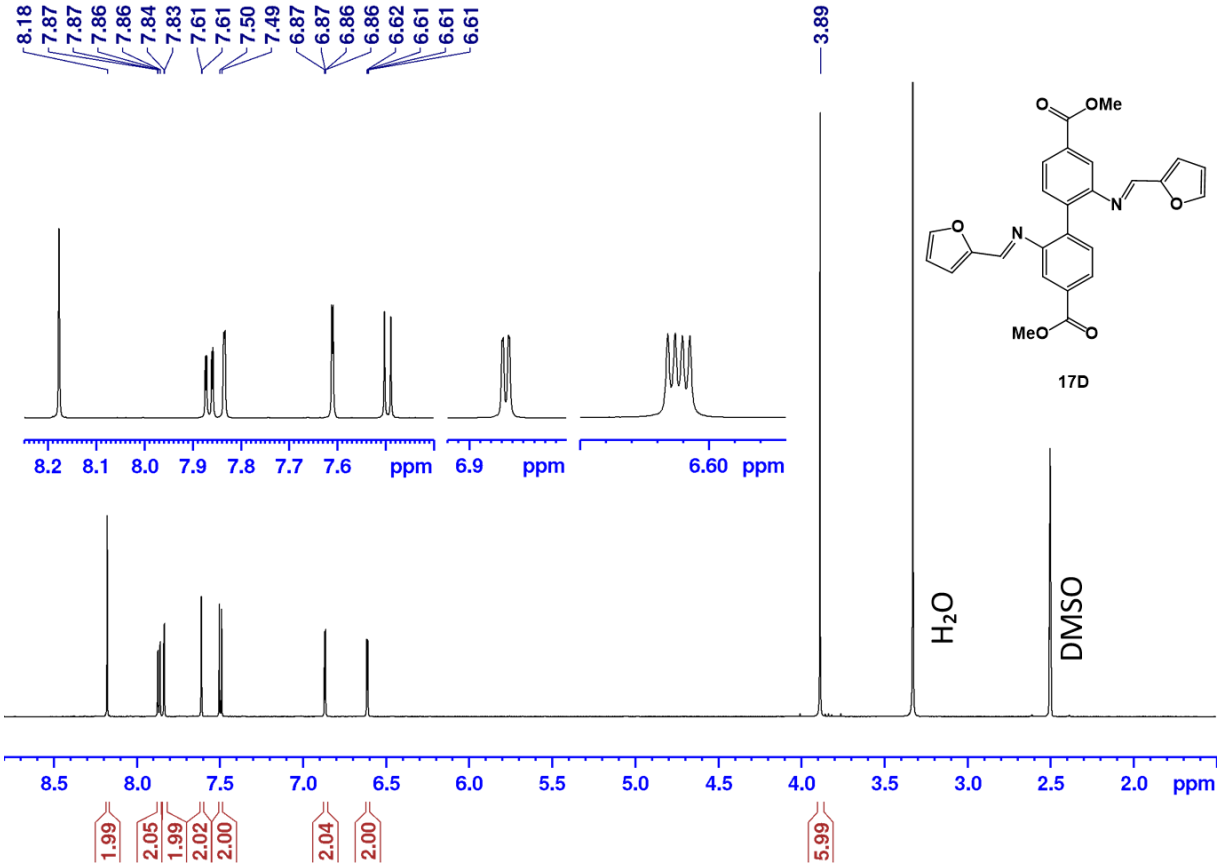

Figure S35 ^{1}H-NMR spectrum for compound **17D** (600 MHz, d_6-DMSO).

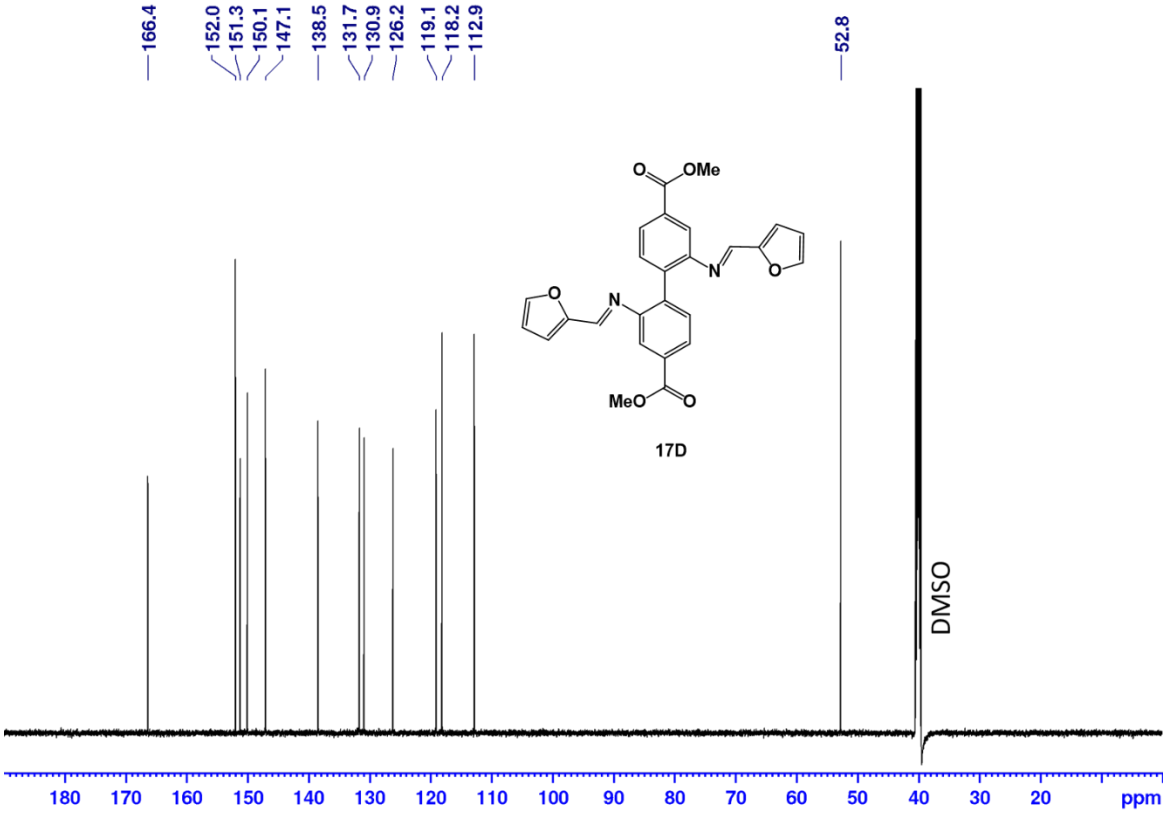

Figure S36 ^{13}C-NMR spectrum for compound 1**7D** (600 MHz, d_6-DMSO).

Crystallographic data

Table S1 Crystal and refinement data for **1-CuI**, **2** and **6**.

	1-CuI	**2**	**6**
Crystal data			
Chemical formula	$C_{24}H_{23}CuIN_5O_4S$	$C_{22}H_{18}BrN_3O_4$	$C_{20}H_{22}N_2O_4$
M_R	667.97	468.30	354.39
Crystal system, space group	Triclinic, $P^{-}1$	Monoclinic, *C*2/*c*	Monoclinic, $P2_1/c$
Temperature (K)	100	100	100
a, b, c (Å)	8.0374 (4), 11.6978 (5), 14.5335 (7)	31.0160 (19), 7.7802 (5), 22.1756 (14)	15.4871(11), 7.1292(5), 16.7429(11)
α, β, γ (°)	103.517 (1), 91.611 (1), 101.739 (1)	90, 130.465 (1), 90	90, 112.786(2), 90
V (Å3)	1296.68 (11)	4071.2 (4)	1704.3(2)
Z	2	8	4
Radiation type	Mo *K*α	Mo *K*α	Mo Kα
μ (mm^{-1})	2.15	2.05	0.097
Crystal size (mm)	0.43 × 0.31 × 0.07	1.2 × 0.2 × 0.1	0.3 × 0.06 × 0.02
Data collection			
Diffractometer	Bruker Photon 100 area detector	Bruker D8 Venture	Bruker D8 Venture
Absorption correction	Multi-scan *SADABS*	Multi-scan *SADABS2016*/2 (Bruker,2016/2) was used for absorption correction. wR2(int) was 0.1341 before and 0.0552 after correction. The Ratio of minimum to maximum transmission is 0.6372. The l/2 correction factor is Not present.	Multi-scan *SADABS2016*/2 (Bruker,2016/2) was used for absorption correction. wR2(int) was 0.1014 before and 0.0563 after correction. The Ratio of minimum to maximum transmission is 0.9346. The l/2 correction factor is Not present.
T_{min}, T_{max}	0.453, 0.860	0.475, 0.746	0.696, 0.745
No. of measured, independent and observed [I > 2σ(I)] reflections	54757, 7979, 7567	41542, 6244, 4966	12815, 2092, 1650
R_{int}	0.101	0.164	0.052
Θ_{max} (°)	-	-	22.0
$(\sin \theta/\lambda)_{max}$ ($Å^{-1}$)	0.716	0.717	0.528
Refinement			
$R[F^2 > 2\sigma(F^2)]$, $wR(F^2)$, S	0.027, 0.072, 1.06	0.054, 0.153, 1.03	0.0436, 0.1085,
No. of reflections	7979	6244	2092
No. of parameters	332	279	239
H-atom treatment	H atoms treated by a mixture of independent and constrained refinement	H atoms treated by a mixture of independent and constrained refinement	H-atom parameters constrained
		$w = 1/[s^2(F_o^2) + (0.0662P)^2 + 11.7604P]$ where $P = (F_o^2 + 2F_c^2)/3$	
$\Delta\rho_{max}$, $\Delta\rho_{min}$ (E $Å^{-3}$)	1.07, -1.79	2.22, -1.77	0.54, -0.52

Computational details

The Gaussian16 program was used to fully optimize the structures at DFT level without geometry and symmetry limitations.[6] For the geometry optimization, the PBE0 functional using the 6-311+G** basis-set was chosen after a benchmark,[7,8] in which the distances and angles of the optimized structure were compared to the ones of a Single Crystal-XRD structure. The 6-311+G** basis-set was used for all atoms and it is of a split-valence triple-ζ quality and includes diffuse functions as well as polarization functions to all atoms used. The M06 functional using the def-2svp basis-set was selected for all TD-DFT calculations after a thorough method benchmarking,[9,10] in which the electronic excitation bands were compared to the ones found experimentally. For higher numerical accuracy in all calculations, the integration ultrafine pruned grid was used (99 590). Implicit solvation using the SMD method was added in both geometry optimization and TD-DFT calculations.[11] Vibrational frequencies were calculated, in order to confirm that the optimized geometry is that of an energy minimum, that is, no imaginary frequencies could be found.

Geometry optimization benchmarking

The crystal structure of compound **6** was used as a starting point for all geometry optimizations. PBE0 and B3LYP both with and without GD3BJ empirical dispersion were considered due to their known accuracy and low computational cost.[7,12–14] Those functionals were used with the split valence and triple-ζ Karlsruhe basis-sets (def-2svp, def-2tzvp), and the split-valence triple-ζ Pople basis-set including diffuse function (6-311+G**). All basis-sets used included polarization functions on all atoms (H, C ,N, O). All C-C, C-N, C-O bond distances, and the dihedral angles from the diazepine ring for the optimized geometries were measured and are listed in Table S3. All bond distances and four dihedral angles compared to those of crystal structure were calculated and the RMSD is shown in Table S2 and Figure S37. The PBE0 method with the 6-311+G** basis-set was chosen since it has the lowest RMSD values while using a relatively low computational time (41 h).

Table S2 Root-mean-square deviations (RMSD) values, energies, and CPU job time for the different method and basis-set combinations benchmarked.

Method	Basis-set	RMSD (bond distances)	RMSD (dihedral angles)	RMSD (bond distances + dihedral angles)	Energy [Hartree]	Job CPU time [h]
B3LYP	def-2svp	0.0131	12.6	4.45	-1184.957862	10
	def-2tzvp	0.00944	10.6	3.76	-1186.267151	211
	6-311+G**	0.0115	10.3	3.64	-1186.135829	54
B3LYP-gd3bj	def-2svp	0.0121	14.0	4.95	-1185.060894	10
	def-2tzvp	0.00865	10.9	3.85	-1186.370728	138
	6-311+G**	0.0104	10.5	3.70	-1186.239194	55
PBE0	def-2svp	0.0114	11.0	3.90	-1183.623501	14
	def-2tzvp	0.00875	9.38	3.32	-1184.898676	130
	6-311+G**	0.00877	9.08	3.21	-1184.768402	41
PBE0-gd3bj	def-2svp	0.0113	11.8	4.19	-1183.678300	9
	def-2tzvp	0.00890	9.67	3.42	-1184.953768	159
	6-311+G**	0.00868	9.30	3.29	-1184.823412	63

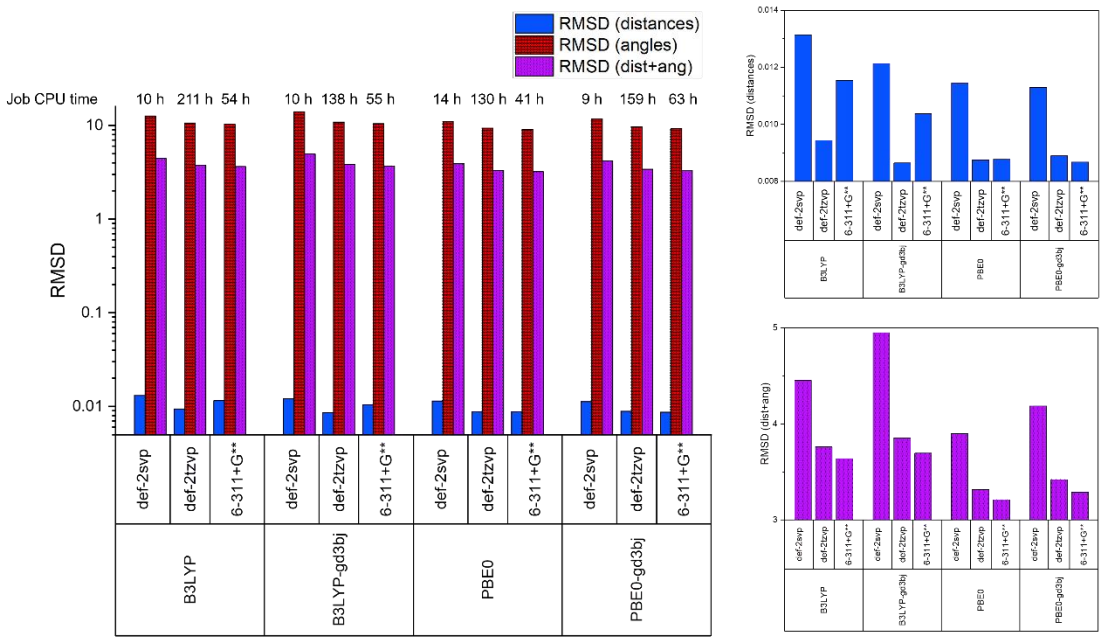

Figure S37 Left: RMSD values for the different method and basis-set combinations benchmarked (note the logarithmic scale). Right, top: RMSD for the distances. Right, bottom: sum of RMSD for the bond distances and dihedral angles for the benchmarked combinations.

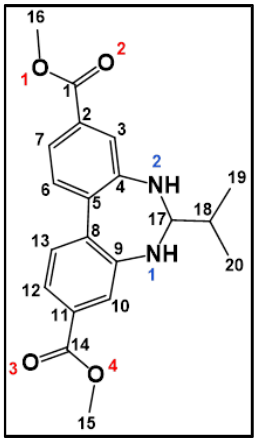

Figure S38 Numbering of carbons (black), oxygens (red) and nitrogens (blue) on **6** used for benchmarking.

Table S3 Distances and dihedral angles measured for the geometry optimization structures and the obtained SC-XRD structure.

Method	B3LYP			B3LYP-GD3BJ			PBE0			PBE0-GD3BJ			Crystal Structure
Basis-set	def-2svp	def-2tzvp	6-311+G**	def-2svp	def-2tzvp	6-311+G**	def-2svp	def-2tzvp	6-311+G**	def-2svp	def-2tzvp	6-311+G**	
Distance													Distance (Å)
C1-O1	1.348	1.349	1.351	1.347	1.348	1.351	1.339	1.340	1.341	1.338	1.339	1.341	1.34
C1-O2	1.210	1.209	1.211	1.211	1.209	1.211	1.207	1.205	1.207	1.207	1.205	1.207	1.206
C1-C2	1.492	1.488	1.490	1.490	1.486	1.487	1.487	1.483	1.484	1.486	1.482	1.483	1.479
C2-C3	1.390	1.382	1.385	1.390	1.381	1.385	1.386	1.378	1.381	1.386	1.378	1.381	1.375
C2-C7	1.405	1.398	1.401	1.404	1.397	1.400	1.400	1.394	1.397	1.400	1.393	1.396	1.392
C3-C4	1.414	1.405	1.408	1.412	1.403	1.406	1.410	1.401	1.404	1.409	1.400	1.403	1.403
C4-C5	1.430	1.420	1.422	1.428	1.418	1.420	1.425	1.415	1.418	1.424	1.414	1.417	1.419
C4-N2	1.378	1.381	1.387	1.377	1.381	1.386	1.370	1.375	1.380	1.370	1.374	1.380	1.37
C5-C6	1.416	1.409	1.413	1.415	1.408	1.412	1.412	1.405	1.409	1.411	1.405	1.408	1.414
C5-C8	1.488	1.484	1.488	1.484	1.481	1.484	1.483	1.479	1.482	1.481	1.477	1.480	1.501
C6-C7	1.387	1.378	1.382	1.386	1.377	1.381	1.383	1.375	1.379	1.383	1.375	1.378	1.372
C8-C9	1.421	1.412	1.415	1.419	1.410	1.413	1.417	1.408	1.411	1.415	1.407	1.410	1.413
C8-C13	1.413	1.405	1.409	1.411	1.404	1.407	1.409	1.401	1.404	1.408	1.400	1.403	1.401
C9-C10	1.401	1.393	1.396	1.399	1.390	1.394	1.397	1.389	1.392	1.396	1.388	1.391	1.392
C9-N1	1.403	1.403	1.406	1.401	1.401	1.404	1.394	1.395	1.398	1.393	1.394	1.397	1.391
C10-C11	1.398	1.390	1.394	1.397	1.390	1.393	1.393	1.386	1.389	1.393	1.386	1.389	1.379
C11-C12	1.403	1.396	1.399	1.403	1.395	1.399	1.399	1.392	1.395	1.399	1.392	1.395	1.396
C11-C14	1.490	1.486	1.487	1.488	1.483	1.485	1.485	1.481	1.482	1.484	1.480	1.481	1.476
C12-C13	1.390	1.383	1.386	1.390	1.382	1.386	1.387	1.380	1.383	1.387	1.380	1.383	1.373
C14-O3	1.211	1.209	1.212	1.211	1.209	1.211	1.207	1.206	1.208	1.207	1.206	1.208	1.214
C14-O4	1.348	1.349	1.352	1.348	1.348	1.351	1.339	1.340	1.342	1.339	1.340	1.341	1.343
C15-O4	1.425	1.434	1.438	1.424	1.433	1.437	1.415	1.422	1.425	1.415	1.422	1.425	1.446
C16-O1	1.425	1.434	1.438	1.424	1.433	1.437	1.415	1.422	1.425	1.414	1.422	1.424	1.444
C17-N1	1.465	1.472	1.477	1.464	1.471	1.476	1.456	1.463	1.467	1.456	1.463	1.466	1.463
C17-N2	1.445	1.444	1.449	1.443	1.441	1.446	1.435	1.434	1.438	1.434	1.433	1.437	1.427
C17-C18	1.548	1.543	1.546	1.543	1.537	1.540	1.539	1.533	1.536	1.536	1.530	1.533	1.524
C18-C19	1.535	1.533	1.537	1.533	1.531	1.535	1.527	1.525	1.528	1.526	1.524	1.527	1.518
C18-C20	1.533	1.531	1.535	1.531	1.528	1.532	1.525	1.522	1.525	1.524	1.521	1.524	1.524
Dihedral angle													Dihedral angle (°)
C9-N1-C17-C18	-154.24	-151.02	-150.00	-153.42	-149.63	-148.57	-152.73	-149.47	-148.48	-152.06	-148.65	-147.60	-147.82
C4-N2-C17-C18	202.97	200.34	199.87	206.02	200.90	200.18	199.92	197.94	197.51	201.72	198.51	197.89	179.52
N1-C17-C18-C19	-57.21	-55.09	-54.59	-57.59	-55.69	-55.19	-57.42	-55.28	-54.81	-57.64	-55.60	-55.13	-52.75
N2-C17-C18-C19	66.36	69.42	70.00	66.00	68.77	69.34	66.28	69.41	69.94	66.13	69.04	69.59	71.26

Functional benchmarking

To benchmark the functional used in the TD-DFT calculations, the experimental UV-Vis spectrum of **6** in acetonitrile was used as reference. A range of both pure and hybrid functionals were considered (M06-L,[16] ωB97XD,[17] B3LYP,[14] PBE0,[7] M06,[9] ωB97X,[18] LC-ωPBE,[19] CAM-B3LYP,[20] BHandH,[21] BHandHLYP[21] and M06-2X[9]). All functionals were benchmarked using the def-2svp basis-set.[10] The TD-DFT calculations used the structure optimized with the PBE0/6-311+G** functional and basis-set. The calculated bands from the TD-DFT calculations are shown in Figure S39, Figure S40 and Figure S41. The calculated bands show that the use of the pure M06L functional results in red-shifted bands in the visible range, as well as blue-shifted bands in the UV range. The bands calculated by the CAM-B3LYP, M06-2X, BHandH, BHandHLYP and LC-ωPBE functionals have strong blue-shifts compared to the experimental data, resulting in a RMSD of respectively, 31, 33, 36, 37 and 47 nm. The calculated bands by the M06 functional are in accordance with the ones found experimentally, having a RMSD of 6 nm. Changing the basis-set to the triple-ζ def-2tzvp basis-set yielded marginally better results (RMSD = 5 nm). However, the computational time increased from 8 h to 158 h. The bands calculated by the B3LYP functional were in good agreement with the UV bands observed experimentally. However, the band in the visible range was red-shifted by ca. 15 nm, yielding a RMSD of 8 nm. While the bands calculated with the PBE0 functional over 300 nm are in good agreement with the ones found experimentally, all bands in the UV region are slightly blue-shifted, yielding a RMSD of 8 nm. The inclusion of empirical dispersion with the ωB97XD functional (RMSD = 32 nm) results in bands that are less blue-shifted than with the ωB97X functional (RMSD = 42 nm). A visual representation of the RMSD and MAE for the benchmarked functionals is shown in Figure S42. M06 was chosen as the functional for further computations , as it showed the best agreement with the experimental UV-Visible spectrum.

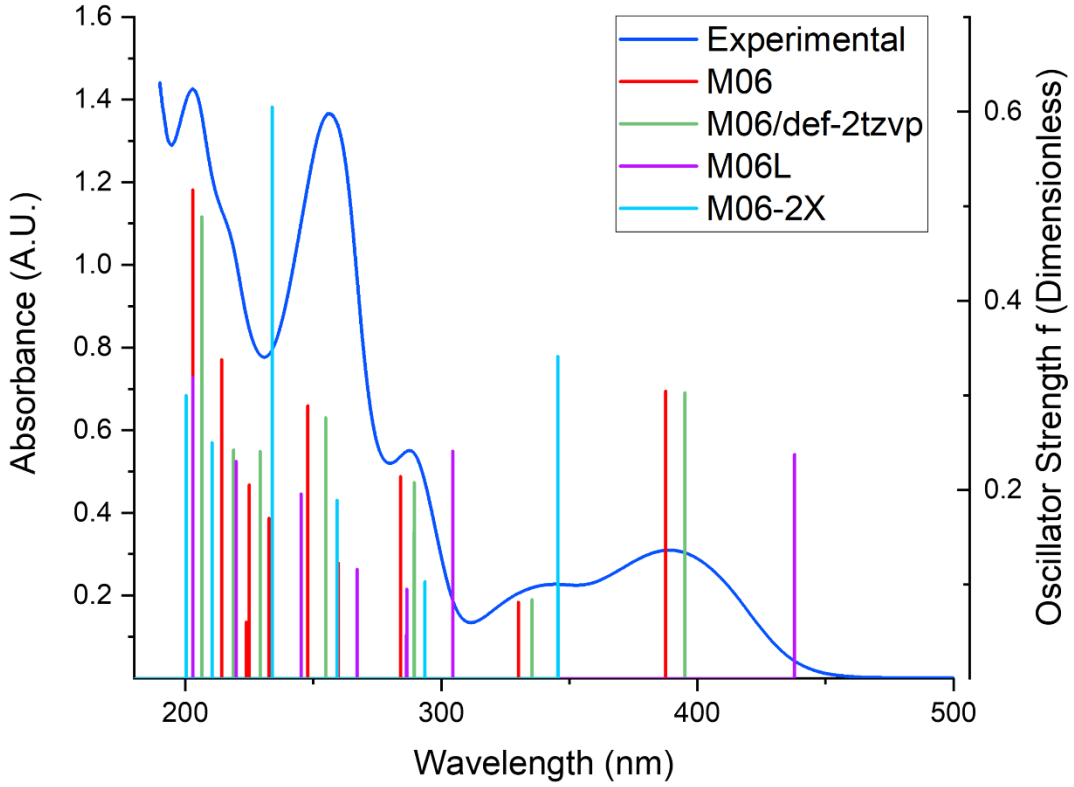

Figure S39 Experimental UV-Visible spectrum of **6** in MeCN and TD-DFT bands calculated for the Minnesota benchmarked functionals.

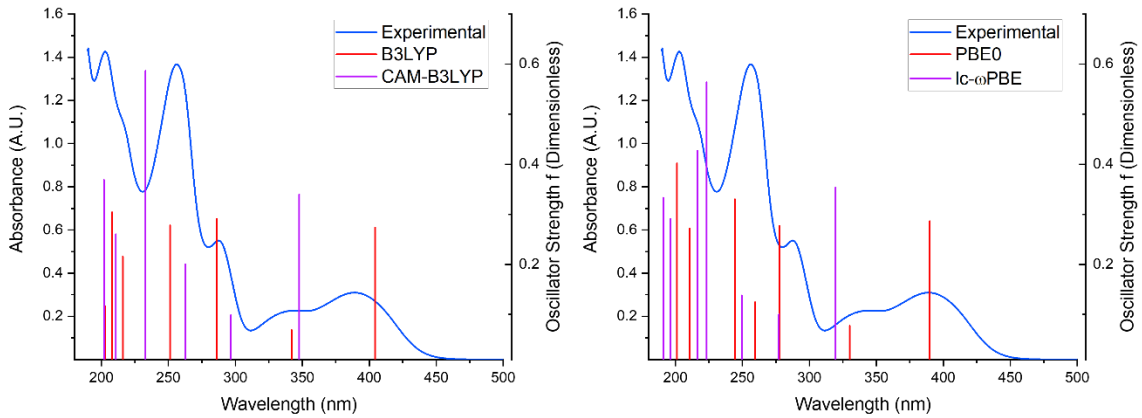

Figure S40 Experimental UV-Visible spectrum of **6** in MeCN and TD-DFT bands calculated for benchmarked functionals. Left: B3LYP and CAM-B3LYP.Right: PBE0 and LC-ωPBE.

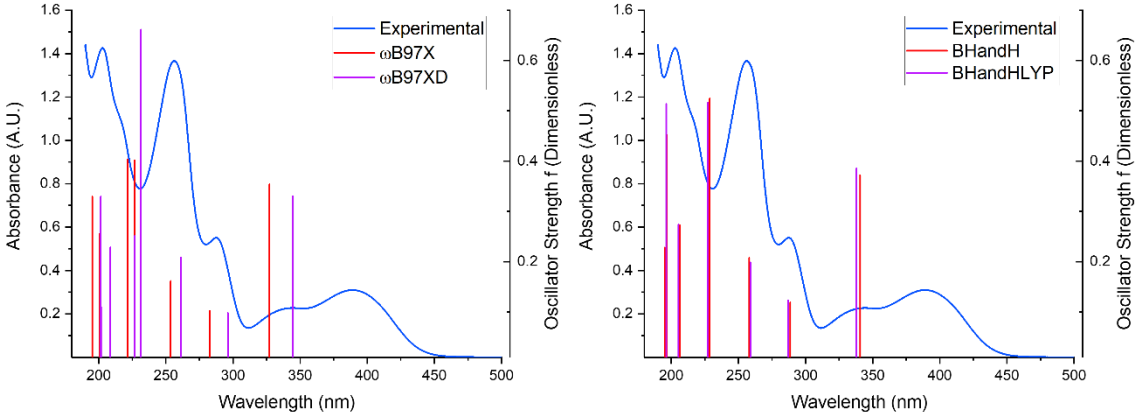

Figure S41 Experimental UV-Visible spectrum of **6** in MeCN and TD-DFT bands calculated for benchmarked functionals. Left: ωB97X and ωB97XD . Right: BHandH and BHandHLYP.

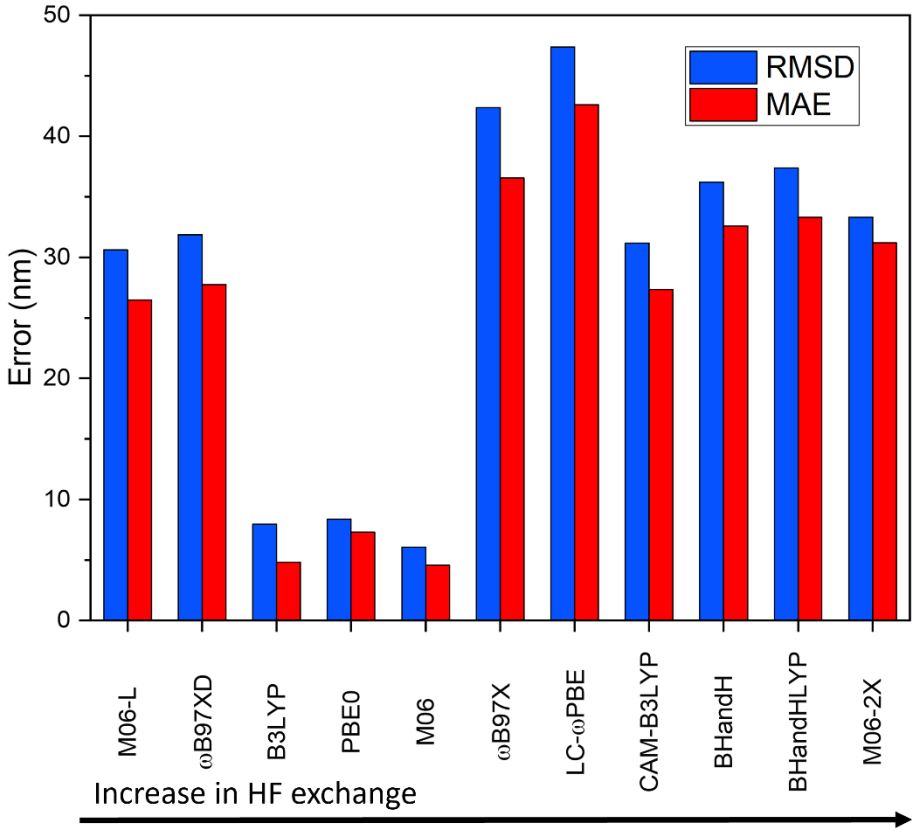

Figure S42 Root-mean-square deviation (RMSD) and mean absolute error (MAE) in nm for the series of functionals employed for the benchmarking, arranged in order of increasing HF exchange percentage.

TD-DFT calculations

The TD-DFT(M06) calculation using implicit solvation (MeCN) for the starting material (**SM**) together with the calculated molecular orbitals involved in the main electronic transitions are shown in Figure S43.

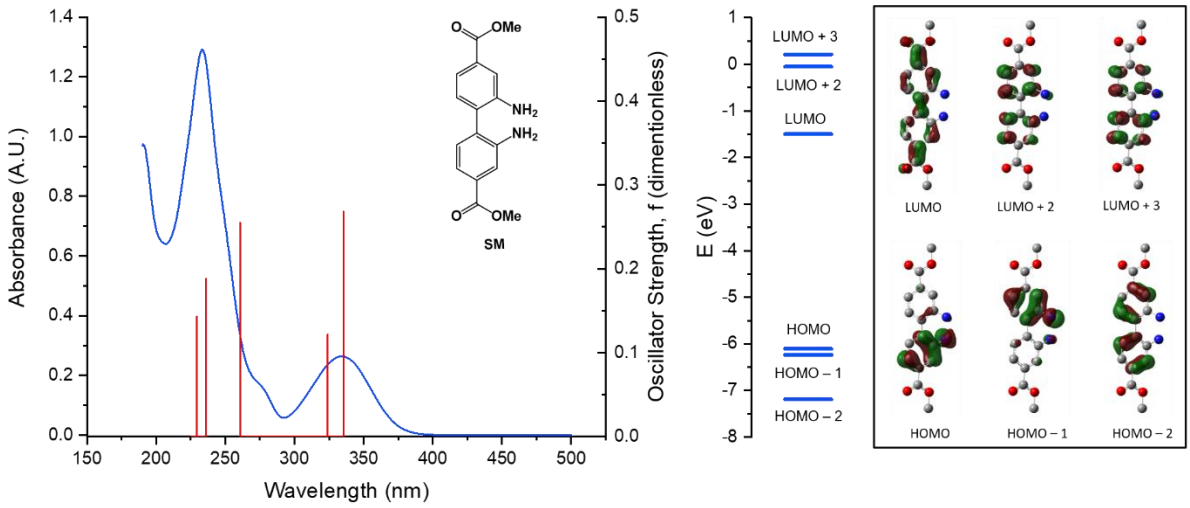

Figure S43 Left: Experimental UV-Visible spectrum of **SM** in MeCN (blue curve) and the main TD-DFT(M06) electronic excitations (red lines). Right: Calculated molecular orbitals for **SM** in MeCN and frontier orbitals involved in the main TD-DFT(M06) electronic transitions, see Table 4 in the main text for more details. Hydrogens were omitted for clarity. Frontier orbitals are shown with an isovalue of 0.05 a.u.

Optimized geometries and energies (Hartree)

SM E = -1028.918305

C	-3.98216400	1.35218600	-0.44589500
C	-2.65697700	1.36108200	-0.89668900
C	-1.91002600	2.52509200	-0.95690800
C	-2.49664400	3.73055600	-0.56685200
C	-3.81911000	3.75282100	-0.13774200
C	-4.57780300	2.57889500	-0.07964800
H	-2.20220800	0.41798900	-1.18368000
H	-0.87991200	2.50933500	-1.29321300
H	-4.28368100	4.69121200	0.14618600
C	-4.71210800	0.06174100	-0.40406400
C	-4.77231000	-0.71338100	-1.56854000
C	-5.27659900	-0.45540700	0.78666300
C	-5.36588100	-1.96353200	-1.59219200
H	-4.34108900	-0.30918500	-2.47933000
C	-5.87222400	-1.72325600	0.75461100
C	-5.91763900	-2.47306500	-0.41501500
H	-5.40813500	-2.54453100	-2.50602900
H	-6.29764700	-2.12090100	1.67005800
C	-6.54978900	-3.81670500	-0.45805100
O	-6.62756000	-4.49874700	-1.45622900
O	-7.02818100	-4.20171100	0.72640900
C	-1.67625800	4.96716100	-0.63479400
O	-0.52453000	4.99811100	-1.00895000
O	-2.34329100	6.05205800	-0.23748300
C	-1.62014700	7.28645900	-0.27325800
H	-1.30054400	7.51485600	-1.29213500
H	-2.31714300	8.04465500	0.08046300
H	-0.74909900	7.24017300	0.38359000
C	-7.65318200	-5.48842800	0.76650700
H	-7.97099700	-5.62793500	1.79867200
H	-8.51731800	-5.51623800	0.09948900
H	-6.94430600	-6.26871100	0.48205200
N	-5.17435800	0.21922800	1.99185200
H	-5.28571600	1.22600400	1.92771800
H	-5.75813200	-0.16549100	2.72301900
N	-5.88439900	2.62568600	0.38372500
H	-6.29359400	3.55052300	0.39375800
H	-6.51345900	1.94476700	-0.02342500

6 E = -1184.768402

O	1.28003000	5.99305900	9.86080900
O	8.13798400	-2.19344600	12.43281000
O	9.96856700	-0.91507300	12.24175400
O	2.64101100	7.04401700	8.42480800
N	8.24751600	3.28765300	9.95249000
H	9.23875000	3.30618700	10.15136100
N	6.76472300	4.25957000	8.32147600
H	6.89259100	5.19663600	7.97437700
C	7.87952600	-0.07024000	11.46182000
C	3.39573500	5.04405500	9.48784500
C	7.65782400	2.12163900	10.44837400
C	5.33743700	3.04281100	9.95840100
C	6.51673400	-0.29622700	11.26768500
H	6.07778900	-1.24379300	11.55382500
C	5.60957900	4.10495900	9.05997500
C	4.61835000	5.07591600	8.84568800
H	4.80635300	5.88478500	8.14553000
C	6.26225700	1.94810300	10.33484100
C	4.08521800	3.05247000	10.60327200
H	3.88916100	2.28300400	11.34077800
C	3.12067500	4.01401300	10.38999500
H	2.17985300	3.98667100	10.92415800
C	5.73744100	0.70071100	10.70956500
H	4.68047600	0.51285500	10.55796400
C	7.98032200	3.51958500	8.52906000
H	7.86386900	2.54054000	8.04026400
C	8.43842900	1.12585000	11.02867300
H	9.50950500	1.26783400	11.14129100
C	2.43162600	6.13122000	9.18687700
C	8.78281800	-1.07252800	12.07487800
C	9.14488300	4.24658300	7.84114400
H	8.77718600	4.47719900	6.83271600
C	8.95057900	-3.20027500	13.03022300
H	9.73410600	-3.52106400	12.34059800
H	8.27824400	-4.02643500	13.25521700
H	9.41621700	-2.82573600	13.94414300
C	10.35672400	3.33311700	7.68669900
H	10.80090200	3.07059300	8.65356000
H	11.13666000	3.83034500	7.10377900
H	10.09570700	2.40177400	7.17626600
C	9.52590700	5.55790500	8.52696400
H	8.67297300	6.22887100	8.66302500
H	10.27277800	6.08922700	7.93066200
H	9.95866600	5.38519000	9.51700700
C	0.30679000	7.00544100	9.61918100
H	0.02737900	7.02551300	8.56375200
H	0.69509600	7.98657600	9.90029300
H	-0.55083100	6.74307900	10.23632600

References

1 K. T. Hylland, S. Øien-Ødegaard, R. H. Heyn and M. Tilset, *Eur. J. Inorg. Chem.*, 2020, **2020**, 3627–3643.
2 G. R. Fulmer, A. J. M. Miller, N. H. Sherden, H. E. Gottlieb, A. Nudelman, B. M. Stoltz, J. E. Bercaw and K. I. Goldberg, *Organometallics*, 2010, **29**, 2176–2179.
3 G. M. Sheldrick, *Acta Crystallogr. Sect. Found. Adv.*, 2015, **71**, 3–8.
4 G. M. Sheldrick, *Acta Crystallogr. Sect. C Struct. Chem.*, 2015, **71**, 3–8.
5 O. V. Dolomanov, L. J. Bourhis, R. J. Gildea, J. a. K. Howard and H. Puschmann, *J. Appl. Crystallogr.*, 2009, **42**, 339–341.
6 M. J. Frisch, G. W. Trucks, H. B. Schlegel, G. E. Scuseria, M. A. Robb, J. R. Cheeseman, G. Scalmani, V. Barone, G. A. Petersson, H. Nakatsuji, X. Li, M. Caricato, A. V. Marenich, J. Bloino, B. G. Janesko, R. Gomperts, B. Mennucci, H. P. Hratchian, J. V. Ortiz, A. F. Izmaylov, J. L. Sonnenberg, D. Williams-Young, F. Ding, F. Lipparini, F. Egidi, J. Goings, B. Peng, A. Petrone, T. Henderson, D. Ranasinghe, V. G. Zakrzewski, J. Gao, N. Rega, G. Zheng, W. Liang, M. Hada, M. Ehara, K. Toyota, R. Fukuda, J. Hasegawa, M. Ishida, T. Nakajima, Y. Honda, O. Kitao, H. Nakai, T. Vreven, K. Throssell, J. A. Montgomery Jr., J. E. Peralta, F. Ogliaro, M. J. Bearpark, J. J. Heyd, E. N. Brothers, K. N. Kudin, V. N. Staroverov, T. A. Keith, R. Kobayashi, J. Normand, K. Raghavachari, A. P. Rendell, J. C. Burant, S. S. Iyengar, J. Tomasi, M. Cossi, J. M. Millam, M. Klene, C. Adamo, R. Cammi, J. W. Ochterski, R. L. Martin, K. Morokuma, O. Farkas, J. B. Foresman and D. J. Fox, *Gaussian 16, Revision C.01*, Gaussian Inc., Wallingford CT, 2016.
7 C. Adamo and V. Barone, *J. Chem. Phys.*, 1999, **110**, 6158–6170.
8 R. Krishnan, J. S. Binkley, R. Seeger and J. A. Pople, *J. Chem. Phys.*, 1980, **72**, 650–654.
9 Y. Zhao and D. G. Truhlar, *Theor. Chem. Acc.*, 2008, **120**, 215–241.
10 F. Weigend and R. Ahlrichs, *Phys. Chem. Chem. Phys.*, 2005, **7**, 3297–3305.
11 A. V. Marenich, C. J. Cramer and D. G. Truhlar, *J. Phys. Chem. B*, 2009, **113**, 6378–6396.
12 S. Grimme, S. Ehrlich and L. Goerigk, *J. Comput. Chem.*, 2011, **32**, 1456–1465.
13 J. Wang and B. Durbeej, *J. Comput. Chem.*, 2020, **41**, 1718–1729.
14 A. D. Becke, *J. Chem. Phys.*, 1993, **98**, 5648–5652.
15 A. Schäfer, H. Horn and R. Ahlrichs, *J. Chem. Phys.*, 1992, **97**, 2571–2577.
16 Y. Zhao and D. G. Truhlar, *J. Chem. Phys.*, 2006, **125**, 194101.
17 J.-D. Chai and M. Head-Gordon, *Phys. Chem. Chem. Phys.*, 2008, **10**, 6615–6620.
18 J.-D. Chai and M. Head-Gordon, *J. Chem. Phys.*, 2008, **128**, 084106.
19 O. A. Vydrov and G. E. Scuseria, *J. Chem. Phys.*, 2006, **125**, 234109.
20 T. Yanai, D. P. Tew and N. C. Handy, *Chem. Phys. Lett.*, 2004, **393**, 51–57.
21 A. D. Becke, *J. Chem. Phys.*, 1993, **98**, 1372–1377.